Méthodologie pour l'évaluation de la résistance à l'ouverture d'une maille de filet

Barthélémy Morvan

université de bretagne occidentale

UNIVERSITE BRETAGNE LOIRE

THÈSE / UNIVERSITÉ DE BRETAGNE OCCIDENTALE

sous le sceau de l'Université Bretagne Loire

pour obtenir le titre de

DOCTEUR DE L'UNIVERSITÉ DE BRETAGNE OCCIDENTALE

Spécialité : Génie Mécanique

École Doctorale Des Sciences de la Mer

présentée par

Barthélémy Morvan

Préparée au laboratoire Comportement des Structures en Mer à l'Ifremer et à l'Institut de Recherche Dupuy de Lôme à l'ENSTA Bretagne

Méthodologie pour l'évaluation de la résistance à l'ouverture d'une maille de filet

Methodology for the evaluation of the resistance to opening of a netting mesh

Thèse encadrée par :

Daniel PRIOUR
Directeur de laboratoire HDR, Ifremer / *directeur de thèse*

Guilhem BLES
Maître de conférences, ENSTA Bretagne / encadrant

Nicolas DUMERGUE
Ingénieur, Ifremer / encadrant

Thèse soutenue le 06 décembre 2016
devant le jury composé de :

Gérard RIO
Professeur, Université de Bretagne Sud / *président*

Manuel GONZÁLEZ
Ingénieur de recherche, Universidade da Coruña / *rapporteur*

Frédéric MUTTIN
Enseignant chercheur HDR, EIGSI / *rapporteur*

Barry O'NEILL
Ingénieur de recherche, Marine Scotland Science / *examinateur*

Jean-Yves BILLARD
Professeur, École Navale / *examinateur*

Blaise NSOM
Professeur, Université de Bretagne Occidentale / *examinateur*

Mariko DUNSEATH-TERAO
Professeur, Institut de Physique de Rennes / *examinatrice*

Daniel PRIOUR
Directeur de laboratoire HDR, Ifremer / *directeur de thèse*

DOCTORAL THESIS
of UNIVERSITÉ DE BRETAGNE OCCIDENTALE

for Université Bretagne Loire

École Doctorale Des Sciences de la Mer

Speciality:

Mechanical Engineering

Presented and defended by:

Barthélémy MORVAN

the 6th December 2016

Methodology for the evaluation of the resistance to opening of a netting mesh.

Jury:

Pr. Gérard Rio	Université de Bretagne Sud	*Jury president*
Dr. Manuel González	Universidade da Coruña	*Thesis referee*
Dr. Frédéric Muttin	EIGSI	*Thesis referee*
Dr. Barry O'Neill	Marine Scotland Science	
Pr. Jean-Yves Billard	École Navale	
Pr. Blaise Nsom	Université de Bretagne Occidentale	
Pr. Mariko Dunseath-Terao	Institut de Physique de Rennes	
Dr. Daniel Priour	Ifremer	*Doctoral supervisor*

Supervision:

Dr. Daniel Priour	Ifremer	*Doctoral supervisor*
Dr. Guilhem Bles	ENSTA Bretagne	
Mr. Nicolas Dumergue	Ifremer	

Ifremer

IRDL
Institut de Recherche Dupuy de Lôme
CNRS FRE 3744

UBO
Université de Bretagne Occidentale

École Doctorale des Sciences de la Mer

Région Bretagne

À mon grand-père

Remerciements

Pour commencer, et pour être certain de n'oublier personne, je remercie tous ceux et celles qui ont contribué à la réussite de cette thèse.

Je remercie les membres du jury d'avoir participé à ma soutenance, Gérard Rio qui m'a fait l'honneur de présider mon jury, et Manuel González et Frédéric Muttin qui ont accepté d'être rapporteurs.

Merci à Daniel Priour, le directeur de cette thèse. Merci pour sa disponibilité et la confiance qu'il m'a accordée tout au long de ces trois années. J'espère que le résultat est à la hauteur de ses attentes.

Un grand merci à Guilhem Bles, qui m'a motivé jusqu'au bout. Travailler avec lui a été un réel plaisir. Il est un enseignant pédagogue, un encadrant rigoureux, et un chercheur compétent.

Je remercie également Nicolas Dumergue pour sa participation à ce travail.

Merci à tous les membres des deux laboratoires avec qui j'ai travaillé ou simplement partagé mon quotidien. Je remercie particulièrement Didier, mon voisin de bureau, mon collègue et ami de "galère" ! Je n'oublie pas mes voisins de bureau à l'ENSTA Bretagne, Gaspard, Antoine et Julien.

J'ai eu l'opportunité d'enseigner à l'ENSTA Bretagne durant la thèse. Cela a été un réel plaisir et une expérience très enrichissante. C'est pourquoi je souhaite remercier les différents enseignants référents qui m'ont fait confiance.

Je remercie Ifremer et la Région Bretagne qui ont financé ces travaux.

Merci à mes relecteurs : Daniel, Guilhem, Nicolas et Clarisse.

Un très grand merci à mes parents pour leur encouragement et leur soutien pendant ces années de thèse, et plus largement pendant toute ma scolarité.

Enfin, je souhaite remercier ma compagne, Clarisse, pour tous ces moments d'évasion, pour sa gentillesse et sa grande patience.

Je vous souhaite une bonne lecture !

Barthélémy MORVAN
Brest, le 09 décembre 2016

Contents

List of Figures

List of Tables

CHAPTER

1 Introduction

1.1 General background and motivation

Fisheries and aquaculture remain important sources of food and income for hundreds of millions of people around the world (FAO, 2016). However, despite all the progress in reducing **overfishing** in the last years, several species are still being caught at unsustainable levels: 31.4 % of fish stocks in 2013 were estimated as fished at a biologically unsustainable level and therefore overfished (FAO, 2016).

Thus, to ensure high long-term fishing yields for all stocks and reduce unwanted catches, it is necessary to manage fishing fleets and conserve fish stocks. For this purpose, the **Common Fisheries Policy** (CFP) introduced a fisheries management policy (The European Parliament and the European Council, 11th December 2013). Fisheries management includes **technical measures** to regulate gear usage and where and when fishermen can fish. According to the CFP (The European Parliament and the European Council, 11th December 2013), technical measures can largely be grouped into measures which aim at: limiting catches of small fish (intra-species selectivity), limiting catches of unwanted fish species (inter-species selectivity), limiting catches of protected species (inter-species selectivity), and limiting or preventing damage to parts of the ecosystems. The **selectivity** of fishing gear is its ability to catch only the targeted fishes. To reduce the catch of juvenile fish or unwanted species, the CFP regulates the design and other technical characteristics of the gear (Weissenberger, 2 June 2014). Particularly, the CFP regulates the mesh size to allow smaller fish to escape. However, the mesh size is not the only parameter which determines the catch of one gear. Indeed, the mesh opening varies during a fishing operation, it depends on forces applied on the net (catch, currents, speed of the vessel, towing regularity) and on the twine material: the mesh opening depends on the mesh resistance to opening.

The **mesh resistance to opening** is defined as the relation between the opening

of the mesh and the forces applied on it. Currently, there is no simple methodology for the evaluation of this parameter that could be the basis of regulations for fishing. Indeed, the mesh resistance to opening, that depends on several parameters, is quite difficult to evaluate.

Existing methods for the evaluation of the mesh resistance to opening of nets are based on the solution of the **inverse identification problem**. The inverse identification method consists in finding the inputs of the numerical model, based on the experimental force-displacement responses and the boundary conditions (Uhl, 2007). In case of this study, the searched inputs have to be related to the mesh resistance to opening.

The mechanical structure of twines constituting netting is complex. A netting sample can be described as an assembly of meshes, and the meshes can be considered as assemblies of mesh sides and possibly knots (Fig. 8.1). Several model approaches are possible, depending on the studied basic element: the netting sample, the mesh or the mesh side.

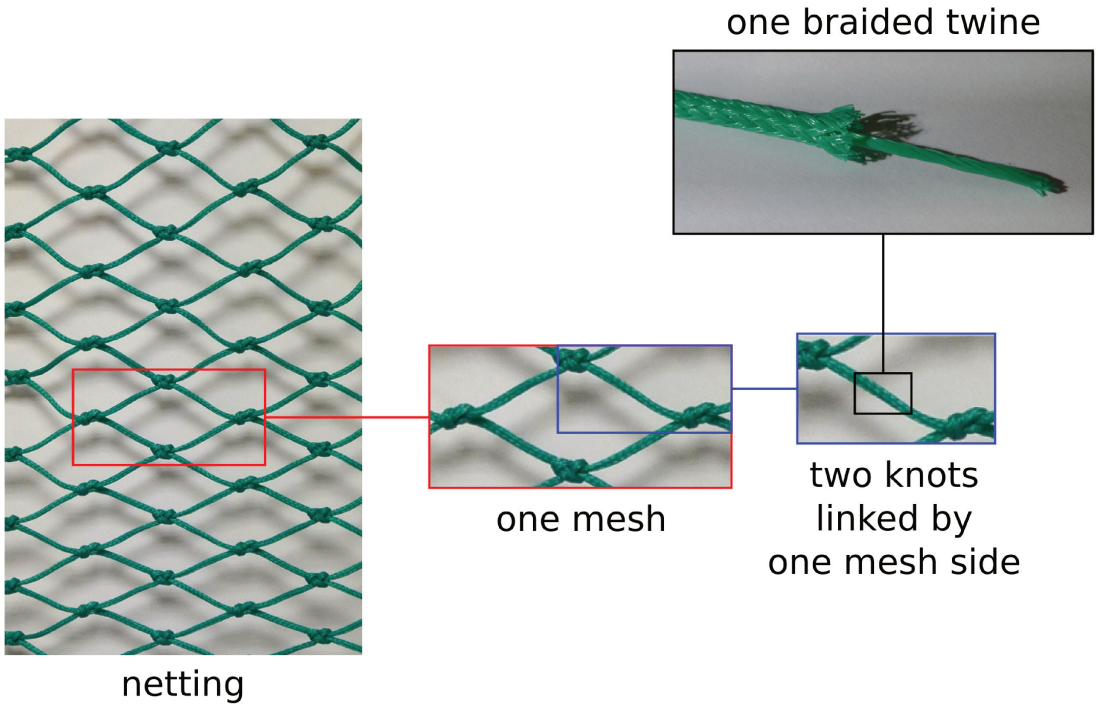

Figure 1.1 – Netting is an assembly of meshes, made up of mesh sides and knots.

Priour (2013), O'Neill (2002) and De la Prada and Gonzales (2013) proposed to model the force-displacement response of one mesh side. By considering that a mesh side behaves like a beam (O'Neill (2002), Sala et al. (2007), De la Prada and Gonzales (2014), Priour (2013)), the **bending stiffness** of the mesh sides appeared to well represent the mesh resistance to opening. Indeed, it was shown that an

increase in twine bending stiffness increased the mechanical resistance of meshes to opening (Sala et al., 2007). Moreover, the influence of the netting bending stiffness on trawl selectivity was demonstrated (Boerema, 1956).

Then, the strong influence of the **codend** on the trawl selectivity was demonstrated (Robertson and Stewart, 1988), even though selectivity in other parts of trawls is increasingly taken into account (Broadhurst et al., 2015). Previous studies showed how the bending stiffness of mesh sides affects the mechanical behaviour, thus the selectivity of codends (Herrmann et al., 2006; Sala et al., 2007). Likewise, Moderhak (2007) theoretically demonstrated how changes in the mesh size and the bending stiffness of mesh sides can impact the shape of a codend and its selectivity. From a theoretical investigation, O'Neill (2003) demonstrated how an increase in twine bending stiffness reduces the diameter of the codend and thus the lateral mesh opening. Bending stiffness may be of significant effects on fish farms: during aquaculture pens towing, the netting sheets parallel and near parallel to the flow experience significant vibration, which in parts is determined by the netting bending stiffness (Johnson and Balash, 2015). Furthermore, bending stiffness is a critical factor to ensure accurate model-test drag measurements on trawl nets (Balash et al., 2016).

Considering these points, and the fact that codends are made from stiffer materials (Herrmann et al., 2006, 2013), it is worthwhile to be able to measure the bending stiffness of mesh sides in fishing nets and in particular in trawl codend nets.

Models and methods were already proposed for the evaluation of the bending stiffness in fishing nets. The best established methods were based on the beam theory (Sala et al., 2007; De la Prada and Gonzales, 2013; Priour and Cognard, 2011). Nevertheless, the existing methods did not allow the identification of the mesh resistance to opening with a simple method or did not take sufficient account of the complexity of the mechanical behaviour. The method presented in Sala et al. (2007) required a complex and expensive device. De la Prada and Gonzales (2013) proposed a method based on suspending tests, but strong assumptions were made. Moreover, the identification strategies of Sala and De la Prada were questionable because of correlations between geometrical parameters. Balash (2012) used the beam model of O'Neill (2002) with its limits. Finally, the method proposed by Priour and Cognard (2011) required closed mesh netting and did not take into account the size of the knots.

1.2 Objectives

The objective of this thesis is to develop and assess a **methodology for the evaluation of the mesh resistance to opening in fishing nets**, and more broadly,

in netting structures. This thesis aims at proposing a simple experimental test that does not require expensive devices to be easily spread in laboratories and in the fishing industry, a simple test combined with a numerical model able to represent the non-linear mechanical behaviour of a tested netting panel. As in the existing methodologies, the inverse identification should be used: the bending stiffness of the model should be adjusted so that the results of the numerical simulations fit the results of the experiments.

1.3 Outline of the thesis

This manuscript is divided into five chapters. In the the **first chapter**, we present the **existing methods** for the assessment of twine bending stiffness. First, three numerical models for the deformation of a mesh side are presented: the analytical model of O'Neill (2002), the fitting model of De la Prada and Gonzales (2013) and the finite triangular element model of Priour (2013). Then, four experimental methods to evaluate the bending stiffness are presented: the method based on the ROD-m prototype of Sala et al. (2007), the suspension of a cylindrical sample of Balash (2012), the simple suspension of a netting sample of De la Prada and Gonzales (2014), and the cantilever netting of Priour and Cognard (2011). Finally, the presented models and experimental methods are discussed.

The **second chapter** deals with the **experimental method**, used and developed by this thesis, and the netting samples. Three types of experiments were performed to evaluate the bending stiffness of twines: a uniaxial tensile test on a classical testing machine, a suspending test of the same type as De la Prada and Gonzales (2014), and a biaxial test close to the one of Sala et al. (2007). A large range of fishing nets commonly used in trawl codends were tested: four materials (three types of polyethylene, polyamide), single and double mesh sides, three sizes of panel (3x3-, 4x10- and 5x25-mesh panels), and a range of mesh side lengths (30, 40, 50 and 60 mm). Finally, the axial stiffness of a polyethylene twine was assessed.

With the **third chapter**, the **experimental results** are given. The objectives of this chapter are to present the mechanical behaviour of netting samples and to compare the results obtained with the three types of experiments. Moreover, the deformation in netting samples and the variation in the results are shown.

The **fourth chapter** describes the **numerical methods** developed during this thesis. First, four models based on the beam theory are presented: a quasi-analytical model for mesh sides, the Timoshenko beam model in the Abaqus Standard Software tool, a finite element model based on corotational 2D beams and a bar element model. Then the inverse identification methods are explained. Regarding the existing methods for the assessment of the bending stiffness of mesh sides in netting

panels, the possible advantages of finite element methods are shown in the following chapter, particularly using the proposed bar element model.

In the **fifth chapter**, the **numerical results** are presented and discussed. First, the bending stiffnesses identified by assuming a diamond shape for the meshes are presented. The influence of parameters on the numerical bending stiffness is studied: the viscosity of the material, the force applied on meshes, the opening of meshes, the size of samples, and the boundary conditions. Regarding the results, it was decided to model the size of the knots using hexagonal meshes. The results with hexagonal meshes are presented and discussed.

Finally, the manuscript finishes with a **conclusion** aiming at presenting an assessment of the results presented in the manuscript, a discussion about the validity of the proposed method and suggestions for further work.

A part of this thesis was submitted and accepted for publication by the "Ocean Engineering" journal (Morvan et al., 2016).

1.4 Major contributions of this thesis

- Uniaxial tensile tests, suspending tests and biaxial tensile tests were performed on a large range of netting samples: two materials (polyethylene or polyamide), two kinds of mesh sides (single or double twine), three sizes of panels (3x3-, 4x10- and 5x25-mesh panels).
- The mechanical behaviour of netting samples was revealed by experimental results and taken into account for the evaluation of the bending stiffness in netting panels.
- A finite element model using bar elements and based on the beam theory was developed. A tool was developed to simulate, using this finite element model, the tests on netting samples and to identify, using inverse identification and the experimental results, the bending stiffness in netting panels. The model captured the heterogeneous deformation field of the netting samples during the suspending tests.
- A methodology for the evaluation of the mesh resistance to opening was proposed and assessed. It was based on a free of rights finite element model and a simple non-expensive experimental setup. Measurement methods were proposed to avoid inconsistencies in the identification results coming from correlations between some parameters.

CHAPTER

2 Existing methods for the assessment of twine bending stiffness

2.1 Models for the netting mesh

Priour (2013), O'Neill (2002) and De la Prada and Gonzales (2013) proposed to model the mechanical behaviour of mesh sides.

2.1.1 Model of Priour

Priour (2013) modelled a mesh by 4 elastic articulated bar elements, linked with springs in the T-direction (Fig. 2.1). In one mesh, the four bar elements modelled the tensile elasticity of the four mesh sides and the springs modelled the bending of the mesh sides.

Priour assumed that the couple between two consecutive mesh sides in the T-direction varies linearly with the angle α in the netting:

$$C = H(\alpha - \alpha_0) \tag{2.1}$$

with α the angle between two consecutive mesh sides in the T-direction in the deformed mesh, α_0 the angle between two consecutive mesh sides in the mesh at rest, and H a constant representing the mesh resistance to opening (N.m/Rad).

2.1.2 Analytical solution of O'Neill

O'Neill (2002) assumed that the mechanical behaviour of a mesh side during the mesh opening was identical to the one of a beam subjected to bending.

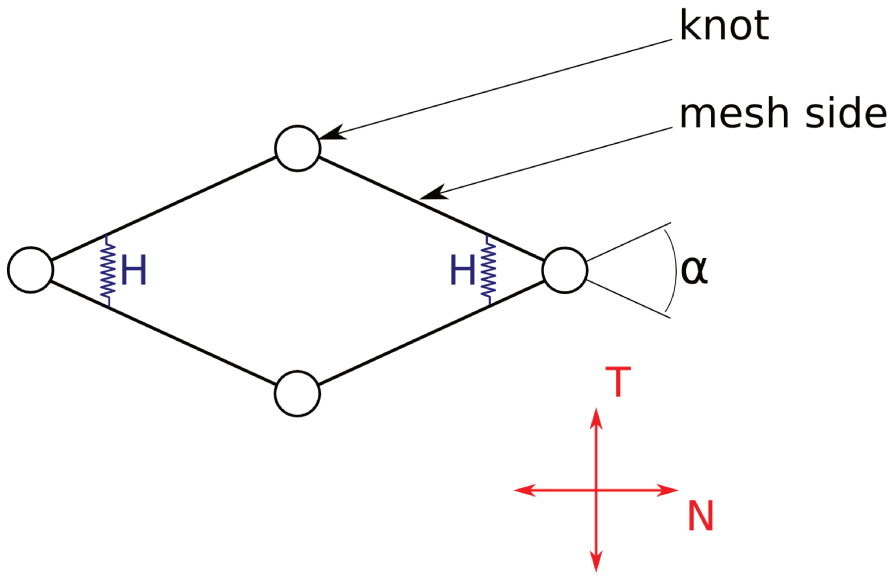

Figure 2.1 – Model of Priour. A mesh modelled by 4 elastic articulated bars linked with springs. H is a constant factor, characteristic of the spring and leading to a couple proportional to the difference $(\alpha - \alpha_0)$, with α the angle between two consecutive mesh sides in the T-direction.

Assumptions

First, O'Neill assumed that the bending moment M, at each point along a mesh side, is proportional to the curvature κ of the twine at this point. The proportional coefficient is the bending stiffness EI:

$$M = EI\ \kappa \tag{2.2}$$

Then, the slope angle of the mesh side near the knot was assumed fixed during the deformation (Fig. 2.2).

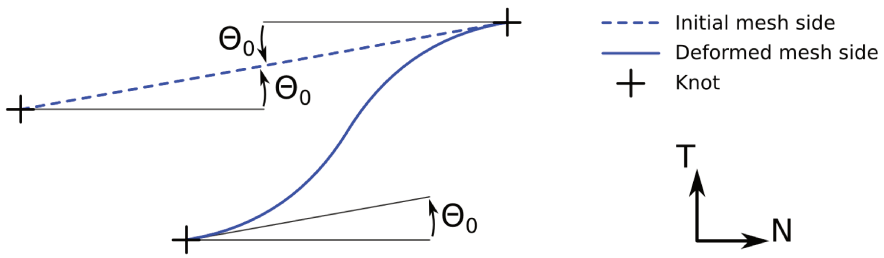

Figure 2.2 – Analytical solution of O'Neill. The slope angle θ_0 of one mesh side near the knot was assumed fixed during the deformation.

Finally, the twine was assumed inextensible. Whatever the axial force in mesh sides, the mesh side length stays the same.

Equation

In the case of a beam subjected to bending, O'Neill had:

$$\frac{EI}{l^2}\frac{\partial \Theta}{\partial s} = \frac{-C}{l} + uf_y - vf_x \tag{2.3}$$

$$\frac{\partial u}{\partial s} = \cos(\Theta) \tag{2.4}$$

$$\frac{\partial v}{\partial s} = \sin(\Theta) \tag{2.5}$$

with:

- EI the bending stiffness $[N.m^2]$
- l the length of the twine $[m]$
- s the scaled arc length along the twine ($s \in [0, 1]$)
- $\Theta(s)$ the slope angle of the twine at the scaled arc length s $[-]$
- $u(s), v(s)$ the normalized spatial coordinates ($[x, y] = [lu, lv]$)
- f_x, f_y the forces components at each end of the twine $[N]$
- C the couple at each end of the twine $[N.m]$

Concerning the boundary conditions, one end of the twine was fixed and the slope angle θ near the ends of the twine was fixed and was equal to θ_0 ($\theta(0) = \theta(1) = \theta_0$).

Analytical solution: method of matched asymptotic expansions

To approximate the analytical solution of Equation 2.3, O'Neill used an asymptotic method, the "MAE" method (method of Matched Asymptotic Expansions). This method is particularly used to solve singular problems for which the solutions change rapidly in a narrow region.

First, O'Neill modified the equation of the problem to solve.

He substituted some variables in Equation 2.3:

- $\epsilon^2 = EI/(l^2 f)$
- $f = \sqrt{{f_x}^2 + {f_y}^2}$

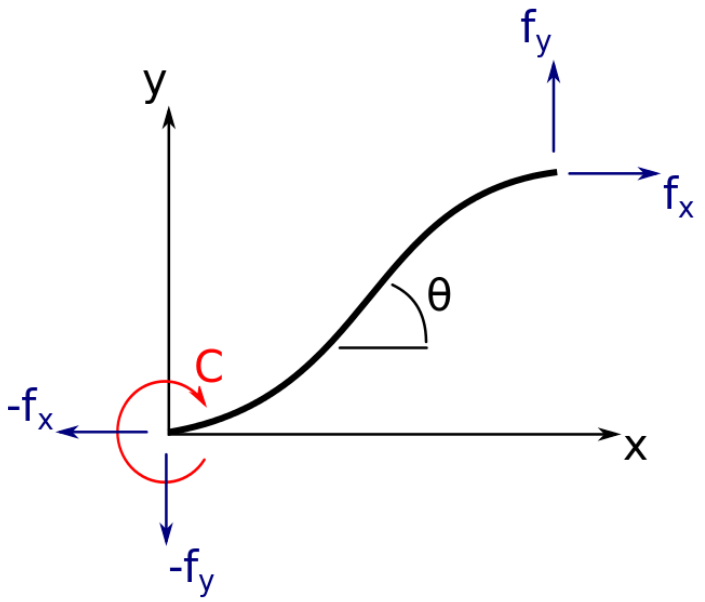

Figure 2.3 – Forces and couple applied on a twine. Reprinted from O'Neill (2002).

- $c = C/(lf)$
- $\beta = \tan^{-1}(f_y/f_x)$
- $\Gamma = \Theta - \beta$
- $X = u\cos(\beta) + v\sin(\beta)$
- $Y = -u\sin(\beta) + v\cos(\beta)$

We will see later that ϵ is quite important in the solution proposed by O'Neill. ϵ is large when the bending stiffness EI is large relatively to $l^2 f$ (square of twine length multiplied by the force value).

Equations (2.3, 2.4, 2.5) became:

$$\epsilon^2 \frac{\partial \Gamma}{\partial s} = c + Y \tag{2.6}$$

$$\frac{\partial X}{\partial s} = \cos(\Gamma) \tag{2.7}$$

$$\frac{\partial Y}{\partial s} = \sin(\Gamma) \tag{2.8}$$

Equation (2.6) gave, after derivations:

$$\epsilon^2 \frac{\partial \Gamma}{\partial s} = c + Y \Rightarrow \frac{\partial}{\partial s}\left(\epsilon^2 \frac{\partial \Gamma}{\partial s}\right) = \frac{\partial}{\partial s}(c + Y) \Rightarrow \epsilon^2 \frac{\partial^2 \Gamma}{\partial s^2} = \frac{\partial Y}{\partial s}$$

Thus:

$$\epsilon^2 \frac{\partial^2 \Gamma}{\partial s^2} = \sin(\Gamma) \tag{2.9}$$

Some analytical solutions to this system were derived by O'Neill in terms of elliptical integrals of the first and second kind. According to the author, these solutions were not convenient and the resulting relationship between the deformation, the bending stiffness and the boundary conditions were not very informative.

Thus, O'Neill used the MAE method to approximate the solution when the value of ϵ is small. Different asymptotic solutions were constructed, outside ("outer" solution) and inside ("inner" solution) the region of rapid change of Γ, and "matched" to establish a solution valid on the whole domain (mesh side).

Outer solution

The outer solution is used in the region of slow change, that means far from the ends of the twine.
In this case, O'Neill assumed that $\epsilon = 0$, and it was solved by neglecting the bending stiffness.

Equation 2.9 became $0 = \sin(\Gamma)$, and:

$$\Gamma_{in}(s) = 0 \tag{2.10}$$

$$\Phi_{in}(s) = s \tag{2.11}$$

$$\Psi_{in}(s) = 0 \tag{2.12}$$

Γ_{in}, Φ_{in} and Ψ_{in} were respectively the outer solutions of γ, X and Y.

$\Gamma_{in} = 0$ was obtained, which was equivalent to $\Theta - \beta = 0$, or $\Theta = \beta$. In other words, the twine was straight in this region. But the boundary conditions at the ends were not taken into account ($\Theta = \Theta(0) = \Theta(1) \neq \Theta_0$).

Inner solution

The inner solution was used in the region of rapid change, that means close to the ends of the twine.

First, the boundary condition on the left was considered, that means when s was close to 0. For that, a new gauge (boundary-layer coordinate) was introduced: $\lambda = s/\epsilon$. λ was also called fast variable (by opposition to s, the slow variable). By fixing λ, the region near $s = 0$ was stretched as ϵ became small.

O'Neill also made the following changes:

- $\Phi_l = X/\epsilon$
- $\Psi_l = Y/\epsilon$
- $\eta_l = \Gamma$ with $\eta_l(\lambda)$ negligible near $s = 1$, so $\eta_l(\infty) = 0$.

And the boundary conditions limits were: $\Phi_l(0) = 0$, $\Psi_l(0) = 0$, $\eta_l(0) = \Gamma(0)$ and $\eta_l(\infty) = 0$.

By using substitutions, integrations and derivations, O'Neill obtained:

$$\Phi_l(\lambda) = \lambda - 2\cos(\frac{\eta_l}{2}) + 2cos(\frac{\Gamma(0)}{2}) \tag{2.13}$$

$$\Psi_l(\lambda) = -2\sin(\frac{\eta_l}{2}) + 2sin(\frac{\Gamma(0)}{2}) \tag{2.14}$$

The same method was used for the inner region on the right (s close to 1), by defining a new gauge: $\sigma = (1 - s)/\epsilon$. The values of $u(1)$ and $v(1)$ were not known, so a constant parameter was used, and O'Neill found:

$$\eta_r(\sigma) = 4\arctan(\tan\frac{\Gamma(1)}{4}\exp(-\sigma)) \tag{2.15}$$

$$\Phi_l(\sigma) = -\sigma + 2\cos(\frac{\eta_r}{2}) \tag{2.16}$$

$$\Psi_l(\sigma) = 2\sin(\frac{\eta_r}{2}) \tag{2.17}$$

Matching inner and outer solutions

The two previous solutions were validated in two different domains. To get a solution for the whole twine, O'Neill superimposed the inner and the outer solutions:

- $\Gamma(s) = \eta_l(s) + \eta_r(s) + \Gamma_{in}(s)$

- $X(s) = \epsilon\Phi_l(s) + \epsilon\Phi_r(s) + \Phi_{in}(s)$
- $Y(s) = \epsilon\Psi_l(s) + \epsilon\Psi_r(s) + \Psi_{in}(s)$

Finally, by making the following inverse changes of parameters $x(s) = X(s)cos(\beta) - Y(s)sin(\beta)$, $y(s) = X(s)sin(\beta) + Y(s)cos(\beta)$ and $\Theta = \Gamma + \beta$, O'Neill found the asymptotic solution of Equations (2.3), (2.4) and (2.5).

O'Neill obtained:

$$\Theta(s) = \eta_l(s) + \eta_r(s) + \beta \tag{2.18}$$

$$x(s) = s\ \cos(\beta) + 2\epsilon\left\{\cos\frac{\Theta(0)+\beta}{2} - \cos\left(\frac{\eta_l(s)}{2}+\beta\right) + \cos\left(\frac{\eta_r(s)}{2}+\beta\right) - \cos\beta\right\} \tag{2.19}$$

$$y(s) = s\ \sin(\beta) + 2\epsilon\left\{\sin\frac{\Theta(0)+\beta}{2} - \sin\left(\frac{\eta_l(s)}{2}+\beta\right) + \sin\left(\frac{\eta_r(s)}{2}+\beta\right) - \sin\beta\right\} \tag{2.20}$$

With:

$$\eta_l(s) = 4\arctan(\tan\frac{\Theta(0)-\beta}{4}\exp(\frac{-s}{\epsilon})) \tag{2.21}$$

$$\eta_r(s) = 4\arctan(\tan\frac{\Theta(1)-\beta}{4}\exp(\frac{s-1}{\epsilon})) \tag{2.22}$$

The author showed that the solution was very accurate when $\epsilon < 0.2$.

2.1.3 Timoshenko beams of De la Prada

In order to propose a method which should not depend on a commercial software tool, De la Prada developed three force models based on interpolation of force-displacement responses obtained with a commercial finite element model (De la Prada and Gonzales (2013)).

Method

The twine was modelled as a two-dimensional beam clamped between two knots.

The force-displacement response of the beam was obtained using the finite element method. The beam was discretized with 20 quadratic three-dimensional beam elements based on the Timoshenko beam theory (Fig. 2.4).

To obtain the force-displacement response, De la Prada performed a series of simulations. For each simulation, one end of the twine was subjected to a displacement, and the force response was calculated.

De la Prada introduced the dimensionless force component f and the dimensionless radial coordinate r:

$$f = F\frac{L^2}{EI} \tag{2.23}$$

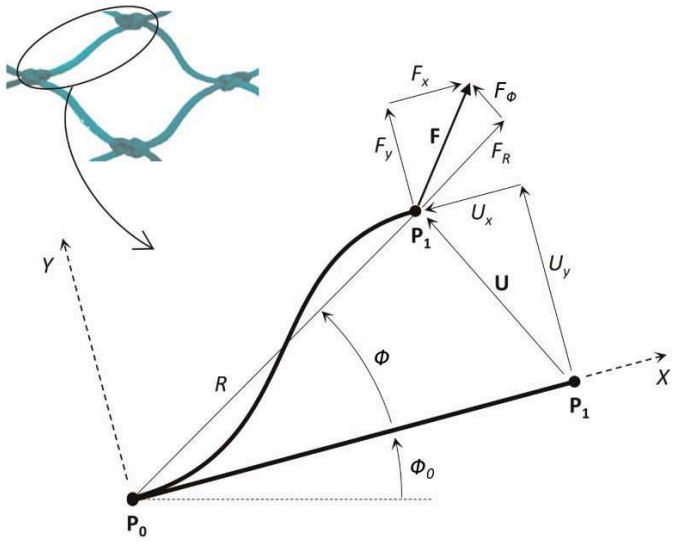

Figure 2.4 – Finite element model of a twine, deformed and not deformed. Reprinted from De la Prada and Gonzales (2013).

$$r = \frac{R}{L} \tag{2.24}$$

with F the force applied at $P1$ (Fig. 2.4), L the length of the unstretched twine, EI the bending stiffness, and R the distance between the two ends of the deformed twine (Fig. 2.4). The dimensionless force components f_r and f_Φ were defined as f with the force components F_r and F_Φ respectively.

She also used dimensionless cartesian coordinates x and y:

$$x = \frac{X}{L} \tag{2.25}$$

$$y = \frac{Y}{L} \tag{2.26}$$

with X and Y the cartesian coordinates of $P1$ (Fig. 2.4) and L the length of the unstretched twine.

Model 1: polynomial surface fitting

In case of polynomial surface fitting, De la Prada proposed to obtain two polynomial surfaces of the force-displacement response previously calculated using a finite element model. The first surface represented the radial component f_r of the calculated force as a function of the position of the displaced end of the twine $(r, \cos(\Phi))$; and the second surface represented the tangential component f_Φ as a function of the position of the displaced end of the twine $(r, \cos(\Phi))$ (figure 2.5).

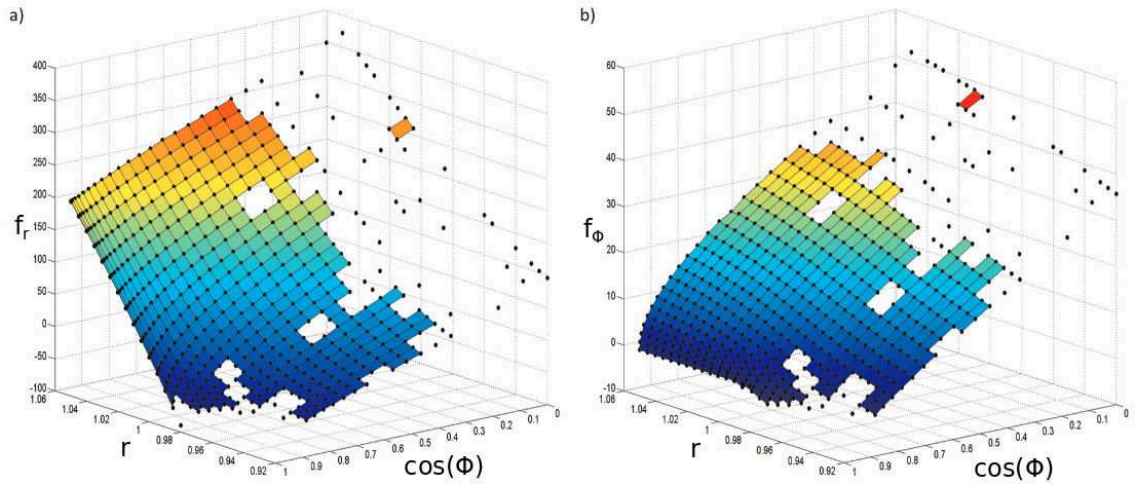

Figure 2.5 – Dimensionless force-displacement responses of a twine with axial rigidity EA = 500N, as a function of the position of its end point $(r, \cos(\Phi))$. r is the dimensionless radial coordinate. (a) dimensionless radial component f_r and (b) dimensionless tangential component f_Φ. Reprinted from De la Prada and Gonzales (2013).

De la Prada used a least squares regression to calculate the surface.
This method is, according to De la Prada, accurate and easy to implement.

Model 2: spline surface fitting

The beam model described in Fig. 2.4 being a conservative system, De la Prada proposed to fit the potential energy of the system, and to evaluate the forces using the obtained gradient force field.

To get a more accurate force field, De la Prada used a spline interpolation providing much better fitting than polynomials.

The dimensionless potential elastic energy ν was defined as a function of the potential elastic energy V, the length of the twine at rest L and the bending stiffness EI:

$$\nu = V\frac{L}{EI} \tag{2.27}$$

The method used to obtain the force-displacement response also allowed De la Prada to obtain the dimensionless potential elastic energy ν, represented by Fig. 2.6 for a twine with an axial stiffness $EA = 500N$. According to De la Prada, in the case of a bigger value of the axial stiffness, the shape of the surface did not change, but its gradient value increased.

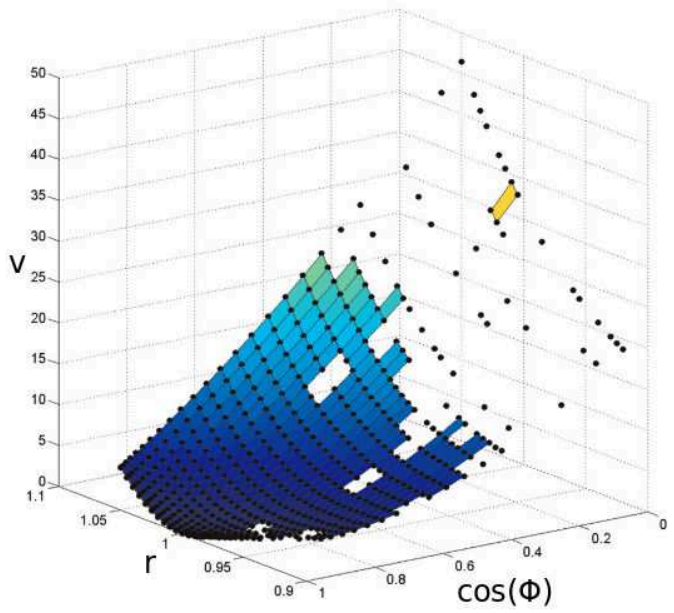

Figure 2.6 – Dimensionless potential elastic energy ν of a twine with an axial stiffness $EA = 500N$, as a function of the position of its end. r is the dimensionless radial coordinate. Reprinted from De la Prada and Gonzales (2013).

The surface representing the dimensionless elastic energy ν of a twine as a function of the position of its end $(r, \cos(\Phi))$ was approximated by a double 2D-spline interpolation.

Model 3: spring-based model for vertical forces

De la Prada proposed a twine force model based on linear spring and allowing the simulation of twines subjected to large axial strain.

The finite element model allowed De la Prada to calculate the force-displacement response of a twine when its end (P1 on Figure 2.4) was subjected to a **vertical force**.

The proposed force model approximated the radial force f_r as a linear spring with variable-length r_{eq}:

$$f_r(r, \cos(\Phi)) = EA\frac{L^2}{EI}(r - r_{eq}(\cos(\Phi))) \tag{2.28}$$

The length function $r_{eq}(\cos(\Phi))$ was calculated so that the obtained radial force was equal to the radial force calcultated with the finite element model.

De la Prada concluded that when $\Phi < 60^\circ$, the fitting was exact and nearly independant of the axial stiffness.

2.1.4 Discussion

Three models for the netting mesh were presented: the model of Priour (2013), the analytical model of O'Neill (2002) and the fitting model of De la Prada and Gonzales (2013).

The three presented models were simple and offered shorter computational time than in case of finite element model. Thus, there were well-fitted for the simulation of netting (illustrated in the following section with the model of Priour). Moreover, the interpolation method proposed by De la Prada could be used to develop a model of mechanical behaviour for netting implemented in membrane elements. Thus it would not be necessary to model each mesh of a netting for a finite element model of a fishing net.

Nevertheless, the interpolation method of De la Prada could introduce errors in the simulations. Then, the approximated solution of O'Neill was accurate only when $\epsilon < 0.2$, that means only when EI was relatively small. Due to the hypothesis of non elongation, the tension in the twine had to be moderated relatively to its elasticity. O'Neill also proposed analytical solutions of the model based on elliptical integrals that did not required an approximation method, but the solutions were not convenient according to the author, and needed more computational time. Finally, Priour (2013) modelled the bending stiffness of mesh sides by linear springs linking consecutive mesh sides in the studied direction. Experiments would be necessary to propose a nonlinear and more precise behaviour law for the springs.

2.2 Priour's model for netting

Priour (2013) proposed a finite element method to model the mechanical behaviour of netting.

2.2.1 Triangular elements of Priour

Priour (2013) modelled nets with 3-node membrane triangular elements (Fig. 2.7) by assuming that: a mesh side has an elastic mechanical behaviour, and the mesh sides are parallel and therefore have the same deformation within a triangular element.

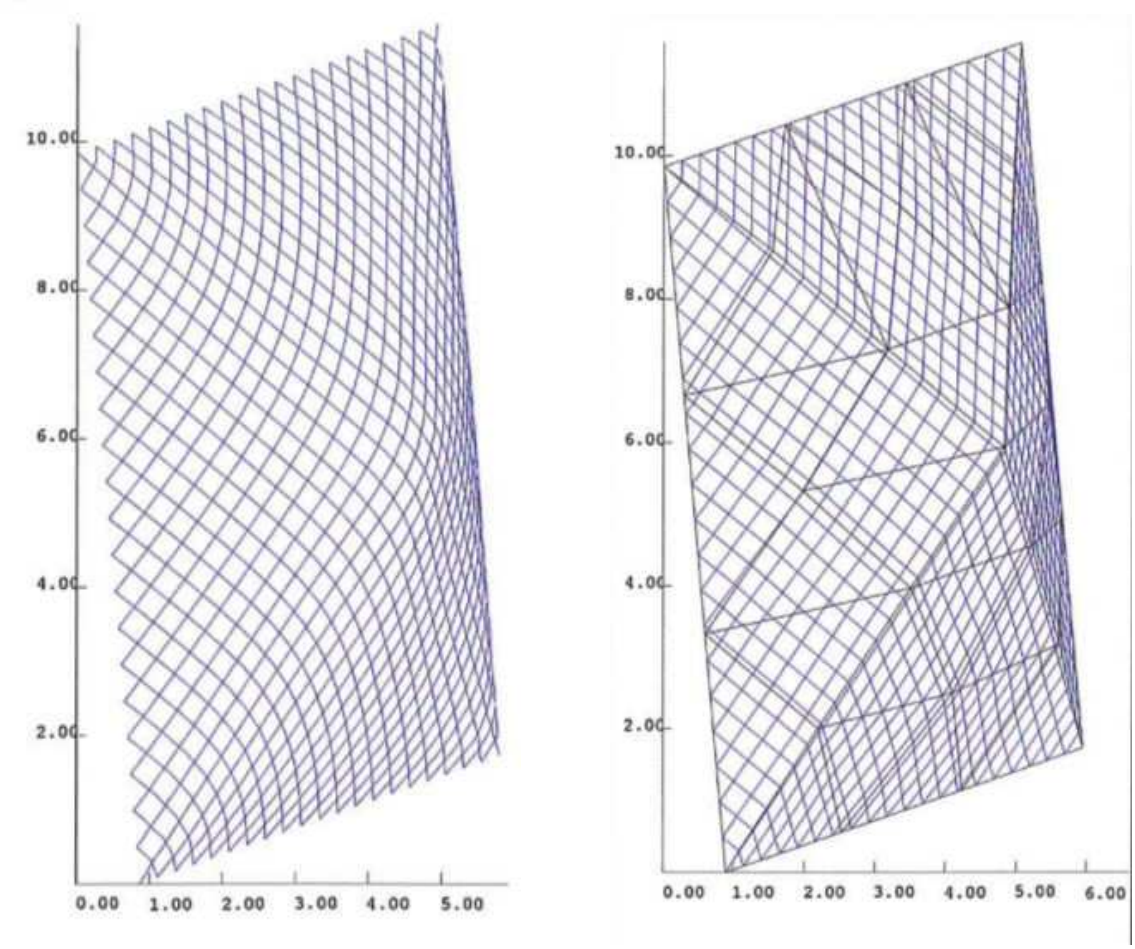

Figure 2.7 – The diamond mesh (left) was decomposed into triangular elements (right). Reprinted from Priour (2013).

2.2.2 Mesh resistance to opening

Priour modelled a mesh with elastic elements and springs as described in Section 2.1.1. The angle between mesh sides in a triangular element was defined as the angle between the twine vectors U and V (Fig. 2.8). The stiffness of springs represented the bending stiffness of mesh sides, thus the mesh resistance to opening.

2.2.3 Flexion outside the netting plane

The bending between two neighbour triangular elements led to a couple between twines crossing the side shared by the two triangular elements (Fig. 2.9).

According to Priour (2013), no numerical model took into account the flexion of the twines outside the netting plane.

The angle between the mesh side vectors U_a and U_b of two triangular elements

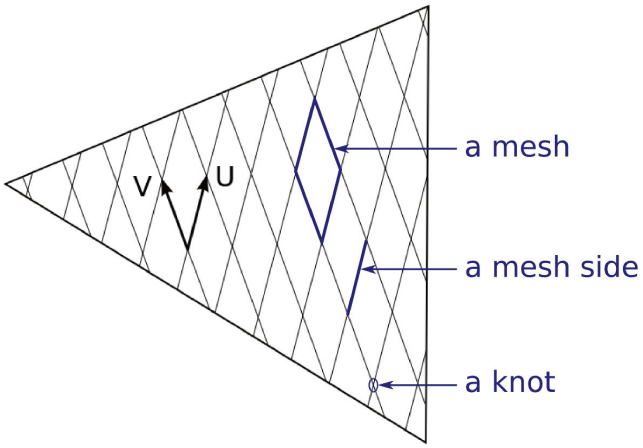

Figure 2.8 – A triangular element. The angle between the twine vectors U and V leads to a couple. Adapted from Priour (2013).

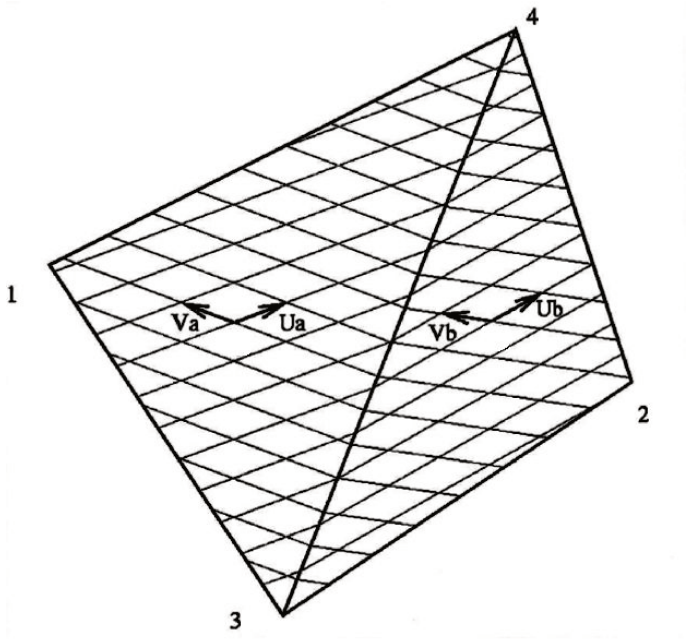

Figure 2.9 – Two triangular elements (134 and 243). The angle between the mesh side vectors U_a and U_b leads to a bending couple between the two triangular elements around the side 34. Reprinted from Priour (2013).

134 and 243 respectively, and the angle between the mesh side vectors V_a and V_b of the two triangular elements 134 and 243 respectively, were assumed to be constant

along the side common to the two elements (Fig. 2.9).

Priour (2013) calculated C_u and C_v, the bending couples on the U mesh side and on the V mesh side respectively, using the equation:

$$C = \frac{EI}{R} \tag{2.29}$$

with C the bending couple on the mesh side ($N.m$), EI the bending stiffness ($N.m^2$) and R the radius of curvature of the twine (m).

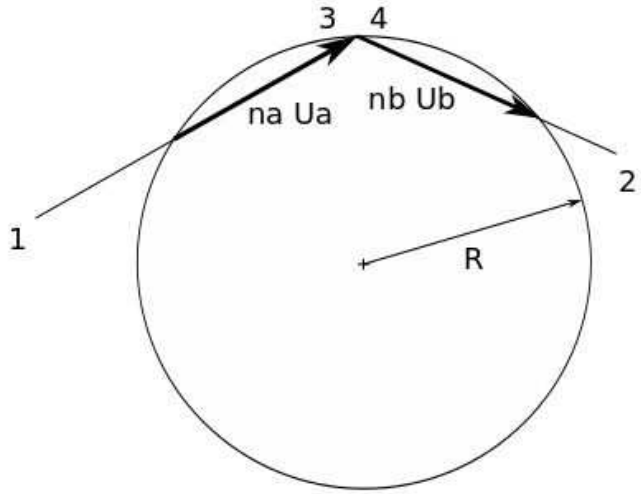

Figure 2.10 – Profile view of the two triangular elements. The radius of curvature R is estimated from the average length of twine vector U in each triangle: n_aU_a and n_bU_b. Reprinted from Priour (2013).

To calculate the couple C_u, Priour estimated the radius of curvature of the U twines from the average lengths of the U twines n_aU_a and n_bU_b in the triangular elements A and B respectively (Fig. 2.10). The radius of curvature was calculated from the circumscribed circle in the triangle of sides n_aU_a, n_bU_b and $n_aU_a + n_bU_b$.

Finally, the model proposed by Priour (2013) could be used for diamond or hexagonal meshes.

2.2.4 Discussion

This finite element model was well-fitted for the simulation of netting. It could model trawl made of thousands of meshes with a computational and a numerical efficiency.

Priour modelled the bending stiffness in mesh sides, inside the netting plane, with linear springs between consecutive mesh sides. As discussed in Section 2.1, experiments would be necessary to propose a nonlinear and more precise behaviour

law for the springs.

Outside the netting plane, Priour assumed that the mesh sides behaved like beams. Thus, the couple between two consecutive triangular elements was assumed proportional to the curvature between these elements. We can note that the proposed method is quite easy to implement.

The model could be used to show the effect of the mesh resistance to opening on the shape, and so on the selectivity of a trawl codend for example. Works are necessary on the springs which model the bending stiffness of the mesh sides and on the estimation of the couple between two triangular elements to accurately simulate the effect of the bending stiffness.

2.3 Methods to evaluate the bending stiffness

All methods used inverse identification and required a model of mesh mechanical behaviour.

2.3.1 Sala et al.

To evaluate the mesh resistance to opening, Sala et al. (2007) proposed a method based on the model of O'Neill (2002), previously described. To directly and simply use the analytical model of O'Neill, Sala used a prototype experimental device allowing to obtain a uniform deformation in the tested netting sample.

Experimental method

The prototype (Fig. 2.11), named Resistance to Opening and Deflection Meter (ROD-m), incorporated four tension load cells and four stepping motors and was designed so that all the mesh sides of the netting panel would undergo the same deformation. Three-by-three mesh netting panels could be mounted on the experimental device, using steel hooks on linear guideways. The two outer hooks on each guideway were free to move along its length in response to the deformation of the netting.

The resulting positions and measurements of the four load cells were recorded.

Each netting sample was subjected to a series of pretension cycles to remove the irreversible part of the elongation and to safeguard against knot slippage.

Sala et al. (2007) performed a complete set of measurements on a netting sample in these steps:

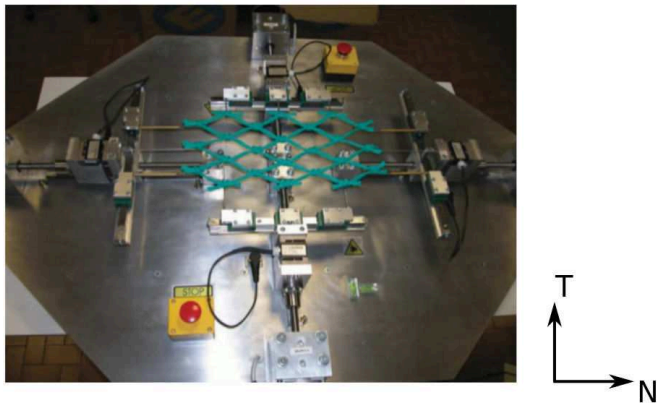

Figure 2.11 – General view of the ROD-m equipment and a North Sea PE double-twine netting panel specimen during the test. This device allows to obtain a uniform deformation in the tested netting sample. Reprinted from Sala et al. (2007).

1. A netting panel was mounted on the ROD-m in a predetermined initial position.

2. The netting panel was stretched until the load forces reach 29.4 N in the T-direction (and subsequently 58.9, 88.3, 117.7 and 147.2 N) for single-twine mesh, and 58.9 N (and subsequently 117.7, 176.6, 235.4 and 294.3 N) for double twine mesh.

3. The sample was submitted to a relaxation step of 5 minutes (the displacement was blocked during 5 minutes).

4. Steps 2 and 3 were repeated until the maximum value (147.2 or 294.3 N) of the load in the N-direction was reached.

5. The load cells in the N-direction were moved back to the initial position and the position of the load cells in the T-direction was increased.

6. Steps 2 to 5 were repeated four times, at which point the positions of the load cells in the T-direction were such that the mesh opening was approximately square.

Numerical method

The asymptotic solution proposed by O'Neill (2002) to model the mechanical behaviour of meshes under tension was used by Sala et al. (2007) in the regression analysis.

Thus Sala et al. (2007) assumed that the bending moment of the twine was proportional to the curvature, that there was no twine extension and that the slope angle where the mesh sides emerge from the knots was fixed.

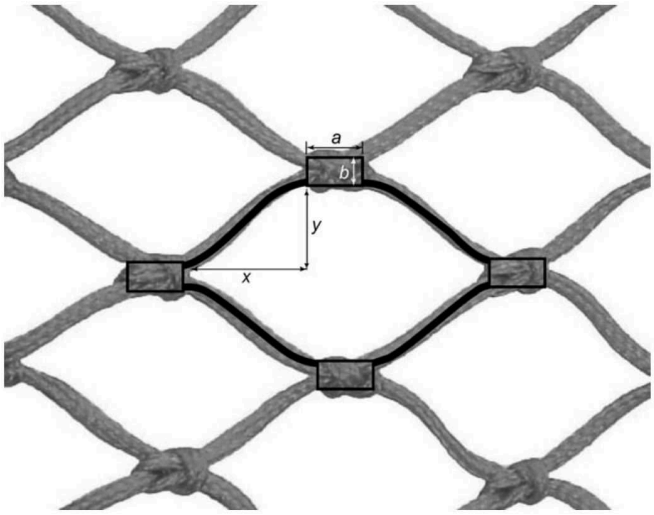

Figure 2.12 – Netting material and definition of the geometrical parameters of the mesh model. On this scheme, θ_0, the slope angle at either end of the mesh sides is shown to be zero. Reprinted from Sala et al. (2007).

Sala defined an idealized panel of netting (Fig. 2.12). The knots were represented by rectangles from the corners of which the mesh sides emerge. The mechanical (twine bending stiffness) and geometrical (mesh side length, knot dimensions, angle at which a mesh side emerges from a knot) parameters of the netting panel were estimated by minimizing the difference between the experimental measures and the numerical results.

Results

On table 2.1, results of the inverse identifications of Sala et al. (2007) for North Sea netting materials are presented. In some cases, a knot dimension was estimated negative. The slope angle θ_0 at the knot was assumed to be zero, otherwise the fitted solutions were not consistent.

Discussion

The proposed method was useful. The identified parameters were, according to the authors, consistent between different panels of the same netting material (Table 2.1). Thus, the method seemed robust. Then, the estimates of the bending stiffness provided quantitative means to compare the mesh resistance to opening of different netting panels. Moreover, the identified bending stiffness could be used in codend

Netting	**Panel**	**a** $[mm]$	**b** $[mm]$	**m** $[mm]$	**EI** $[N.mm^2]$
PE single 4997 Rtex	1	-1.2	0.9	47.5	288
	2	0.8	1.8	45.4	234
	3	0.5	1.7	45.7	244
	4	-0.1	1.6	46.6	286
PE double 16520 Rtex	1	9.5	4.9	50.7	544
	2	8.3	4.2	52.3	661
	3	9.6	4.7	51.8	602
	4	9.9	5.0	50.8	502
PE double 18772 Rtex	1	10.3	5.9	48.2	909
	2	11.2	6.9	48.5	716
	3	7.6	5.4	52.5	889
	4	10.3	6.1	49.4	942
PE double 16214 Rtex	1	13.9	4.9	61.3	691
	2	13.4	4.7	59.9	625
	3	13.0	4.2	61.3	703
	4	14.4	4.7	60.5	719
PE double 19934 Rtex	1	9.0	5.6	60.7	960
	2	8.2	5.0	62.3	1232
	3	9.8	6.0	60.5	942
	4	9.4	5.7	61.2	1013

Table 2.1 – Summary of the results of Sala et al. (2007) for North Sea netting materials. (a, b) represents the knot size, m the mesh side length, EI the bending stiffness. The slope angle θ_0 near the knot is assumed to be zero. For each netting material, Sala presents the between-panel variation. Reprinted from Sala et al. (2007).

models to take into account the mechanical behaviour of meshes.

However, the biaxial experimental set-up presented in Sala et al. (2007) required a complex and expensive device (not commercially available yet). Because of the correlations between the parameters (a, b, m, EI and θ_0), particularly between θ_0 and EI, Sala assumed $\theta_0 = 0$. The other parameters remained unconstrained. As a result, the estimated parameters were sometimes out of physical limits.

2.3.2 Balash

Balash (2012) also used the model proposed in O'Neill (2002).

Experimental method

Balash (2012) proposed to attach a net to hoops in transverse mesh orientation (Fig.

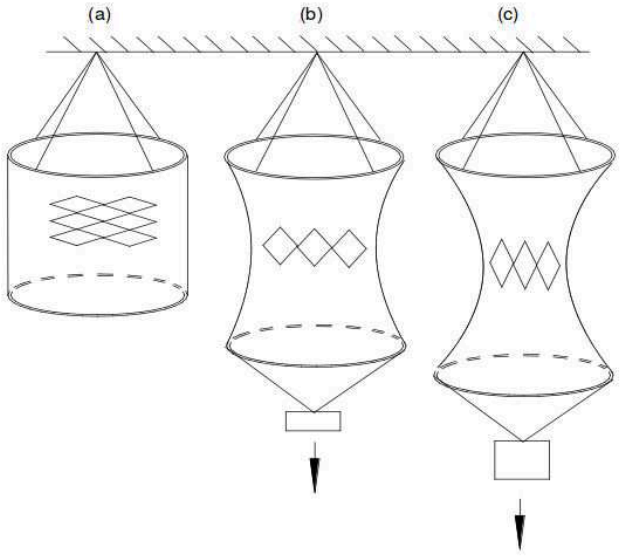

Figure 2.13 – A net is attached in transverse mesh orientation: (a) with no load applied (the weight of the net and the bottom hoop only); (b, c) the net acquires a hourglass shape as the load gradually increases. Reprinted from Balash (2012).

Retail name	Construction properties
24ply Polyethylene	twisted 24 ply, single twine, knotted
Hampidjan Dynex	1.0 mm braided, single twine, knotless
Euroline Premium Plus	1.0 mm braided, single twine, knotted

Table 2.2 – List of netting samples tested in Balash (2012).

2.13). The mesh opening in the middle section of the netting sample was measured in the two directions.

Netting samples

Balash tested three prawn nets that were commonly used by the trawl operators in Australia (Table 2.2).

Numerical method

Balash rearranged the solution proposed by O'Neill (2002):

$$EI = f\left\{\frac{x - a - L_{ms}\cos(\beta)}{4\left\{\cos(\frac{\theta_0+\beta}{2}) - cos(\beta)\right\}}\right\} \tag{2.30}$$

With:

- EI the bending stiffness $[N.m^2]$

f $[N]$	θ_0 $[-]$	β $[-]$	**EI** $[N.mm^2]$
9.8	-2.19	0.4	59
14.7	8.12	0.4	61
19.6	1.66	0.4	58
24.5	1.59	0.4	59
29.4	1.52	0.4	56
49.0	1.42	0.4	56
68.7	1.37	0.4	54
88.3	1.33	0.4	49
107.9	1.32	0.4	52

Table 2.3 – Bending stiffness EI of 24ply polyethylene netting for several loading values (f). Results obtained by Balash (2012).

- θ_0 the slope angle of the twine near the knot (Fig. 2.2) $[-]$
- β the angle between the direction of the force and the N-direction $[-]$, defined by $\beta = \tan^{-1}(f_y/f_x)$, with f_x and f_y the forces components at each end of the mesh side.
- L_{ms} the mesh side length at rest $[m]$. By using the model for twines of O'Neill, the mesh side length was assumed constant.
- x the length of the mesh side in the N-direction $[m]$. The parameter is represented in Figure 2.12.
- a the length of the knot in the N-direction $[m]$. The parameter is represented in Figure 2.12.

Using equation 2.30 and the experimental openings of the meshes in the middle of attached nets, Balash (2012) could evaluate the bending stiffness EI of the twines. Indeed, the measurement of the opening allowed the calculation of the parameter x in the equation.

Results

The bending stiffnesses identified for one of the samples (24ply PE) are presented in Table 2.3. Fig. 2.14 shows the comparison of bending stiffnesses identified by Sala et al. (2007) and Balash (2012).

Discussion

With the experimental setup proposed by Balash, the meshes in the middle of the sample (cylinder) were submitted to forces close to the ones applied on meshes in trawl codend. However, the author chose to use the model proposed by O'Neill

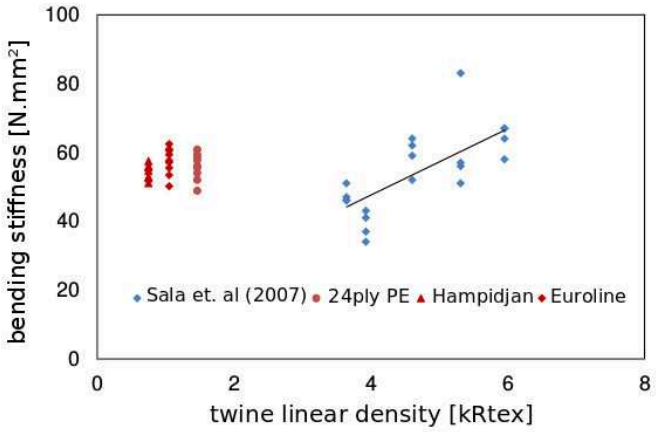

Figure 2.14 – Bending stiffness as a function of twine linear density: data from Sala et al. (2007) (blue dots) and Balash (2012) (red dots). The netting samples tested by Balash are described in Table 2.2. The netting samples tested by Sala et al. (2007) are made of polyamide. Reprinted from Balash (2012).

(2002) that makes, as discussed previously, strong assumptions. According to Balash, the linear relationship between bending stiffness and linear twine density presented by Sala et al. (2007) was not applicable for cases of low twine linear density. But the tests of Balash and Sala were of two different types, and the tested netting samples were made of different materials and structures.
Finally, further experimentation is required to robustly evaluate the bending stiffness with this method.

2.3.3 De la Prada

De la Prada and Gonzales (2014) offered a simple uniaxial experimental set-up, which stretches a netting sample in the T-direction of the meshes while leaving free its deformation in the N-direction. De la Prada used the model proposed by O'Neill (Section 2.1.2) and her model of twine deformation previously described (Section 2.1.3). De la Prada assumed a uniform deformation in suspended netting samples.

Experimental method

A rectangular netting sample was attached between an upper fixed bar and a bottom free bar (Fig. 2.15). The free bar was parallel to the fixed bar and could move in the T-direction. The knots attached to the bars could freely move in the N-direction of the netting when the sample was stretched. The sample was stretched by applying a force F_{panel} to the free bar. The length L_{panel} of the panel in the T-direction was calculated as $L_{panel} = D_0 - (D_R + D_L)/2 - D_1 - D_2$. The distances D_0, D_1 and D_2

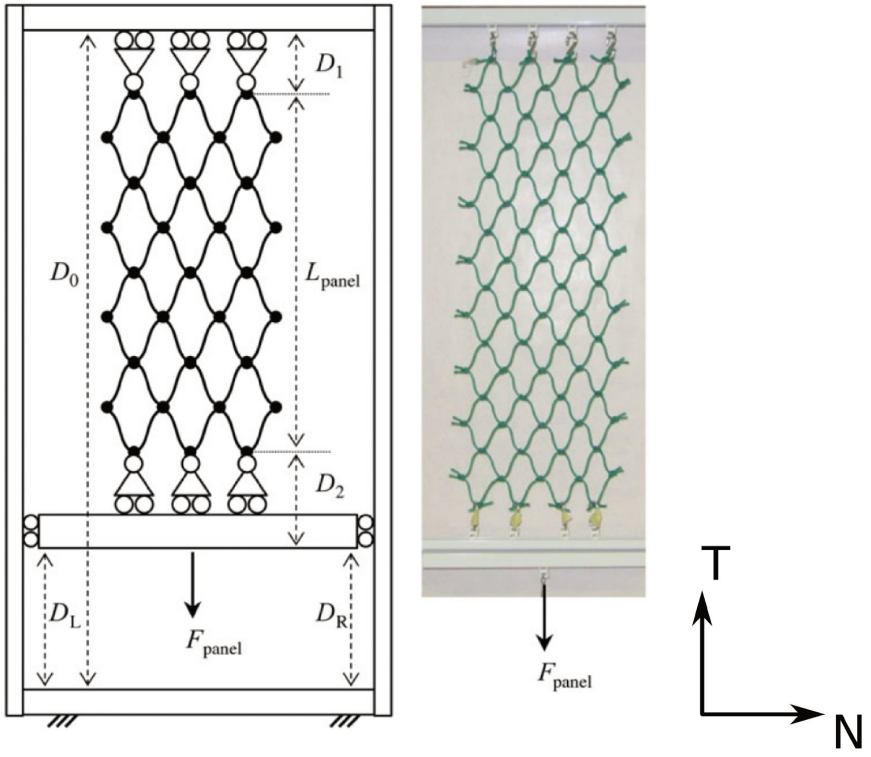

Figure 2.15 – Design of the experimental set-up and general view of a netting sample during a test. Reprinted from De la Prada and Gonzales (2014).

were measured at the beginning of the experiment and distances D_R and D_L were measured for each value of F_{panel}.

De la Prada and Gonzales (2014) tested 7 different, new and unused netting samples, commonly used in commercial North Sea trawls.

The steps of one test were:

1. A netting panel was mounted on the experimental device and the distances D_1 and D_2 were measured. F_{panel} was equal to the weight of the bottom free bar and hooks (0.7 N).

2. F_{panel} was increased and ranged from 0.7 N to 10.5 N.

3. D_R and D_L were measured at every minute. When the values were stabilized, they were recorded.

4. Steps 2 and 3 were repeated until L_{panel} reached 80 % of $m_T.L_{ms}$, where m_T was the number of meshes of the sample in the T-direction and L_{ms} the length

at rest of one mesh side. According to De la Prada and Gonzales (2013), above this value, the mesh sides were submitted more to traction than to bending.

According to De la Prada and Gonzales (2014), in fishing gear, high tensile forces could generate plastic deformations in twines and knots. To simulate such a situation, the author applied the maximum value F_{panel}, reached in step 4, for 1 hour to the netting. Then, the applied force was decreased. Thus, De la Prada and Gonzales (2014) obtained data from a loading and an unloading cycle.

Numerical method

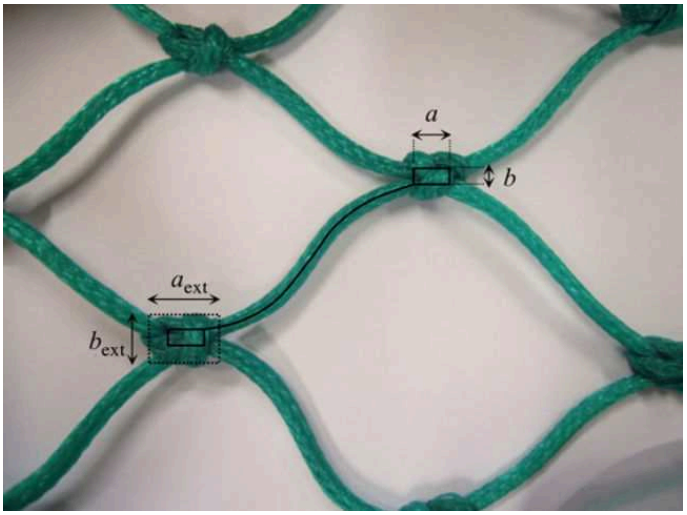

Figure 2.16 – Idealized netting where mesh sides are modelled as beams emerging from the corners of rectangular knots. a and b are the dimensions of idealized knots, estimated by fitting theoretical models for mesh resistance to opening to experimental data, a_{ext} and b_{ext} are the measured dimensions of knots. Reprinted from De la Prada and Gonzales (2014).

Concerning the geometry of netting samples, De la Prada and Gonzales (2014) made the same assumptions as Sala et al. (2007): the deformation field applied to the panel, represented in Figure 2.16, was assumed to be homogeneous, so all the meshes experienced the same deformation; knots were rectangles of size (a,b); twines emerged from the knots at the corners of the rectangles.

The variables used for the inverse identifications were: the distance y_{knots} between the two knots at the ends of a mesh side in the T-direction; the force applied on twines in the T-direction. Four parameters were evaluated: the bending stiffness EI, the mesh side length at rest L_{ms}, the height of knots b and the slope angle of mesh sides near the knots θ_0. The uni- axial experimental set-up of De la Prada did not provide measurements of transverse data that could be used to estimate the knot width a. Note that De la Prada suggested that the knot width a could also be estimated as $a = (L_{mesh} - 2L_{twine})/2$, with L_{mesh} the nominal mesh size and L_{twine}

Estimation strategy	Constraint applied on parameter		
	$\mathbf{L_{ms}}$	**b**	θ_0
1	-	-	-
2	min/max	min/max	min/max
3	fixed	fixed	min/max
4	-	-	fixed

Table 2.4 – Description of the parameter estimation strategies used by De la Prada and Gonzales (2014) in the regression analysis.

the twine length.

De la Prada and Gonzales (2014) used and compared 4 models: the exact and the asymptotic solutions proposed by O'Neill (2002) (Section 2.1.2), and the polynomial and the spline models developed by De la Prada and Gonzales (2013) (Section 2.1.3).

To avoid estimations out of physical limits and reduce the computational cost, De la Prada and Gonzales (2014) applied constraints to the parameters. The author found a relationship between the dimensions a_{ext} and b_{ext}.

By fixing or constraining the values of parameters between minimum and maximum physical limits, De la Prada used 4 parameters estimation strategies summarized in Table 2.4.

Results

Table 2.5 summarizes the results of the analysis of De la Prada and Gonzales (2014) with four different parameter estimation strategies, for netting samples made of polyethylene with nominal stretched mesh size of 80 mm and mesh side diameter of 4 mm. R^2 is the coefficient of variation that represents the accuracy of the fit. Results show the importance in the choice of the parameter estimation strategy.

Concerning the asymptotic solution of O'Neill, the author was cautious since the value of the parameter ϵ usually ranged from 0.3 and 0.6 in most part of the performed experiments. Indeed, the asymptotic solution of O'Neill is very close to the exact solution when $\epsilon < 0.2$ (O'Neill, 2002).

Discussion

The uniaxial experimental set-up proposed by De la Prada and Gonzales (2014) does not require an expensive and complex experimental device as the ROD-m used by Sala et al. (2007) (Section 2.3.1).

However, De la Prada assumed that all meshes experience the same deformation. The meshes in the top of the suspended panel are submitted to more weight than

Strategy	**Model**	**EI** $[N.mm^{-2}]$ [%]	$\mathbf{L_{ms}}$ $[mm]$	**b** $[mm]$	θ_0 [°]	$\mathbf{R^2}$
1	Exact	92 ± 66	32	3	19	0.9995
	Polynomial	107 ± 31	43	-10	25	0.9994
	Spline	50 ± 86	25	9.7	9	0.9996
2	Exact	119 ± 2	32	3.8	19	0.9949
	Polynomial	66 ± 8	33.4	0.0	17	0.9987
	Spline	67 ± 98	27.9	6.3	15	0.9996
3	Exact	126 ± 3	32	4	19	0.9920
	Polynomial	99 ± 12	32	4	15	0.9780
	Spline	126 ± 11	32	4	19	0.9904
4	Exact	35 ± 4	20.6	13.9	-	0.9995
	Polynomial	28 ± 12	21.1	12.2	-	0.9929
	Spline	33 ± 4	20.3	13.8	-	0.9996

Table 2.5 – Result of the analysis of De la Prada and Gonzales (2014) with four different parameter estimation strategies, for netting samples made of polyethylene with nominal stretched mesh size of 80 mm and mesh side diameter of 4 mm. The results were obtained with the exact ("Exact") solution proposed by O'Neill (2002), and the polynomial ("Polynomial") and the spline ("Spline") models developed by De la Prada and Gonzales (2013).

those in the bottom due to the self-weight of the sample. Thus, this assumption can be acceptable only when the sample is submitted to large forces.

Then, De la Prada applied manual pretensions on the new and unused samples. Thus, the value of the applied load are not known and the samples are probably submitted to different pretensions. Otherwise, according to the results of De la Prada and Gonzales (2014), a netting sample had a different behaviour during the unloading after the loading with creep steps (the duration of these steps is not known), so the results showed the importance to characterize the visco-plastic mechanical behaviour of netting.

Finally, De la Prada tested only one sample of each material and could not offer an average estimation of the mesh resistance to opening. The shown results could be affected by scattering coming from the sample manufacturing process.

2.3.4 Cognard and Priour

Priour and Cognard (2011) proposed a different experimental method to evaluate the bending stiffness of mesh sides of netting panels.

Experimental method

One end of the netting panel was horizontally anchored and the other end was free (Fig. 2.17). The sample was submitted to its own weight.

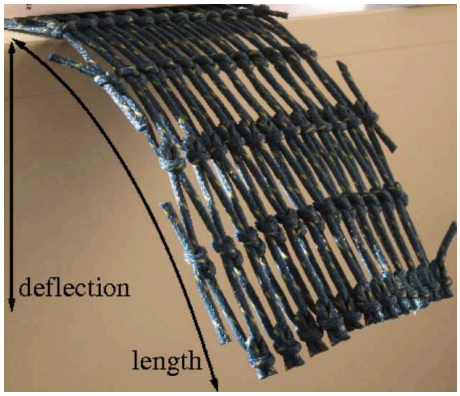

Figure 2.17 – Cantilever netting. A netting sample is anchored at one end and free at the other end. Reprinted from Priour and Cognard (2011).

Numerical method

Assuming that one netting sample behaves as one beam, and using the measured deflection and length of the netting sample (Fig. 2.17), Priour and Cognard (2011) identified a bending stiffness EI of a tested sample out of the netting plan. The bending stiffness was adjusted to obtain the same deflection as experimentally (Fig. 2.18).

Results

The results of the identifications are presented in Figure 2.19.

Discussion

The method proposed in Priour and Cognard (2011) is simple and does not require an expensive and complex experimental device.

Nevertheless, more tests and numerical identifications are necessary to evaluate the consistency of the method. It was noted that the identified bending stiffness was different depending on the orientation of the netting panel, that it was probably due to the asymmetry of the structure, particularly of the knot asymmetry.
Moreover, we can wonder if the identified bending stiffness in the plane will be the same as out of the plane since the asymmetry of the structure. The effect of the mechanical behaviour of the knots (not taken into account in the model) on the identified bending stiffness was probably different in and out of the netting plane.

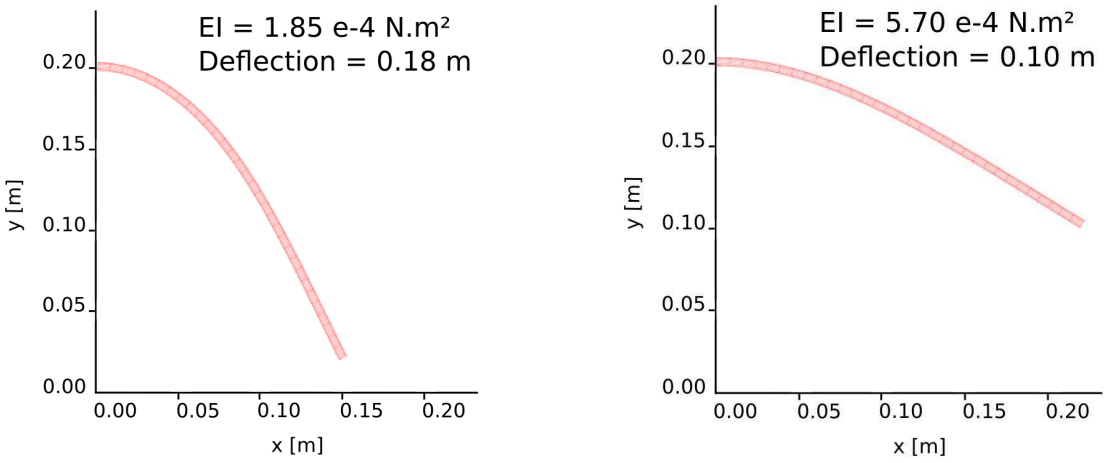

Figure 2.18 – Numerical simulation of a cantilever netting panel. The bending stiffness is adjusted to obtain the same deflection as experimentally. As expected, a higher value of bending stiffness is identified when the deflection is smaller. Reprinted from Priour and Cognard (2011).

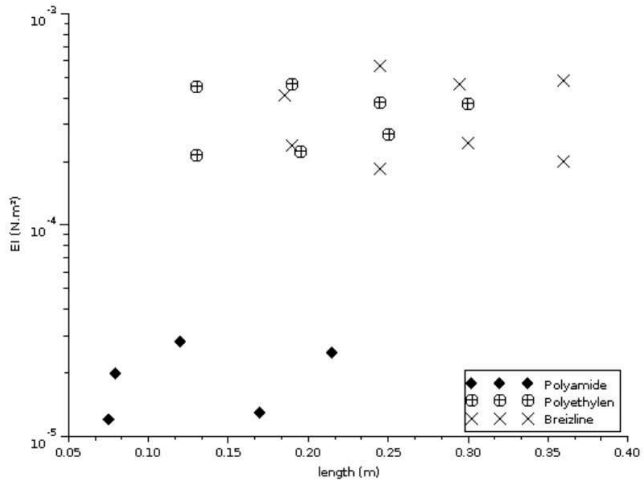

Figure 2.19 – Bending stiffnesses identified for netting samples made of polyamide, Green polyethylene and Brezline polyethylene. The identified bending stiffness is different depending on the face of the sample that is above. Note that a base-10 log scale was used for the Y-axis. The length is described in Figure 2.17. Reprinted from Priour and Cognard (2011).

This out-of-plane stiffness could be a useful parameter for the simulation of fishing trawls.

2.4 Discussion

Three models for the netting **mesh** that are used for the modelling of the mesh resistance to opening were presented: the model of Priour (2013), the analytical model of O'Neill (2002) and the fitting model of De la Prada and Gonzales (2013). The three models are simple and offer shorter computational time than in case of a finite element model. The three models are well-fitted for the simulation of netting.

Priour (2013) proposed a finite element method to **model** the mechanical behaviour **of netting**. It could model trawl made of thousands of meshes with a computational and a numerical efficiency. Nevertheless, works are necessary on the springs which model the bending stiffness of the mesh sides and on the estimation of the couple between two triangular elements to accurately simulate the effect of the bending stiffness.

Four experimental methods to evaluate the bending stiffness were presented: the method based on the ROD-m prototype of Sala et al. (2007), the suspension of a cylindrical sample of Balash (2012), the simple suspension of a netting sample of De la Prada and Gonzales (2014), and the cantilever netting of Priour and Cognard (2011).

First, the analytical model proposed in O'Neill (2002) was used in the methods presented in Sala et al. (2007), Balash (2012) and De la Prada and Gonzales (2014). Nevertheless, O'Neill assumed that there is no elongation in mesh sides, and the proposed approximation is valid only in case of a relatively low value of bending stiffness or high loading forces.

The biaxial experimental set-up presented in Sala et al. (2007) required a complex and expensive device (not commercially available yet) whereas De la Prada and Gonzales (2014) proposed to suspend netting samples. In spite of the low cost of the experiment proposed by De la Prada, she expected uniform deformation in suspended netting samples, which is probably a strong assumption.

Sala et al. (2007) and De la Prada and Gonzales (2014) took into account the size of the knots: the size of the knots was evaluated by inverse identification, the structure of the knot and the variation in the results making the experimental measurement of the dimensions of knots difficult. Nevertheless, the results of the identifications were not always consistent because of the strong correlations between the geometrical parameters.

Priour and Cognard (2011) did not take into account the knots, contrary to Sala and De la Prada. It would be necessary to study the effect of the size of the knots on the results of the identifications. Moreover, the method proposed in Priour and Cognard (2011) required closed mesh netting.

The method presented in Balash (2012) is interesting because of the cylindrical shape of the tested netting sample, similar to the shape of a trawl codend. Nevertheless, by choosing to use the asymptotic model proposed by O'Neill, the author made strong assumptions: no twine elongation, accuracy only when $\epsilon < 0.2$. The

method could be studied in-depth (more experimental tests, descriptions of the results and identifications).

The existing studies give information for setting up a methodology in order to evaluate the bending stiffness in mesh sides.

First, elongation, shear and torsion in mesh sides could be taken into account in the numerical model.

Next, the non-expensive experimental set-up proposed in De la Prada and Gonzales (2014) could be used with a numerical model simulating the non uniform deformation in suspended netting samples. Moreover, this type of test does not require closed meshes.

Then, the effect of the size of knots in the numerical model on the identified mesh resistance to opening could be studied. A method could be proposed to measure the experimental knot size.

Finally, the proposed method could be validated by tests on a large range of netting samples with different materials, mesh side lengths, sample sizes, loading levels.

CHAPTER

3 Experimental method and netting samples

3.1 Experiments

Three types of experiments were performed in order to evaluate the bending stiffness of mesh sides: a uniaxial tensile test on a classical testing machine, a suspending test of the same type as De la Prada and Gonzales (2014), and a biaxial test of the same type as Sala et al. (2007).

During uniaxial tensile tests, the size of netting samples in one direction was controlled and the evolution of the opening of one mesh was accurately measured. In case of suspending tests, that were designed to be simple and non-expensive to carry out, the openings of all the meshes were known. Finally, in case of biaxial tensile tests, the application of forces is similar to the one in a dragged trawl codend.

3.1.1 Uniaxial tensile tests

In this first type, measurements were performed on a LR5Kplus tensile testing machine, with a 250 N load cell, of the company Lloyd instruments. The uniaxial tensile tests were controlled by the jaw displacement. Relaxation stages were performed by blocking the jaw movement. A LASERSCAN 200 non-contacting extensometer (Lloyd instruments) allowed the measurement of the height of the central mesh in the middle of the sample (L_{mesh} on Fig 3.1).

Concerning the load, we measured the sum of the effects of the jaw displacement (mechanical response of the netting sample), the weight of the netting panel and the weight of the device which allowed the fixation of the sample. We defined the loads Fm_N (horizontal on Fig. 3.1) and Fm_T (vertical on Fig. 3.1) as the loads applied on one mesh in the N-direction and the T-direction respectively. So, knowing the load F measured by the force sensor, the weight P_{panel} of the sample and the weight

P_{device} of the device, we calculated the **force by mesh** Fm_T applied on the mesh in the middle of the netting sample:

$$Fm_T = \frac{F - \frac{P_{panel}}{2} - P_{device}}{4} \tag{3.1}$$

The tested netting samples had 10 meshes in the T-direction and 4 meshes in the N-direction.

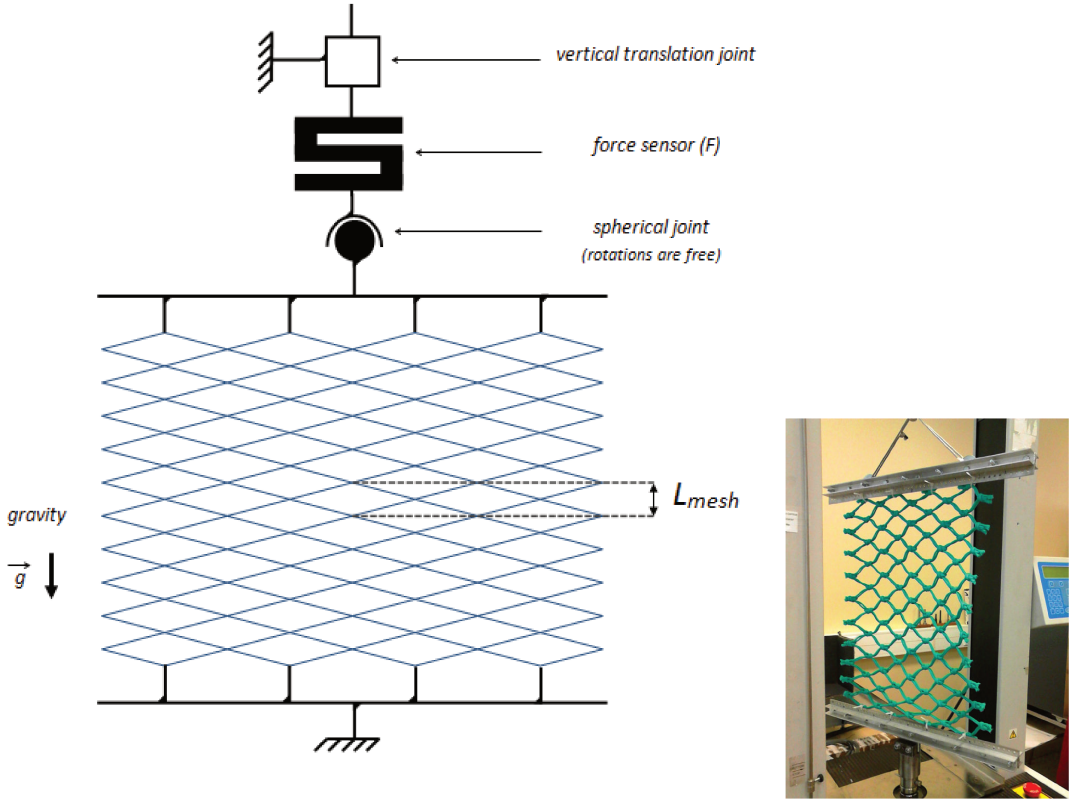

Figure 3.1 – Plan (left) and photograph (right) of the experimental set up of the uniaxial tensile test. The height L_{mesh} of the mesh in the middle of the netting sample is measured.

3.1.2 Suspending tests

Each rectangular panel of netting was suspended by its top boundary so that the T-direction of the netting was vertical. The panel was subjected to its own weight and to forces per mesh $\mathbf{Fm_T}$ applied in the T-direction on the knots at the bottom (Fig. 3.2).

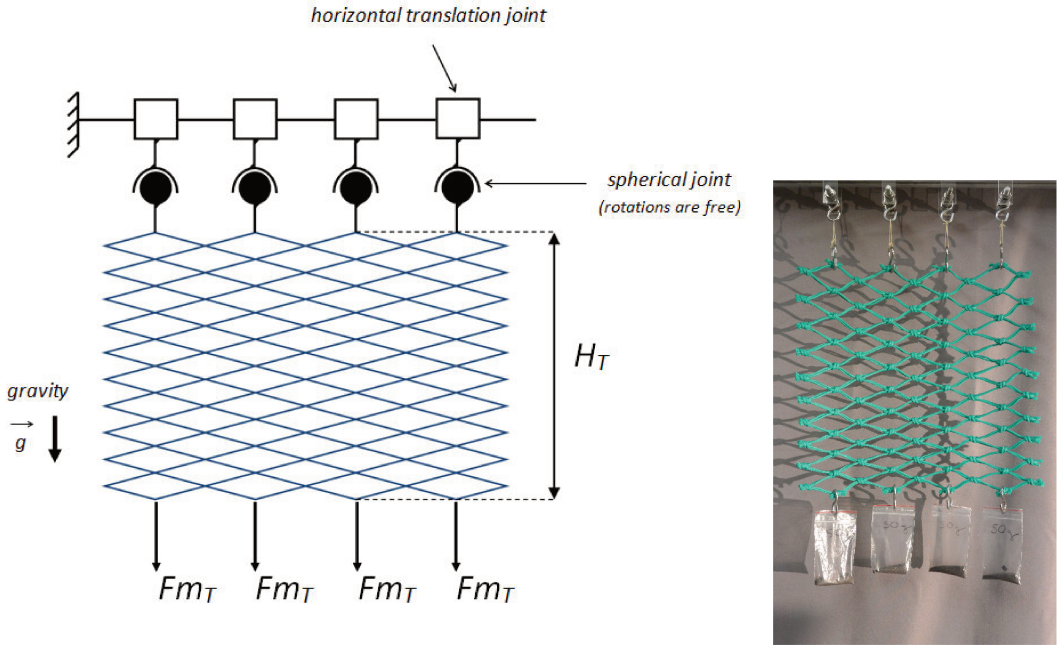

Figure 3.2 – Plan (left) and photograph (right) of the experimental setup of the suspending test. The panel is suspended from one of its ends and is subjected to its own weight and to forces Fm_T applied on bottom knots. Fm_T is called the force per mesh.

When a panel was suspended, the positions of all the nodes of the netting panel were measured. The use of a camera with a software designed and implemented in the laboratory allowed the recording of pictures with a chosen frequency. Note that the software allowed the application of optical corrections. Then, targets defined by the user on the first picture were identified in all the pictures. So the displacements of all these targets were measured during the recording.

In the case of a netting panel which had 10 meshes in the T-direction, the positions of 5 knots allowed the calculation of the heights of the four quarters $H1$, $H2$, $H3$ and $H4$ (Fig. 3.3 left), and the total height of the netting panel H_T (Fig. 3.2). In the case of a netting panel which had 25 meshes in the T-direction, the positions of 6 knots allowed the calculation of the heights of the five fifths $H1$, $H2$, $H3$, $H4$ and $H5$ (Fig. 3.3 right), and the total height of the netting panel H_T. These heights ($H1$ to $H5$) will be used later in the manuscript to study the non uniform strain in suspended netting panels and to validate the ability to simulate the deformed sample with the proposed model.

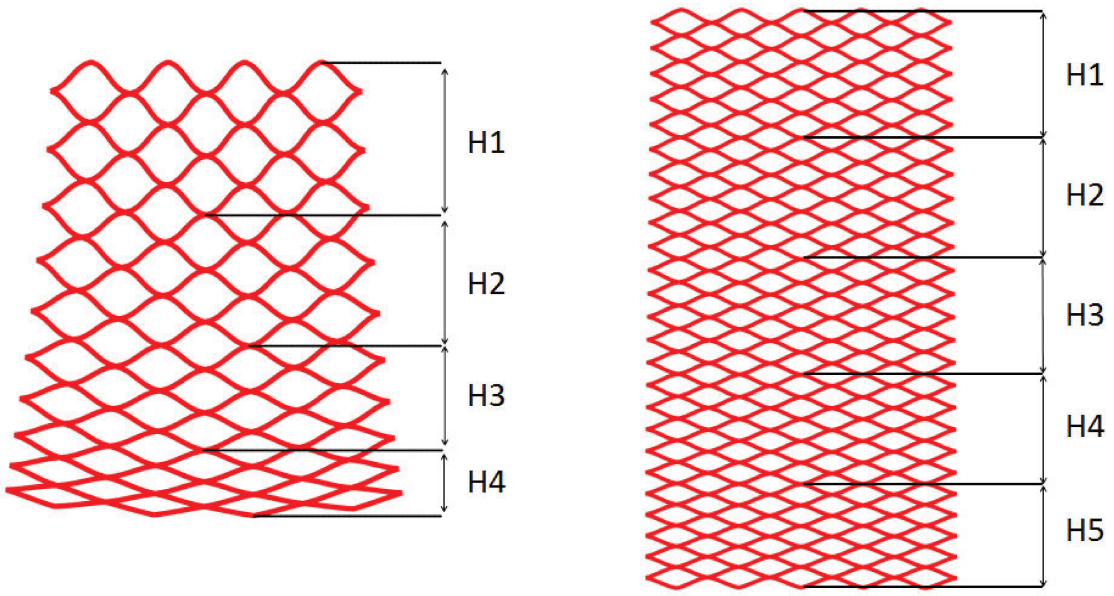

Figure 3.3 – Definition of heights for a 4x10-mesh netting panel (left) and a 5x25-mesh netting panel (right). The heights are measured vertically. The total height H_T of the panel is the sum of H1, H2, H3 and H4 for a 4x10-mesh netting panel, and the sum of H1, H2, H3, H4 and H5 for a 5x25-mesh netting panel.

3.1.3 Biaxial tensile tests

The netting was mounted on a device and submitted to forces on a netting sample in the T- and N-directions simultaneously.

The device is symmetric along the two directions T and N. The boundary conditions are described in Figure 3.4. The knots are free to move in the direction perpendicular to the frame plan but the weight of a tested sample is low, considering the applied forces per mesh Fm_T and Fm_N in the T and N directions respectively. Thus the displacements of the knots out of the plane are low. Anyway, the proposed numerical model, presented in section 5.2.3, was able to cope with this out-of-plane deformation.

To apply the forces on the samples, we suspended bags filled with iron dust to the extremities of the sample (Fig. 3.5, at the top). The ropes linking the knots to the bags are fixed to the knots with hooks (Fig. 3.5, bottom left). We used linear motion ball bearings to convert the weights of the filled bags into planar tensile forces (Fig. 3.5, bottom right).

When a panel was tested on the biaxial tensile device, the positions of all the nodes of the sample were measured using a camera, in the same way as in case of

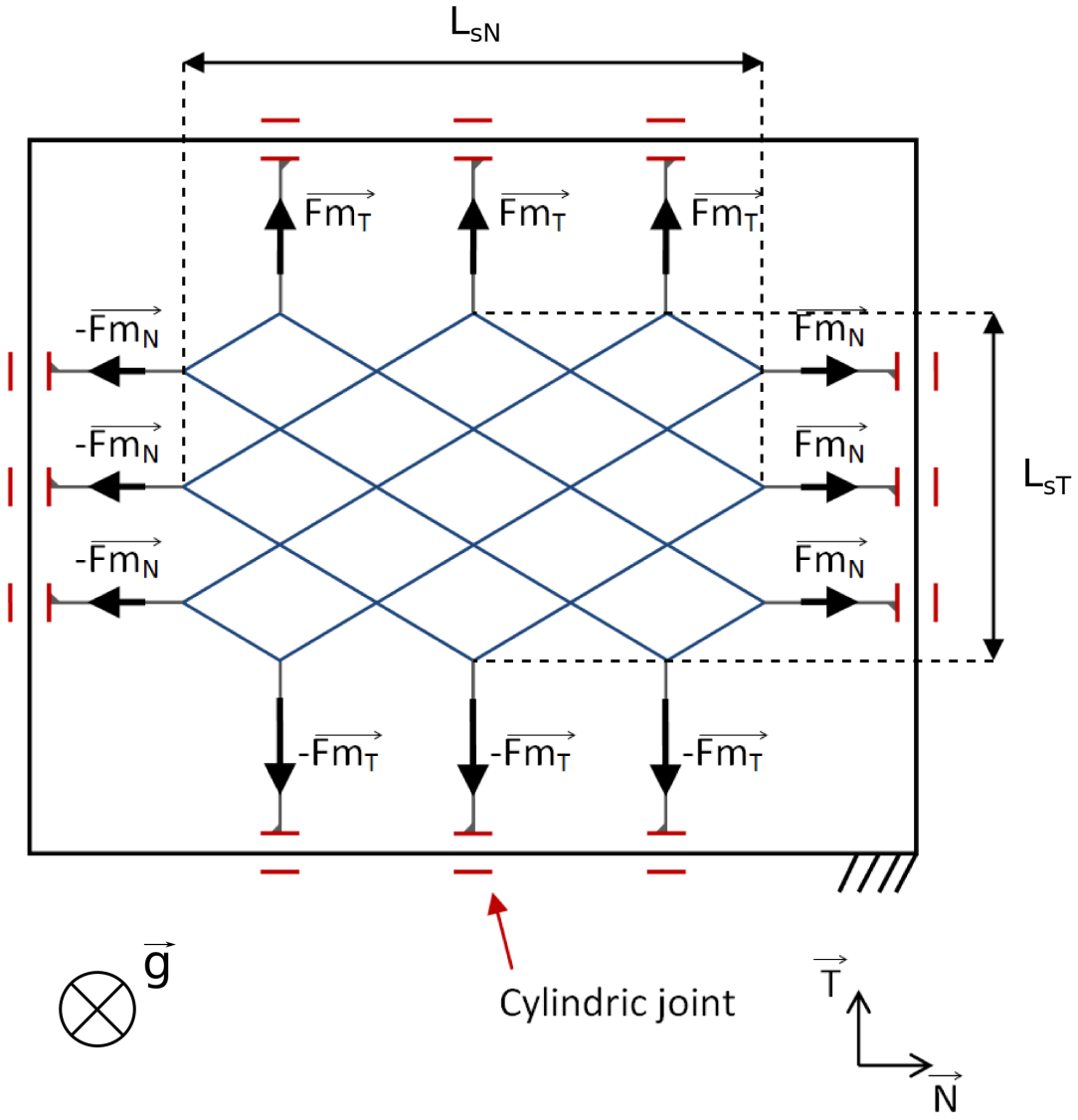

Figure 3.4 – Experimental setup plan of the biaxial tensile test. The panel of size 3x3-meshes, mounted on the device, is subjected to forces per mesh Fm_T and Fm_N in the T and N directions respectively. L_{sT} and L_{sN} are the length of the sample in the T and N directions respectively.

suspending tests (Section 3.1.2). The camera was fixed over the frame plane. Assuming that the deformation is homogeneous in the tested sample, we could work with the total lenghts L_{sT} and L_{sN} of the sample in the T- and N- directions respectively (Fig. 3.4).

The biaxial tensile tests with the machine, we made and presented here, are probably less efficient for the force and displacement measure acquisitions than

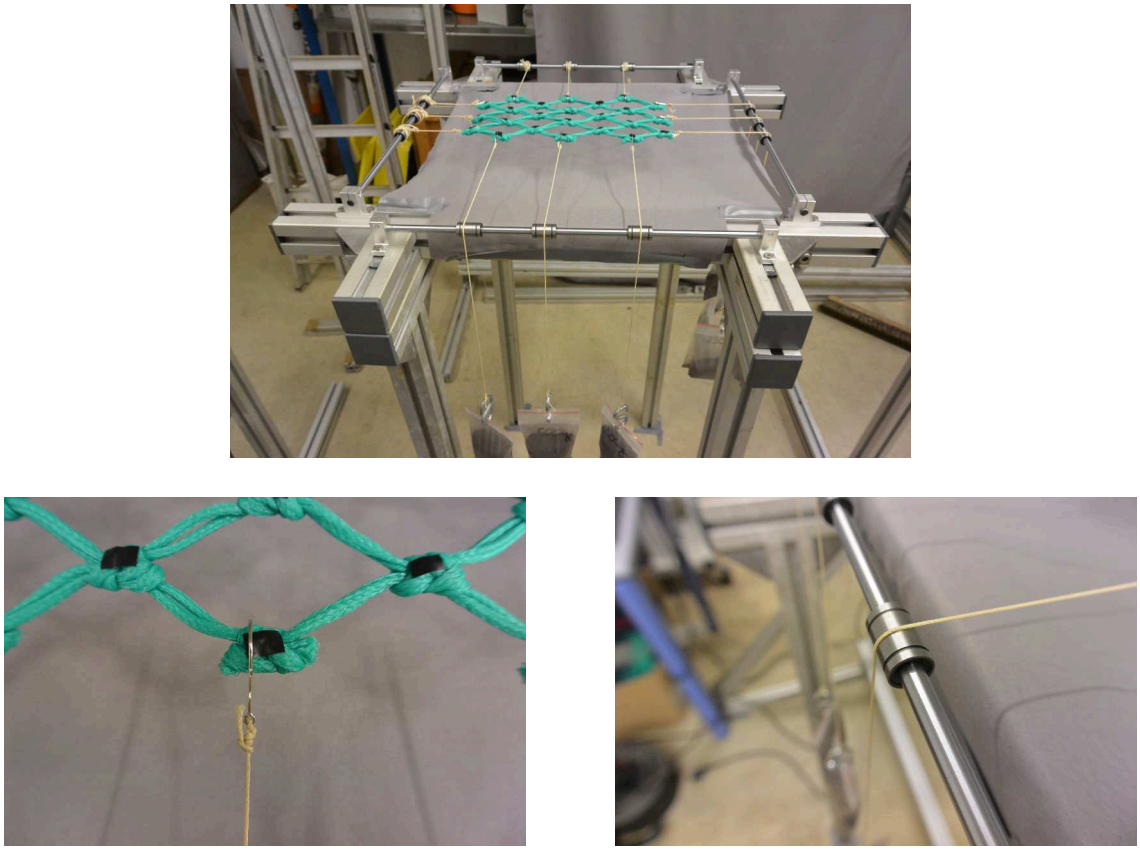

Figure 3.5 – At the top: general view of the experimental biaxial-tension device allowing to apply forces on a netting sample in the T- and N-directions simultaneously. At the bottom: ropes are connected to knots with hooks (left) and to the sides of the device frame with linear motion ball bearings (right).

those with the ROD-m protype of Sala et al. (2007). But, the dispersion in the results could be observed by testing some similar netting samples in the same conditions and could show the consistence of the accuracy (Chapter 4). Finally, this experimental device is less expensive than the one designed by Sala et al. (2007).

3.2 Netting samples for experiments

The tested netting samples were produced by the Le Drezen company (F-29730 Le Guilvinec, France). The netting types were those commonly used in trawl codends. The netting samples were made of two materials: polyethylene (PE) or polyamide (PA); two kinds of mesh sides were used: single twine or double twine; three sizes of panel were used: 3x3-mesh for biaxial tensile tests, 4x10-mesh and 5x25-mesh panels for tensile or suspending tests.

Eight types of samples were used:

- Single twine *green* PE netting, mesh side length of 40 mm, 4x10-mesh sample (Section 3.2.4)
- Double twine *green* PE netting, mesh side length of 49 mm, 3x3-mesh sample (Section 3.2.4)
- Double twine *green* PE netting, mesh side length of 49 mm, 4x10-mesh sample (Section 3.2.4)
- Double twine *green* PE netting, mesh side length of 49 mm, 5x25-mesh sample (Section 3.2.4)
- Double twine *green* PE netting, mesh side length of 60 mm, 4x10-mesh sample (Section 3.2.4)
- Single twine *Breztop* PE netting, mesh side length of 40 mm, 4x10-mesh sample (Section 3.2.5)
- Single twine *Brezline* PE netting, mesh side length of 60 mm, 4x10-mesh sample (Section 3.2.6)
- Single twine PA netting, mesh side length of 29.5 mm, 4x10-mesh sample (Section 3.2.7)

The chosen number of meshes in the netting samples was a compromise: the number of meshes had to be large enough to reduce the measurement errors (difficulty to define the center of a knot coming from the knot shape) and to reduce the possible variations in the results coming from the heterogeneity in the netting structure (initially the mesh opening was not uniform in a netting sample), and the number of meshes had to be not too large to take into account the available amount of netting. In case of suspending tests, there were two sizes of netting samples, 4x10- and 5x25- mesh samples, to study the influence of the number of meshes on the results of the identifications (Chapter 6). In case of biaxial tensile tests, 3x3-mesh samples were used regarding the experimental testing machine size and in order to reduce the effect of gravity on the off-plane vertical displacements. In case of uniaxial tensile tests, the displacement of the jaw of the tensile testing machine being limited, 4x10-mesh netting samples were used. Finally, for each type of netting panel, several samples were tested to measure the possible variation in the experimental results.

The netting samples were initially submitted to a pre-tension step to safeguard against knot slippage (Klust, 1983) and to remove the irreversible part of the elongation (Sala et al., 2004). This step was performed by suspending 400 N to each 4x10- or 5x25-mesh netting sample during 1 hour. The 3x3-mesh netting samples were submitted to 150 N. During the pre-tension step, the netting samples were

suspended either in the N-direction (usually) or in the T-direction. After the suspension step, the netting samples were let at rest on a horizontal plane during 2 hours.

Please note that all the samples of the same type (same material, same mesh side length, same mesh structure) come from an unique panel. Thus, they were submitted to the same process (temperature during the stretching step, duration, tensile forces).

3.2.1 Netting definitions

According to the International Organization for Standardization (ISO, 2003), a **netting** is *a meshed structure of indefinite shape and size composed of one yarn or of one or more systems of yarns interlaced or joined, or obtained by other means, for example by stamping or cutting from sheet material or by extrusion.*

A **mesh** is *a design formed opening, surrounded by netting material.* They are three types of mesh shapes: diamond mesh that is a mesh *composed of four sides of the same length*, square mesh that is a mesh *in which adjacent sides are at right angles*, and hexagonal mesh that is a mesh *composed of six sides, out of which the length of one pair of opposite sides can be different from that of the other four sides, in case of an irregular hexagon.* During my works, only netting with diamond meshes have been used. We will see later that, due to the knot size, it coud be relevant from a modelling point of view to consider an hexagonal shape for the meshes.

The **length of mesh side** L_{ms} is *the distance between two sequential knots or joints, measured from centre to centre when the yarn between those points is fully extended.*

In ISO (2003), general directions of a netting yarns are given:

- The **N-direction** is *the direction at right angles (Normal) to the general course of the netting yarn* (when the netting is stretched in this direction, the knots tend to tighten).
- The **T-direction** is *the direction parallel to the general course of the netting yarn* (when the netting is stretched in this direction, the knots tend to open).
- The **AB-directions** are *the directions parallel to a rectilinear sequence of mesh bars.*

The directions N and T, in the case of knotted netting, can be also defined relatively to the knot orientation (Fig. 3.6).

We defined, with these directions, the distances L_N and L_T between the centres of opposite knots, in the N-direction and the T-direction respectively.

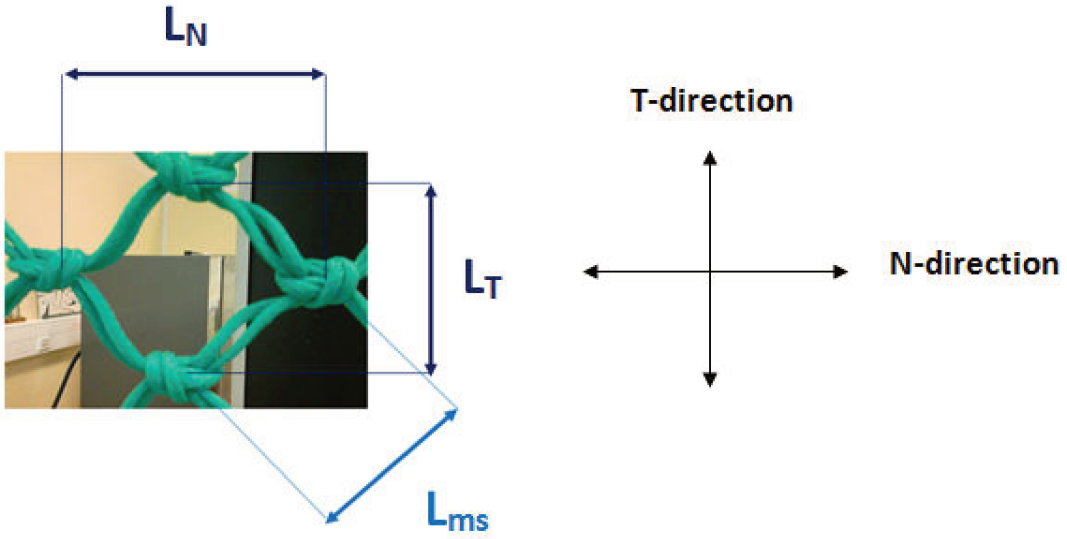

Figure 3.6 – Definition of the N-direction and of the T-direction, and definition of the parameters L_N , L_T and L_{ms} in a diamond netting mesh. The directions are related to the orientation of knots.

The International Organization for Standardization also defined the **opening of mesh**: it is, for knotted netting, *the longest distance between two opposite knots in the same mesh when fully extended in the N-direction*, and for knotless netting, *the inside distance between two opposite joints in the same mesh when fully extended along its longest possible axis.*

To work with dimensionless parameters which do not depend on the mesh side length, the **dimensionless openings** o_N and o_T in the N-direction and the T-direction respectively were introduced. The opening o_i , in the direction i, is the ratio of the distance L_i (Fig. 3.6) by the mesh side length L_{ms} (Eq. 3.2).

$$o_i = \frac{L_i}{L_{ms}} \tag{3.2}$$

3.2.2 Initial measurements

In order to evaluate the input parameters required by the numerical models presented in chapter 5, the following sample characteristics were measured:

- The mass m of the netting panel.

- The initial width H_{N0} and height H_{T0} of the netting panel (at rest) in the N-direction and the T-direction respectively. The panel position at rest was obtained by laying the netting panel free of load on a vibrating horizontal plane, where it remained free of load, until a stable position was reached.
- The characteristic length of the netting mesh sides L_{ms} and the mesh angle α_0 (angle between two consecutive mesh sides in the T-direction) at rest were derived from a simple cosinus equation and the initial dimensions of the panel (Fig. 3.7).

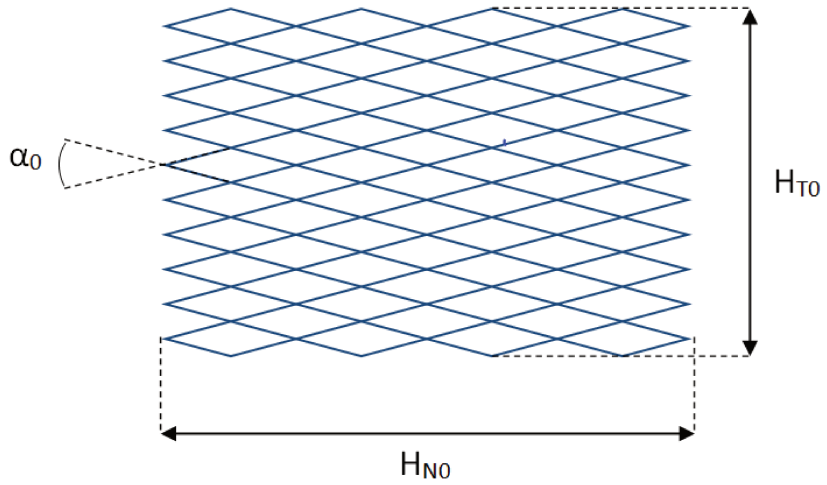

Figure 3.7 – Dimensions H_{N0} and H_{T0} of a netting panel allow the characteristic length of the mesh sides L_{ms} and the mesh angle α_0 at rest to be calculated.

The area density ρ_0 of each netting panel at rest was calculated using the mass m and the initial lengths H_{N0} and height H_{T0}:

$$\rho_0 = \frac{m}{H_{N0}.H_{T0}} \tag{3.3}$$

3.2.3 Knots

The knots in all the tested samples were of the same type, represented in Figure 3.8.

3.2.4 Green polyethylene braided netting

We investigated single and double twine netting made of *green* polyethylene. The *green* polyethylene-fibre braided twine is the basic polyethylene product of Le Drezen company.

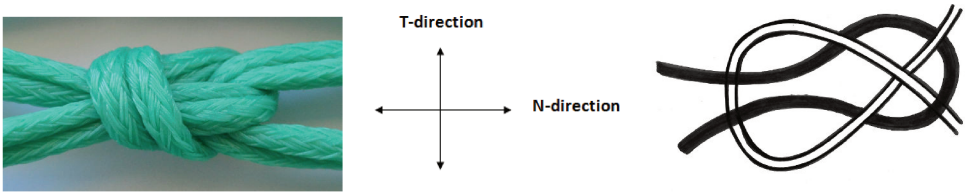

Figure 3.8 – Left: knot in a double twine netting made up of polyethylene braided twines. Right: scheme of the knot.

This twine is made up of a core and a sheath (Fig. 3.9). The core and the sheath are composed of 20 and 64 fibres respectively. In the core, fibres are twisted, whereas in the sheath 16 threads made up of 4 fibres are braided. The linear density of the twine is 5590.4 $10^{-6} \pm 10.6\ 10^{-6}\ kg.m^{-1}$, that is 5590.4 ± 10.6 tex. The diameter of the fibres, measured with a digital microscope, is 290 μm (Fig. 3.9). The diameter of the twine is 3.14 ± 0.01 mm. The pitch of the braided sheath, which is the longitudinal distance required for one revolution of a thread around the twine, is 26.12 ± 0.62 mm.

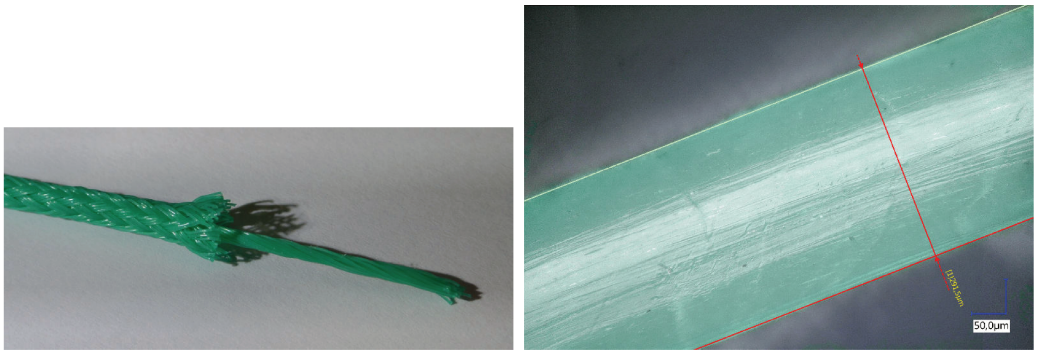

Figure 3.9 – Left: Green PE braided twine. Right: Green PE fibre.

The mesh sides of the single twine netting were composed of only one polyethylene-fibre braided twine. While the mesh sides of the double twine netting were composed of two polyethylene-fibre braided twines.

Single twine *green* PE netting, mesh side length of 40 mm, 4x10-mesh sample

In the case of **single twine netting**, the length of mesh sides was 40.44 ± 0.3 mm. The samples had 4 and 10 meshes in the N-direction and T-direction respectively (Fig. 3.7). Ten samples were used in suspension tests and one in the uniaxial tensile test. The mass and the dimensions at rest H_{N0} and H_{T0} are given by Table 3.1 and 3.2.

sample number	mass [kg]	H_{N0} [m]	H_{T0} [m]	ρ_0 $[kg.m^{-2}]$	H_T [m] ($Fm_T = 0.324$ N)	H_T [m] ($Fm_T = 0.814$ N)	H_T [m] ($Fm_T = 1.795$ N)	H_T [m] ($Fm_T = 2.776$ N)
1	0.0614	0.320	0.097	1.978	0.201	0.294	0.436	0.505
2	0.0612	0.318	0.095	2.026	0.193	0.289	0.427	0.495
3	0.0624	0.323	0.095	2.034	0.200	0.300	0.427	0.507
4	0.0622	0.320	0.100	1.944	0.197	0.289	0.430	0.501
5	0.0618	0.318	0.097	2.004	0.195	0.291	0.429	0.503
6	0.0626	0.325	0.102	1.888	0.205	0.303	0.440	0.507
7	0.0618	0.323	0.103	1.857	0.212	0.304	0.433	0.498
8	0.0611	0.320	0.100	1.909	0.192	0.286	0.423	0.491
9	0.0617	0.324	0.098	1.943	0.195	0.293	0.433	0.497
10	0.0614	0.320	0.098	1.958	0.197	0.288	0.435	0.513

Table 3.1 – Mass and dimensions of the **4x10**-mesh single twine netting samples of *green* polyethylene type. The length of mesh sides is 40.44 ± 0.3 mm. H_T is the total length of the suspended panel in the T-direction after a creep step of 30 minutes. Each sample was submitted to a pre-tension step in the N-direction. m is the mass of the netting sample, H_{N0} and H_{T0} are the width and the heigth of the netting sample at rest respectively, ρ_0 is the area density at rest, and H_T is the height of the suspended netting sample.

Double twine *green* PE netting, mesh side length of 49 mm, 3x3-mesh sample

In the case of **double twine netting**, samples with two different mesh side lengths and three different sizes were tested.

Tables 3.3, 3.4, 3.5 give the characteristics of samples with 3 meshes in the N-direction and the T-direction. These samples have been used for biaxial tests. Samples have been tested with $Fm_N = 0$ N in Table 3.3, with $Fm_N = Fm_T$ in Table 3.4 and with $Fm_N = 2Fm_T$ in Table 3.5.

sample number	mass [kg]	H_{N0} [m]	H_{T0} [m]	ρ_0 $[kg.m^{-2}]$
1	0.0619	0.319	0.100	1.940

Table 3.2 – Mass and dimensions of one **4x10**-mesh single twine netting sample of *green* polyethylene type. The length of mesh sides is 40.44 ± 0.3 mm. The sample was submitted to a pre-tension step in the N-direction and was used in uniaxial tensile test. m is the mass of the netting sample, H_{N0} and H_{T0} are the width and the heigth of the netting sample at rest respectively, and ρ_0 is the area density at rest.

sample number	mass [kg]	H_{N0} [m]	H_{T0} [m]	ρ_0 $[kg.m^{-2}]$	H_T [m] ($Fm_T = 0.981$ N)	H_T [m] ($Fm_T = 1.962$ N)	H_T [m] ($Fm_T = 4.905$ N)
1	0.041	0.29	0.048	2.945	0.099	0.122	0.168
2	0.041	0.286	0.051	2.811	0.101	0.126	0.178
3	0.040	0.288	0.052	2.671	0.10	0.12	0.172
4	0.041	0.287	0.052	2.747	0.098	0.124	0.177
5	0.040	0.286	0.052	2.690	0.102	0.131	0.183

Table 3.3 – Mass and dimensions of the **3x3**-mesh double twine netting samples of *green* polyethylene type. The length of mesh sides is 49 ± 0.2 mm. The samples were tested in biaxial tests with $Fm_N = 0$ N. Each sample was submitted to a pre-tension step in the N-direction. m is the mass of the netting sample, H_{N0} and H_{T0} are the width and the heigth of the netting sample at rest respectively, ρ_0 is the area density at rest, and H_T is the height of the suspended netting sample.

Double twine *green* PE netting, mesh side length of 49 mm, 4x10- and 5x25-mesh samples

Table 3.6 give the characteristics for samples with 4 and 10 meshes in the N-direction and T-direction respectively, and Table 3.7 for samples with 5 and 25 meshes in the N-direction and T-direction respectively. These samples were tested in suspending

sample number	mass [kg]	H_{N0} [m]	H_{T0} [m]	ρ_0 $[kg.m^{-2}]$	$H_N \vert H_T$ [m] ($Fm_T = 0.981$ N)	$H_N \vert H_T$ [m] ($Fm_T = 1.962$ N)
1	0.041	0.29	0.045	3.142	0.277|0.092	0.27|0.105
2	0.041	0.288	0.045	3.164	0.28|0.09	0.278|0.102
3	0.0395	0.285	0.050	2.772	0.280|0.09	0.274|0.101
4	0.0394	0.284	0.046	3.016	0.278|0.088	0.273|0.097
5	0.0398	0.287	0.052	2.667	0.278|0.091	0.271|0.106

Table 3.4 – Mass and dimensions of the **3x3**-mesh double twine netting samples of *green* polyethylene type. The length of mesh sides is 49 ± 0.2 mm. The samples were tested in biaxial tests with $Fm_N = Fm_T$. Each sample was submitted to a pre-tension step in the N-direction. m is the mass of the netting sample, H_{N0} and H_{T0} are the width and the heigth of the netting sample at rest respectively, ρ_0 is the area density at rest, and H_N and H_T are the width and the heigth of the suspended netting sample respectively.

tests.

Double twine *green* PE netting, mesh side length of 60 mm, 4x10-mesh sample

Tables 3.8 and 3.9 give the characteristics for samples with 4 and 10 meshes in the N-direction and T-direction respectively, and a mesh side length of 60 ± 0.3 mm. The samples, described in Table 3.8, were tested in suspending tests while the netting panels presented in Table 3.9 were tested in uniaxial tensile tests.

3.2.5 Breztop polyethylene braided netting

We tested **single twine netting** made of *Breztop* polyethylene. The *Breztop* polyethylene-fibre braided twine is a product of Le Drezen company.

This twine is made up of a core and a sheath (Fig. 3.10). The core and the sheath are composed of 30 and 32 fibres respectively. In the core, fibres are twisted,

sample number	mass [kg]	H_{N0} [m]	H_{T0} [m]	ρ_0 $[kg.m^{-2}]$	$H_N \vert H_T$ [m] ($Fm_T = 1.962$ N)	$H_N \vert H_T$ [m] ($Fm_T = 3.924$ N)	$H_N \vert H_T$ [m] ($Fm_T = 4.905$ N)
1	0.040	0.287	0.047	2.965	0.284|0.08	0.285|0.083	0.286|0.085
2	0.0393	0.285	0.055	2.507	0.283|0.08	0.281|0.085	0.283|0.090
3	0.041	0.289	0.047	3.018	0.284|0.077	0.285|0.083	0.284|0.085
4	0.0396	0.287	0.048	2.874	0.285|0.077	0.283|0.085	0.283|0.086
5	0.0408	0.289	0.0475	2.972	0.285|0.077	0.283|0.083	0.282|0.085

Table 3.5 – Mass and dimensions of the **3x3**-mesh double twine netting samples of *green* polyethylene type. The length of mesh sides is 49 ± 0.2 mm. The samples were tested in biaxial tests with $Fm_N = 2Fm_T$. Each sample was submitted to a pre-tension step in the N-direction. m is the mass of the netting sample, H_{N0} and H_{T0} are the width and the heigth of the netting sample at rest respectively, ρ_0 is the area density at rest, and H_N and H_T are the width and the heigth of the suspended netting sample respectively.

whereas in the sheath 16 threads made up of 2 fibres are braided. The linear density of the twine is 2080.8 10^{-6} ± 82.4 10^{-6} $kg.m^{-1}$, that is 2080.8 ± 82.4 tex. The diameter of the fibres, measured with a digital microscope, is 200 μm (Fig. 3.10). The diameter of the twine is 2.5 ± 0.01 mm. The pitch of the braided sheath, which is the longitudinal distance required for one revolution of a thread around the twine, is 13.75 ± 0.25 mm.

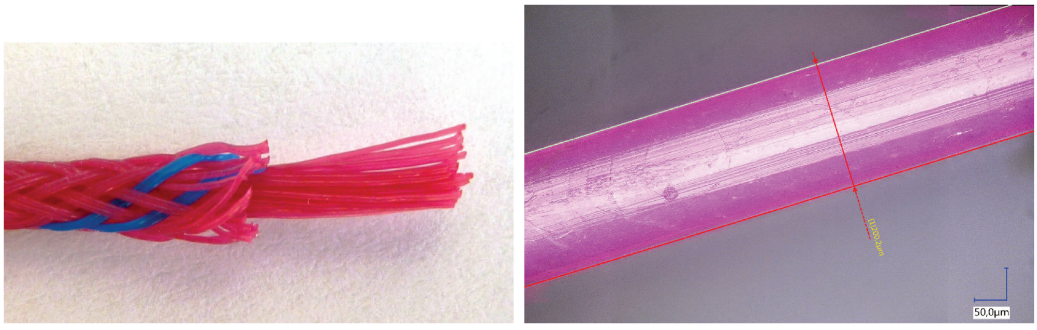

Figure 3.10 – Left: Breztop braided twine. Right: Breztop fibre.

sample number	mass [kg]	H_{N0} [m]	H_{T0} [m]	ρ_0 $[kg.m^{-2}]$	H_T [m] ($Fm_T = 0.0$ N)	H_T [m] ($Fm_T = 0.655$ N)	H_T [m] ($Fm_T = 1.146$ N)	H_T [m] ($Fm_T = 2.617$ N)	H_T [m] ($Fm_T = 5.070$ N)
1	0.164	0.358	0.400	1.145	0.425	0.495	0.540	0.620	0.685
2	0.164	0.351	0.435	1.074	0.455	0.510	0.545	0.625	0.685
3	0.163	0.360	0.390	1.161	0.430	0.485	0.530	0.620	0.680
4	0.163	0.353	0.425	1.086	0.450	0.510	0.545	0.620	0.685
5	0.164	0.364	0.365	1.234	0.400	0.460	0.505	0.600	0.670

Table 3.6 – Mass and dimensions of the **4x10**-mesh double twine netting samples of *green* polyethylene type. The length of mesh sides is 49 ± 0.2 mm. H_T is the total length of the suspended panel in the T-direction after a creep step of 30 minutes. Each sample was submitted to a pre-tension step in the T-direction. m is the mass of the netting sample, H_{N0} and H_{T0} are the width and the heigth of the netting sample at rest respectively, ρ_0 is the area density at rest, and H_T is the height of the suspended netting sample.

The length of mesh sides was 40 ± 0.2 mm. The samples had 4 and 10 meshes in the N-direction and T-direction respectively. Ten samples were tested. The mass and the dimensions at rest H_{N0} and H_{T0} are given by Table 3.10.

3.2.6 Brezline polyethylene braided netting

We investigated **single twine netting** made of *Brezline* polyethylene. The *Brezline* polyethylene-fibre braided twine is a product of Le Drezen company.

This twine is made up of a core and a sheath (Fig. 3.11). The core and the sheath are composed of 24 and 64 fibres respectively. In the core, fibres are twisted, whereas in the sheath 16 threads made up of 4 fibres are braided. The linear density of the twine is 8009.7 10^{-6} ± 229.4 10^{-6} $kg.m^{-1}$, that is 8009.7 ± 229.4 tex. The diameter of the fibres, measured with a digital microscope, is 340 μm (Fig. 3.11). The diameter of the twine is 4 ± 0.01 mm. The pitch of the braided sheath, which is the longitudinal distance required for one revolution of a thread around the twine, is 21.2 ± 0.2 mm.

The length of mesh sides was 59.84 ± 0.6 mm. The samples had 4 and 10 meshes in the N-direction and T-direction respectively. Ten samples were tested. The mass and the dimensions at rest H_{N0} and H_{T0} are given by Table 3.11.

sample number	mass [kg]	H_{N0} [m]	H_{T0} [m]	ρ_0 $[kg.m^{-2}]$	H_T [m] ($Fm_T = 0.0$ N)	H_T [m] ($Fm_T = 1.146$ N)	H_T [m] ($Fm_T = 2.127$ N)	H_T [m] ($Fm_T = 3.108$ N)	H_T [m] ($Fm_T = 4.089$ N)	H_T [m] ($Fm_T = 5.070$ N)
1	0.482	0.493	0.405	3.334	0.605	0.870	1.075	1.240	1.360	1.475
2	0.493	0.504	0.400	3.443	0.585	0.855	1.060	1.230	1.340	1.450
3	0.490	0.489	0.387	3.517	0.590	0.855	1.040	1.230	1.340	1.470
4	0.481	0.494	0.375	3.543	0.590	0.850	1.030	1.210	1.330	1.450
5	0.485	0.494	0.380	3.536	0.595	0.850	1.040	1.215	1.340	1.460

Table 3.7 – Mass and dimensions of the **5x25**-mesh double twine netting samples of *green* polyethylene type. The length of mesh sides is 49 ± 0.2 mm. H_T is the total length of the suspended panel in the T-direction after a creep step of 30 minutes. Each sample was submitted to a pre-tension step in the N-direction. m is the mass of the netting sample, H_{N0} and H_{T0} are the width and the heigth of the netting sample at rest respectively, ρ_0 is the area density at rest, and H_T is the height of the suspended netting sample.

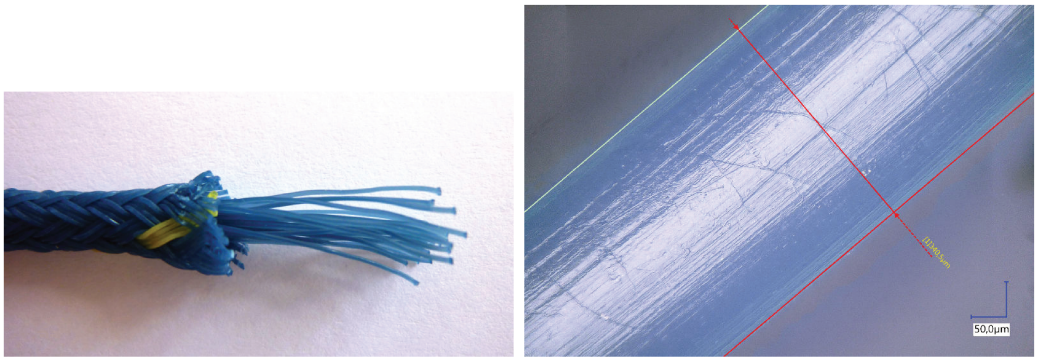

Figure 3.11 – Left: Brezline braided twine. Right: Brezline fibre.

3.2.7 Polyamide braided netting

We investigated **single twine netting** made of polyamide braided twines.

This twine is made up of a braided sheath composed of 16 threads. The linear density of the twine is 2766.5 10^{-6} ± 69.7 10^{-6} $kg.m^{-1}$, that is 2766.5 ± 69.7 tex. The diameter of the twine is 2.32 ± 0.1 mm. The pitch of the braided sheath, which is the longitudinal distance required for one revolution of a thread around the twine,

sample number	mass [kg]	H_{N0} [m]	H_{T0} [m]	ρ_0 $[kg.m^{-2}]$	H_T [m] ($Fm_T = 0.0$ N)	H_T [m] ($Fm_T = 0.4905$ N)	H_T [m] ($Fm_T = 0.981$ N)	H_T [m] ($Fm_T = 2.4525$ N)	H_T [m] ($Fm_T = 4.905$ N)
1	0.178	0.466	0.143	2.671	0.245	0.433	0.545	0.738	0.829
2	0.177	0.455	0.180	2.161	0.285	0.458	0.560	0.737	0.830
3	0.179	0.465	0.135	2.851	0.237	0.423	0.540	0.725	0.815
4	0.179	0.465	0.140	2.750	0.233	0.425	0.530	0.730	0.830
5	0.180	0.458	0.167	2.353	0.275	0.470	0.575	0.745	0.820

Table 3.8 – Mass and dimensions of the **4x10**-mesh double twine netting samples of *green* polyethylene type. The length of mesh sides is 60 ± 0.3 mm. H_T is the total length of the suspended panel in the T-direction after a creep step of 30 minutes. Each sample was submitted to a pre-tension step in the N-direction. m is the mass of the netting sample, H_{N0} and H_{T0} are the width and the heigth of the netting sample at rest respectively, ρ_0 is the area density at rest, and H_T is the height of the suspended netting sample.

sample number	mass [kg]	H_{N0} [m]	H_{T0} [m]	ρ_0 $[kg.m^{-2}]$
1	0.179	0.464	0.145	2.661
2	0.181	0.465	0.142	2.741

Table 3.9 – Mass and dimensions of two **4x10**-mesh double twine netting samples of *green* polyethylene type. The length of mesh sides is 60 ± 0.3 mm. The samples were tested in uniaxial tensile tests. Each sample was submitted to a pre-tension step in the N-direction. m is the mass of the netting sample, H_{N0} and H_{T0} are the width and the heigth of the netting sample at rest respectively, and ρ_0 is the area density at rest.

is 7 ± 0.5 mm.

The length of mesh sides was 29.5 ± 0.6 mm. The samples had 4 and 10 meshes in the N-direction and T-direction respectively. Ten samples were tested. The mass

sample number	mass [kg]	H_{N0} [m]	H_{T0} [m]	ρ_0 $[kg.m^{-2}]$	H_T [m] ($Fm_T = 0.324$ N)	H_T [m] ($Fm_T = 0.814$ N)	H_T [m] ($Fm_T = 1.795$ N)	H_T [m] ($Fm_T = 2.776$ N)
1	0.0184	0.318	0.080	0.723	0.407	0.558	0.624	0.648
2	0.0184	0.318	0.087	0.665	0.398	0.552	0.626	0.650
3	0.0184	0.318	0.085	0.681	0.417	0.563	0.634	0.655
4	0.0183	0.317	0.087	0.664	0.423	0.568	0.629	0.653
5	0.0183	0.318	0.082	0.702	0.419	0.560	0.628	0.651
6	0.0186	0.317	0.084	0.698	0.428	0.571	0.633	0.656
7	0.0184	0.317	0.090	0.645	0.414	0.563	0.629	0.651
8	0.0184	0.317	0.087	0.667	0.430	0.569	0.629	0.650
9	0.0183	0.318	0.086	0.669	0.434	0.574	0.631	0.653
10	0.0184	0.318	0.085	0.681	0.424	0.567	0.626	0.650

Table 3.10 – Mass and dimensions of the **4x10**-mesh single twine netting samples of *Breztop* polyethylene type. H_T is the total length of the suspended panel in the T-direction after a creep step of 30 minutes. Each sample was submitted to a pre-tension step in the N-direction. m is the mass of the netting sample, H_{N0} and H_{T0} are the width and the heigth of the netting sample at rest respectively, ρ_0 is the area density at rest, and H_T is the height of the suspended netting sample.

and the dimensions at rest H_{N0} and H_{T0} are given by Table 3.12.

sample number	mass [kg]	H_{N0} [m]	H_{T0} [m]	ρ_0 $[kg.m^{-2}]$	H_T [m] ($Fm_T = 0.324$ N)	H_T [m] ($Fm_T = 0.814$ N)	H_T [m] ($Fm_T = 1.795$ N)	H_T [m] ($Fm_T = 2.776$ N)
1	0.1165	0.470	0.138	1.796	0.370	0.509	0.702	0.802
2	0.1165	0.467	0.128	1.949	0.361	0.510	0.711	0.814
3	0.1158	0.474	0.128	1.909	0.343	0.494	0.697	0.807
4	0.1189	0.479	0.125	1.986	0.343	0.501	0.707	0.816
5	0.1182	0.478	0.132	1.873	0.358	0.514	0.714	0.818
6	0.1186	0.475	0.135	1.849	0.361	0.512	0.710	0.810
7	0.1154	0.472	0.126	1.940	0.346	0.495	0.691	0.797
8	0.1196	0.480	0.144	1.730	0.399	0.547	0.746	0.848
9	0.1175	0.483	0.128	1.901	0.392	0.547	0.749	0.854
10	0.1187	0.480	0.133	1.859	0.379	0.532	0.737	0.849

Table 3.11 – Mass and dimensions of the **4x10**-mesh single twine netting samples of *Brezline* polyethylene type. H_T is the total length of the suspended panel in the T-direction after a creep step of 30 minutes. Each sample was submitted to a pre-tension step in the N-direction. m is the mass of the netting sample, H_{N0} and H_{T0} are the width and the heigth of the netting sample at rest respectively, ρ_0 is the area density at rest, and H_T is the height of the suspended netting sample.

sample number	mass [kg]	H_{T0} [m]	H_{N0} [m]	ρ_0 $[kg.m^{-2}]$	H_T [m] ($Fm_T = 0.0$ N)	H_T [m] ($Fm_T = 0.324$ N)
1	0.0209	0.222	0.125	0.753	0.264	0.427
2	0.0211	0.235	0.128	0.701	0.242	0.441
3	0.0212	0.235	0.113	0.798	0.223	0.448
4	0.0208	0.227	0.115	0.797	0.205	0.429
5	0.0212	0.235	0.112	0.805	0.196	0.446
6	0.0211	0.232	0.110	0.827	0.198	0.436
7	0.0207	0.225	0.105	0.876	0.250	0.428
8	0.0212	0.235	0.130	0.694	0.265	0.442
9	0.0210	0.232	0.113	0.801	0.242	0.435
10	0.0209	0.235	0.125	0.711	0.235	0.447

Table 3.12 – Mass and dimensions of the **4x10**-mesh single twine netting samples of polyamide type. H_T is the total length of the suspended panel in the T-direction after a creep step of 30 minutes. Each sample was submitted to a pre-tension step in the N-direction. m is the mass of the netting sample, H_{N0} and H_{T0} are the width and the heigth of the netting sample at rest respectively, ρ_0 is the area density at rest, and H_T is the height of the suspended netting sample.

3.3 Evaluation of the axial stiffness of twine

Tensile tests have been performed on the LR5Kplus tensile testing machine to evaluate the axial stiffness of twines constituting the studied fishing nets. Because of the complex visco-elasto-plastic behaviour of the polyethylene, it is not straightforward to evaluate the axial stiffness. We proposed to assess this stiffness by measuring the moduli of short-time behaviour according to Bles et al. (2009) and the moduli of long-time behaviour.

3.3.1 Experimental method

A tensile test has been performed on a twine constituting the green polyethylene braided netting presented in Section 3.2.4.

We measured the applied force and the elongation of the twine. We measured the distance between two points along the twine using a LASERSCAN 200 non-contacting extensometer (Lloyd instruments). In order to increase the strain-measure precision of the Laserscan extensometer, we made a special measurement device (Fig. 3.12).

The loading path was a monotonic loading interrupted by 8 relaxation stages when the jaw displacement was blocked. The strain rate was 2.10^{-4} s^{-1} and the load at the beginning of the relaxation stages increased from 100 to 900 N, by 100 N steps. The duration of the eight relaxation stages was 15 minutes.

A result of this test is given by Figures 3.13 left and 3.14.

3.3.2 Short-time modulus of elasticity

Bles et al. (2009) noted that the measurements after relaxations and creeps of the initial modulus were in agreement and provided a characteristic evolution of a short-time modulus.

We calculated the moduli of short-time behaviour by calculating the slope at the beginning of each load step, just after a relaxation stage (Fig. 3.13). The evolution of the moduli with the logarithmic strain in the case of the studied braided twine is shown in Figure 3.13. For a small logarithmic strain (< 0.055), we will suppose that the short-time modulus of elasticity is inferior to 14000 N.

3.3.3 Long-time modulus of elasticity

The stress relaxations during relaxation stages show that the twine presents a visco-elastic behaviour. If we assume that the effect of the viscosity is relaxed at the end of each relaxation stage, we can evaluate the long-time elastic behaviour of the twine. Indeed, with these assumptions, the elastic component of the Force-Strain behaviour links the points at the ends of each relaxation step. We calculated a linear

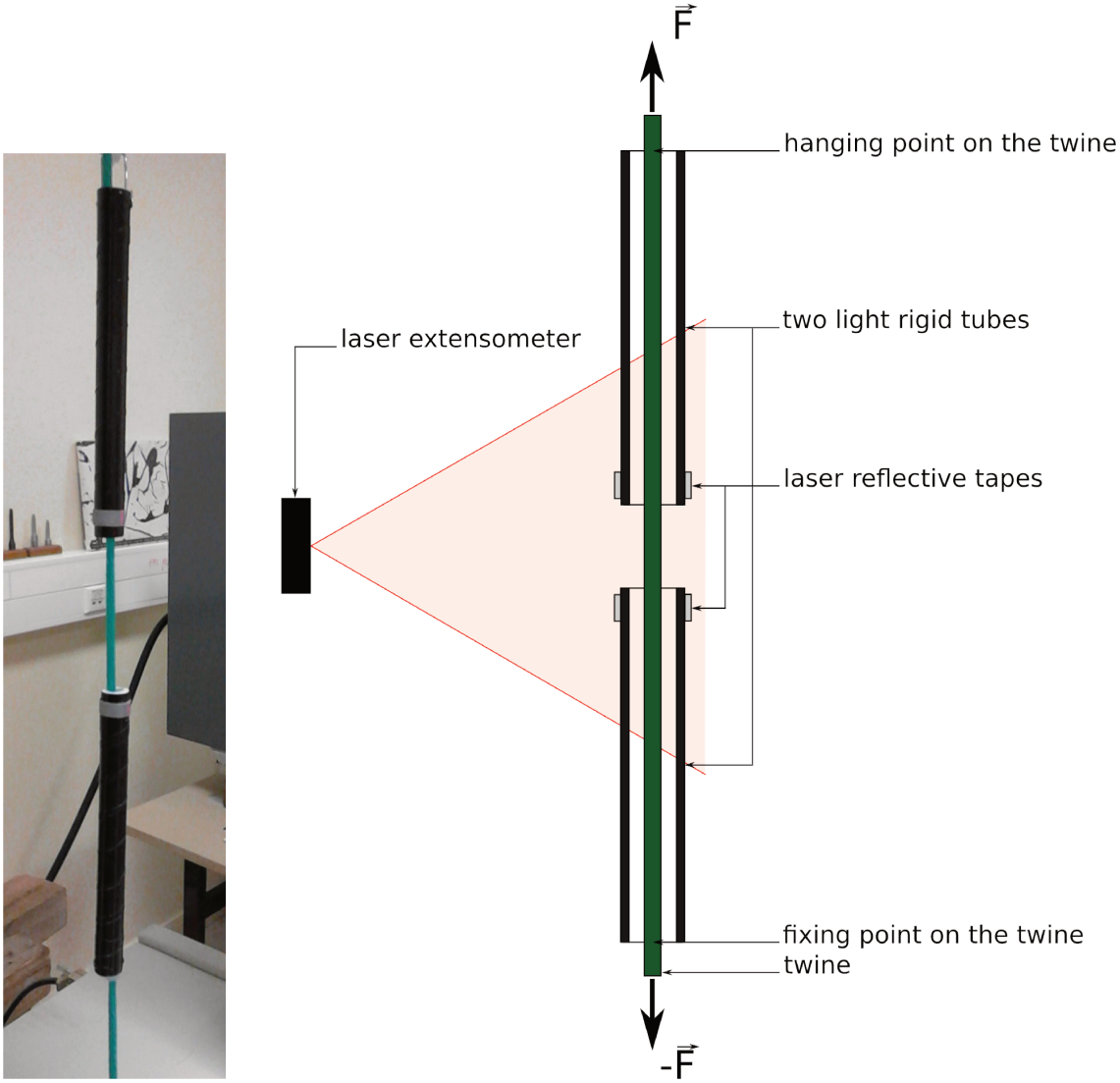

Figure 3.12 – Measurement device allowing to accurately measure the distance between two points on the twine using a non-contacting extensometer in spite of the torsion in the twine during the test.

regression on the points at the ends of each relaxation step (red line in Fig. 3.14). The slope of the line is 2444 N, and the coefficient of determination $R^2 = 0.992$.

Thus, for the chosen logarithmic strain, we can assume that the axial tensile stiffness is equal to 2444 N.

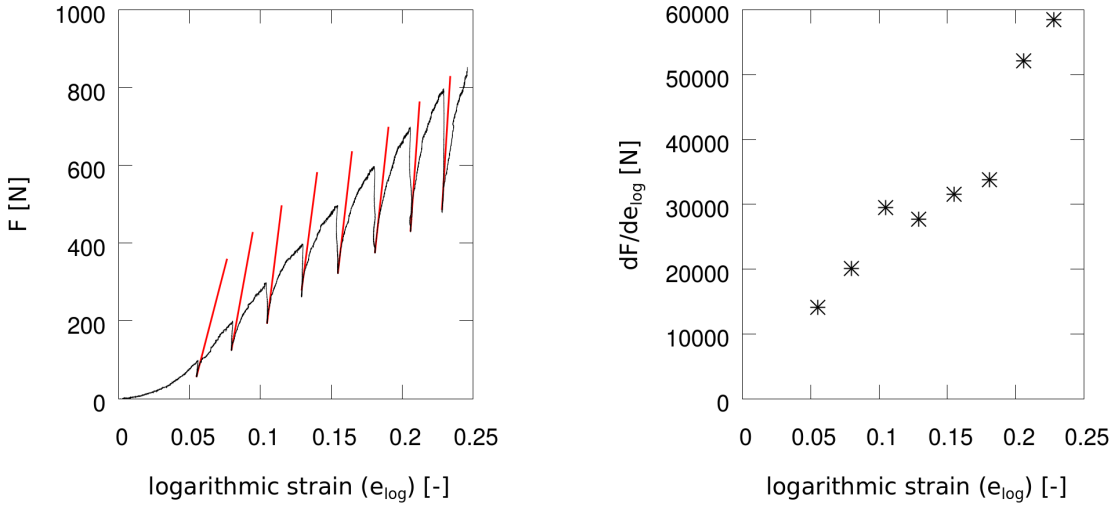

Figure 3.13 – Left: the black line presents the load as a function of the logarithmic strain e_{log}, and the red segments indicate the slope (short-time modulus) just after each relaxation stage. Right: evolution of the short-time modulus, obtained with the slopes in the figure on the left.

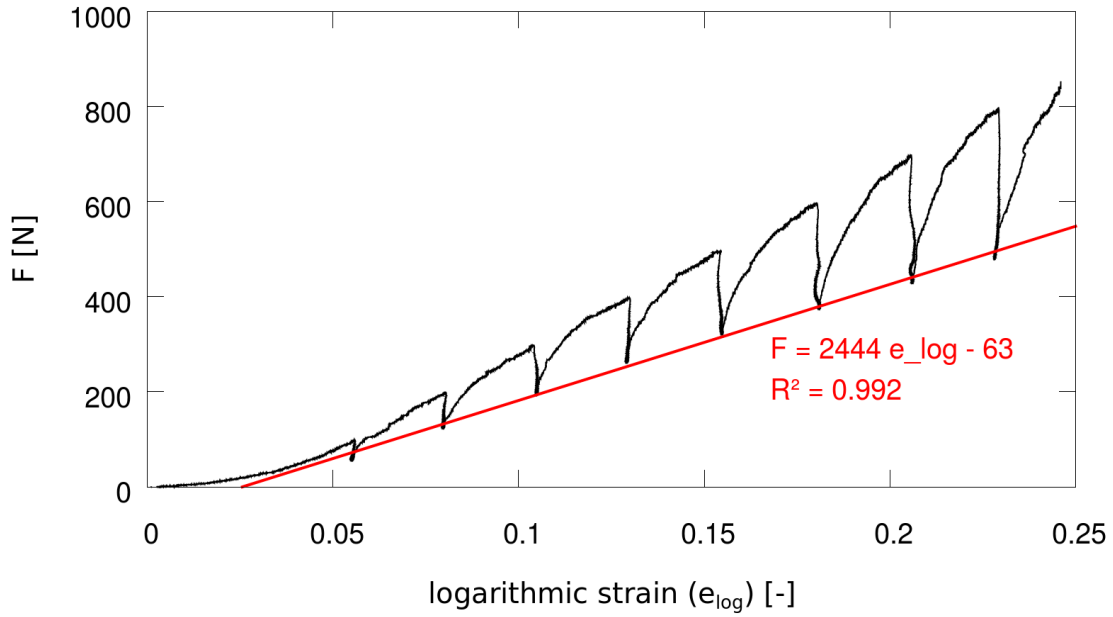

Figure 3.14 – The black line presents the experimental result of the load as a function of the logarithmic strain, and the red line was obtained with a linear regression.

3.3.4 Discussion

A tensile test performed on a twine constituting the green polyethylene braided netting allowed us to evaluate the short-time and long-time Young's moduli of elasticity.

The short-time modulus increases when the axial strain increases. We can assume that, for a small logarithmic strain (< 0.055), the short-time modulus of elasticity is inferior to 14000 N. However, it was necessary to evaluate the long-time axial stiffness of the twine. For that, the twine presenting a visco-elastic behaviour, it was assumed that the viscosity effect was removed at the end of each relaxation step. We found an axial tensile stiffness equal to 2444 N for the chosen logarithmic strain.

These results will be used in the numerical models to evaluate the effect of the axial stiffness during suspending, uniaxial and biaxial tensile tests.

CHAPTER

4 Experimental results

4.1 Uniaxial tensile tests

4.1.1 Experimental results

Results of two tests on two netting samples are presented: Figures 4.1 and 4.2 show the result in case of a 4x10-mesh double twine *Green* PE netting sample with a mesh side length of 60 mm (described in Table 3.9), and Figure 4.3 shows the result in case of a 4x10-mesh single twine *Green* PE netting sample with a mesh side length of 40 mm (described in Table 3.2). A load and unload cycle interrupted by several relaxation stages was imposed. The controlled jaw displacement rate was 100 $mm.min^{-1}$. The duration of the relaxation stages was 15 minutes.

Figures 4.4 and 4.5 present the result of a cyclic tensile test on a double twine *Green* PE netting sample.

4.1.2 Uniaxial stress state

Regarding the structure of netting, we could wonder if the force applied on the centre mesh was uniaxial.

First, the shape of the deformed netting sample (Fig. 4.6) showed boundary effects. The boundary effects did not seem to apply a transverse force on the central mesh. Indeed, the width along the height of the sample appeared to be constant around the centre of the sample.

Then, the simulation of a netting sample tested in a uniaxial tensile test using the finite element method (Abaqus Standard tool) revealed a compression force in the N-direction in the meshes along the longitudinal plane of symmetry of the sample (Tables D.1 and D.2). By simulating a uniaxial tensile test on a netting sample submitted to a force by mesh Fm_T in the T-direction of 1 N, a compression

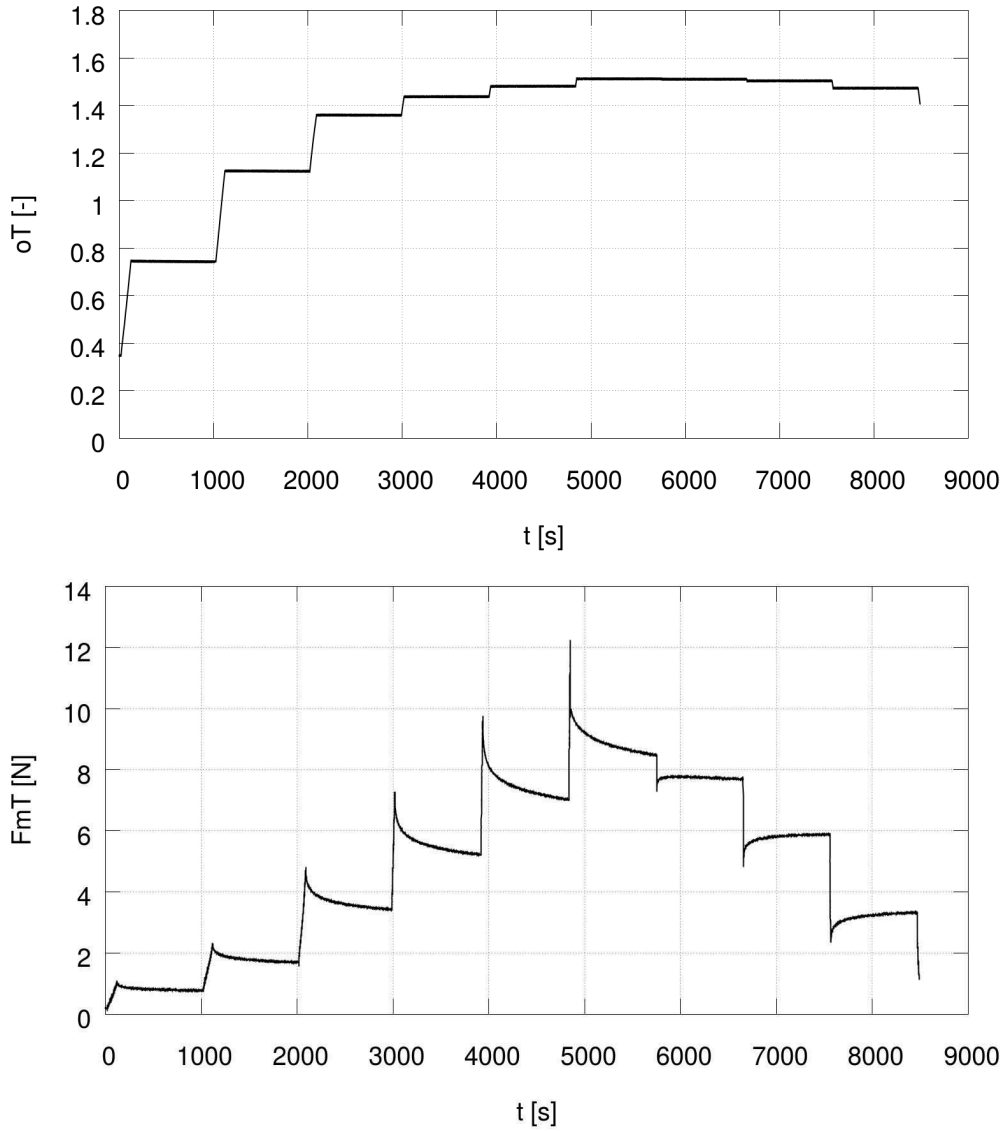

Figure 4.1 – Result of a tensile test including relaxation stages of 15 minutes on a **4x10-mesh double twine *Green* PE netting sample** (Table 3.8). At the top, evolution of the opening in the T-direction of the mesh in the middle of the netting panel. At the bottom, evolution of the force by mesh Fm_T in the T-direction applied on the mesh in the middle of the netting panel. The length of the mesh sides is 60 mm. The evolution of the force by mesh Fm_T during the relaxation steps reveals the viscosity of the material.

force Fm_N in the mesh in the middle of the netting sample equal to $-0.32\ N$ was revealed ($Fm_N/Fm_T = -0.32$, Table D.1). If the force by mesh Fm_T applied in the T-direction was $12.5\ N$, the force by mesh Fm_N in the N-direction in the mesh in the middle of the netting panel was $-0.52\ N$ ($Fm_N/Fm_T = -0.04$, Table D.2).

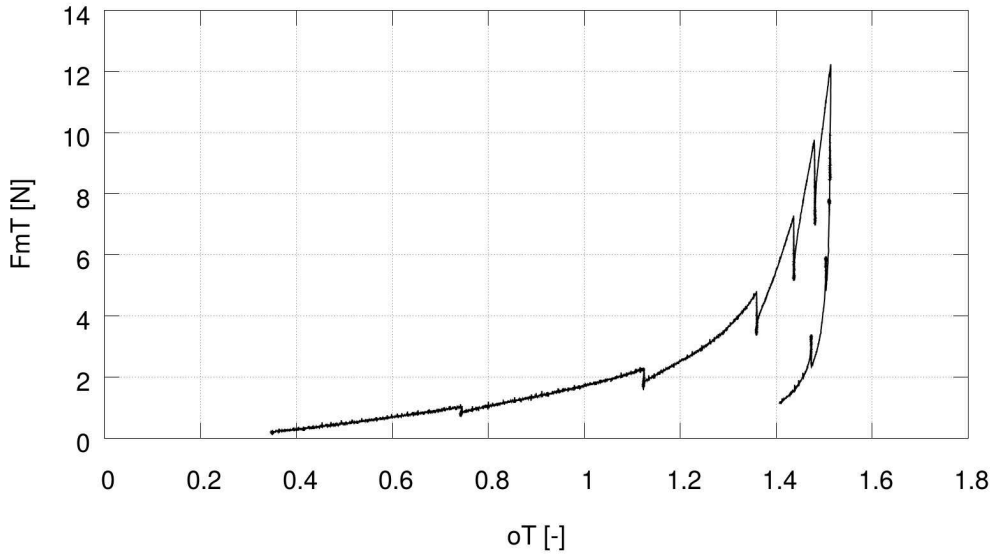

Figure 4.2 – Result of a tensile test including relaxation stages of 15 minutes on a **4x10-mesh double twine *Green* PE netting sample** (Table 3.8). Evolution of the force by mesh Fm_T in the T-direction applied on the mesh in the middle of the netting panel as a function of the opening o_T in the T-direction. The length of the mesh sides is 60 mm.

The mesh in the middle of a netting sample tested on the tensile testing machine is not in a perfect uniaxial stress state.

By increasing the distance between the boundaries and the centre of the tested samples, thus by using longer samples in the T-direction, we could reach a uniaxial stress state. However, because of the limited displacement course of the tensile testing machine, a special tensile machine should be necessary.

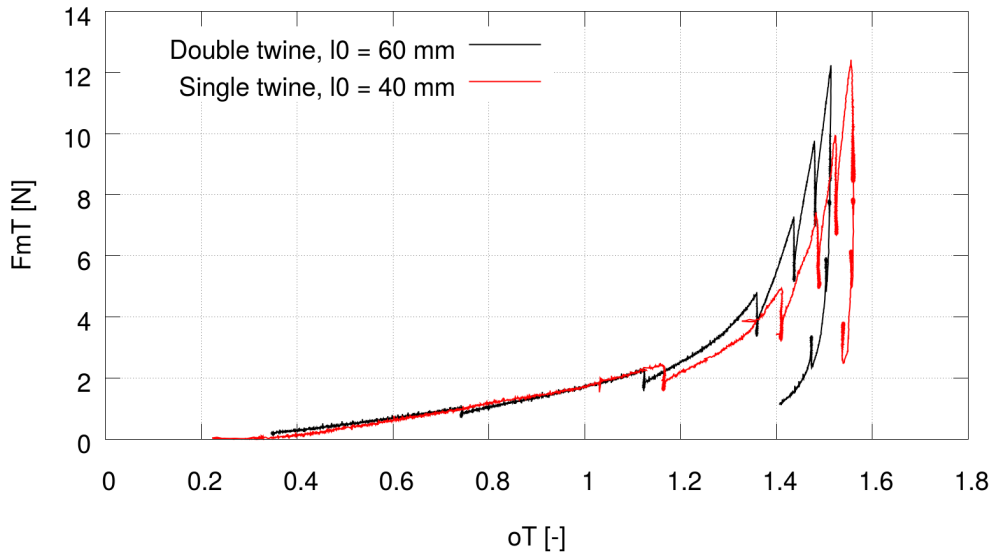

Figure 4.3 – Results of tensile tests including relaxation stages of 15 minutes on a **4x10-mesh single twine *Green* PE netting sample** with a mesh side length of 40 mm (red, Table 3.2) and on a **4x10-mesh double twine *Green* PE netting sample** with a mesh side length of 60 mm (black, Figure 4.2). Evolution of the force by mesh Fm_T in the T-direction applied on the mesh in the middle of the netting panel as a function of the opening o_T in the T-direction.

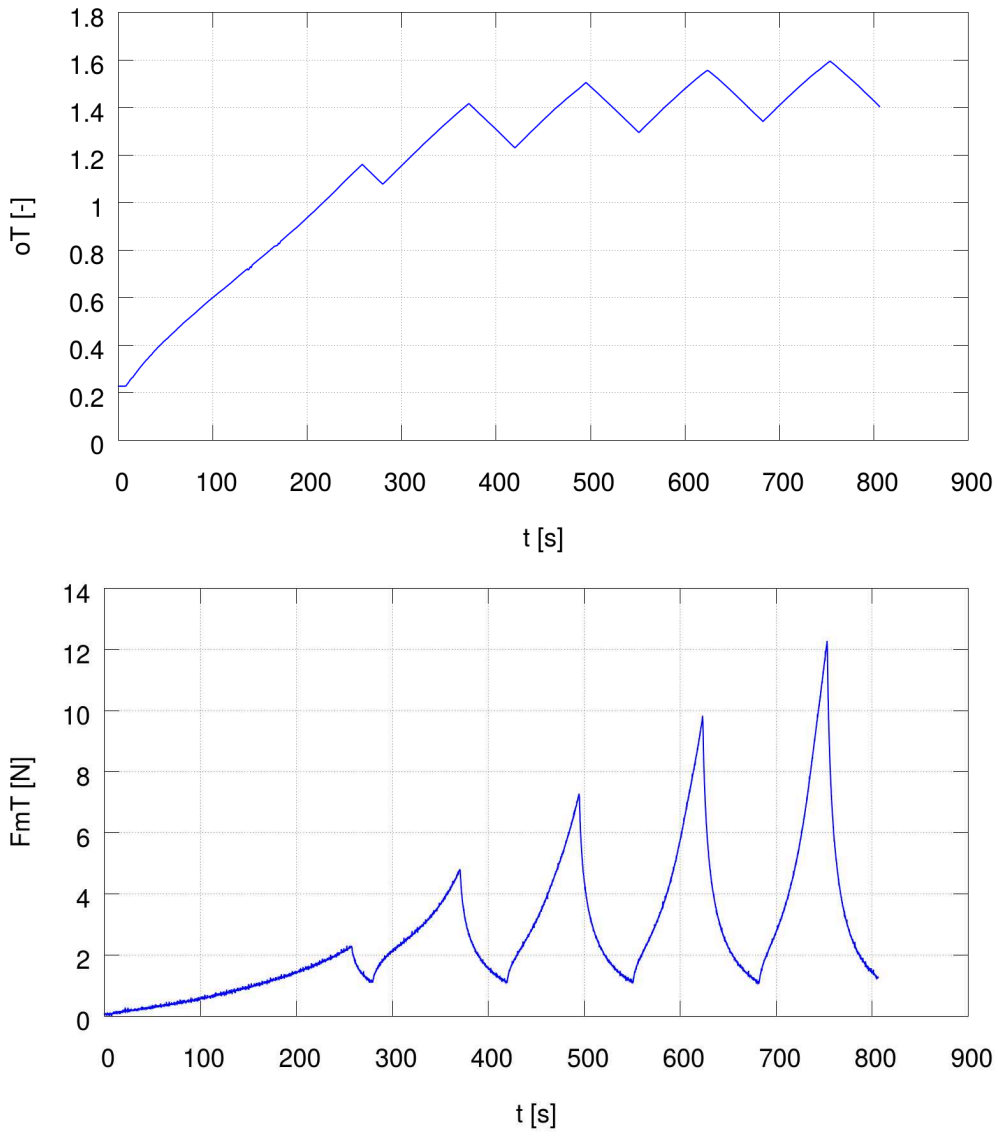

Figure 4.4 – Result of a cyclic test on a **4x10-mesh double twine *Green* PE netting sample** (Table 3.8). At the top, evolution of the opening in the T-direction of the mesh in the middle of the netting panel. At the bottom, evolution of the force by mesh Fm_T in the T-direction applied on the mesh in the middle of the netting panel. The length of the mesh sides is 60 mm.

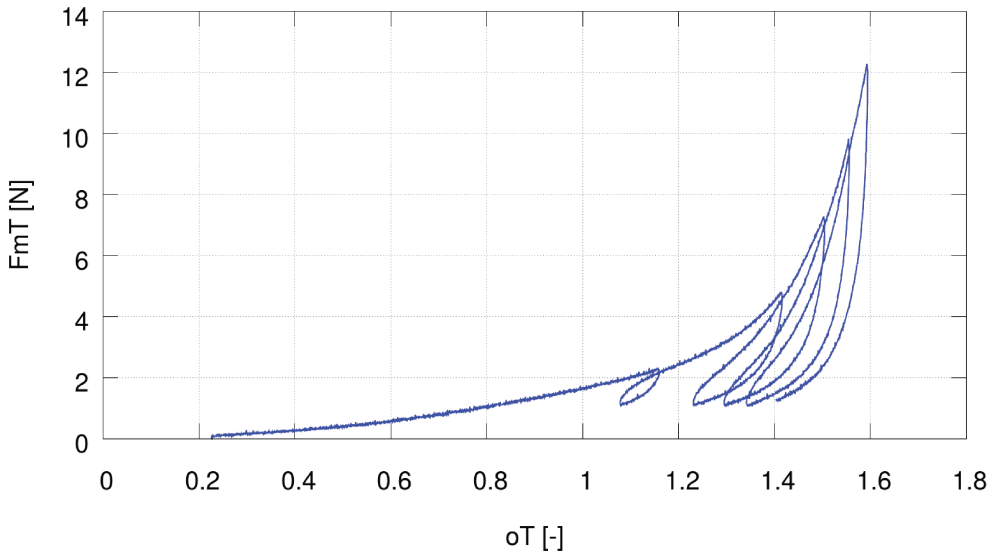

Figure 4.5 – Result of a cyclic test on a **4x10-mesh double twine *Green* PE netting sample** (Table 3.8). Evolution of the force by mesh Fm_T in the T-direction applied on the mesh in the middle of the netting panel as a function of the opening o_T in the T-direction. The length of the mesh sides is 60 mm.

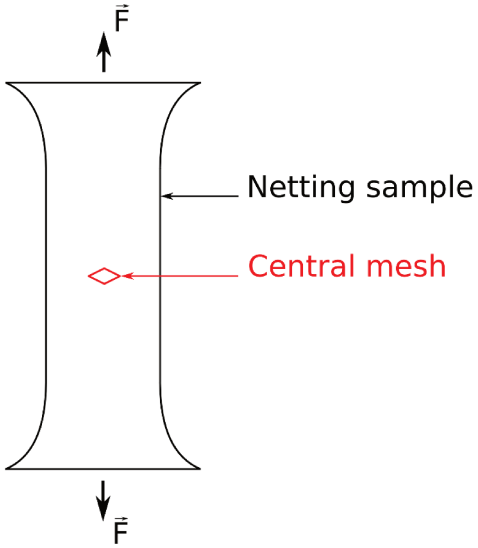

Figure 4.6 – Shape of a netting sample tested in a uniaxial tensile test.

4.2 Suspending tests

4.2.1 Evolution of the heights

Figures 4.7 to 4.9 present the evolution of the total height in the T-direction H_T of 4x10-mesh single twine samples made of Green PE (Fig. 4.7), Breztop PE (Fig. 4.8) and Brezline PE (Fig. 4.9) during suspending tests. Each netting sample was subjected to a force by mesh Fm_T successively equal to 0.324 N, 0.814 N, 1.795 N and 2.776 N.

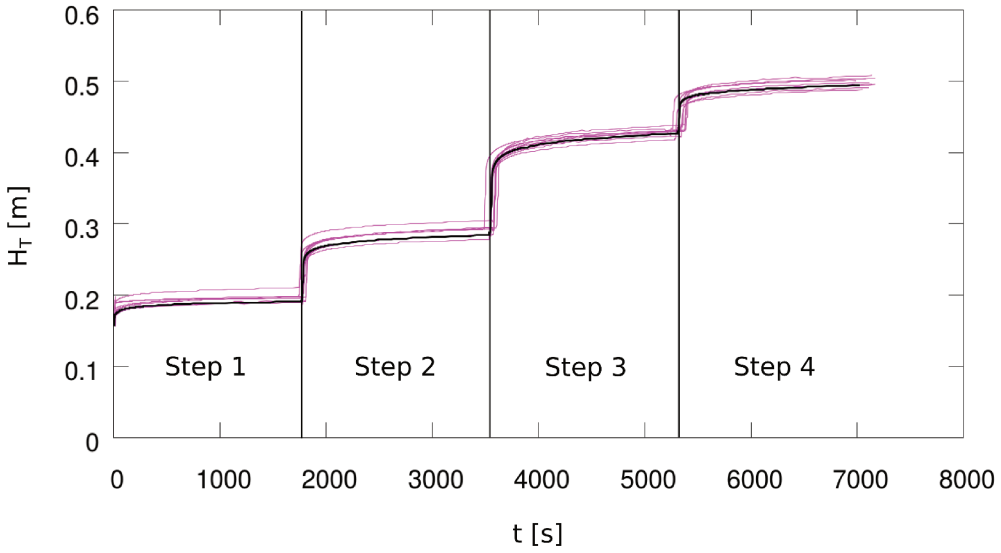

Figure 4.7 – Results of experimental suspending tests on 10 **4x10-mesh single twine *Green* PE netting samples** (Table 3.1). Evolution of the total height in the T-direction of each sample subjected to a force by mesh Fm_T successively equal to 0.324 N (Step 1), 0.814 N (Step 2), 1.795 N (Step 3) and 2.776 N (Step 4). The black line represents the evolution of one representative netting panel. The evolution of the height H_T during the creep steps reveals the viscosity of the material.

4.2.2 Heights in the panels

Figures 4.10 to 4.15 show the experimental (and numerical) heights for a range of suspended netting samples. The heights were measured at the end of the creep steps of 30 minutes.

The numerical results are presented in details in Section 6.1.2.

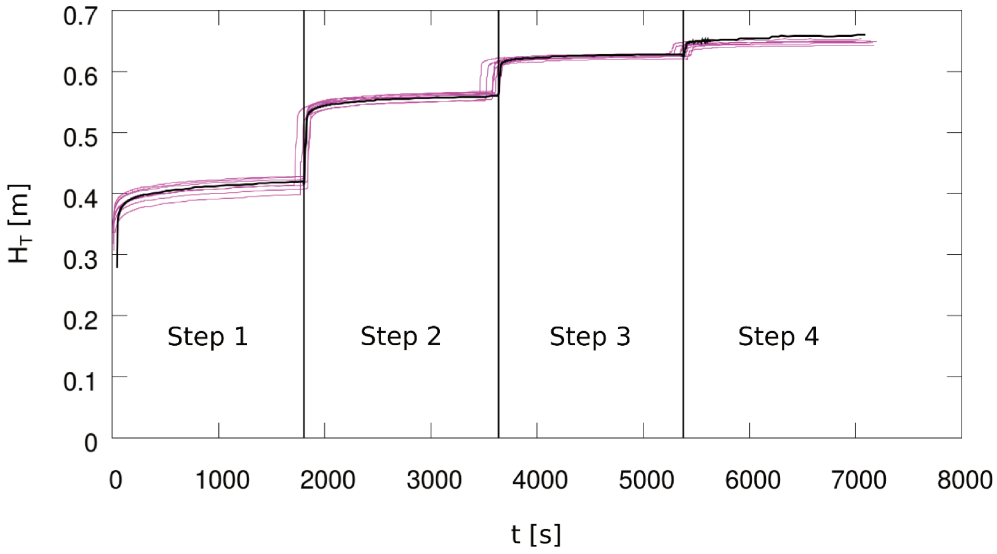

Figure 4.8 – Results of experimental suspending tests on 10 **4x10-mesh single twine *Breztop* PE netting samples** (Table 3.10). Same comments as Fig. 4.7.

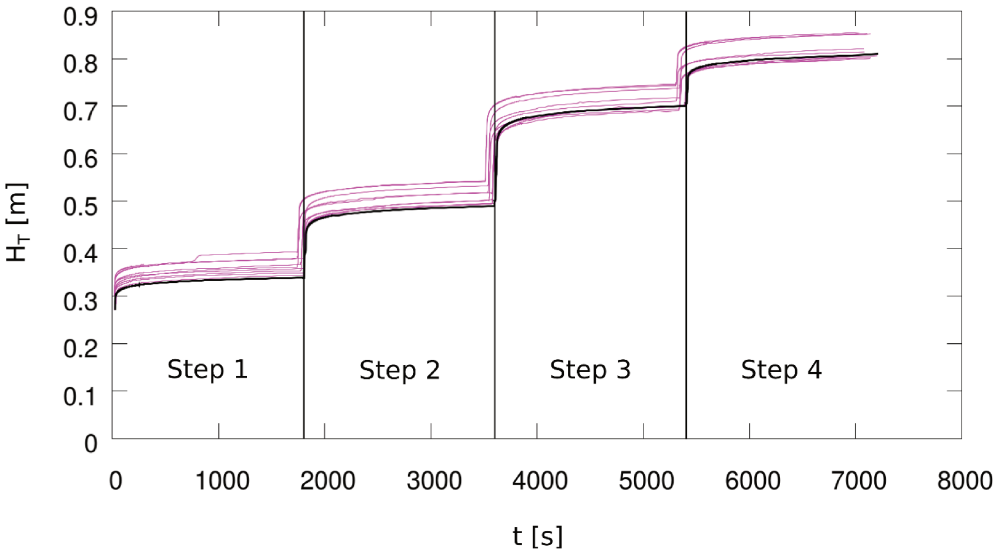

Figure 4.9 – Results of experimental suspending tests on 10 **4x10-mesh single twine *Brezline* PE netting samples** (Table 3.11). Same comments as Fig. 4.7.

4.2.3 Force by mesh versus opening

Figure 4.16 shows the evolution of the force by mesh Fm_T as a function of the mean value of the mesh opening in the T-direction o_T. We compared 3 types of double twine Green PE netting samples: 4x10-mesh samples with a mesh side length of

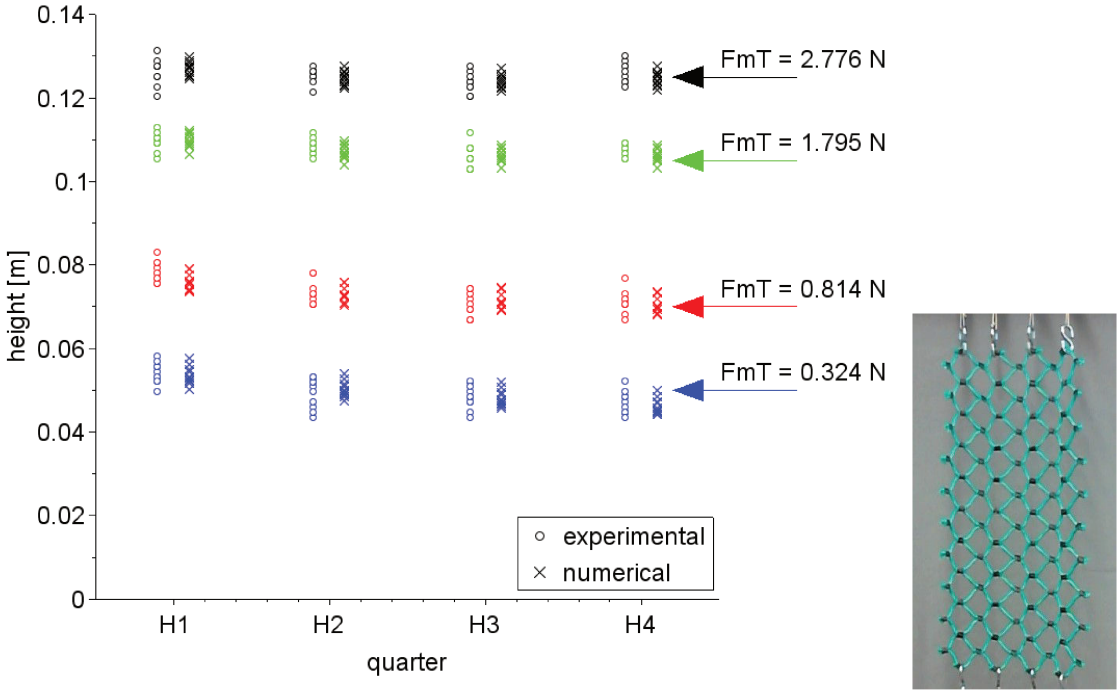

Figure 4.10 – Left: Results of experimental suspending tests and their numerical simulations on 10 **4x10-mesh single twine *Green* PE netting samples**. Heights of the quarters H1 to H4 (defined in Fig. 3.3) after 30 minutes of the creep stages at 4 loading levels Fm_T. Right: Picture of one suspended 4x10-mesh single twine *Green* PE netting sample subjected to a force by mesh in the T-direction Fm_T of 2.8 N.

50 mm and pre-tensioned in the T-direction (Table 3.6), 4x10-mesh samples with a mesh side length of 60 mm and pre-tensioned in the N-direction (Table 3.8), 5x25-mesh samples with a mesh side length of 50 mm and pre-tensioned in the N-direction (Table 3.7). Measurements were taken on 5 samples of each netting panel type and of the end of the creep stages of 30 minutes.

We calculated the mean values and the standard deviation of the opening o_T by considering, for each netting type, the openings of the meshes on the vertical centre line of the 5 samples. That means the meshes 2, 9, 16, . . . , 65 in case of a 4x10-mesh sample (Fig. A.1) and the meshes 3, 12, 21, . . . , 219 in case of a 5x25-mesh sample (Fig. A.2).

The force by mesh Fm_T was described in Section 3.1.2 (Fig. 3.2).

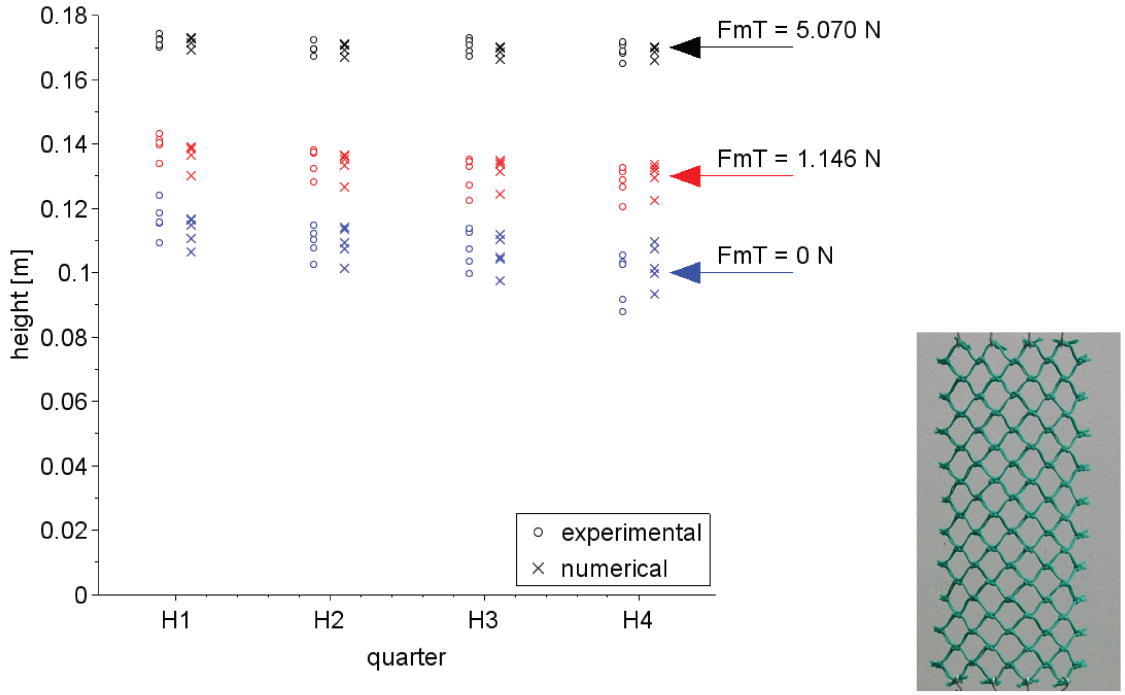

Figure 4.11 – Left: Results of experimental suspending tests and their numerical simulations on 5 **4x10-mesh double twine *Green* PE netting samples**. Heights of the quarters H1 to H4 after 30 minutes of the creep stages at 3 loading levels Fm_T. Right: Picture of one suspended 4x10-mesh double twine *Green* PE netting sample subjected to a force by mesh in the T-direction Fm_T of 2.6 N.

4.2.4 Openings and curvature

Figure 4.17 represents the opening in the T-direction o_T as a function of the opening in the N-direction o_N in case of 4x10-mesh double twine Green PE netting samples with a mesh side length of 60 mm during suspending tests. The suspending tests on 5 samples allowed to calculate the mean openings (mean on the 5 samples) of the 10 meshes along the vertical line passing through the centre of the sample (meshes 2, 9, 16, ..., 65 in Fig. A.1) for 5 different loading levels.

In Figure 4.17, the red circle arc represents the relation between the opening o_T and o_N modelling a mesh side by one bar element articulated at its ends (Fig. 4.18). This mesh could represent an ideal mesh without twine bending stiffness.

By assuming that a half mesh side could be modelled by a circle arc with a radius R, the curvature $\frac{1}{R}$ is a function of o_T, o_N and L_{ms} (Eqs. B.3, B.6 and B.9). Thus we could represent this approximation of $\frac{1}{R}$ as a function of the experimental opening in the T-direction o_T (Fig. 4.19). The result was fitted with a polynomial regression.

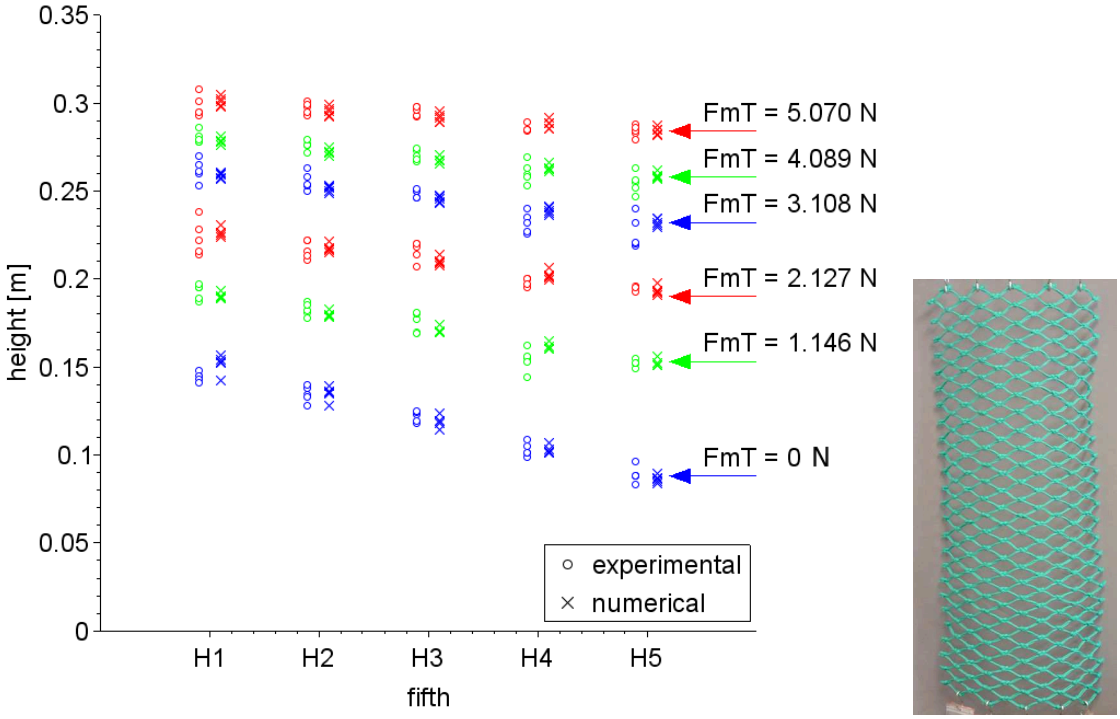

Figure 4.12 – Left: Results of experimental suspending tests and their numerical simulations on 5 **5x25-mesh double twine *Green* PE netting samples**. Heights of the fifths H1 to H5 (defined in Fig. 3.3) after 30 minutes of the creep stages at 6 loading levels Fm_T. Right: Picture of one suspended 5x25-mesh double twine *Green* PE netting sample subjected to a force by mesh in the T-direction Fm_T of 2.1 N.

By assuming that a half mesh side could be modelled by a circle arc and that there is no stretching in the mesh side, we can express the openings o_N and o_T in the N- and T-direction respectively (Eqs. B.14 to B.16). The obtained relation between o_N and o_T, represented in Figure 4.17 (blue solid line), is close to the experimental relation between o_N and o_T (blue '+').

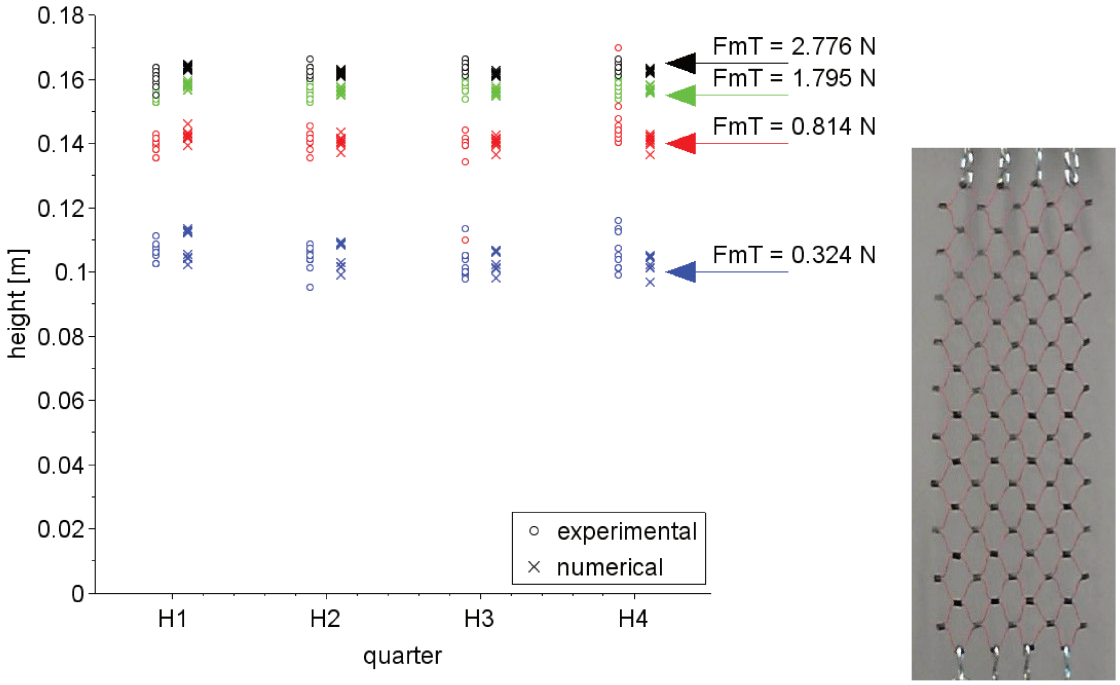

Figure 4.13 – Left: Results of experimental suspending tests and their numerical simulations on 10 **4x10-mesh single twine *Breztop* PE netting samples**. Heights of the quarters H1 to H4 after 30 minutes of the creep stages at 4 loading levels Fm_T. Right: Picture of one suspended 4x10-mesh single twine *Breztop* PE netting sample subjected to a force by mesh in the T-direction Fm_T of 0.8 N.

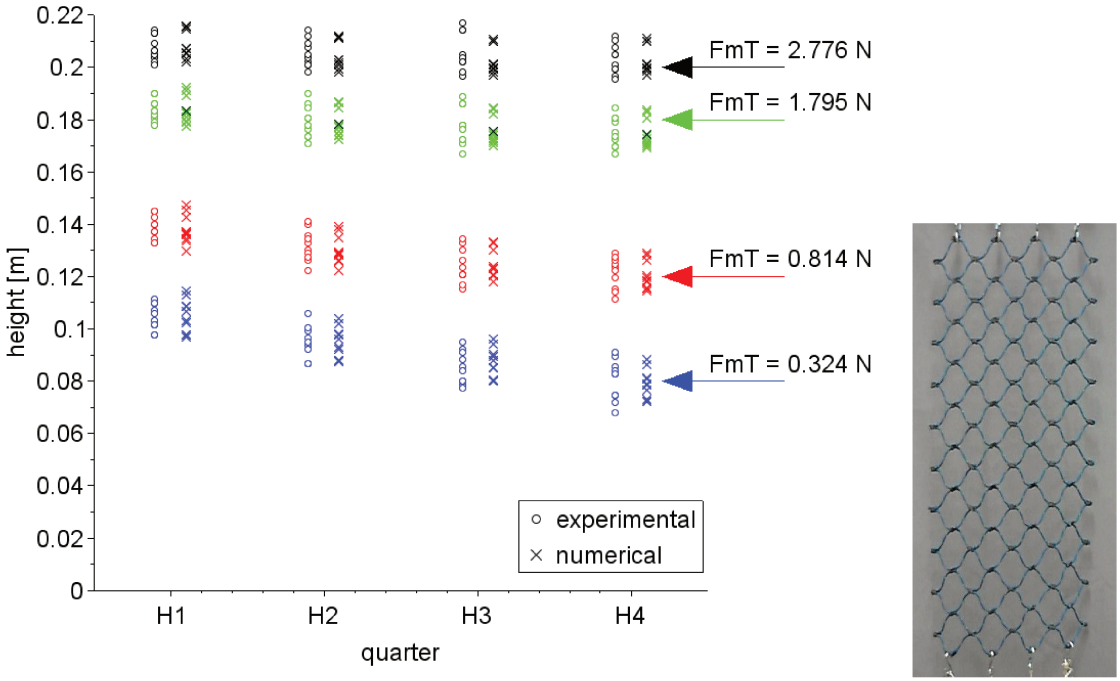

Figure 4.14 – Left: Results of experimental suspending tests and their numerical simulations on 10 **4x10-mesh single twine *Brezline* PE netting samples**. Heights of the quarters H1 to H4 after 30 minutes of the creep stages at 4 loading levels Fm_T. Right: Picture of one suspended 4x10-mesh single twine *Brezline* PE netting sample subjected to a force by mesh in the T-direction Fm_T of 2.8 N.

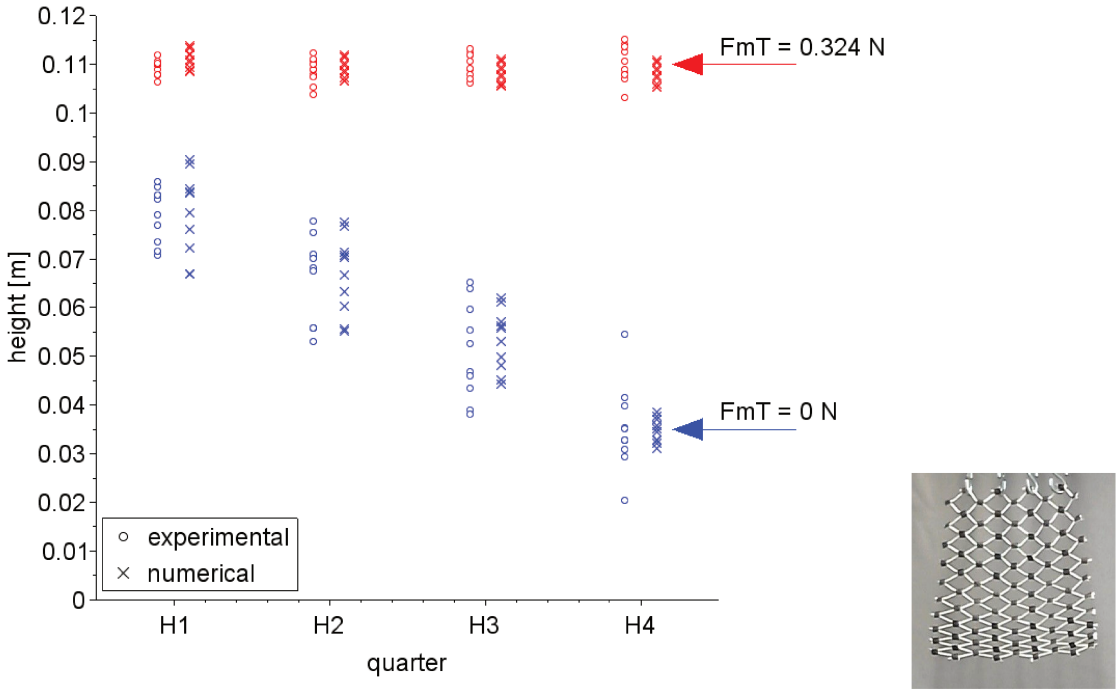

Figure 4.15 – Left: Results of experimental suspending tests and their numerical simulations on 10 **4x10-mesh single twine PA netting samples**. Heights of the quarters H1 to H4 for 2 loading levels Fm_T. Right: Picture of a suspended 4x10-mesh single twine *Green* PE netting sample.

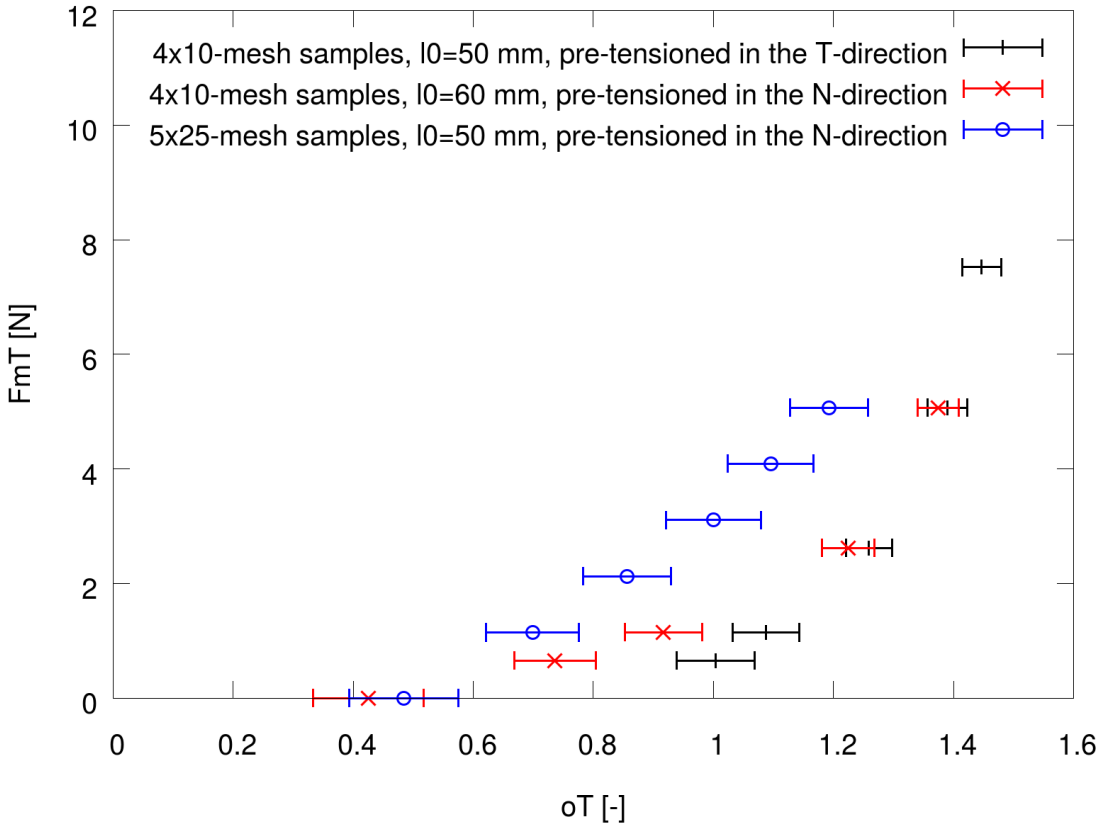

Figure 4.16 – Results of experimental suspending tests on **double twine *Green* PE netting samples**. Force by mesh applied in the T-direction Fm_T as a function of the mean value (± standard deviation) of the mesh opening in the T-direction o_T. Measurements were taken on 5 samples of each netting panel type and at the end of the creep stages of 30 minutes.

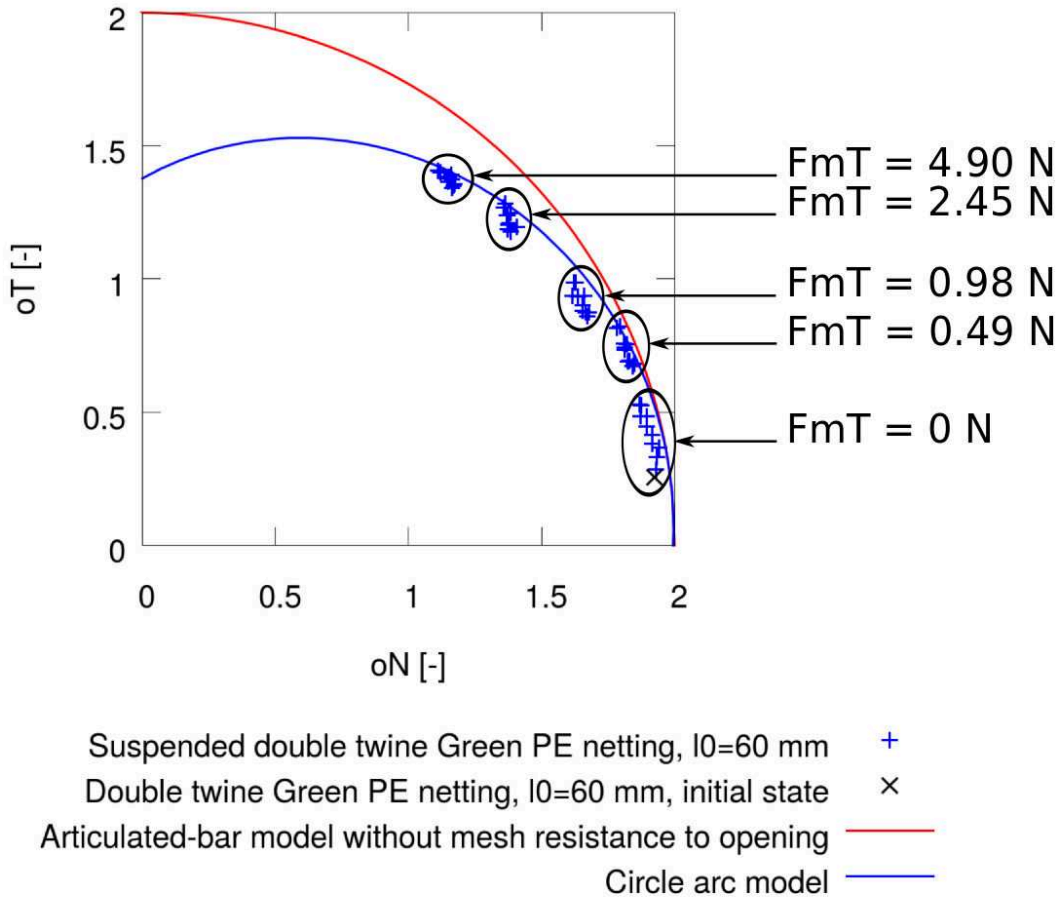

Figure 4.17 – Suspending tests on 5 **double twine *Green* PE netting samples** with a mesh side length of 60 mm. Mean experimental openings of the meshes in the centre horizontally and from the top to the bottom (blue '+') and openings of an ideal netting in which a mesh side is modelled by one bar and without mesh resistance to opening (red solid line, scheme of one mesh in Fig. 4.18). The blue solid line represents the relation between o_N and o_T by modelling the half mesh side by a circle arc and by assuming that there is no twine stretching.

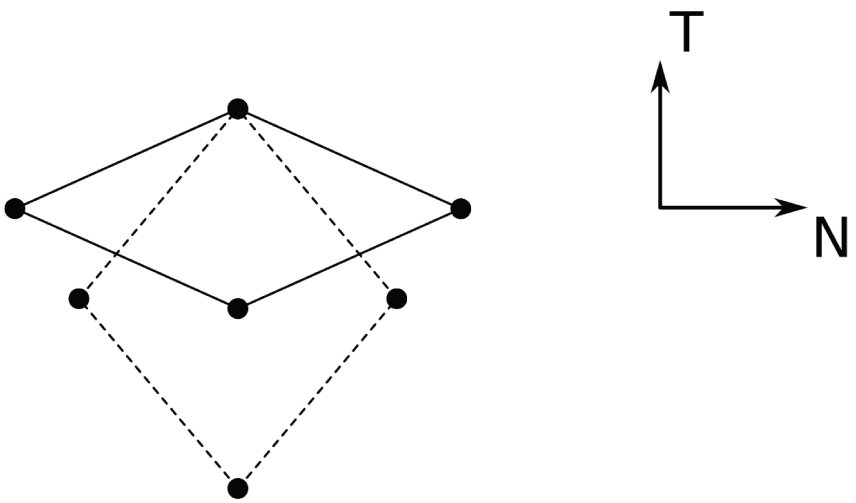

Figure 4.18 – Ideal mesh without mesh resistance to opening: each mesh side is modelled by one bar articulated at its ends.

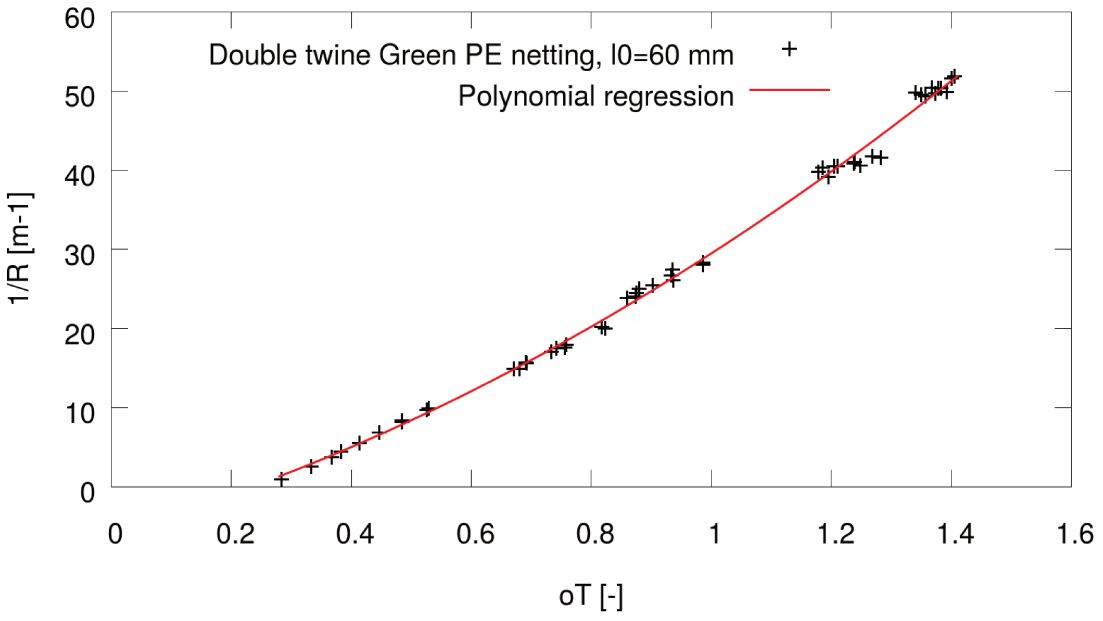

Figure 4.19 – Suspending tests on 5 **double twine *Green* PE netting samples** with a mesh side length of 60 mm. The curvature (1/R) is approximated by assuming that the half mesh side can be modelled by a circular arc. The equation of the fitted curve is $1/R = 13.6957 o_T^2 + 21.6076 o_T - 5.8163$, and the coefficient of determination of the polynomial regression is 0.996938.

4.3 Biaxial tensile tests

Figure 4.20 shows the evolution of the force by mesh Fm_T as a function of the opening o_T in the T-direction in case of biaxial tensile tests. For each type of loading ($Fm_N = 0\ N$, $Fm_N = Fm_T$ and $Fm_N = 2Fm_T$), 5 samples of double twine Green PE netting with a mesh side length of 50 mm were tested.

The deformation of the netting samples is assumed to be uniform. The measurements were performed after creep steps of 30 minutes. Nevertheless, the viscoelastic behaviour was observable on the displacement time-evolution only when $Fm_N = 0\ N$.

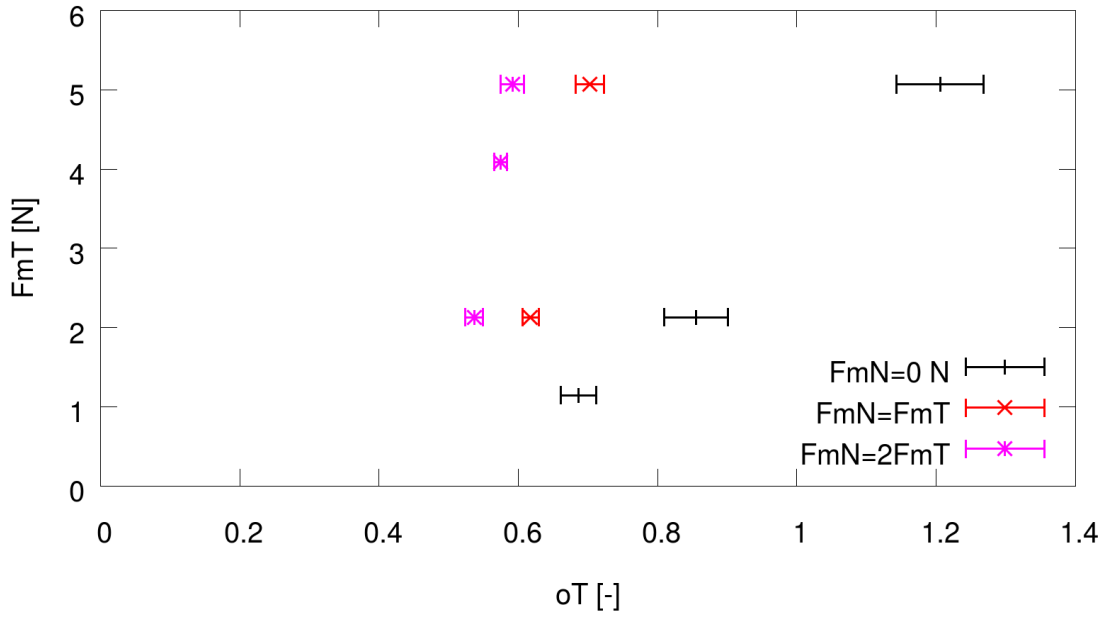

Figure 4.20 – Results of biaxial tensile tests on **double twine *Green* PE netting samples**. Force by mesh applied in the T-direction Fm_T as a function of the mean value ($\pm$ standard deviation) of the mesh opening in the T-direction o_T. For each of the 3 loading types, 5 samples were tested. The mesh side length at rest of the samples is 50 mm.

4.4 Comparisons between results obtained with uniaxial, biaxial and suspending tests

In Figures 4.21 and 4.22, results of a uniaxial tensile test and suspending tests on 4x10-mesh double twine *Green* PE netting samples are compared. Figure 4.23 shows

the evolution of the force by mesh applied in the T-direction Fm_T as a function of the mean value of the mesh opening in the T-direction o_T in cases of suspending tests and biaxial tensile tests.

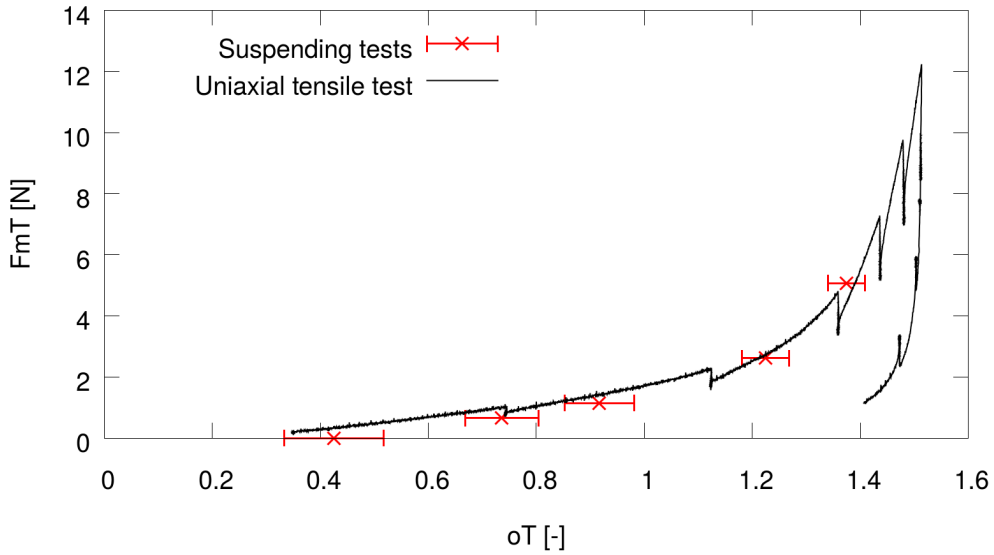

Figure 4.21 – Results of a uniaxial tensile test (black) and suspending tests (red) on **4x10-mesh double twine *Green* PE netting samples** (Tables 3.9 and 3.8). Force by mesh applied in the T-direction Fm_T as a function of the mean value ($\pm$ standard deviation) (for suspending tests only) of the mesh opening in the T-direction o_T. In case of the suspending tests, measurements were taken on 5 samples and at the end of each creep stage of 30 minutes. The mesh side length at rest of the samples is 60 mm. The results of the uniaxial tensile test are close to the results of the suspending tests.

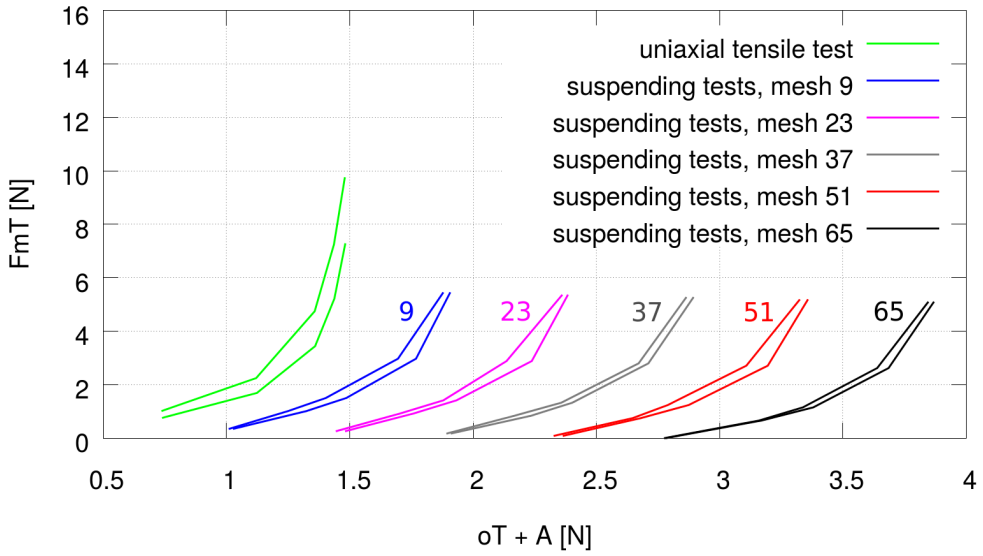

Figure 4.22 – Results of a uniaxial tensile test and suspending tests on **4x10-mesh double twine Green PE netting samples**. The results at the beginning and the end of each creep or relaxation step are represented. For convenience, a constant value A, depending on the studied mesh, was added to the represented opening. The meshes are numbered from the left to the right and from the top to the bottom (Fig. A.1). The mesh side length at rest of the samples is 60 mm. The distance between the results at the beginning and at the end of each creep or relaxation step provides a quantitative evaluation of the effect of the viscosity on the mechanical behaviour of netting.

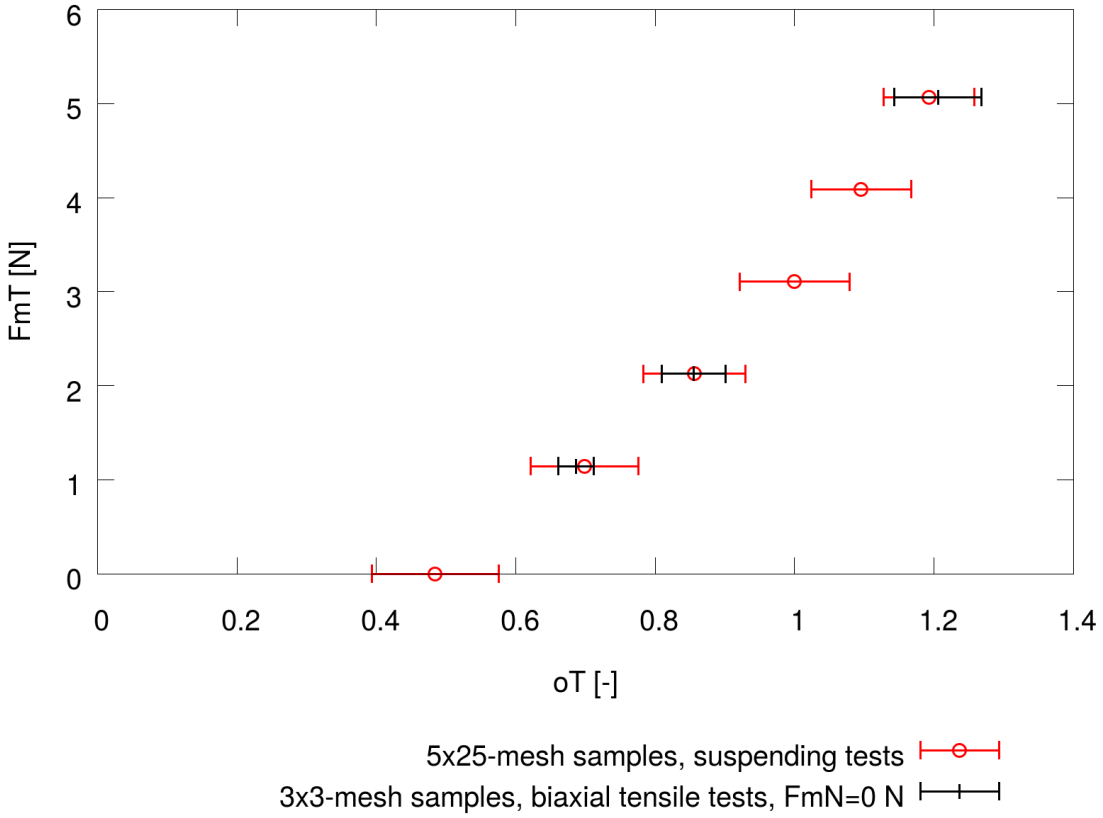

Figure 4.23 – Results of suspending tests (red) and biaxial tensile tests (black) on **double twine *Green* PE netting samples** (Tables 3.7 and 3.3). Force by mesh applied in the T-direction Fm_T as a function of the mean value (± standard deviation) of the mesh opening in the T-direction o_T. In case of the suspending tests, measurements were taken at the end of each creep stage of 30 minutes. The mesh side length at rest of the samples is 50 mm. Similar results are obtained with the suspending tests and the biaxial tensile tests.

4.5 Visco-elasto-plastic mechanical behaviour scheme

Regarding the experimental results, the mechanical behaviour of meshes in a netting made of polymer material can be assumed visco-elasto-plastic. This behaviour was well described in Bles et al. (2009) in case of the study of a polyamide-fiber strap.

The force applied on one mesh of netting Fm can be assumed to be the superimposition of three forces components Fm_e, Fm_v and Fm_p (Eq. 4.1).

$$Fm(o, \dot{o}, \mu) = Fm_e(o) + Fm_v(o, \dot{o}) + Fm_p(o, \mu) \tag{4.1}$$

The force component Fm_e is non-linear elastic. The force component Fm_v is viscoelastic and related to the opening rate $\dot{o}$, and eventually to the opening o. The force component Fm_p is elastoplastic and irreversible and related to the opening o and to a cycle-history parameter μ.

Figure 4.24 qualitatively illustrates its mechanical behaviour modelled by a visco-elasto-hysteresis model. This figure shows the typical shape of the stress-strain cycles often observed with materials woven in polymer fibers. It represents well, in case of netting, the shape of force-opening cycles obtained with uniaxial tensile tests. The viscoelastic behaviour is represented in Fig. 4.24a, the non-linear elastic behaviour in Fig. 4.24b, the elastoplastic behaviour in Fig. 4.24c and the superimposition of all these components is represented in Fig. 4.24d.

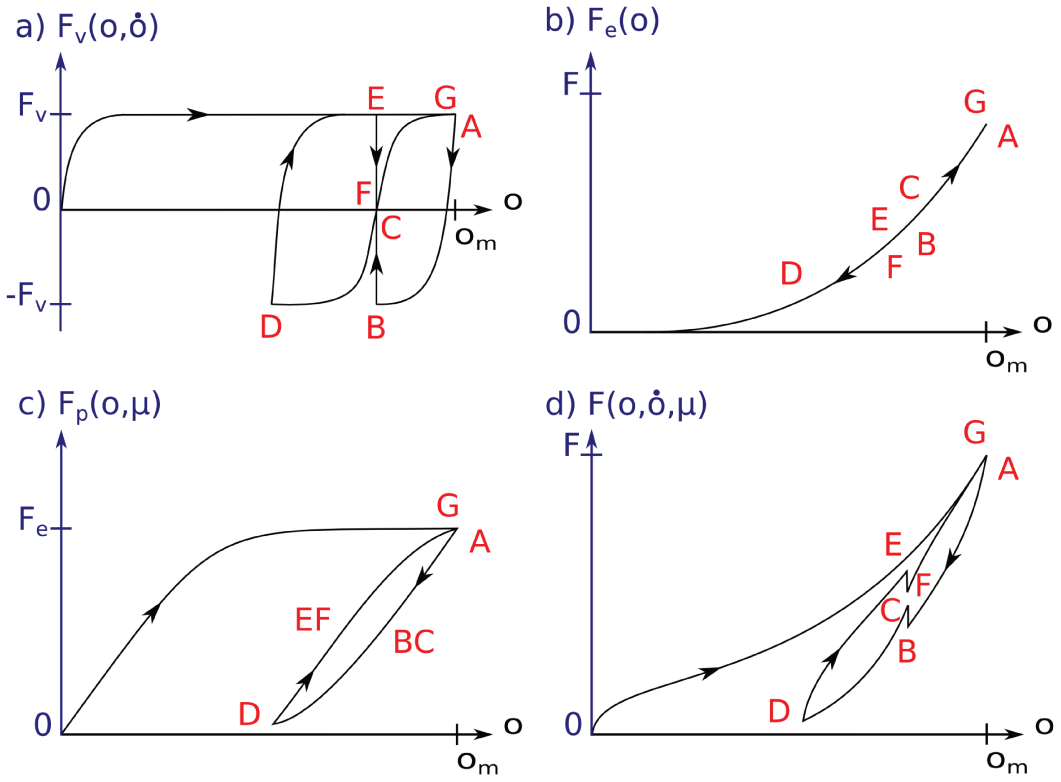

Figure 4.24 – Cyclic mechanical behaviour of the three force components of the visco-elasto-hysteresis model from Bles et al. (2009). The viscoelastic behaviour (a), the non-linear elastic behaviour (b), the elastoplastic behaviour (c), and the superimposition of all these components (c) are represented.

4.6 Discussion

The uniaxial tensile tests and the suspending tests provide results which reveal the visco-elasto-plastic mechanical behaviour of the netting samples.

The viscosity is revealed with the evolution of the forces during relaxation steps (Fig. 4.1), the force response during cyclic tests and the evolution of the height H_T during the creep steps (Figs. 4.7 to 4.9). Non-linear elasticity is seen on Figures 4.2, 4.3 and 4.5.

Figure 4.1 shows that the opening o_T was still high during the unload (with relaxation stages of 15 minutes). Thus, the mesh did not come back to its initial state. The structure presented a permanent deformation (or a long-term viscosity).

Regarding the evolution of the height H_T during the creep stages (Figs. 4.7 to 4.9), we can assume that in case of the suspending tests of netting made of Green PE, Breztop PE or Brezline PE, the contribution of the viscous component of the

strain is cancelled after 30 minutes of creep. In case of netting made of PA, we observed viscosity that vanishes in a very short time.

Figures 4.7 to 4.15 show small variation in the results provided by suspending tests: the results obtained with several samples of the same type of netting are very close. In Figures 4.10 to 4.15, it can be seen that the heights (H_1 to H_5) increase when the applied load increases, as expected. It can also be seen that, for each loading level Fm_T, the height at the top quarter H_1 (or fifth) is higher than at the bottom quarter H_4 (or fifth H_5). Thus, the deformation of the netting is not uniform, which is due to gravity. This point is important: suspending tests are simple to carry out but the deformation in suspended netting samples is not uniform.

Figure 4.16 shows that the pre-tension step in the T-direction caused a permanent deformation in this direction. The applied force by mesh Fm_T increases faster when the opening o_T increases in case of a mesh side length of 50 mm than in case of a mesh side length of 60 mm. Thus the resistance to opening of netting in case of a mesh side length of 50 mm is higher than in the case of a mesh side length of 60 mm. This difference could be explained by the different geometry of the structure, the influence of knots on the mechanical behaviour of netting, and/or the different interactions between the two twines constituting the mesh side. Indeed, in case of a double twine netting, the interactions between the twines can be assumed stronger when the mesh side is shorter.

In Figure 4.17, the difference between experimental data and the articulated-bar model reveals the bending in the mesh sides that reduces the distance between knots. By modelling the shape of a half mesh side with a circle arc, a polynomial relation was found between the curvature $\frac{1}{R}$ and the mesh opening in the T-direction o_T (Fig. 4.19). By assuming that a half mesh side could be modelled by a circle arc and that there is no axial stretching in the mesh side, the obtained relation between the openings o_N and o_T, in the N- and T-direction respectively, was close to the experimentally obtained relation (Fig. 4.17). The curvature being directly linked to the bending stiffness in the beam theory, the study of some parameters as functions of the opening o_T (or o_N) appears consistent.

The biaxial tensile tests show that the larger the force in the N-direction Fm_N is, the smaller the mesh opening in the T-direction is, as expected (Fig. 4.20).

The use and consistency of the three types of experiments are validated by the comparisons of the results. First, Figure 4.21 shows that the result of the uniaxial tensile test is close to the ones of the suspending tests in case of a 4x10-mesh double twine Green PE netting in spite of the different boundary conditions. Despite the difference in the loading (speed, boundary conditions) and in the duration of the creep and relaxation steps, Figure 4.22 reveals a visco-elastic behaviour qualitatively similar in the two types of experiments. Then, the comparison of the

responses force-opening, obtained with suspending and uniaxial tensile tests on the biaxial tensile device (Fig. 4.23), allows us to validate the biaxial tensile machine. Indeed, it validates the realization of the boundary conditions with linear motion ball bearings (Section 3.1.3).

Finally, the visco-elasto-plastic behaviour observed in the experimental results gives us information to set up the experimental design. First, the measurements would have to be made after, at least, 30 minutes of creep in case of suspending tests and 15 minutes of relaxation in case of uniaxial tensile tests. In case of biaxial tensile tests, a measure of the effect of the viscosity was out of reach of our experimental device. Thus, the viscosity effect was assumed negligible. Then, the cyclic behaviour shows that, during the loading step, the loading needs to be only increasing, optionally interrupted by creep or relaxation steps. These elements for the experimental design could be confirmed with the numerical results.

CHAPTER

5 Numerical methods

5.1 Quasi-analytical approach

A quasi-analytical model based on the beam theory and allowing large rotations is proposed to simulate the tensile test, assuming that the load applied on the mesh in the middle of the netting panel is supposed to be uniaxial, only in the T-direction. Contrary to the model proposed in O'Neill (2002), no approximation is made ($\epsilon < 0.2$) and the ratio $\epsilon = \sqrt{EI/(l^2 f)}$ could be lower and higher than 0.2.

We developed the model with the programing language C++. The notations used are defined in Figure 5.1.

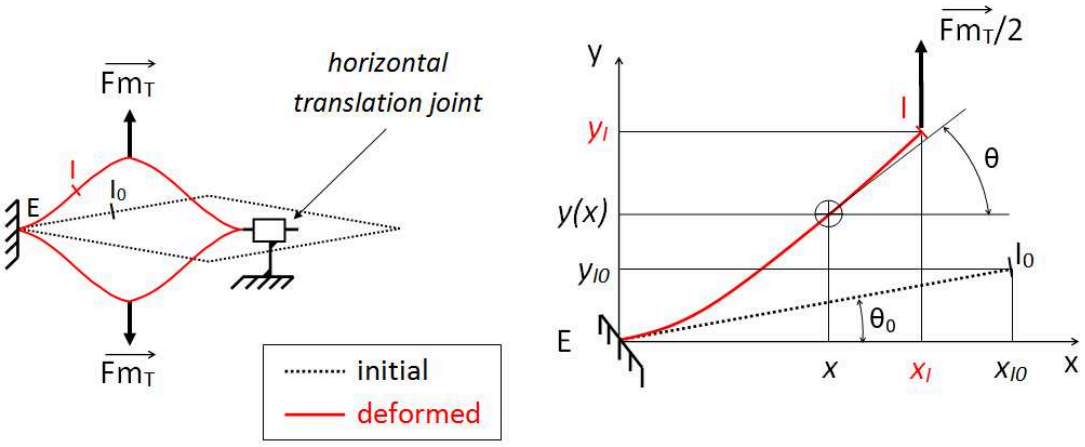

Figure 5.1 – Left: application of a load Fm_T on a mesh. Right: kinematic of the twine between points E and I.

First, the bending moment M is related to the curvature as follows:

$$M = EI\frac{d\theta}{ds} \tag{5.1}$$

where EI is the bending stiffness, s is the curvilinear abscissa, θ is the mesh angle, and $\frac{d\theta}{ds}$ is the curvature.

The bending moment is given by:

$$M = \frac{Fm_T}{2}(x_I - x) \tag{5.2}$$

along the center line of the beam.

The curvature is a function of $y(x)$ as follows:

$$(\frac{d\theta}{ds}) = \cos^2(\theta)y''(x)\frac{1}{\sqrt{1+[y'(x)]^2}} = \frac{y''(x)}{[1+[y'(x)]^2]^{3/2}} \tag{5.3}$$

By using relations 5.1, 5.2 and 5.3, the following expression is obtained:

$$\forall x \in [0; x_I] \qquad \frac{Fm_T}{2}(x_I - x) = EI\frac{y''(x)}{[1+[y'(x)]^2]^{3/2}} \tag{5.4}$$

The boundary conditions are:

$$y(x=0) = 0 \tag{5.5}$$

$$\theta(x=0) = \theta_0 \Leftrightarrow y'(x=0) = \tan(\theta_0) \tag{5.6}$$

The length of the mesh side is assumed to be constant:

$$\forall t \in \mathbf{R}^+ \qquad L_{ms} = L_{ms0} \tag{5.7}$$

$$\int_E^I \mathrm{d}s = \int_{E_0}^{I_0} \mathrm{d}s = \frac{L_{ms0}}{2} \tag{5.8}$$

$$\frac{L_{ms0}}{2} = \int_0^{x_I} \frac{\delta s}{\delta x}\,\mathrm{d}x = \int_0^{x_I} \sqrt{1+[y'(x)]^2}\,\mathrm{d}x \tag{5.9}$$

To work with dimensionless parameters, $\bar{x}$ and $\bar{y}$ are defined by:

$$\bar{x} = \frac{2x}{L_{ms0}} \qquad \bar{y} = \frac{2y}{L_{ms0}} \tag{5.10}$$

And u is defined by:

$$\forall x \in [0; x_I] \qquad u(\bar{x}) = y'(x) \tag{5.11}$$

Using equations 5.10 and 5.11, relations 5.4, 5.6 and 5.9 become 5.12, 5.13 and 5.14 respectively.

$$\forall \bar{x} \in [0; \bar{x}_I] \qquad \frac{Fm_T}{2}(\frac{L_{ms0}}{2})^2(\bar{x}_I - \bar{x}) = EI\frac{u'(\bar{x})}{[1 + [u(\bar{x})]^2]^{3/2}} \tag{5.12}$$

$$u(\bar{x} = 0) = \tan(\theta_0) \tag{5.13}$$

$$\int_0^{\bar{x}_I} \sqrt{1 + [u(\bar{x})]^2}\, \mathrm{d}\bar{x} = 1 \tag{5.14}$$

The solutions of the differential equation 5.12 are:

$$\forall \bar{x} \in [0; \bar{x}_I] \qquad \frac{Fm_T}{2EI}\frac{{L_{ms0}}^2}{4}\bar{x}[\bar{x}_I - \frac{\bar{x}}{2}] = \frac{u(\bar{x})}{\sqrt{1 + [u(\bar{x})]^2}} + K \tag{5.15}$$

where $K \in \mathbf{R}$.
Using relation 5.13 with relation 5.15, we obtain:

$$\forall \bar{x} \in [0; \bar{x}_I] \qquad \frac{Fm_T}{2EI}\frac{{L_{ms0}}^2}{4}\bar{x}[\bar{x}_I - \frac{\bar{x}}{2}] = \frac{u(\bar{x})}{\sqrt{1 + [u(\bar{x})]^2}} - \frac{\tan(\theta_0)}{\sqrt{1 + \tan^2(\theta_0)}} \tag{5.16}$$

To simplify the equation, we defined v by:

$$\forall \bar{x} \in [0; \bar{x}_I] \qquad v(\bar{x}) = \frac{u(\bar{x})}{\sqrt{1 + [u(\bar{x})]^2}} \tag{5.17}$$

So u can also be defined by:

$$\forall \bar{x} \in [0; \bar{x}_I] \qquad u(\bar{x}) = \frac{v(\bar{x})}{\sqrt{1 - [v(\bar{x})]^2}} \tag{5.18}$$

where $v \in]-1;1[$.
Then relation 5.16 leads to:

$$\forall \bar{x} \in [0;\bar{x}_I] \qquad v(\bar{x}) = \frac{Fm_T}{2EI}\frac{{L_{ms0}}^2}{4}\bar{x}[\bar{x}_I - \frac{\bar{x}}{2}] + sin(\theta_0) \tag{5.19}$$

By using relations 5.18, 5.19 and 5.14, the value of $\bar{x}_I$ can be evaluated by an iterative algorithm (e.g. dichotomy algorithm).

Using the relations 5.10 and 5.11, $\bar{y}$ becomes:

$$\forall \bar{x} \in [0;\bar{x}_I] \qquad \bar{y}(\bar{x}) = \int_0^{\bar{x}} u(\bar{x})\,\mathrm{d}\bar{x} \tag{5.20}$$

So $\bar{y}_I$ can be calculated by:

$$\bar{y}_I = \int_0^{\bar{x}_I} u(\bar{x})\,\mathrm{d}\bar{x} \tag{5.21}$$

Finally, the displacement of the half mesh side, and so the opening of the mesh in the middle of the netting panel during the tensile test, submitted to a tensile force Fm_T, can be calculated by relations 5.18, 5.19 and 5.21.

5.2 Finite element model

5.2.1 Abaqus Standard Software tool

Description

The mechanical behaviour of netting used in case of uniaxial tensile tests was modelled using the Abaqus Standard finite element code.
A mesh side was assumed to behave like a Timoshenko beam. In Abaqus, we model a mesh side with a planar beam that uses linear interpolation and a 2D hybrid formulation (B21H type in Abaqus).
Timoshenko beams allow for transverse shear deformation and can be subject to large axial strains. Hybrid beam element types are used for geometrically nonlinear analysis when the beam undergoes large rotations.
In this study, we modelled a mesh side with 20 B21H elements. The shear modulus was supposed to be very high so that its value has negligible effect on the results of mesh resistance to opening. The axial stiffness EA of the beam elements was determined using the results presented in Section 3.3.

Pre- and post-processing program

To simulate the experimental tests, post-process the results and perform an inverse identification iteration loop (Section 5.2.5), a software has been designed and implemented. The pre-post-processing program has been implemented with the programming language Python. The steps of the program are described in Figure 5.2.

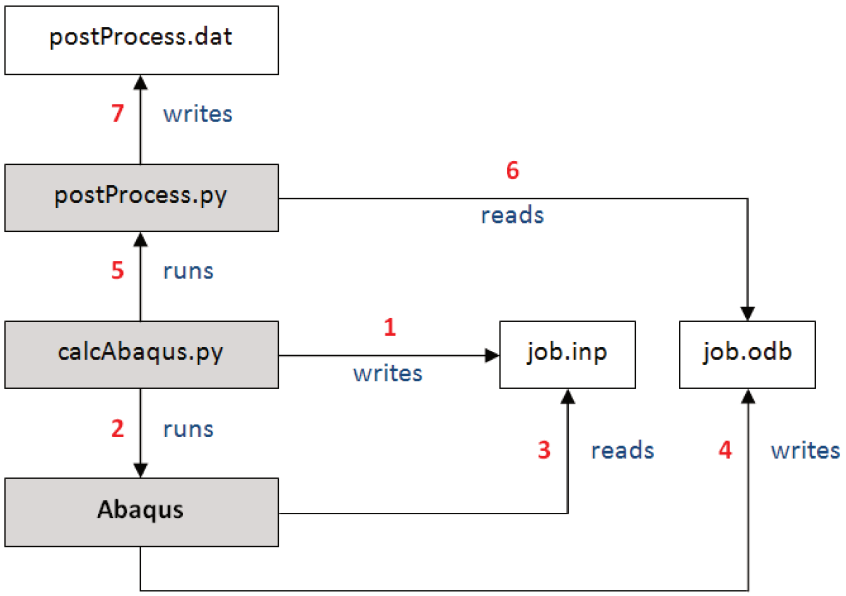

Figure 5.2 – Diagram representing the steps of the pre- and post-processing program. The program allows the simulation of netting samples, suspended or tested on the uniaxial tensile machine, and the data post-processing.

The input geometrical parameters are: the number of meshes of the samples n_T and n_N in the T and N directions respectively, the length at rest l_{ms} of a mesh side, the slope angle at rest θ_0 near the knot, the section area A and the area moment of inertia I of a twine, and the boundary conditions.

The input material parameters are: the volumetric mass density ρ, the Poisson's ratio ν, the Young's modulus E and the shear modulus G.

We also chose the number of elements per mesh sides.

The parameters E, A and I are calculated regarding the chosen values for the bending stiffness EI and the axial stiffness EA. We chose a Poisson's ratio ν equal to 0.5.

Influence of some parameters

Figure 5.3 shows the influence of the bending stiffness EI and the applied force per mesh Fm_T on the height of a suspended netting panel.

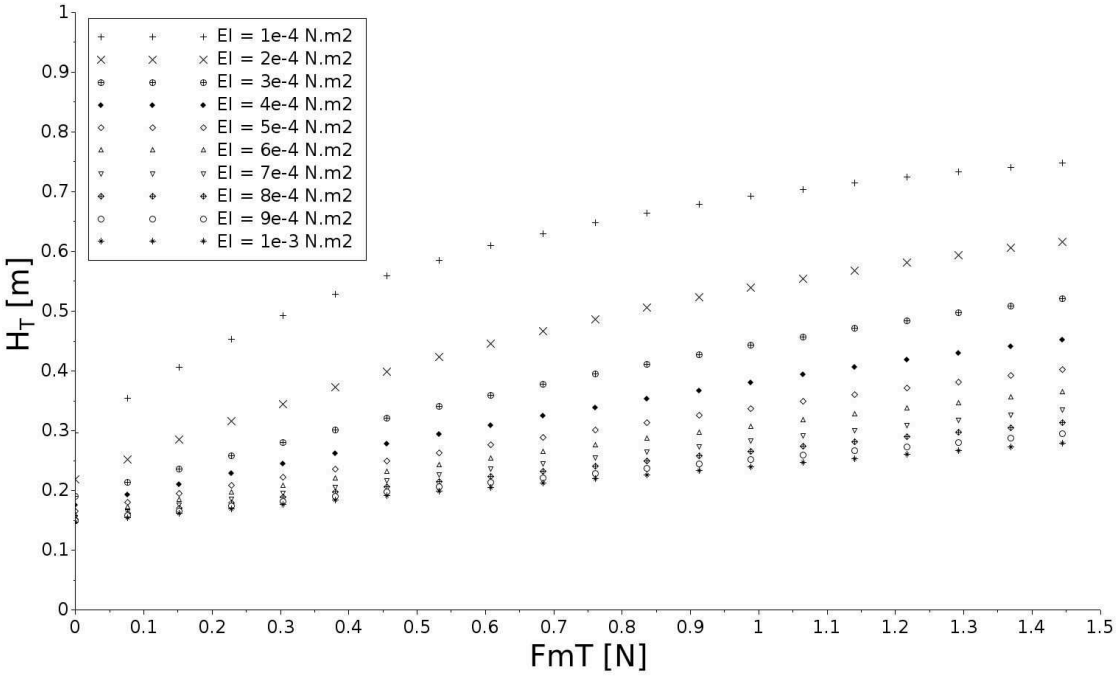

Figure 5.3 – Total height H_T of a suspended 4x10-mesh netting panel in the T-direction as a function of the applied force per mesh Fm_T and the bending stiffness of the mesh sides EI. The mass of the sample equals to 0.154 kg, the length of the mesh sides equal to 0.049 m, the angle at rest θ_0 between mesh sides and the N-direction is 7.5 °. The axial stiffness EA and the shear modulus G were chosen so that their values had negligible effect on the results of mesh resistance to opening. A mesh side was meshed with 20 Timoshenko beam elements.

5.2.2 Corotational formulation

We developed a finite element model using corotational 2D beams.

The problem is not linear. First we assume that the non-linearities come from the geometry. Thus, we assume that the large transformations of the twines are linked to large rotations, large displacements and small strains of the constituent elements. To work with large rotations and small strain, we chose the corotational approach presented by Le et al. (2011).

The main idea of this approach is to decompose the motion of the element into rigid body and pure deformational parts. Strain is measured in a local coordinates system fixed to the elements and that moves and rotates with it. This approach allows the use of an existing material model for small strain.

We developed this model using the programming language Python. The model showed mechanical and computational results in agreement with the Abaqus software tool. This model is a first step toward the development of a 3D finite element model.

Moreover, it offered the possibility to take into account the transverse shear in twines and to use optionally a non-linear material law.

5.2.3 Bar Element model

The bar element model presented in this section is a new and simple model for netting implemented using the programming language C. It was based on Priour (2013) and on the model for bending in twines described in this section. The model was presented in Morvan et al. (2016).

A netting structure is discretized into bar elements, the extremities of which are denoted nodes and are subject to forces. When the geometry of the netting structure, the external forces acting on it and the rigidity of the structure are known, the equilibrium position is obtained with the following steps:

- **Step 1.** First, an initial position of the structure (i.e. an initial position of the nodes) is determined.
- **Step 2.** Then, the forces on those nodes are calculated depending on the nodal positions.
- **Step 3.** Finally, the equilibrium position of the structure is obtained using an incremental iterative method such as the Newton-Raphson scheme (Ortega and Rheinboldt, 2000).

The numerical model proposes specific modelling, respectively for the aligned elements and for the non-aligned elements of the structure at rest.

A mesh side connects two knots and is modelled as a beam. And more precisely, with this original model, a mesh side is modelled as an assembly of aligned elements (Section 5.2.3). In this document, the mesh is generally assumed to be diamond, and the knot is represented as a node and can be modelled with only non-aligned elements (Section 5.2.3). This model can also be used for square meshes. In this case the square is considered as a diamond with a hanging ratio of 0.707 and the

same modelling is used: an assembly of aligned elements for the mesh sides and non-aligned elements for the knots. When the knots are large-sized, it could be worth considering the mesh as hexagonal. In this case aligned and non-aligned elements are used to model the knots.

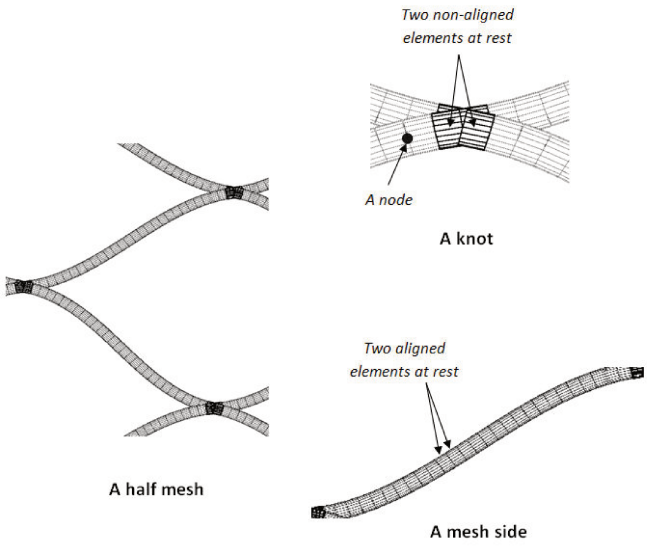

Figure 5.4 – Netting model. A knot is modelled with, at least, two non-aligned elements at rest (diamond meshes), and mesh sides are modelled with aligned elements.

Aligned elements to model mesh sides

The numerical model of a mesh side is based on Priour (2013). In this model, a mesh side is assumed to behave like a beam and is discretized into bar elements (Fig. 5.4 and Fig. 5.5). These elements are aligned and of equal length at rest. In order to represent the beam behaviour, bending stiffness is introduced between two consecutive elements: the couple between the two elements increases when the angle between them increases. The expression of the couple is obtained from the basic equation giving the curvature of an elastic beam subject to a specific moment:

$$C = \frac{EI}{R} \tag{5.22}$$

where E is the Young's modulus, I is the moment of inertia and R is the radius of curvature of the beam centreline at the node under consideration. The product EI stands for the bending stiffness of the beam.

However, Equation 5.22 is valid under the strong assumptions of a symmetrical beam, the transverse sections of which remain plane and normal to the centreline

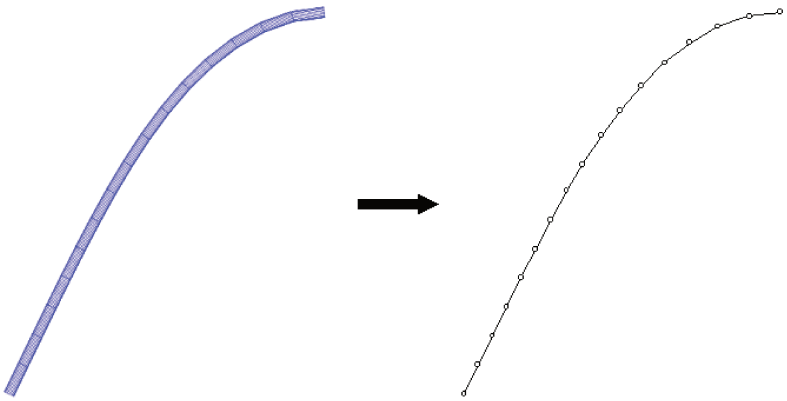

Figure 5.5 – Mesh side discretized into bar elements. A bar element connects two nodes.

after bending. Even if these assumptions are not generally fulfilled in the case of a netting, Eq. 5.22 is still used for the sake of simplicity.

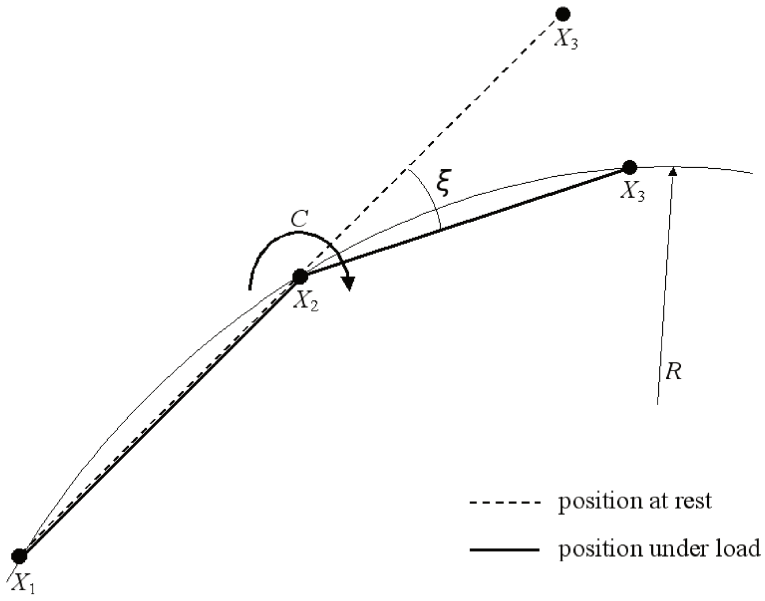

Figure 5.6 – Two consecutive bar elements in a mesh side. When the angle ξ between elements increases, the couple C increases.

The radius of curvature R is given by the radius of the circumcircle of the triangle defined by two consecutive bar elements (Fig. 5.6). The radius R of the circumcircle

of triangle 123 is given by the formula :

$$R = \frac{|X_{12}|\,|X_{23}|\,|X_{31}|}{4\sqrt{p(p-|X_{12}|)(p-|X_{23}|)(p-|X_{31}|)}} \tag{5.23}$$

where p is the semiperimeter of the circumcircle:

$$p = \frac{|X_{12}| + |X_{23}| + |X_{31}|}{2} \tag{5.24}$$

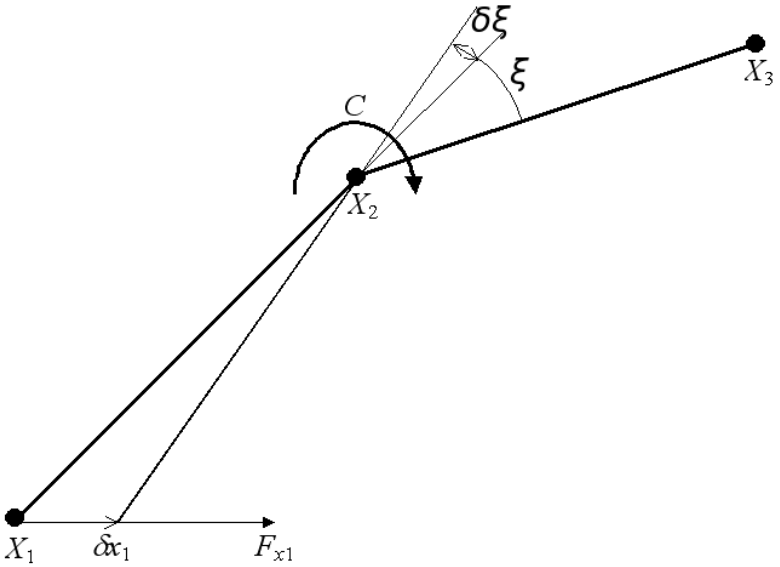

Figure 5.7 – Virtual work principle. δx_1 generates an external work $F_{x,1}\ \delta x_1$ and an internal work $C\delta\xi$.

Once the couple C is calculated, the forces on the nodes are expressed using the virtual work principle. Let us consider a virtual displacement δx_1 of the node 1 along the x-axis (Fig. 5.7). That displacement produces an external virtual work $\delta W_e = F_{x,1}\delta x_1$. It causes a variation $\delta\xi$ of the angle ξ between the two consecutive bar elements and generates an internal virtual work $\delta W_i = C\delta\xi$. From the basic virtual work equation, which is $\delta W_e = \delta W_i$, one obtains:

$$F_{x,1} = C\frac{\delta\xi}{\delta x_1} = C\frac{\partial\xi}{\partial x_1} \tag{5.25}$$

Doing the same for all the nodes 1, 2 and 3 and along the x, y and z-axis, one obtains the equations:

$$\begin{aligned} F_{x,1} &= C\frac{\partial \xi}{\partial x_1};\ F_{x,2} = C\frac{\partial \xi}{\partial x_2};\ F_{x,3} = C\frac{\partial \xi}{\partial x_3} \\ F_{y,1} &= C\frac{\partial \xi}{\partial y_1};\ F_{y,2} = C\frac{\partial \xi}{\partial y_2};\ F_{y,3} = C\frac{\partial \xi}{\partial y_3} \\ F_{z,1} &= C\frac{\partial \xi}{\partial z_1};\ F_{z,2} = C\frac{\partial \xi}{\partial z_2};\ F_{z,3} = C\frac{\partial \xi}{\partial z_3} \end{aligned} \tag{5.26}$$

The partial derivatives of the angle ξ in terms of the nodal coordinates are obtained from the identity:

$$\cos\xi = \frac{< X_{12}, X_{23} >}{|X_{12}|\,|X_{23}|} \tag{5.27}$$

and the forces on the nodes are given in vectorial form by:

$$\begin{aligned} F_1 &= \frac{EI}{|X_{12}|\,|X_{23}|\,R\sin\xi}\left[\frac{< X_{12}, X_{23} > X_{12}}{|X_{12}|^2} - X_{23}\right] \\ F_2 &= \frac{EI}{|X_{12}|\,|X_{23}|\,R\sin\xi}\left[-\frac{< X_{12}, X_{23} > X_{12}}{|X_{12}|^2} + \frac{< X_{12}, X_{23} > X_{23}}{|X_{23}|^2} + X_{23} - X_{12}\right] \\ F_3 &= \frac{EI}{|X_{12}|\,|X_{23}|\,R\sin\xi}\left[-\frac{< X_{12}, X_{23} > X_{23}}{|X_{23}|^2} + X_{12}\right] \end{aligned} \tag{5.28}$$

Non-aligned elements to model knots

Let us now consider a node corresponding to a knot of the netting (node 2 in Fig. 5.8). From the netting structure, one can see that the angle at rest between the two consecutive elements on either side of this node is non-zero (Fig. 5.4 and Fig. 5.8). Thus, Equation 5.22 does not work for this kind of node.

To express the couple on such a node (node 2 in Fig. 5.8), one builds a virtual bar element 23'. To obtain the virtual node 3', node 3 is rotated by the angle ξ_0 around node 2, where ξ_0 is the angle at rest between the two bar elements (Fig. 5.8):

$$X_{3'} = X_2 + \mathbf{R}\,(X_3 - X_2) \tag{5.29}$$

where $\mathbf{R}$ is the rotation matrix by the angle ξ_0 around the axis normal to the plan (X_{12}, X_{23}) around the node X_2 and it reads:

$$\mathbf{R} = \begin{pmatrix} n_x^2 + (1-n_x^2)c & n_x n_y(1-c) + n_z s & n_x n_z(1-c) - n_y s \\ n_x n_y(1-c) + n_z s & n_y^2 + (1-n_y^2)c & n_y n_z(1-c) + n_x s \\ n_x n_z(1-c) - n_y s & n_y n_z(1-c) + n_x s & n_z^2 + (1-n_z^2)c \end{pmatrix} \tag{5.30}$$

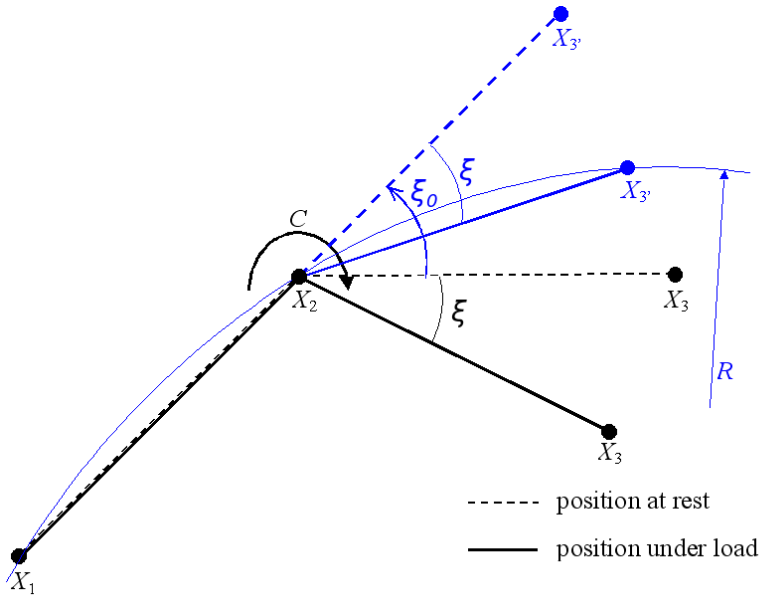

Figure 5.8 – Couple acting on the node 2. The angle at rest ξ_0 is not null.

where,

$$\begin{aligned} c &= \cos \xi_0, \\ s &= \sin \xi_0, \end{aligned} \tag{5.31}$$

$$\begin{pmatrix} n_x \\ n_y \\ n_z \end{pmatrix} = \frac{X_{21} \wedge X_{23}}{|X_{21} \wedge X_{23}|}$$

Moreover, the couple at node 2 is assumed to be completely carried by the bar elements 12 and 23' while node 3 is rigidly connected to node 3'. Therefore, the couple at node 2 can be expressed by Equation 5.22 on the bar elements 12 and 23'. One only has to replace point X_3 by point $X_{3'}$ in Equation 5.23 of the curvature radius.

Then, the expression of nodal forces in this case is obtained by replacing the curvature radius in Equation 5.28:

$$
\begin{aligned}
F_1 &= \frac{2EI}{|X_{12}|\,|X_{23'}|\,R\sin\xi}\left[\frac{< X_{12}, X_{23} > X_{12}}{|X_{12}|^2} - X_{23}\right] \\
F_2 &= \frac{2EI}{|X_{12}|\,|X_{23'}|\,R\sin\xi}\left[-\frac{< X_{12}, X_{23} > X_{12}}{|X_{12}|^2} + \frac{< X_{12}, X_{23} > X_{23}}{|X_{23}|^2} + X_{23} - X_{12}\right] \\
F_3 &= \frac{2EI}{|X_{12}|\,|X_{23'}|\,R\sin\xi}\left[-\frac{< X_{12}, X_{23} > X_{23}}{|X_{23}|^2} + X_{12}\right]
\end{aligned}
\tag{5.32}
$$

The vector $X_{23'}$ is easily calculated using Equation 5.29.

Equilibrium position of the netting

Once the equations of all the nodal forces in terms of nodal positions are formulated, one can solve them using an iterative procedure such as the Newton-Raphson scheme for instance. Thus, from a defined initial position X^0, position X is iteratively adapted until equilibrium is reached. In fact, one can only find an approximate solution by this method, therefore the equilibrium position is considered to have been reached when the total nodal force $F(X)$ is close enough to zero within an acceptable tolerance.

The iterative incrementation of X is given by the following recurrence relation formula:

$$
\begin{aligned}
X^{(0)} &= X^0 \\
X^{(k+1)} &= X^{(k)} + \Delta X^{(k)}
\end{aligned}
\tag{5.33}
$$

The iterative increment reads:

$$
\Delta X^{(k)} = -\left[\frac{\partial F}{\partial X}(X^{(k)})\right]^{-1} F(X^{(k)}) \tag{5.34}
$$

$-\left[\frac{\partial F}{\partial X}\right]$ is the tangent stiffness matrix

Applicability to hexagonal meshes

Modelling diamond meshes is possible using the models of aligned elements and non-aligned elements previously described. Modelling hexagonal meshes is also possible. In the case of diamond meshes, 2, 3 or 4 non-aligned elements connected to one node are used to model a knot (Fig. 5.4). To model the knots of hexagonal meshes, non-aligned and possibly aligned elements are used. In fact, in this case, a knot can be modelled as a beam (aligned elements at rest) connected to 4 mesh sides with non-aligned elements. In Fig. 5.9, non-aligned elements are used 3 times to connect the half knots to the two mesh sides: between the first mesh side and the knot, between the second mesh side and the knot and between the two mesh sides.

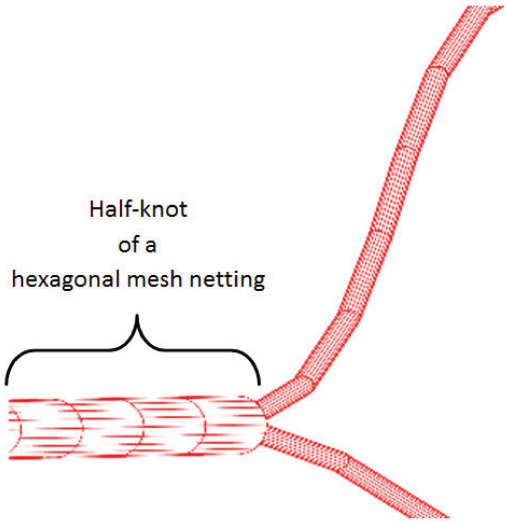

Figure 5.9 – A half knot and two mesh sides in the case of hexagonal meshes. The model of non-aligned elements is used up to 3 times to connect a knot to 2 mesh sides: between the first mesh side and the knot, between the second mesh side and the knot and finally between the two mesh sides.

In Fig. 5.10, there is a modelling of netting made up of 8 by 10 hexagonal meshes which is not equilibrated at the top and equilibrated at the bottom. The netting sample is loaded by gravitational forces only, and the top boundary is fixed vertically and free horizontally.

The hexagonal sides made up of twines are 0.05 m long, a diameter of 0.004 m, a density of 1100 $Kg.m^{-3}$, and a bending stiffness EI of 10^{-5} $N.m^2$ which is an acceptable value for twines made of polyethylene. They are modelled with 7 bar elements. The horizontal sides that represent the knots are 0.025 m long, a diameter of 0.009 m, a density of 1100 $Kg.m^{-3}$, and a bending stiffness EI of 10^{-4} $N.m^2$. They are modelled with 5 bar elements.

Comparison of the proposed model with an analytical solution (continuum mechanics) and the finite element code Abaqus

In a trawl, the bending moments have an effect on the deformations of the mesh sides, and more generally on the shape of the fishing gear. Thus, a simple example permitting the loading of two twines with bending moments, in two directions, is used to compare the proposed numerical model for netting with validated models.

Description of the example

Let us consider a frame made up of two cylindrical bars of the same length and which are at an angle of 90 degrees at rest. The frame is built in at one extremity

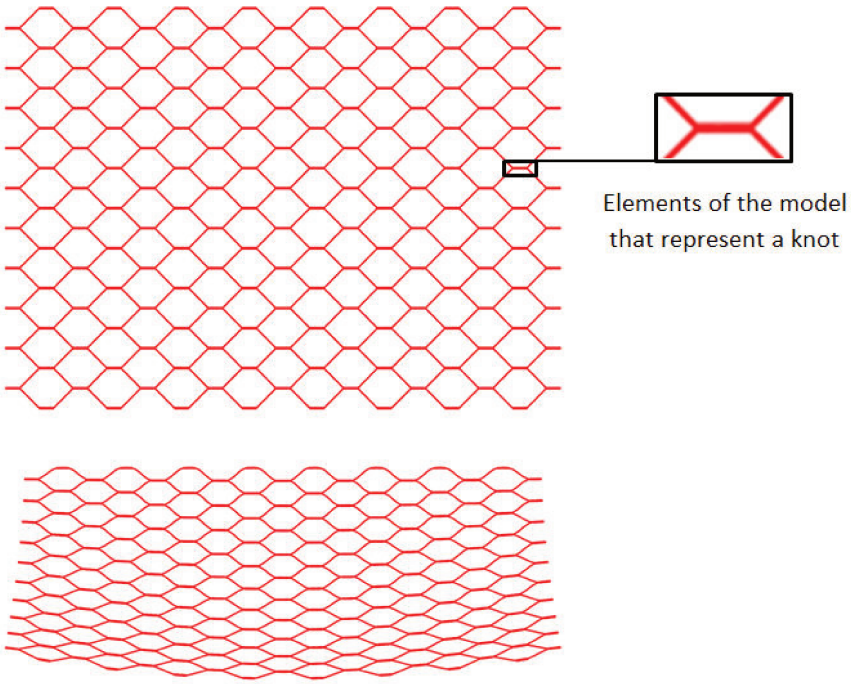

Figure 5.10 – Netting made of hexagonal meshes, not equilibrated at the top and equilibrated at the bottom. The top boundary is fixed vertically and can slide horizontally. The netting sample is loaded by its own weight.

and free at the other end, on which a vertical load is applied (Fig. 5.11). Two different load values are applied : firstly, a low load of $0.1N$ as in the case of small deflections (affording an easy analytical solution), and secondly, a larger load of $1N$ for large deflections.

The length l_0 and the section diameter of bars are arbitrarily and respectively $1m$ and $0.02m$ so that their size meets the beam assumption. An elasticity modulus of $300MPa$, in the range of rigid polymers generally used for nets, is considered. From these values, the moment of inertia, and the tensile stiffness are deduced. All these data are displayed in Table 5.1.

name	description	value
l_0	bar length	$1\ m$
D	beam section diameter	$0.02\ m$
E	material Young's modulus	$3\ 10^8\ N/m^2$
ES	tensile stiffness	$9.42\ 10^4\ N$
EI	bending stiffness	$2.36\ N.m^2$

Table 5.1 – Numerical data for the simple example displayed in Figure 5.11.

Modelling

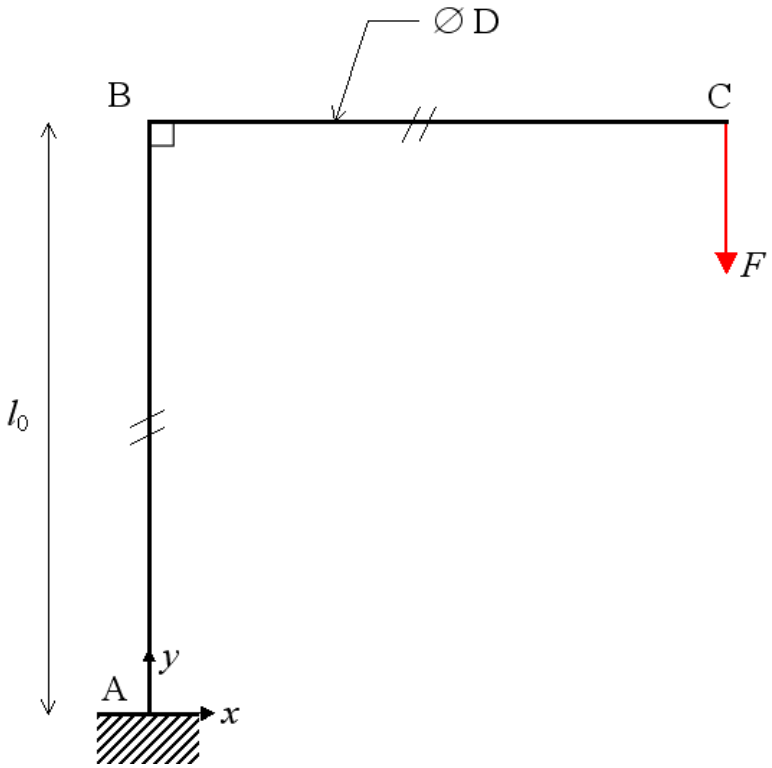

Figure 5.11 – Simple example. The two bars are modelled with aligned elements, and the fixation (in B) is modelled with non-aligned elements.

The frame is discretized with elements of the same length. The displacement of the nodes on bars AB and BC, except for node B, are expressed using the set of equations of the aligned elements model (Eq. 5.28). Concerning the displacement of node B and the nodes on either side of it, they are expressed using the set of equations of the non-aligned elements model (Eq. 5.32). The number of bar elements of the mesh is set at 20, which was found to be enough to achieve convergence.

The results provided by our numerical model are compared, on one hand, with the solution given by the theory of the strength of materials when small deflection behaviors can be assumed; on the other hand, when large deflection behaviors are considered, by the finite element software Abaqus. The closed-form solution Popov and Balan (1998) assumes elongation and deflection of the beams and yields the following formula for the displacement of any node along the bar AB:

$$U = \begin{pmatrix} \dfrac{FL_0y^2}{2EI} \\ \\ -\dfrac{Fy}{ES} \end{pmatrix} \tag{5.35}$$

and for the displacement of any node along the bar BC, one has:

$$U = \begin{pmatrix} \frac{FL_0{}^3}{2EI} \\ -\frac{FL_0}{ES} - \frac{FL_0{}^2 x}{EI} - \frac{FL_0 x^2}{2EI} + \frac{Fx^3}{6EI} \end{pmatrix} \tag{5.36}$$

where x, y are the coordinates of a given point along the frame.

Concerning the Abaqus model of the frame, it uses a regular mesh of 3-node quadratic plane beam elements (i.e. B22 beam element type) and takes geometric non-linearity into account. The number of beam elements is 20, which was found to achieve convergence.

Results and Discussion

The nodal displacements, respectively when the load equals 0.1N and 1N, are plotted in Figure 5.12. The couple along the frame with the applied load 0.1N and 1N is displayed respectively in Figure 5.13. One can see that the curves of displacement and couple obtained by the different methods are superimperposed. The discrepancies between the proposed method and the references (i.e. the closed-form solution under small deflection assumption and Abaqus) are extremely low in the example. It shows that the proposed modelling can be used to accurately describe the displacement of a netting modelled as beams, the traverse sections of which are symmetric and remain plane and perpendicular to the mean fiber after bending.

5.2.4 Comparison of twine models

We compared models by simulating a mesh side, clamped at one end and subject to a vertical force F at the other end. The material properties of the simulated mesh side were chosen close to properties measured in netting commonly used in trawl codends: the mesh side length l_{ms} was 0.049 m, the mesh angle at rest α_0 was 15 °, the Young's modulus was 16.554 10^6 $N.m^{-2}$ and the bending stiffness EI was 6.0 10^{-4} $N.m^2$.

We compared three models: the analytical model of O'Neill, the proposed bar element model and the Timoshenko beam model of the Abaqus software tool.

The model proposed by O'Neill (2002) was described in Section 2.1.2. We used the approximated solutions that was accurate, according to O'Neill (2002), when $\epsilon_{ONeill} < 0.2$. ϵ_{ONeill} is defined by Equation 5.37.

$$\epsilon^2_{ONeill} = EI/(l^2 f) \tag{5.37}$$

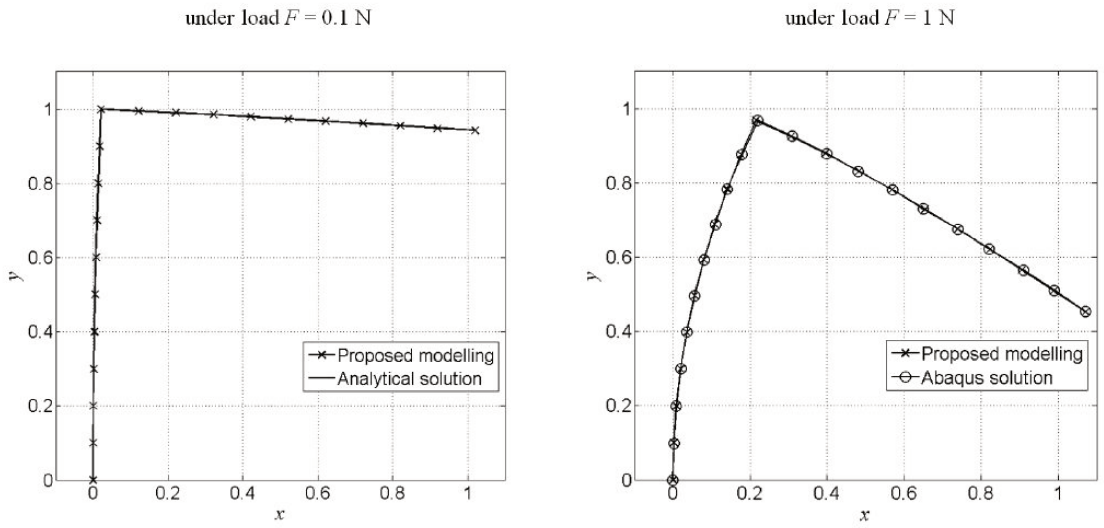

Figure 5.12 – Deformation along the frame when it is subjected to vertical forces of 0.1 N (left) and 1 N (right). Comparison of nodal positions of the bar element model with the analytical solution and the Abaqus solution. The concordance is pretty good.

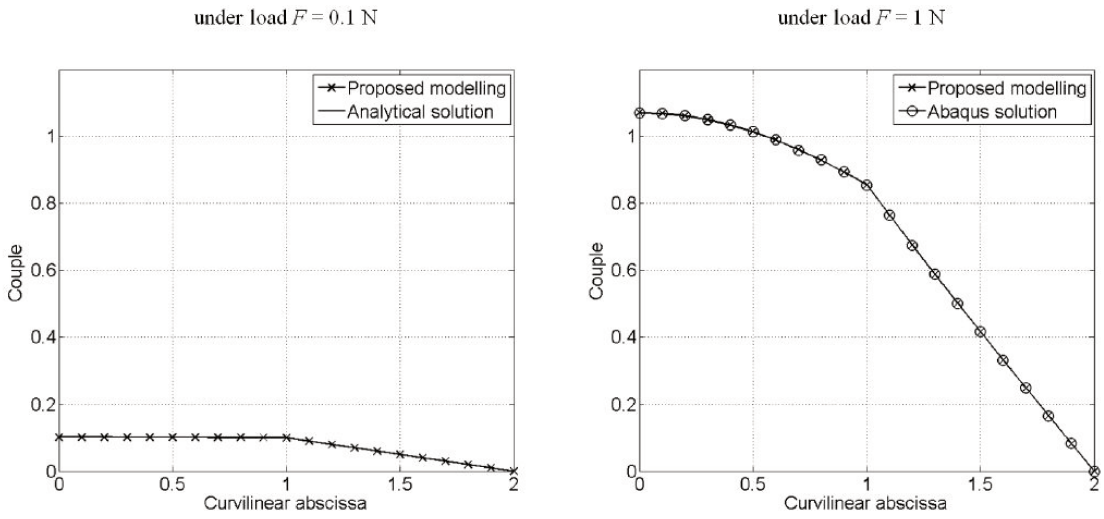

Figure 5.13 – Couple along the frame when it is subjected to vertical forces of 0.1 N (left) and 1 N (right). Comparison of couples along the frame of the bar element model with the analytical solution and the Abaqus solution. The concordance is pretty good.

The proposed bar element model was described in Section 5.2.3. A mesh side was meshed into 20 bar elements.

The used of the Timoshenko beam elements of the Abaqus Standard software tool was presented in Section 5.2.1. Since the model of De la Prada and Gonzales (2013) is based on an existing finite element model and interpolation methods, we could assume that the obtained results would be close to the ones obtained with the Abaqus Standard software tool. A mesh side was meshed into 20 B21H elements (2-node linear beam in a plane, hybrid formulation).

The comparisons were based on the shape of the simulated mesh side and on the curvature radius R along the twine. The results are shown in Figures 5.14, 5.15, 5.16 and 5.17 for an applied vertical force value equalled to 2 N, 5 N, 10 N and 20 N respectively.

F=2 N
ϵ=0.35

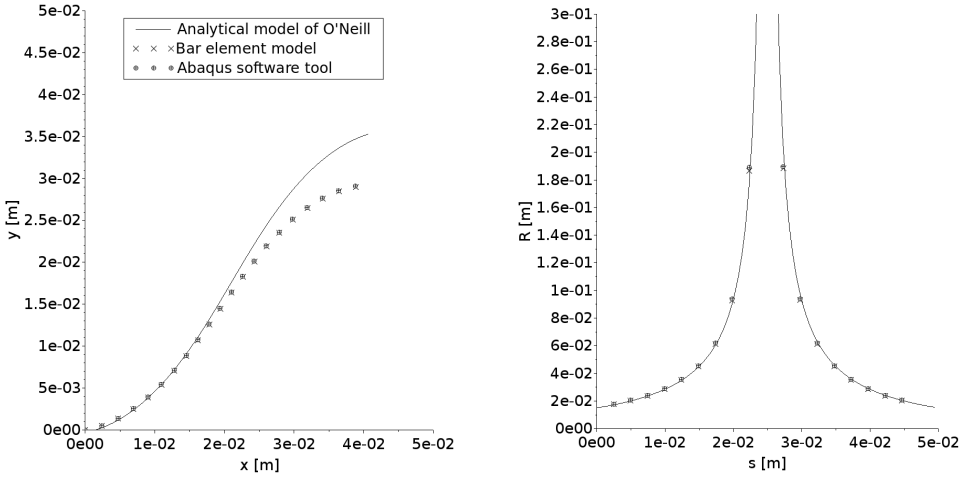

Figure 5.14 – Results of simulations of a mesh side subject to a vertical force value of **2 N** with several models: the analytical model of O'Neill, the proposed bar element model and the Timoshenko beam model of the Abaqus software tool. Comparisons of the models for the shape of the twine (left) and the curvature radius R along the twine (right). s is the curvilinear abscissa along the mesh side ($0 < s < l_0$). The accuracy parameter ϵ_{ONeill} equals to **0.35**.

The comparisons show that the bar element model provides results close to the results obtained with the Abaqus Standard software tool, whatever the applied force. As expected, the O'Neill's model gives different results when $\epsilon_{ONeill} > 0.2$ (Figures 5.14 and 5.15). When the force value is higher, $\epsilon_{ONeill} < 0.2$, and the shape of the twine simulated with the O'Neill's model is closer to the one obtained with finite element models (Figures 5.16 and 5.17). Nevertheless, for higher force value, one sees a difference that can be explained by the fact that O'Neill (2002) assumed that

F=5 N
ϵ=0.22

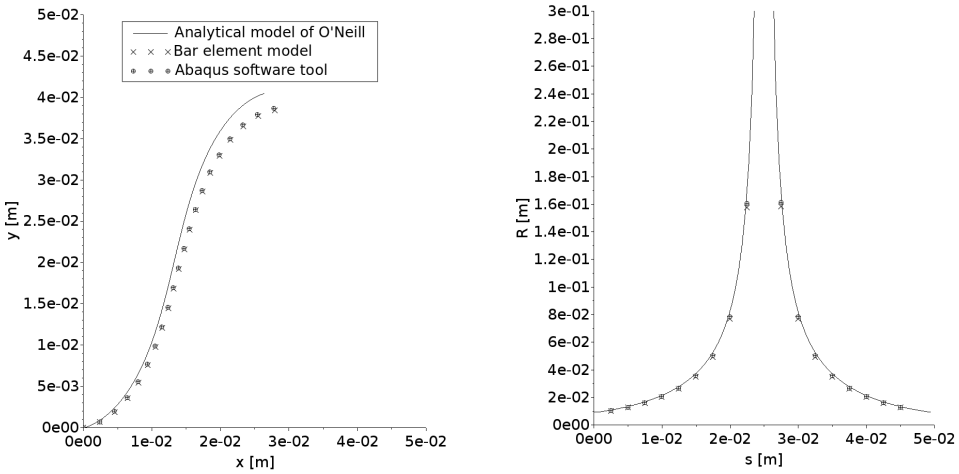

Figure 5.15 – As in Figure 5.14 with a vertical force value of **5 N**. The accuracy parameter ϵ_{ONeill} equals to **0.22**.

F=10 N
ϵ=0.16

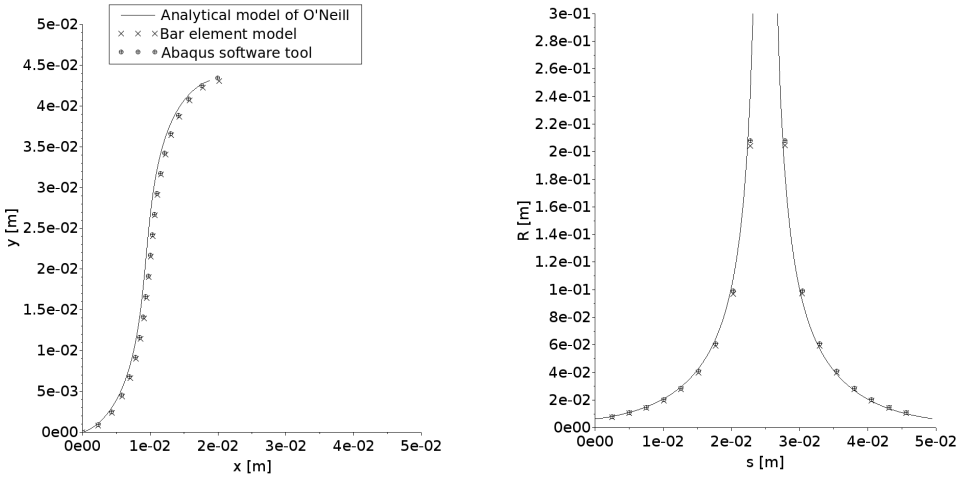

Figure 5.16 – As in Figure 5.14 with a vertical force value of **10 N**. The accuracy parameter ϵ_{ONeill} equals to **0.16**.

there was no elongation in the mesh side.

Thus, the finite element models were more accurate for the simulation of a mesh side subject to a vertical force at one of its ends than the analytical model of O'Neill (2002). Moreover, the bar element model showed good results regarding these ones obtained with the Abaqus Standard software tool.

F=20 N
ϵ=0.11

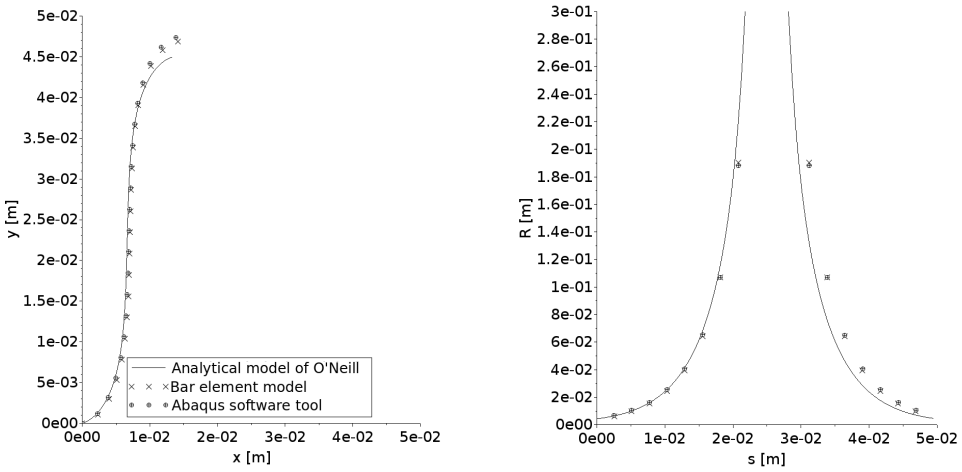

Figure 5.17 – As in Figure 5.14 with a vertical force value of **20 N**. The accuracy parameter ϵ_{ONeill} equals to **0.11**.

5.2.5 Inverse identification method

Three different tests were performed: uniaxial tensile tests on a tensile machine, suspension tests and biaxial tensile tests on an own designed and made device.

The three mesh side models used for the study were presented previously: the Timoshenko beam model of the Abaqus Standard software tool (Section 5.2.1), our quasi-analytical beam model (Section 5.1), and our bar element model (Section 5.2.3).

Whatever the model, we knew the applied forces and the positions of all the knots. These known positions were used to calculate **objective functions** and identify, by minimizing or searching the zero of this function, the value of the bending stiffness EI.

Uniaxial tensile tests

In case of the uniaxial tensile tests, the objective function was the difference between the experimental and the numerical height of the mesh in the middle of the netting panel.

The zero of the function was searched using the dichotomy method (or bisection method). This method was quick enough for our problem, simple and robust.

Suspending tests

In case of the suspending tests, the objective function was calculated by using two different methods: firstly, the objective function was the mean distance between the coordinates of the experimental and the numerical knots; secondly, the objective function was the difference between the experimental and the simulated suspended sample height.

Firstly the objective function was the mean distance between the coordinates of the experimental and the numerical knots, it was minimized using the Nelder-Mead (or downhill simplex) algorithm proposed by Nelder and Mead (1965). The objective function s is defined by Equation 5.38.

$$s = \sum_{i=1}^{n} \sqrt{(x_i^{exp} - x_i^{num})^2 + (y_i^{exp} - y_i^{num})^2} \tag{5.38}$$

With (x_i^{exp}, y_i^{exp}) the experimental cartesian coordinates of the knot i, (x_i^{num}, y_i^{num}) the numerical cartesian coordinates of the knot i and n the number of knots.

Secondly the objective function was the difference between the experimental and the simulated suspended sample height, it was minimized using the dichotomy method.

$\mathbf{Fm_T}$ $[N]$	0.324	0.814	1.795	2.776
$\mathbf{EI_{xy}}$ $[N.m^2]$	2.013 10^{-4}	2.097 10^{-4}	2.038 10^{-4}	2.163 10^{-4}
$\mathbf{EI_h}$ $[N.m^2]$	2.066 10^{-4}	2.168 10^{-4}	2.146 10^{-4}	2.270 10^{-4}
Relative difference: $\frac{EI_h - EI_{xy}}{EI_{xy}}$ [%]	2.6	3.4	5.3	4.9

Table 5.2 – Single twine green PE netting, 4x10-mesh sample. Bending stiffnesses EI_{xy} and EI_h evaluated by inverse identification using the coordinates of all the knots and the total height H_T of the suspended samples respectively, at the end of creep stages of 30 minutes. The mean relative difference between the bending stiffnesses identified using the two methods equals to 4.04 %.

For example, we identified the bending stiffness of 10 4x10-mesh samples of single twine green PE netting using these two methods (Table 5.2). We calculated a mean relative difference of 4.04 % between the bending stiffness identified using the measured coordinates of all the knots and the bending stiffness evaluated using the height of the netting panel. Thus, for convenience, we decided to identify the parameter with only the height of the netting sample that needs a more simple and non-expensive experimental method.

Biaxial tensile tests

In case of the biaxial tensile tests, the objective function was the difference between the result of the division L_{sT}/L_{sN} obtained with experimental and numerical data. L_{sT} and L_{sN} are the total lengths of the netting sample in the T- and N-directions respectively. The zero of the function was reached using the dichotomy method.

CHAPTER

6 Numerical results

6.1 Diamond meshes

In this section, the bending stiffness values were evaluated assuming a diamond shape for the meshes and using the inverse identification method previously described in Section 5.2.5. This means that the knots in netting were modelled by points.

The results of the identifications for netting samples subject to uniaxial tensile tests (Section 6.1.1), suspending tests (Section 6.1.2) and biaxial tensile tests (Section 6.1.3) are presented.

The bending stiffness is identified using the quasi-analytical model and the Abaqus Standard software tool in case of uniaxial tensile tests, and the bar element model in cases of suspending tests and biaxial tensile tests.

6.1.1 Uniaxial tensile tests

Using the experimental results of the uniaxial tensile tests (Fig. 3.1) and the identification method presented in Section 5.2.5, we identified the bending stiffness EI of braided twines constituting the netting sample. The evolution of the bending stiffness EI is presented on Figure 6.1. The evolutions of this parameter during the whole test, including relaxation stages, identified using the quasi-analytical model and the Abaqus Standard software tool, are presented.

Figures 6.2 and 6.3 show, respectively, the influence of the force by mesh in the T-direction and the influence of the opening o_T on the bending stiffness. For these two figures, the bending stiffness was identified using the finite element model of Abaqus at the beginning (0 min) and at the end (15 min) of the relaxation stages.

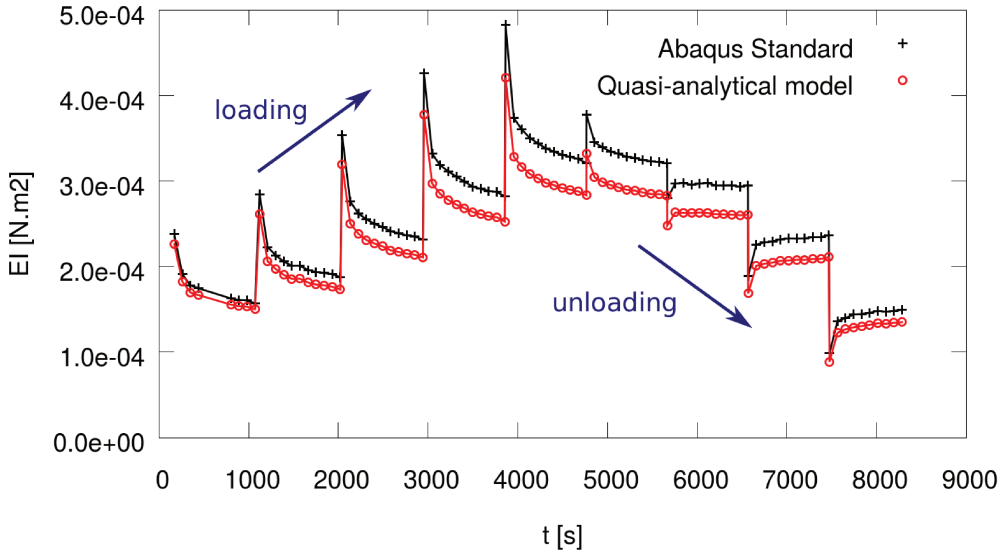

Figure 6.1 – **Single twine *Green* PE netting** with a mesh side length of 40 mm. Evolution of the identified bending stiffness EI. Experimental results were presented in Figures 4.1 and 4.2.

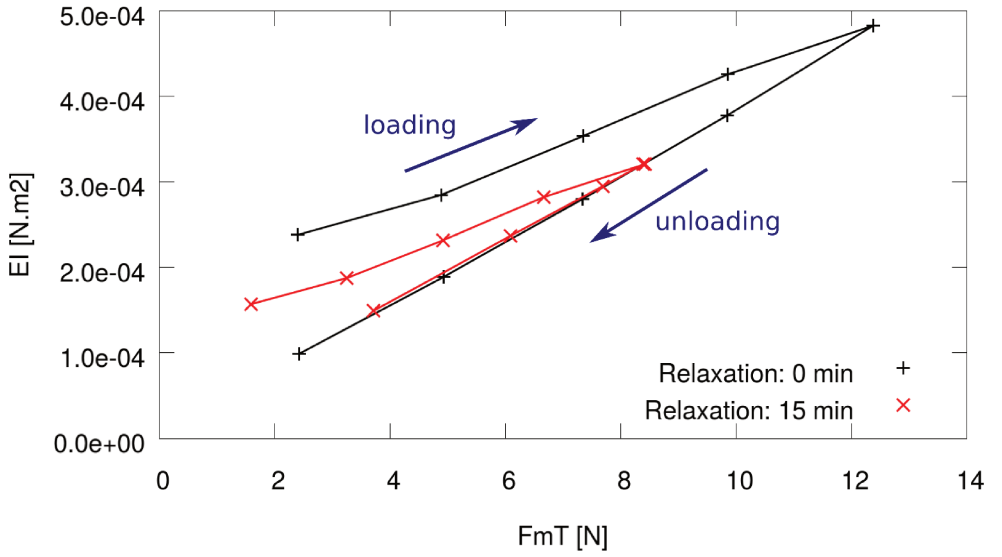

Figure 6.2 – **Single twine *Green* PE netting** with a mesh side length of 40 mm. Evolution of the bending stiffness EI, identified using the Abaqus Standard software tool at 0 minute ('+', black line) and at 15 minutes ('x', red line) of each relaxation stage, as a function of the applied load Fm_T. Experimental results were presented in Figures 4.1 and 4.2.

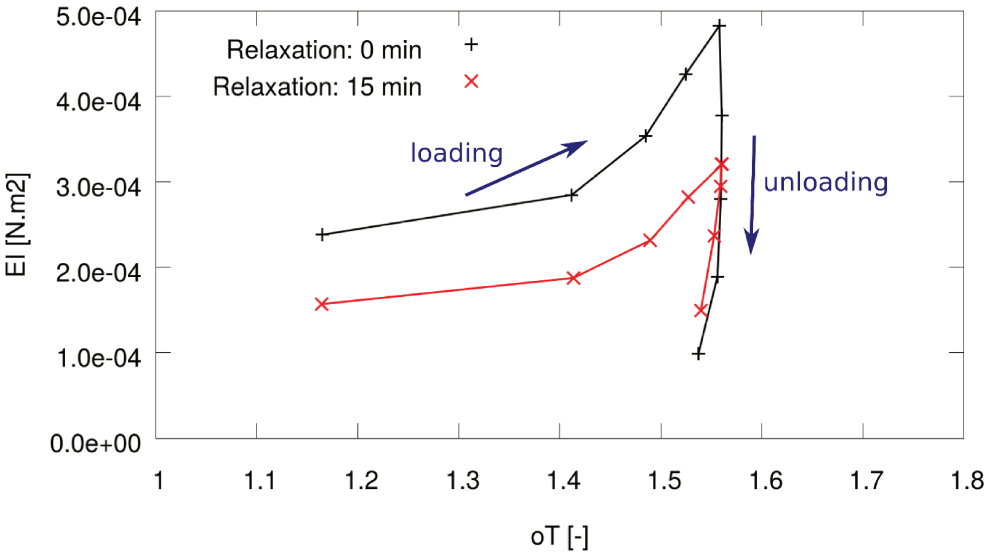

Figure 6.3 – **Single twine *Green* PE netting** with a mesh side length of 40 mm. Evolution of the bending stiffness EI, identified using the Abaqus Standard software tool at 0 minute ('+', black line) and at 15 minutes ('x', red line) of each relaxation stage, as a function of the opening in the T-direction o_T. Experimental results were presented in Figures 4.1 and 4.2.

6.1.2 Suspending tests

Influence of the viscosity of the material on the identified bending stiffness

The identified evolution of the bending stiffness, in case of suspending tests on single twine Green PE netting, is presented on Figure 6.4.

Comparisons of the experimental and the numerical heights

For a range of suspended netting samples, the bending stiffness EI was identified by the inverse identification algorithm minimizing the difference between the numerical and experimental total heights H_T of the netting panel at the end of the creep stages (Section 5.2.5). We used the bar element model to simulate the suspended samples. The measurement of the total heights H_T of the netting panel, subject to different levels of force per mesh Fm_T, are given in Tables 3.1, 3.6, 3.7, 3.10 and 3.11.

Once the bending stiffness was identified, we compared the experimental and numerical heights $H1$, $H2$, $H3$ and $H4$ for a 4x10-mesh netting sample and $H1$, $H2$, $H3$, $H4$ and $H5$ for a 5x25-mesh netting sample.

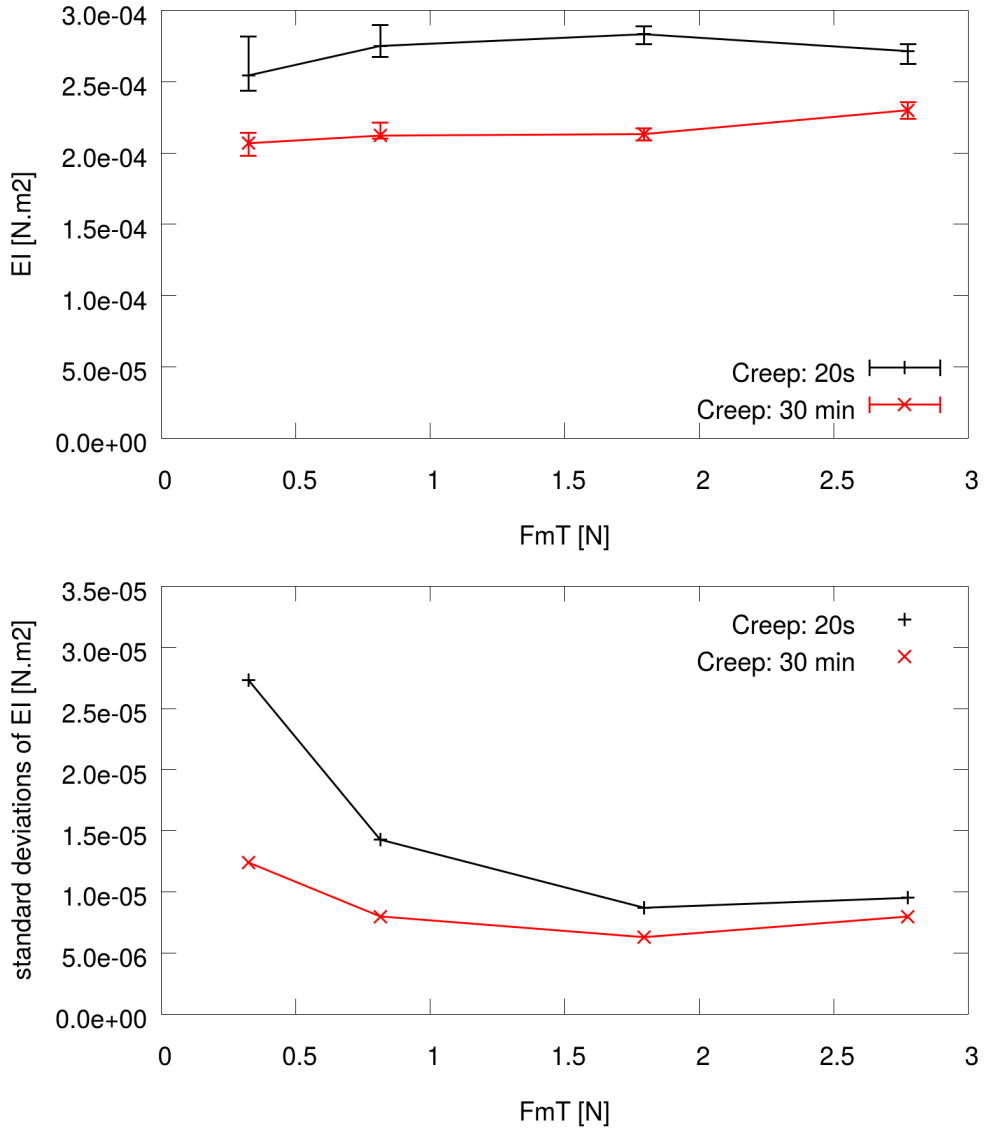

Figure 6.4 – Suspending tests on 10 **4x10-mesh single twine *Green* PE netting** samples with a mesh side length of 40 mm. Medians of the bending stiffness EI with first and third quartiles (above) and standard deviation (below) of EI at the beginning (20 s) and at the end (30 min) of each creep stage. The bending stiffness was identified using the Abaqus software tool.

Figures 4.10 to 4.15 show the numerical and experimental heights for each sample and each loading level. The numerical results fit, quite well, the experimental measures.

Bending stiffness

Figures 6.5 to 6.10 present the evolution of the bending stiffness EI, identified as explained in Section 5.2.5, as a function of the applied load Fm_T. These figures also present the coefficient of variation (ratio of the standard deviation to the mean) of the bending stiffness EI as a function of the applied load Fm_T.

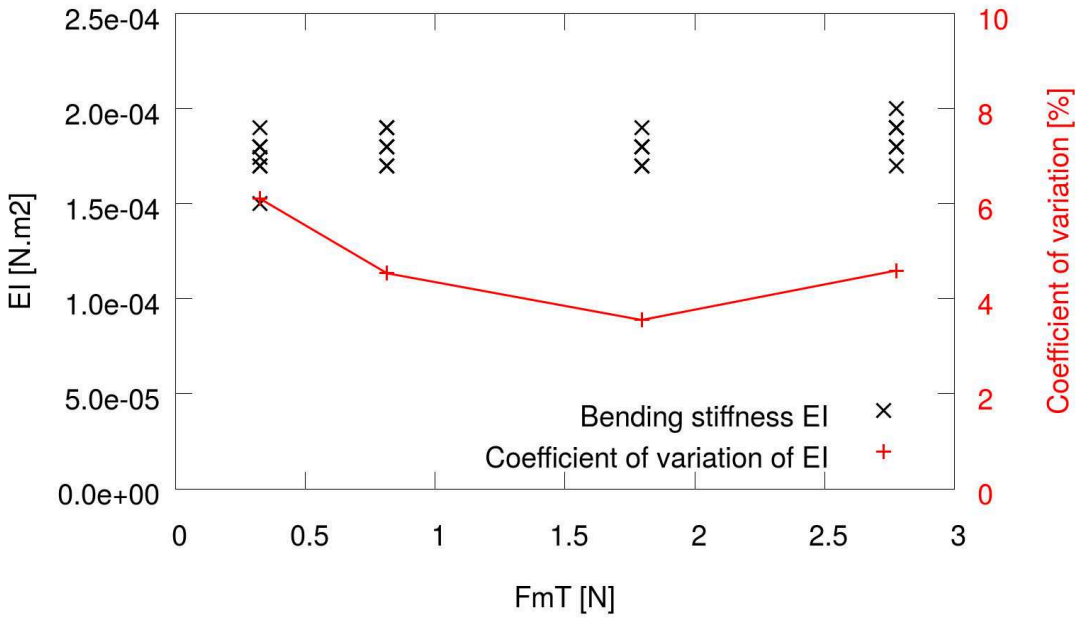

Figure 6.5 – **Single twine *Green* PE netting, 4x10-mesh sample**. The length of mesh sides at rest is 40 mm. Results of the numerical model identified on the experimental suspending tests; evolutions of the bending stiffness EI and its coefficient of variation (ratio of the standard deviation to the mean) as a function of the applied load Fm_T, for ten netting samples.

Influence of the size of the samples on the identified bending stiffness

Figure 6.11 shows the evolution of the bending stiffness EI as a function of the applied load Fm_T in the cases of 4x10-mesh and 5x25-mesh double twine *Green* PE netting samples ($l_{ms} = 50\ mm$). In Figure 6.12, the bending stiffness EI is represented as a function of the opening o_T.

6.1.3 Biaxial tensile tests

The results of the identifications of the bending stiffness EI of double twine Green PE netting samples subject to biaxial tensile tests are presented in Figures 6.13 and

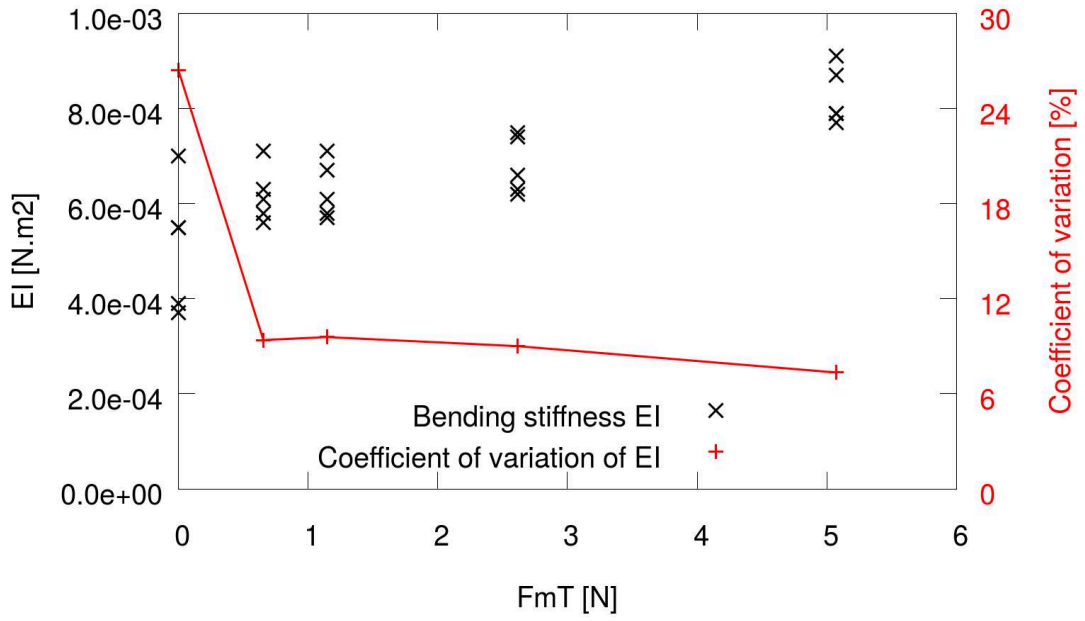

Figure 6.6 – **Double twine *Green* PE netting, 4x10-mesh sample**. The length of mesh sides at rest is 50 mm. Results of the numerical model identified on the experimental suspending tests; evolutions of the bending stiffness EI and its coefficient of variation (ratio of the standard deviation to the mean) as a function of the applied load Fm_T, for five netting samples.

6.14. The bending stiffness is represented as a function of the applied Fm_T (Fig. 6.13) and as a function of the opening o_T (Fig. 6.14).

6.1.4 Discussion

Figure 6.1 shows the importance of taking into account the viscosity of the material, which influences greatly the identified bending stiffness. Thus, with the assumption of a visco-elasto-plastic behaviour, the relaxation stages permit to reduce the effect of viscosity and to improve the evaluation of the bending stiffness; indeed, the higher the relaxation duration is, the less the rate dEI/dt is, then the less the effect of the time on the value of EI is. Figure 6.3 shows that the opening o_T was still high during the unload (with relaxation stages of 15 minutes). So the mesh did not come back to its initial state. The structure presented a permanent deformation or a long-term viscosity.

Figure 6.1 shows that the bending stiffness identified with the analytical model is lower than the one evaluated with the Abaqus Standard software tool. The relative difference between the two curves ranges from 4.40 % for a force by mesh value of 1.59 N to 12.77 % for a force by mesh value of 12.38 N. According to the finite ele-

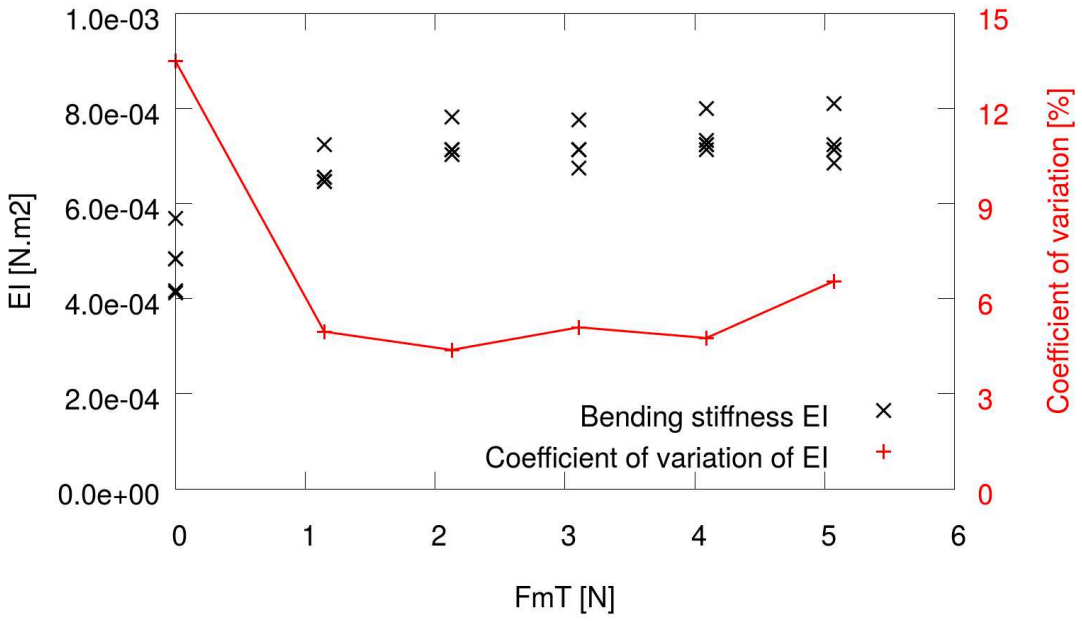

Figure 6.7 – **Double twine *Green* PE netting, 5x25-mesh sample**. The length of mesh sides at rest is 50 mm. Results of the numerical model identified on the experimental suspending tests; evolutions of the bending stiffness EI and its coefficient of variation (ratio of the standard deviation to the mean) as a function of the applied load Fm_T, for five netting samples.

ment model of tensile test, the mesh in the middle is submitted to a tensile force in the T-direction and a compression force in the N-direction. However, the analytical model only takes into account the tensile force. We can assume that to obtain the same mesh opening in the T-direction without compression force in the N-direction, a lower bending stiffness is necessary. We can note that for a low force level, in case of a tensile test, the bending stiffness identified with the analytical model is close to the one evaluated with the beam element model.

Figures 6.2 and 6.3 show the evolution of the identified bending stiffness as a function of the force applied on the mesh Fm_T and as a function of the opening o_T respectively. We can note that the variation of the parameter EI during the test is smaller when it has been calculated at the end of each relaxation step in spite of the fact that the contribution of the viscosity is not completely relaxed after a relaxation step of 15 minutes (Fig. 4.1).

During the tensile test on single twine Green PE netting, the force by mesh at the beginning of relaxation stages ranged from 2.40 N to 12.38 N (Fig. 6.2). During suspending tests on the same type of netting, netting panels were submitted to forces by mesh added at the bottom ranging from 0.3235 N to 2.775 N (Fig. 6.4).

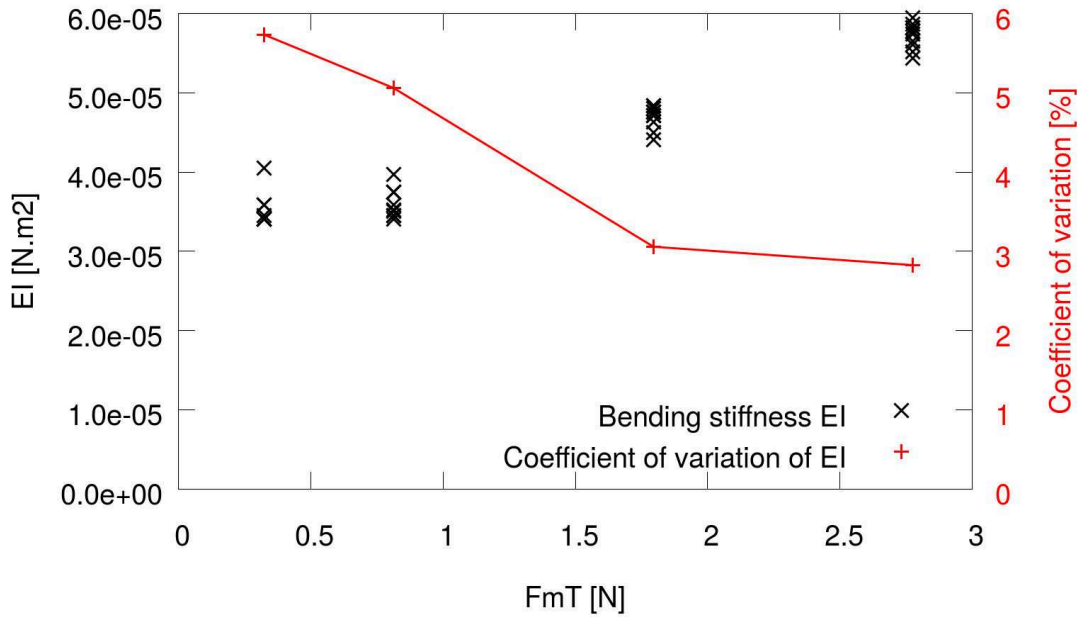

Figure 6.8 – **Single twine *Breztop* PE netting, 4x10-mesh sample**. The length of mesh sides at rest is 40 mm. Results of the numerical model identified on the experimental suspending tests; evolutions of the bending stiffness EI and its coefficient of variation (ratio of the standard deviation to the mean) as a function of the applied load Fm_T, for ten netting samples.

The force by mesh applied on the uppermost meshes was higher and ranged from 0.46 N to 2.91 N due to the effect of gravity. The load applied on meshes during suspending tests on single twine Green PE netting were only around a quarter of the load applied during the tensile test. With this loading level, a smaller opening o_T of the mesh is observed during the suspending test than during the tensile test, therefore a smaller variation of the identified bending as presented on Figure 6.4. We can note that the bending stiffness identified for the smallest value of force by mesh with the tensile test is close to the ones identified with the suspending tests.

When the force Fm_T and thus the mesh opening increases, the tensile forces in the mesh sides increase so we may expect the twine diameter to decrease. A smaller diameter means a smaller moment of inertia I. Thus, we may expect a decrease in EI when the loading level increases. However, the results do not show any decrease in EI when Fm_T increases. In cases of single twine Green PE netting (Fig. 6.3), double twine *green* PE netting (Fig. 6.6), single twine *Breztop* PE netting (Fig. 6.8) and single twine PA netting (Fig. 6.10), we note an increase in the bending stiffness. It could be due to the complexity of the twine braided structure: when the loading level increases, the shear force and the bending moment through the twine section increase, so the shape of the section may change drastically and this could

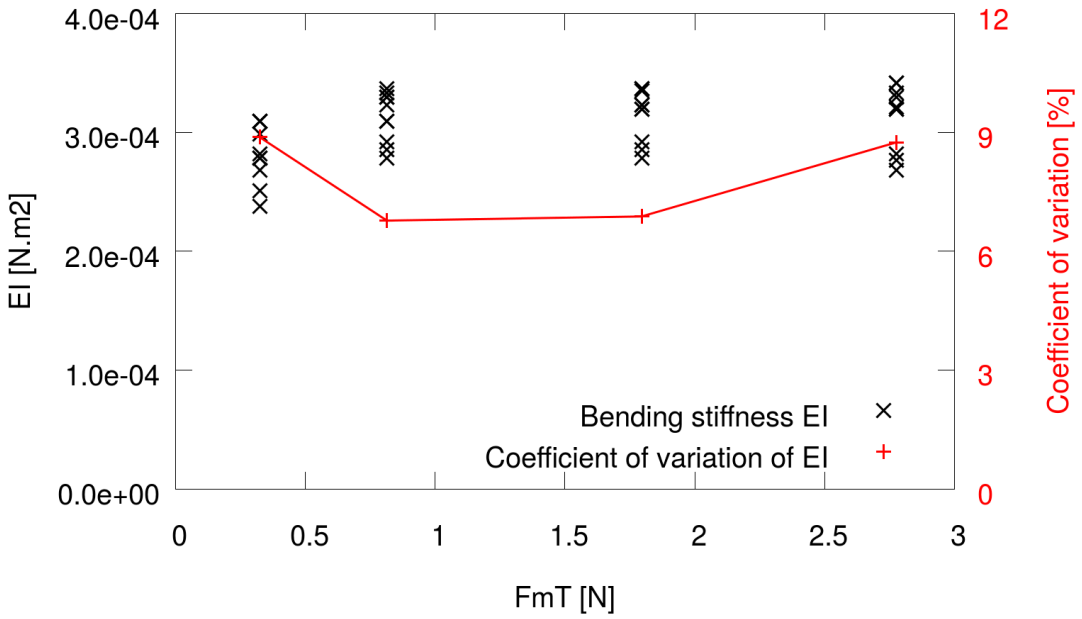

Figure 6.9 – **Single twine *Brezline* PE netting, 4x10-mesh sample**. The length of mesh sides at rest is 60 mm. Results of the numerical model identified on the experimental suspending tests; evolutions of the bending stiffness EI and its coefficient of variation (ratio of the standard deviation to the mean) as a function of the applied load Fm_T, for ten netting samples.

affect the bending stiffness EI.

The comparison of the experimental and numerical heights H_1, H_2, H_3 and H_4 for a 4x10-mesh netting and H_1, H_2, H_3, H_4 and H_5 for a 5x25-mesh netting (Figs. 4.10 to 4.15), shows that the bar element model captures the heterogeneous deformation field of the netting samples during the suspending tests. Indeed, despite a noticeably decrease of the height from the top quarter H_1 (or fifth) to the bottom quarter H_4 (or fifth H_5) (Figs. 4.12, 4.14 and 4.15), the numerical model gives height values similar to experiments for all tested types of fishing nets.

Moreover, Fig. 6.11 shows that in case of double twine green PE netting, the bending stiffness EI does not depend on the size of the sample: for 4x10- and 5x25-mesh netting samples, the evaluated bending stiffnesses are similar, whatever the loading level. However, the mesh opening values are higher in case of 4x10-mesh netting (Fig. 6.12). This difference can be explained by the difference in the direction of application of the loading during the pre-tension step (N-direction in case of 5x25-mesh netting and T-direction in case of 4x10-mesh netting). Thus, despite a different size and a different pre-tension, the evolution of the identified bending stiffness as a function of the applied force Fm_T is identical. Moreover, we observed

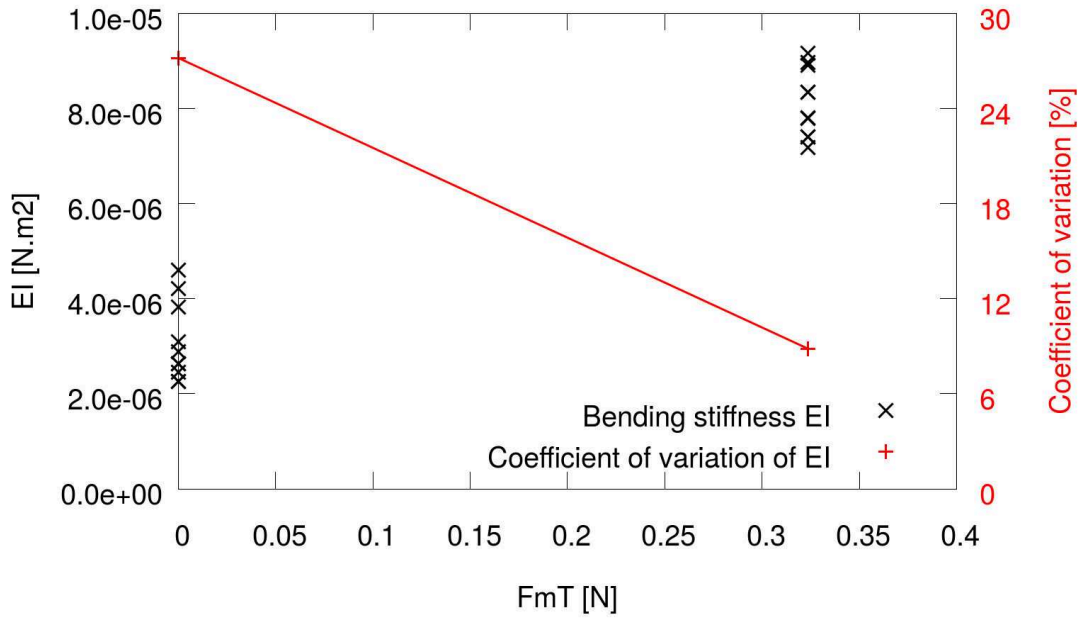

Figure 6.10 – **Single twine PA netting, 4x10-mesh sample**. The length of mesh sides at rest is 30 mm. Results of the numerical model identified on the experimental suspending tests; evolutions of the bending stiffness EI and its coefficient of variation (ratio of the standard deviation to the mean) as a function of the applied load Fm_T, for ten netting samples.

an identical evolution as a function of the opening o_T with an opening shift due to a plastic deformation of the 4x10-mesh netting in the T-direction during the pretension step.

Figs. 6.5 to 6.10 show that the coefficient of variation of EI is the highest when the value of Fm_T is close to zero. In case of higher loading level, the coefficient of variation is below 10%.

The biaxial tensile tests allow the study of the influence of a loading Fm_N in the N-direction on the evaluated bending stiffness EI. First, whatever the loading level in the N-direction, a significant increase of the identified bending stiffness with the force in the T-direction is observed (Fig. 6.13). The bending stiffness as a function of the force by mesh Fm_T is slightly higher in case of $Fm_N = Fm_T$ than in the case of $Fm_N = 2Fm_T$. Figure 6.14 shows different bending stiffness values as a function of the opening o_T for the two loading types. The mesh opening in the T-direction o_T is reduced when the loading level in the N-direction is increased, as expected. The identified bending stiffness in case of biaxial tensile tests is revealed higher than in case of suspending tests for a same opening value o_T (Fig. 6.12 and 6.14). We expected to evaluate identical bending stiffness values in cases of suspending tests

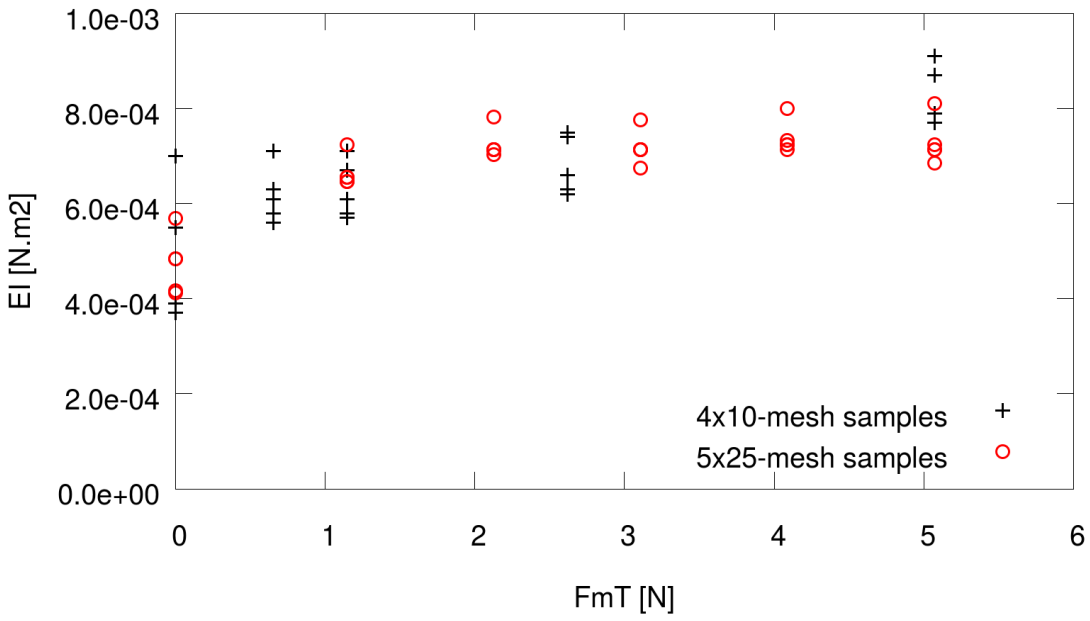

Figure 6.11 – **Double twine *green* PE netting** with a mesh side length of 50 mm at rest. Results of the numerical model identified on the experimental suspending tests; evolutions of the bending stiffness EI as a function of the applied load Fm_T, for five 4x10-mesh netting samples and five 5x25-mesh netting samples. This shows that the bending stiffness is independent of the size of the panels (4x10- and 5x25-mesh netting samples). The size of the netting samples does not affect the evaluation of EI.

and biaxial tensile tests since the bending stiffness should not depend on the loading type.

The increase in the identified bending stiffness when the force by mesh Fm_T increases, and the different results between the identifications from biaxial tensile tests and suspending tests, could be explained by the fact that the knot sizes were not taken into account. It was decided to model the knot sizes for the identification of the bending stiffness. The results are presented in the following section.

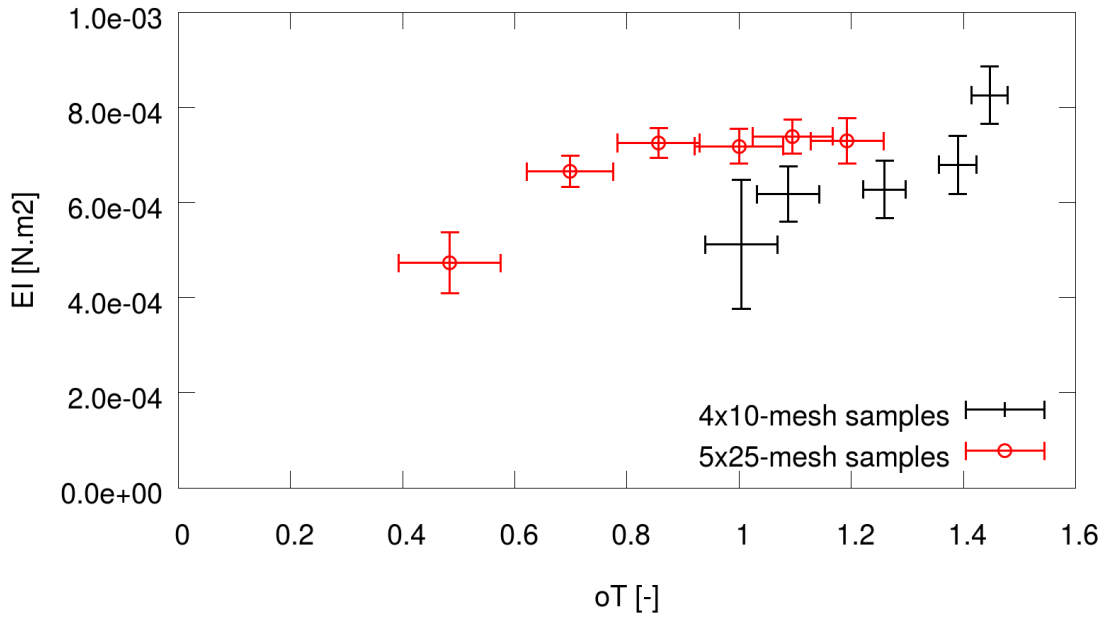

Figure 6.12 – **Double twine *green* PE netting**. Results of the numerical model identified on the experimental suspending tests; evolutions of the mean of the bending stiffness EI as a function of the opening o_T, for five 4x10-mesh netting samples and five 5x25-mesh netting samples. The vertical and horizontal solid lines represent the standard deviations. The 4x10-mesh samples were submitted to a pre-tension step in the T-direction whereas the 5x25-mesh samples were submitted to a pre-tension step in the N-direction.

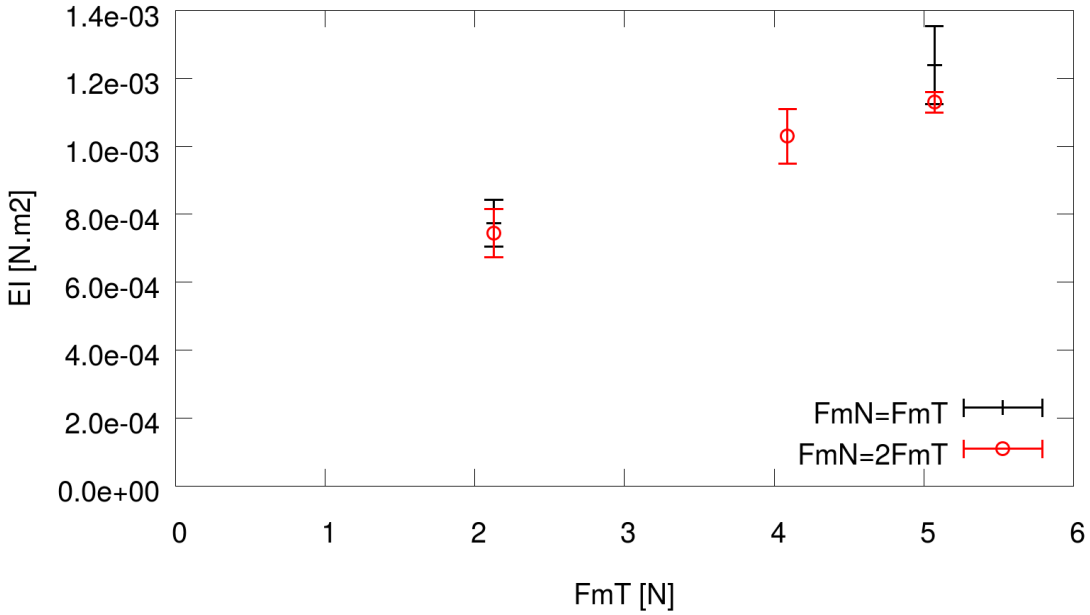

Figure 6.13 – **Double twine *Green* PE netting samples**. Results of the numerical model identified on the experimental biaxial tensile tests; evolutions of the mean of the bending stiffness EI as a function of the applied load Fm_T. For each of the 2 loading types, 5 samples were tested. The vertical solid lines represent the standard deviations. The mesh side length at rest of the samples is 50 mm.

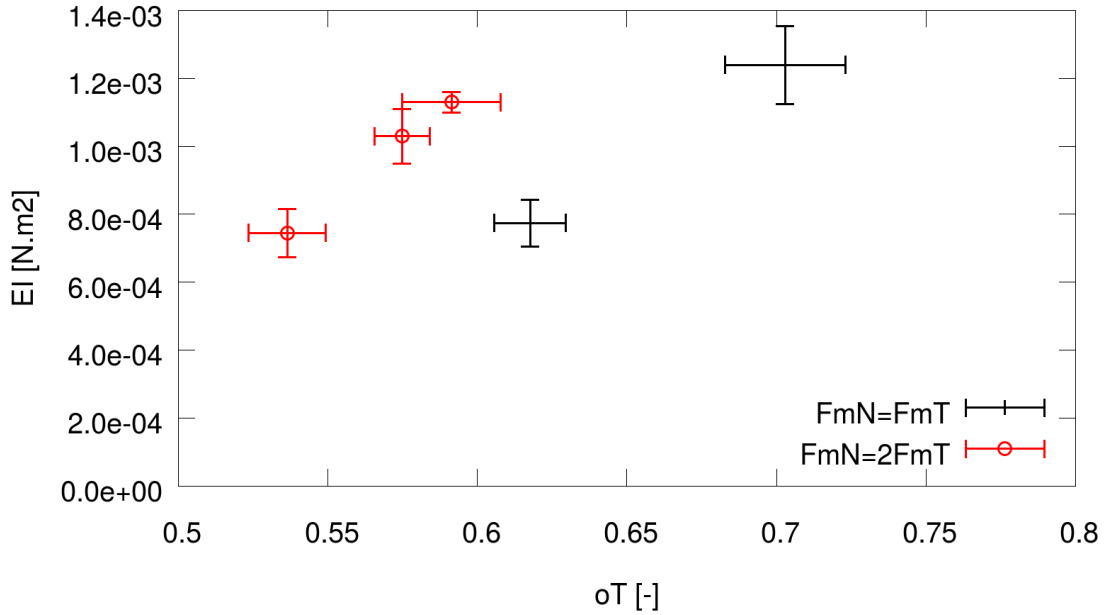

Figure 6.14 – **Double twine *Green* PE netting samples**. Results of the numerical model identified on the experimental biaxial tensile tests; evolutions of the mean of the bending stiffness EI as a function of the opening o_T. For each of the 2 loading types, 5 samples were tested. The vertical and horizontal solid lines represent the standard deviations. The mesh side length at rest of the samples is 50 mm.

6.2 Hexagonal meshes

By modelling the knots by points, thus by assuming a diamond shape, an increase in the identified bending stiffness when the force by mesh Fm_T increased, and different results between the identifications from biaxial tensile tests and suspending tests, were observed (Section 6.1).

This section presents the results of the identifications of the bending stiffness by taking into account the knot sizes in the modelling.

We evaluated the bending stiffness of 4x10- and 5x25-mesh double twine Green PE netting samples with mesh side lengths l_0 of 50 mm or 60 mm. All the simulations were made with our bar element model and the experimental heights were measured after creep stages during 30 minutes.

6.2.1 Evaluation of the size of the knots

Sala et al. (2007) and De la Prada and Gonzales (2014) modelled a knot as a rectangle of size (a, b) from the corners of which the mesh sides emerged (Sections 2.3.1 and 2.3.3). These authors identified the two geometrical parameters a and b with other parameters by inverse identification. Nevertheless, because of the correlations between the parameters, despite different parameter estimation strategies, the estimates were sometimes out of physical limits. Moreover, the estimation of these parameters made the identification program more complex.

We decided to measure experimentally the size of the knot. Because of the complex structure of the knot, and the possible variation in the results, the measurements of the dimensions could be difficult.

It was decided to model only the dimension of the knot in the N-direction. Indeed, the knot is not symmetrical, and the distance in the T-direction between the points from where the mesh sides emerge is different at each side of the knot (Fig.6.15). And, although the possibility to model this asymmetry with the bar element model, it would make it more complex.

In order to measure the dimension of the knot L_{knot} in the N-direction, a sample was widely stretched in the T-direction, and the distance between the points from where the mesh sides emerge was measured (Fig. 6.16).

For the double twine Green PE netting, we measured a knot length equalled to 10 mm.

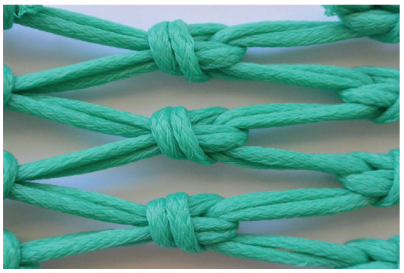

Figure 6.15 – Knots in a double twine *Green* PE netting. The shape of the knot is not symmetrical.

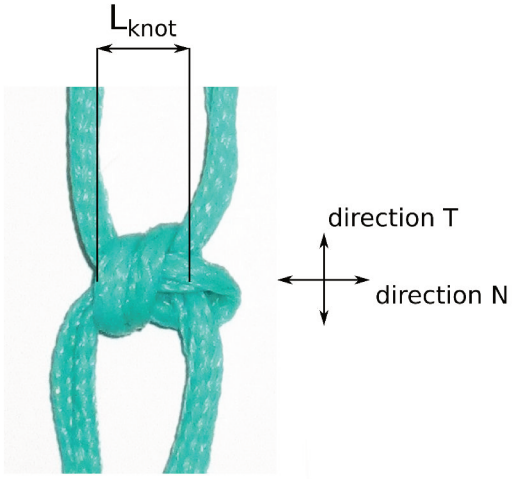

Figure 6.16 – Measurement of the knot length L_{knot} on a netting sample widely stretched in the T-direction.

Regarding the shape and the size of the knot compared to the diameter of the mesh twines, the knot was assumed to be rigid, thus to maintain its shape during the tests (infinite axial and bending stiffnesses).

To validate the measured value, suspended double twine Green PE netting were simulated by identifying the bending stiffness with the bar element model. And the experimental and numerical widths H_{Ntop} (Fig. 6.17) were compared.

The difference between the experimental and numerical values of H_{Ntop}, for two lengths of simulated knots, is presented in Figure 6.18.

We see that the dimensions of the simulated suspended netting samples are closer to the experimental ones in case of a knot length of 10 mm.

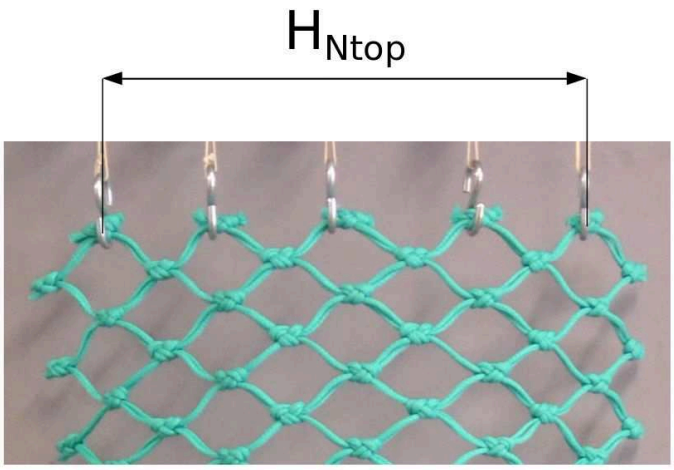

Figure 6.17 – Dimension H_{Ntop} in a suspended netting sample.

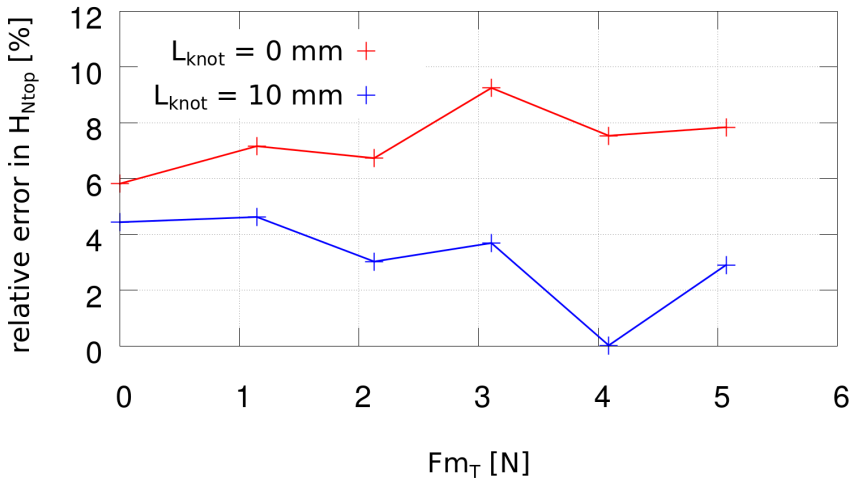

Figure 6.18 – Difference between the experimental and numerical values of H_{Ntop} for two lengths of simulated knots. The relative error is calculated as: $error = (H^{num}_{Ntop} - H^{exp}_{Ntop})/H^{exp}_{Ntop}$ with H^{exp}_{Ntop} and H^{num}_{Ntop} the experimental and numerical values of H_{Ntop} respectively.

6.2.2 Suspending tests

Bending stiffness

The identified bending stiffness in cases of the supending tests on double twine *Green* PE netting as a function of the force by mesh Fm_T and the opening o_T in

the T-direction is shown in Figures 6.19 and 6.20 respectively. In these figures, the influence of the knot length L_{knot} is revealed. As a reminder, the 4x10-mesh netting sample was pre-tensed in the T-direction whereas the 5x25-mesh netting sample was pre-tensed in the N-direction.

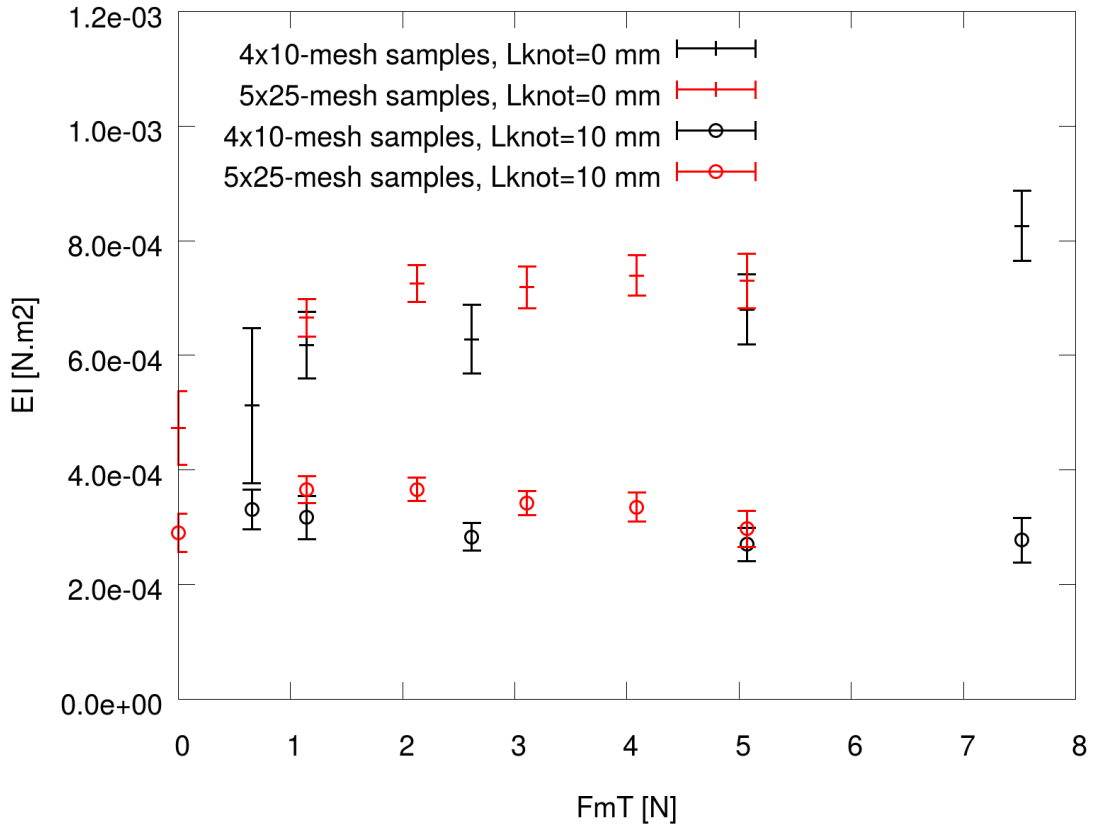

Figure 6.19 – **Double twine *Green* PE netting,** $l_0 = 50\ mm$. Evolution of the identified bending stiffness as a function of the force by mesh in the T-direction Fm_T. The means and the standard deviations are represented. When the knot size is taken into account, the bending stiffness EI is much more constant.

Influence of the experimental mesh side length

Figures 6.21 and 6.22 show the evolution of the identified bending stiffness as a function of the force by mesh Fm_T and the opening o_T in the T-direction respectively in cases of supending tests and two different mesh side lengths. Samples with mesh side length values of 50 mm and 60 mm were simulated. As a reminder, all the samples were pre-tensed in the N-direction, except the 4x10-mesh double twine *Green* PE netting sample with a mesh side length of 50 mm. The length of the

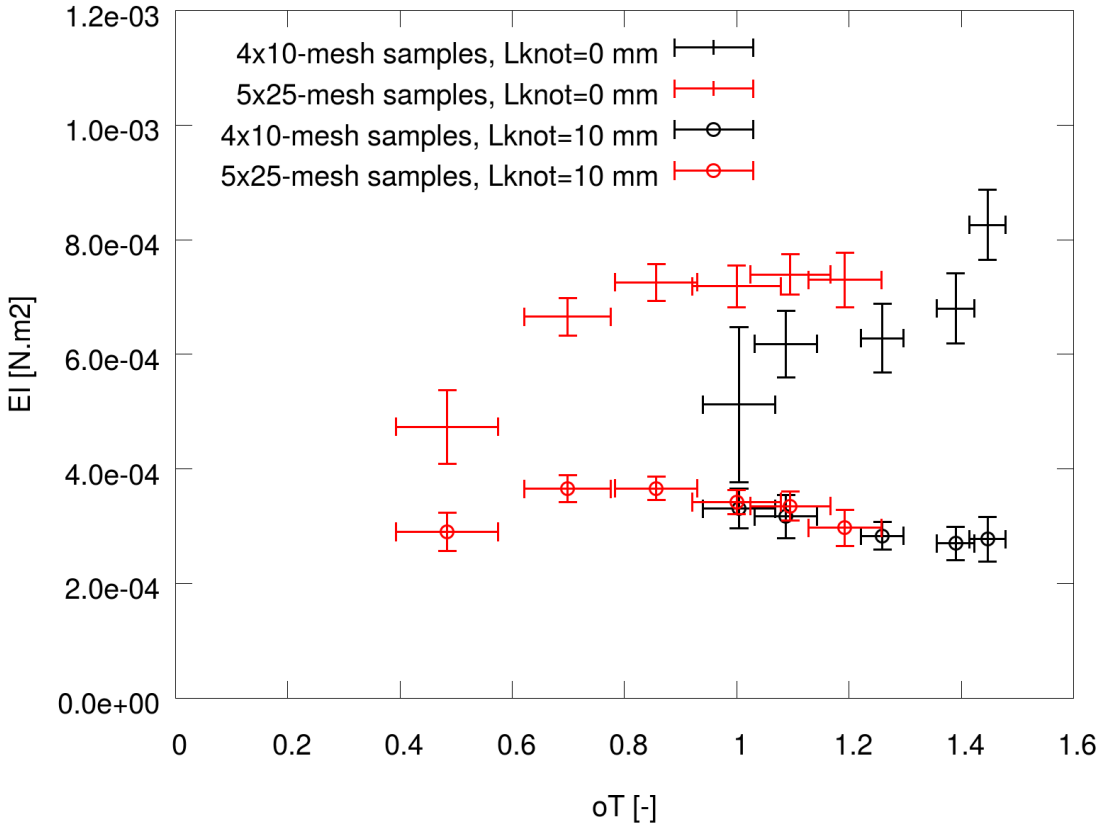

Figure 6.20 – **Double twine *Green* PE netting,** $l_0 = 50\ mm$. Evolution of the identified bending stiffness as a function of the opening in the T-direction o_T. The means and the standard deviations are represented.

numerical knots was 10 mm.

6.2.3 Biaxial tensile tests

Bending stiffness

The identified bending stiffness in cases of the biaxial tensile tests on double twine *Green* PE netting as a function of the force by mesh Fm_T and the opening o_T in the T-direction is shown in Figures 6.23 and 6.24 respectively. In these figures, the influence of the knot length L_{knot} is revealed. The netting samples were submitted to 3 loading types: $Fm_N = 0\ N$, $Fm_N = Fm_T$ and $Fm_N = 2Fm_T$.

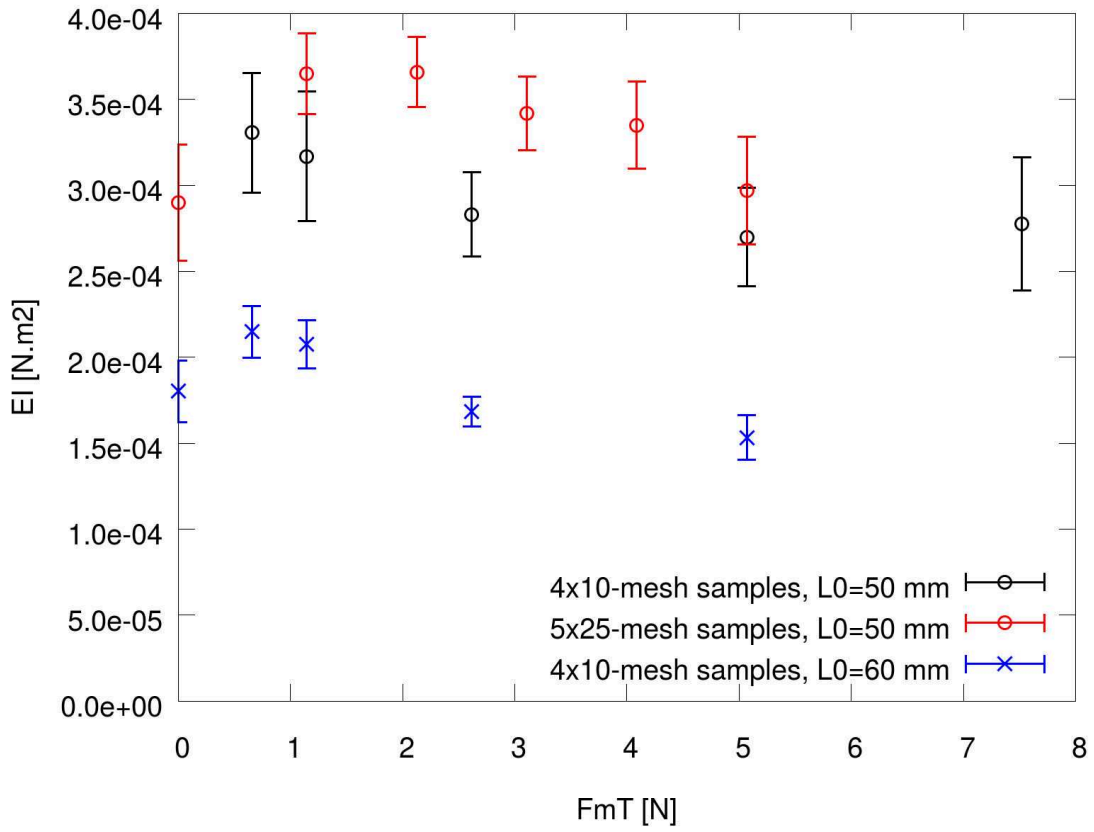

Figure 6.21 – **Double twine *Green* PE netting, comparison of nettings with two different mesh side lengths**. Evolution of the identified bending stiffness as a function of the force by mesh in the T-direction Fm_T. The means and the standard deviations are represented. The modelled knot length value is 10 mm.

Comparison with the identifications on suspended netting samples.

The results of the identifications using experimental data of suspending tests and biaxial tensile tests on double twine *Green* PE netting are compared. The identified bending stiffness is represented as a function of the force by mesh FmT and the opening o_T in the T-direction in Figures 6.25 and 6.26 respectively. The length of the numerical knots was 10 mm.

As seen previously (Section 4.2.4), the curvature $\kappa = 1/R$ can be approximated by assuming that a half mesh side can be modelled by a circle arc with a radius R. The identified bending stiffness, in cases of biaxial tensile tests and suspending tests, is represented as a function of the curvature κ in Figure 6.27.

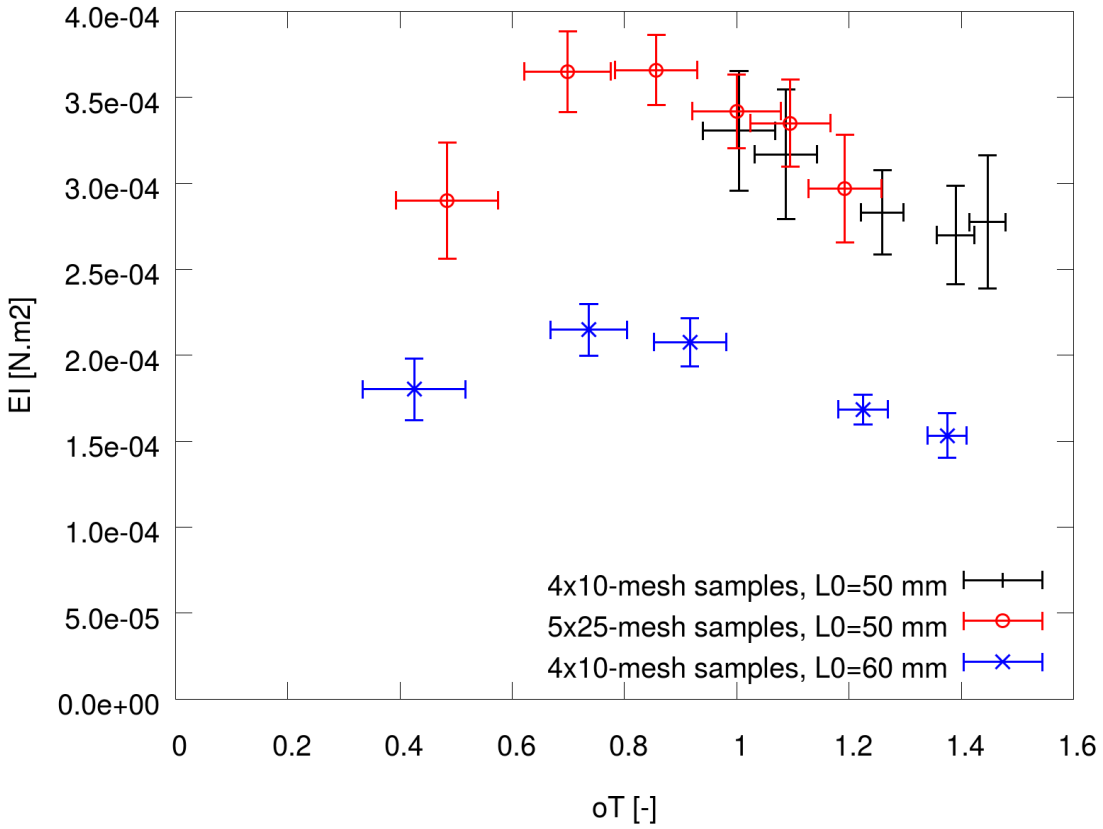

Figure 6.22 – **Double twine *Green* PE netting, comparison of nettings with two different mesh side lengths**. Evolution of the identified bending stiffness as a function of the opening in the T-direction o_T. The means and the standard deviations are represented. The modelled knot length value is 10 mm.

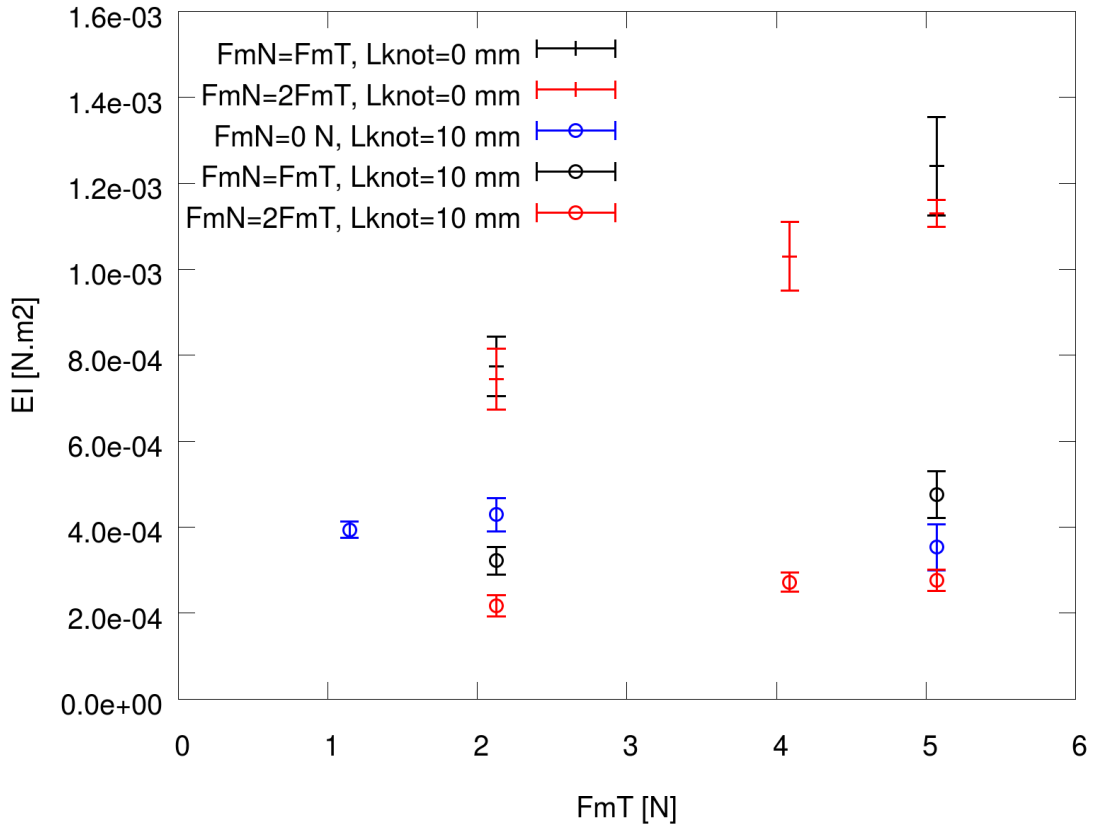

Figure 6.23 – Results of biaxial tensile tests on **double twine *Green* PE netting samples**. Results obtained with the numerical model and the experimental biaxial tensile tests; evolutions of the bending stiffness EI as a function of the applied load Fm_T. For each of the 3 loading types, 5 samples were tested. The mesh side length at rest of the samples is 50 mm. The identified bending stiffness is more constant by taking into account the knot size.

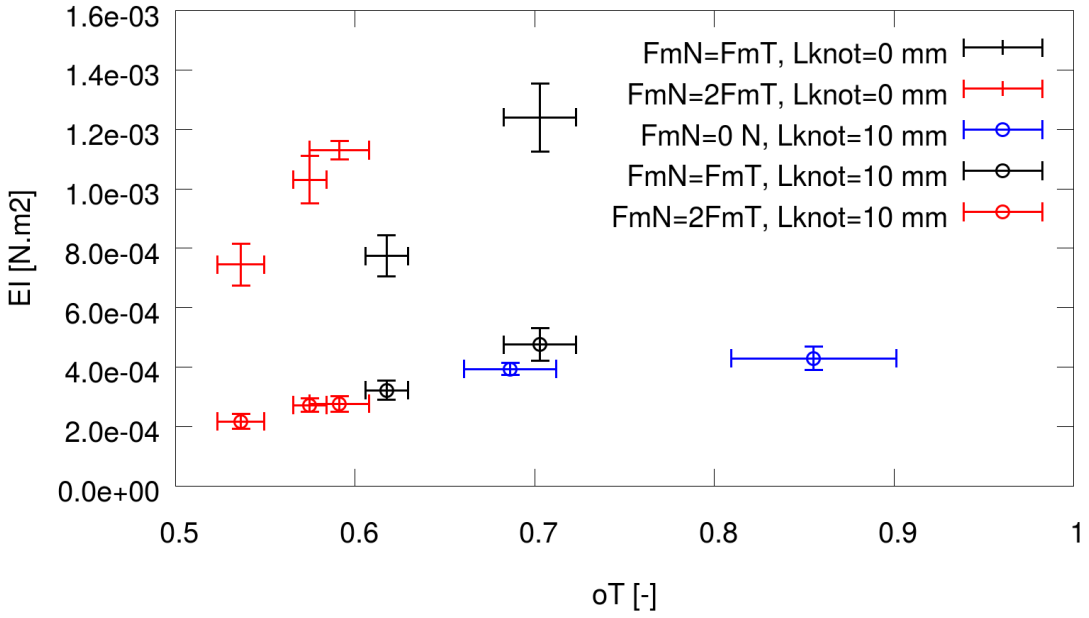

Figure 6.24 – Results of biaxial tensile tests on **double twine *Green* PE netting samples**. Results obtained with the numerical model and the experimental biaxial tensile tests; evolutions of the bending stiffness EI as a function of the opening o_T. For each of the 3 loading types, 5 samples were tested. The mesh side length at rest of the samples is 50 mm.

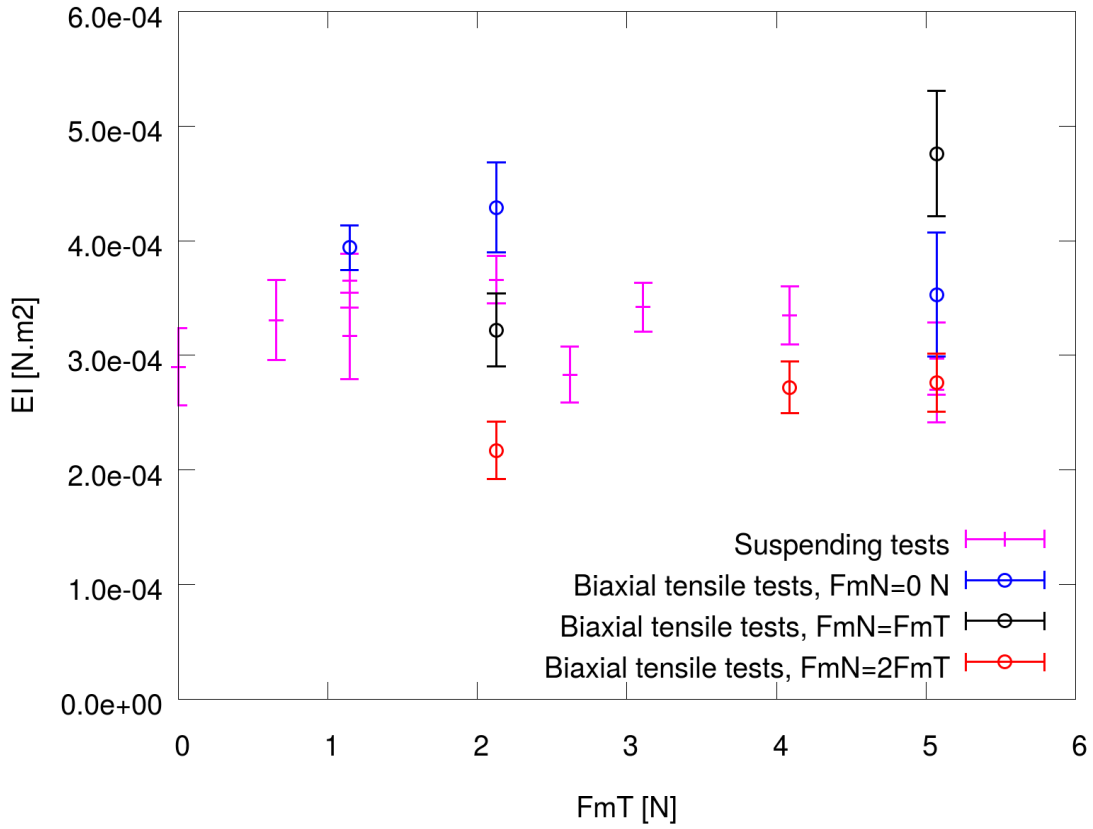

Figure 6.25 – Results of biaxial tensile and suspending tests on **double twine *Green* PE netting samples**. Results obtained with the numerical model and the experimental tests; evolutions of the bending stiffness EI as a function of the applied load Fm_T. For each of the 3 loading types, 5 samples were tested. The mesh side length at rest of the samples is 50 mm. The modelled knot length value is 10 mm.

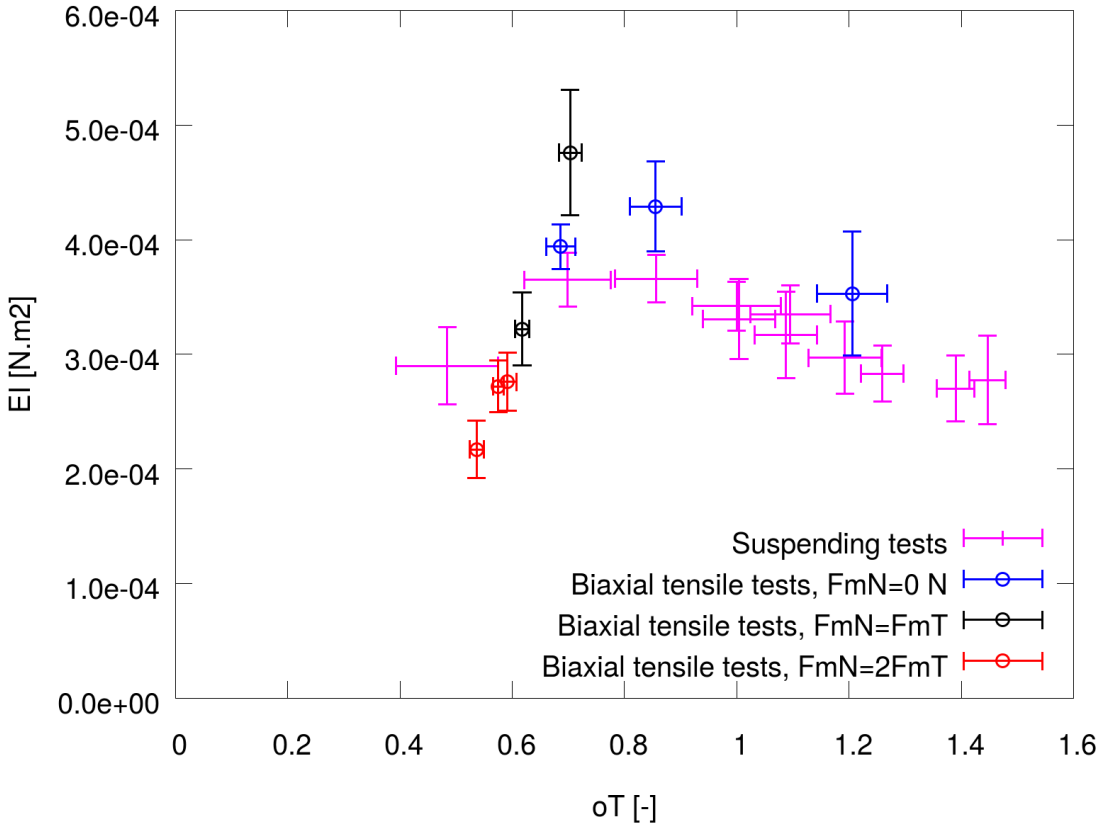

Figure 6.26 – Results of biaxial tensile and suspending tests on **double twine *Green* PE netting samples**. Results obtained with the numerical model and the experimental tests; evolutions of the bending stiffness EI as a function of the opening o_T. For each of the 3 loading types, 5 samples were tested. The mesh side length at rest of the samples is 50 mm. The modelled knot length value is 10 mm.

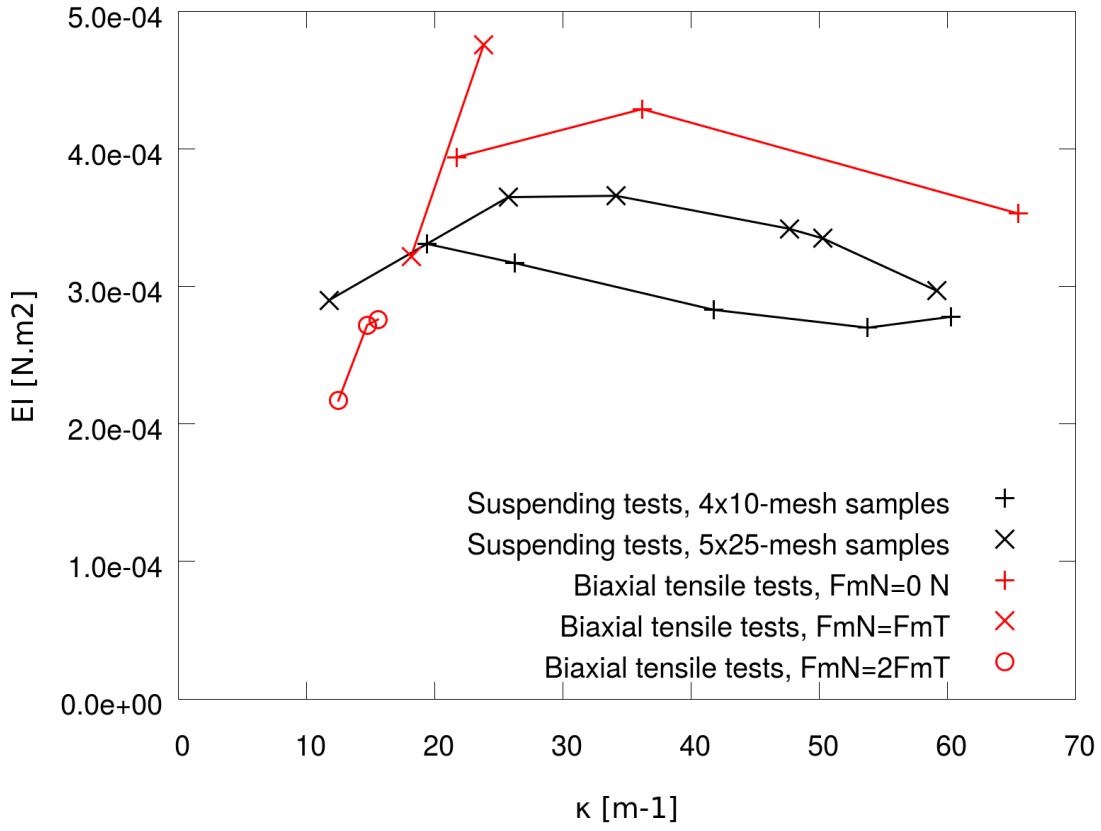

Figure 6.27 – Results of biaxial tensile and suspending tests on **double twine *Green* PE netting samples**. Results obtained with the numerical model and the experimental tests; evolutions of the bending stiffness EI as a function of the curvature κ. In case of suspending tests, 5 4x10-mesh samples and 5 5x25-mesh samples were tested. In case of biaxial tensile tests, for each of the 3 loading types, 5 samples were tested. The mesh side length at rest of the samples is 50 mm. The modelled knot length value is 10 mm.

6.3 Discussion

Using the bar element model and taking into account the knot size, we identify the bending stiffness of 4x10- and 5x25-mesh double twine Green PE netting samples with mesh side lengths l_{ms} of 50 mm or 60 mm.

As expected, the identified bending stiffness is lower when we took into account the length of the knots (Figs. 6.19, 6.20, 6.23 and 6.24). Indeed, the longer the knot in the N-direction is, the shorter the mesh side is and the higher the angle between the mesh side and the N-direction is.

By modelling the knot with a length of 10 mm, we do not observe the same evolution of the identified bending stiffness as by modelling knots by points (diamond mesh). First, the bending stiffness does not increase with the force by mesh Fm_T yet (Figs. 6.19 and 6.23). Moreover, we could assume a constant bending stiffness as a function of the applied force by mesh Fm_T. Then, the evolution as a function of the opening o_T is more consistent. Indeed, Figure 6.20 reveals a continuity between the evolutions of the bending stiffness of the 4x10-mesh samples and the 5x25-mesh samples, in spite of the difference in the pre-tension direction and the sample number of meshes. And the identifications with biaxial tensile tests reveal a continuity between the evolutions of the bending stiffnesses as a function of the opening o_T (Fig. 6.24) of netting samples subjected to 3 different types of biaxial loading. Thus, we could assume that the bending stiffness does not depend on the direction of the pre-tension, on the number of meshes in the suspended sample or on the applied force Fm_N in the N-direction in case of biaxial tensile tests, but the bending stiffness depends on the opening in the T-direction.

Although we expected to identify the same bending stiffness, Figure 6.22 reveals that the bending stiffness of a double twine *Green* PE netting is lower when the mesh side is 60 mm than when the mesh side is 50 mm. This difference may be explained by the effect of the knot on the behaviour of the mesh side and by the interactions, between the two twines constituting the mesh side, which partly depend on the mesh side length. Moreover, although the netting samples have the same structure and are constituted of the same twines, they were submitted to a stretching manufacturing process stage to prevent from knot slides and changes in mesh size after immersion that can be different (temperature, time, tensile forces). Such differences in the process applied to netting panels can provide differences in the mechanical behaviour. We also note that in spite of this bending stiffness level difference, the shape of the evolution of the identified parameter as a function of the opening o_T is very similar for the two types of netting: when the opening in the T-direction increases from 0.46 to 0.8, the bending stiffness increases by up to 19.4 and 26.2 % in cases of a mesh side length of 60 and 50 mm respectively; when the opening in the T-direction increases from 0.8 to 1.37, the bending stiffness decreases by 28.8 and 26.2 % in cases of a mesh side length of 60 and 50 mm respectively.

The results from suspending tests and biaxial tensile tests are close: the evolutions of the bending stiffness EI as a function of the opening o_T are qualitatively and quantitatively close (Fig. 6.26). The value of the bending stiffness identified with measurements coming from the biaxial tensile tests is slightly superior to the one identified with measurements coming from the suspending tests. We could explained this difference by the effect of the biaxial tensile testing machine since the cylindric joints are not perfect, by the biaxial tensile testing setup since the results depend on the application of the load (visco-elasto-plastic mechanical behaviour) and by measurement errors since the knots have not a perfect geometrical shape and the samples in case of biaxial tensile tests have a small number of meshes (3x3-mesh samples).

The curvature in mesh twines was approximated by assuming that a half mesh side can be modelled by a circle arc with a radius R. The evolution of the identified bending stiffness EI as a function of the curvature κ (Fig. 6.27) is consistent with the evolution of the identified bending stiffness EI as a function of the opening o_T (Fig. 6.26). The evolutions of the bending stiffness as a function of the curvature in cases of samples pre-tensed in the T-direction and samples pre-tensed in the N-direction are different.

By assuming that the bending stiffness depends on the opening in the T-direction o_T (related to the opening in the N-direction o_N and to the curvature), and not on the applied force, as shown previously, we could write that tests with larger loading levels should not be useful to evaluate the bending stiffness, that is to say, indirectly, the mesh resistance to opening. Moreover, the measurements on suspending tests allowed us to evaluate a bending stiffness close to the one identified from results of biaxial tensile tests, which validates the identification method using suspending tests.

CHAPTER

7 Conclusions

7.1 Implications of research

The thesis offers scientific advance for the evaluation of the mesh resistance to opening:

- Despite the complex structure and mechanical behaviour of netting, a simple **bar element model** allowing the simulation of netting submitted to large deformations is proposed. The bar element model captured the heterogeneous deformation field of netting whereas the models from the literature do not. It is a compromise between simplicity and accuracy.

- The thesis offers **experimental data** from uniaxial tensile tests, suspending tests and biaxial tensile tests performed on a large range of netting samples: two materials (polyethylene or polyamide), two kinds of mesh sides (single or double twine), three sizes of panel (3x3-, 4x10- and 5x25-mesh panels).

- The **visco-elasto-plastic mechanical behaviour** of netting samples was revealed by experimental results.

- Development of a **more accurate and simpler method** to evaluate the mesh resistance to opening: the method is based on experimental suspension tests as proposed in De la Prada and Gonzales (2013) and requiring a simpler setup than the biaxial setup developed by Sala et al. (2007), and on the bar element numerical model allowing the simulation of non-uniform deformation in suspended panels. This method was submitted and accepted for publication by the "Ocean Engineering" journal (Morvan et al., 2016). Moreover, the method took into account the visco-elasto-plastic mechanical behaviour of netting material: first the measurements were made after creep steps of 30 minutes to reduce the effect of the viscosity; then the applied load was only increased to avoid the hysteresis effect of cyclic loading. The netting samples

were initially submitted to a pre-tension step, introducing a plastic strain but not influencing the identified bending stiffness, to safeguard against knot slippage. We also proposed a method to measure the knot size.

- The relationship between the identified bending stiffness and the mesh opening in the T-direction was shown. Moreover, it was revealed that in case of double twine *Green* PE netting the bending stiffness was **identical** when it was identified using results of experimental **suspending tests** or **biaxial tensile tests**. This result validated the method in case of double twine *Green* PE netting.
- The influence of the numerical-model **knot size** on the evolution of the identified bending stiffness as a function of the applied force or the mesh opening in the T-direction was shown.

7.2 Suggestions for future work

The possible future works are numerous:

- The revealed evolution of the evaluated bending stiffness as a function of the mesh opening and the influence of the mesh side length on the identified bending stiffness showed that the numerical model could be improved by taking into account phenomena influencing the mechanical behaviour of netting. The numerical model could take into account shear and torsion of the twines. The contact-friction interactions in twines could be modelled to provide more accurate numerical results and more elements for the understanding of the mechanical behaviour of netting samples. The experimental data provided by this thesis should be the bases for the improvements of the model.
- Comparisons of the bending stiffnesses identified with measures from suspending tests and biaxial tensile tests on other types of netting could bring a strong validation of the methodology for the identification of the bending stiffness using suspending tests. In the case of results invalidating this assumption, for the sake of simplicity, we would recommend the definition of the bending stiffnesses identified using the method based on suspending tests as a reference in the implementation of a regulation for the mesh resistance to opening in fishing gear.
- The influence of the mesh side length on the identified bending stiffness could be widely studied by testing netting samples with a large range of mesh side length. Tested netting panels with different mesh side lengths should be made of the same twine, and should be made in same conditions (temperature during the stretching step, duration, tensile forces).
- A more accurate model for knots could be proposed. The model could take into account the sizes of the knots in the T- and N-directions, the interactions

between the twines and the knots, the possible change in the section of the twine near the knot, and the asymmetry of the knots.

- Because of the necessity to regulate the selectivity of fishing gear and to be able to identify the mesh resistance to opening with a simple and non-expensive device, we could make the identification software tool, developed in this thesis and based on the bar element model, portable and free. That is to say, to develop a software tool usable from a smartphone for example. In this case, we could expect a wide use of the method presented in this thesis.
- The influence of ageing on netting materials under marine environment on the mesh resistance to opening in fishing gear should be studied. We could imagine a collaboration with fishermen: testing netting before use and after few months of use. Such a work could offer a model to simulate the evolution of the mesh resistance to opening in a fishing gear as a function of its usage.

CHAPITRE

8 Abrégé en français

8.1 Introduction

8.1.1 Contexte général et motivations

La pêche et l'aquaculture constituent d'importantes sources de nourriture et de revenu pour des centaines de millions de personnes dans le monde (FAO, 2016). Néanmoins, nonobstant les progrès dans la réduction de la **surpêche** ces dernières années, plusieurs espèces sont encore actuellement pêchées à des niveaux insoutenables : on estime que 31.4 % des stocks de pêche en 2013 ont été pêchés à un niveau biologique insoutenable et par conséquent surpêchés (FAO, 2016).

Ainsi, pour assurer une pêche durable à long terme et pour réduire les prises non désirées, il est nécessaire de gérer les flottes de pêche et de conserver les stocks de poissons. Dans ce but, la **Politique Commune de la Pêche** (PCP) a introduit une politique de gestion de la pêche (The European Parliament and the European Council, 11th December 2013). La gestion de la pêche comprend des **mesures techniques** pour réglementer l'utilisation des engins de pêche et définir où et quand pêcher. D'après la PCP (The European Parliament and the European Council, 11th December 2013), les mesures techniques peuvent être groupées en mesures qui visent à : limiter les prises de petits poissons (sélectivité intra-espèces), limiter les prises de poissons non désirés (sélectivité inter-espèces), limiter les prises d'espèces protégées (sélectivité inter-espèces), et limiter ou prévenir les dégâts partiels causés aux écosystèmes. La **sélectivité** d'un engin de pêche est sa capacité à n'attraper que les poissons ciblés. Pour réduire les prises de jeunes poissons ou d'espèces non désirées, la PCP réglemente la conception et d'autres caractéristiques techniques de l'équipement (Weissenberger, 2 June 2014). En particulier, la PCP réglemente la taille des mailles pour permettre aux plus petits poissons de s'échapper. Néanmoins, la taille des mailles n'est pas le seul paramètre à déterminer la prise d'un engin de pêche. En effet, l'ouverture des mailles varie durant une opération de pêche, elle dépend

des forces qui s'appliquent sur le filet (taille de la prise, courants, vitesse du bateau, régularité de la traction) et du matériau des fils : l'ouverture des mailles dépend de la résistance à l'ouverture des mailles.

La **résistance à l'ouverture des mailles** est définie par la relation entre l'ouverture de la maille et les forces qui s'y appliquent. Présentement, il n'existe pas de méthodologie simple pour l'évaluation de ce paramètre qui pourrait être la base d'une législation sur la pêche. En effet, la résistance à l'ouverture des mailles, qui dépend de plusieurs paramètres, est assez difficile à évaluer.

Les méthodes existantes pour l'évaluation de la résistance à l'ouverture des mailles de filets sont basées sur la résolution de **problèmes d'identification inverse**. La méthode d'identification inverse consiste à trouver les entrées du modèle numérique, en se basant sur les réponses expérimentales force-déplacement et sur les conditions limites (Uhl, 2007). Dans le cadre de cette étude, les entrées recherchées doivent être liées à la résistance des mailles à l'ouverture.

La structure mécanique des fils constituant le filet est complexe. Un échantillon de filet peut être décrit comme un assemblage de mailles, et les mailles peuvent être considérées comme un assemblage de côtés de maille et, possiblement, de noeuds (Fig. 8.1). Plusieurs approches par modèles sont possibles, selon l'élément de base étudié : l'échantillon de filet, la maille ou le côté de maille.

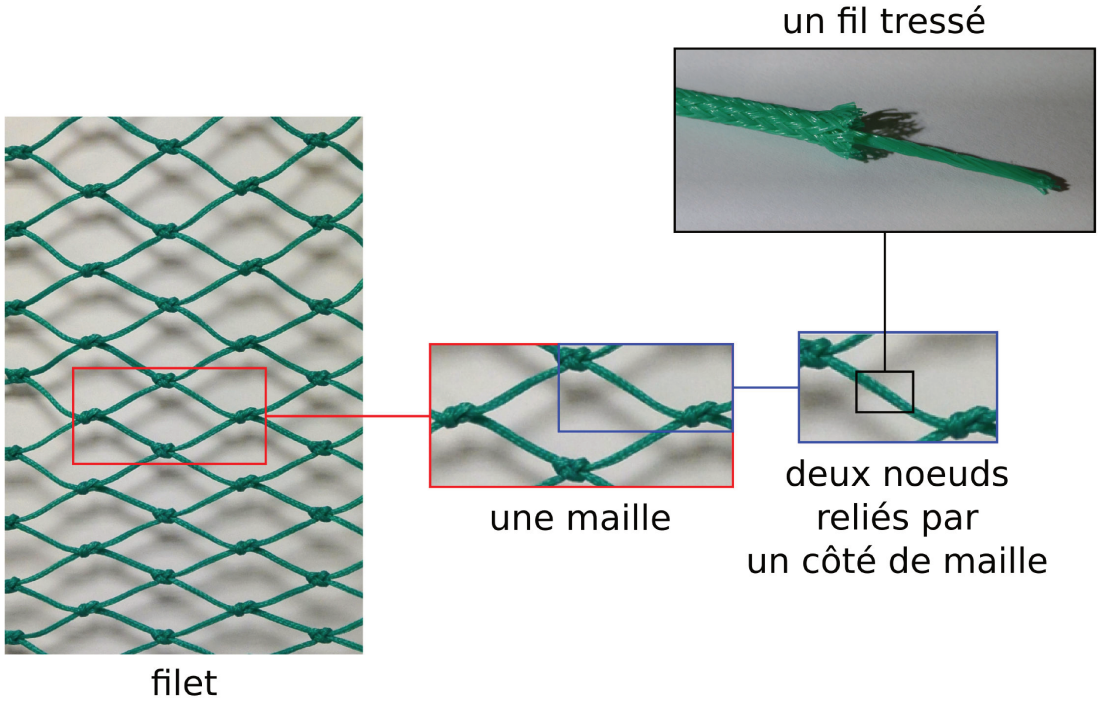

FIGURE 8.1 – Un filet est un assemblage de mailles, constitué de côtés de maille et de noeuds.

Priour (2013), O'Neill (2002) et De la Prada and Gonzales (2013) ont proposé de modéliser la réponse force-déplacement d'un côté de maille. En considérant qu'un côté de maille se comporte comme une poutre (O'Neill (2002), Sala et al. (2007), De la Prada and Gonzales (2014), Priour (2013)), la **raideur en flexion** des côtés de maille est apparue comme une bonne représentation de la résistance à l'ouverture des mailles. En effet, il a été montré qu'une augmentation de la raideur en flexion d'un fil se traduisait par une augmentation de la résistance mécanique à l'ouverture des mailles (Sala et al., 2007). De plus, l'influence de la raideur en flexion du filet sur la sélectivité du chalut a été démontrée (Boerema, 1956).

Ensuite, la forte influence du **cul de chalut** sur la sélectivité du chalut a été démontrée (Robertson and Stewart, 1988), même si la sélectivité des autres parties du chalut est de plus en plus prise en compte (Broadhurst et al., 2015). Des études antérieures ont expliqué l'influence de la raideur en flexion des côtés de maille sur le comportement mécanique, et donc sur la sélectivité des culs de chalut (Herrmann et al., 2006; Sala et al., 2007). De la même manière, Moderhak (2007) a démontré théoriquement l'influence de la taille de maille et de la raideur en flexion des côtés de maille sur la forme d'un cul de chalut et sur sa sélectivité. A partir d'une étude théorique, O'Neill (2003) a montré que l'augmentation de la raideur en flexion dans le fil réduit le diamètre du cul de chalut, et donc l'ouverture latérale des mailles. Dans le cas des fermes piscicoles, la raideur en flexion aurait des effets significatifs : durant la traction des cages aquacoles, les panneaux de filets parallèles ou quasiment parallèles à l'écoulement de l'eau subissent des vibrations significatives, ce qui est en partie déterminé par la raideur en flexion du filet (Johnson and Balash, 2015). En outre, la raideur en flexion est un facteur critique pour assurer des évaluations de trainées de chaluts précises par simulation (Balash et al., 2016).

En considérant ces éléments, et le fait que les culs de chalut sont fabriqués à partir de matériaux plus rigides (Herrmann et al., 2006, 2013), il est intéressant de pouvoir mesurer la raideur en flexion des côtés de maille dans les filets de pêche et en particulier dans les filets de culs de chalut.

Des modèles et des méthodes ont déjà été proposés pour évaluer la raideur en flexion dans les filets de pêche. Les méthodes les mieux établies se basent sur la théorie des poutres (Sala et al., 2007; De la Prada and Gonzales, 2013; Priour and Cognard, 2011). Néanmoins, les méthodes existantes ne permettent pas l'identification de la résistance à l'ouverture des mailles avec une méthode simple ou ne prennent pas suffisamment en compte la complexité du comportement mécanique du filet. La méthode présentée dans Sala et al. (2007) nécessite un dispositif complexe et coûteux. De la Prada and Gonzales (2013) proposent une méthode basée sur des essais de suspension, mais des hypothèses fortes sont faites. De plus, les stratégies d'identification de Sala et de De la Prada sont discutables du fait des corrélations entre les paramètres géométriques. Balash (2012) utilise le modèle poutre de O'Neill (2002) avec ses limites. Pour terminer, la méthode proposée par Priour and Cognard

(2011) nécessite un filet avec des mailles fermées et ne prend pas en compte la taille des noeuds.

8.1.2 Objectifs

Les objectifs de cette thèse sont de développer et d'évaluer une **méthodologie pour l'évaluation de la résistance à l'ouverture des mailles dans les filets de pêche**, et plus largement, dans les structures en filet. Cette thèse a pour objectif de proposer une méthode expérimentale simple qui ne nécessiterait pas d'équipements coûteux pour pouvoir être déployée facilement dans les laboratoires et dans l'industrie de la pêche, combinée avec un modèle numérique capable de représenter le comportement mécanique non-linéaire d'un panneau de filet testé. Comme dans les méthodologies existantes, la méthode d'identification inverse devrait être utilisée : la raideur en flexion du modèle devrait être ajustée pour que les résultats des simulations numériques concordent avec les résultats expérimentaux.

8.1.3 Aperçu de la thèse

Ce manuscrit est divisé en cinq chapitres. Dans le **premier chapitre**, nous présentons **les méthodes existantes** pour l'évaluation de la raideur en flexion d'un fil. Tout d'abord, trois modèles numériques de déformation d'un côté de maille sont présentés : le modèle analytique d'O'Neill (2002), le modèle ajusté de De la Prada and Gonzales (2013) et le modèle éléments finis triangulaires de Priour (2013). Ensuite, quatre méthodes expérimentales pour l'évaluation de la raideur en flexion sont présentées : la méthode basée sur le prototype ROD-m de Sala et al. (2007), la suspension d'un échantillon cylindrique de Balash (2012), la suspension simple d'un échantillon de filet de De la Prada and Gonzales (2014), et le filet en porte-à-faux de Priour and Cognard (2011). Finalement, les méthodes expérimentales et les modèles présentés sont discutés.

Le **second chapitre** traite de la **méthode expérimentale** utilisée et développée par cette thèse, et des échantillons de filets. Trois types d'expériences ont été réalisés pour évaluer la raideur en flexion des fils : un essai de traction uniaxiale sur une machine de traction classique, un essai de suspension du même type que De la Prada and Gonzales (2014), et un essai de traction biaxiale proche de celui de Sala et al. (2007). Un large éventail de filets de pêche communément utilisés dans les culs de chalut ont été testés : quatre matériaux (trois types de polyéthylène, un polyamide), des côtés de maille simples et doubles, trois tailles d'échantillons (échantillons 3x3, 4x10 et 5x25 mailles), et plusieurs longueurs de côtés de maille (30, 40, 50 et 60 mm). Finalement, la raideur axiale d'un fil en polyéthylène a été évaluée.

Dans le **troisième chapitre**, les **résultats expérimentaux** sont donnés. Les objectifs de ce chapitre sont de présenter le comportement mécanique d'échantillons de filets et de comparer les résultats obtenus avec les trois types d'expériences. De plus, la déformation dans les échantillons de filets et la variation dans les résultats sont montrées.

Le **quatrième chapitre** décrit les **méthodes numériques** développées durant cette thèse. Tout d'abord, quatre modèles basés sur la théorie des poutres sont présentés : un modèle quasi-analytique pour les côtés de maille, le modèle poutre de Timoshenko du logiciel Abaqus, un modèle éléments finis basé sur des poutres 2D en formulation corotationnelle et un modèle éléments barres. Les méthodes d'identification inverse sont ensuite expliquées. Au regard des méthodes existantes pour l'évaluation de la raideur en flexion des côtés de maille dans les panneaux de filets, les avantages possibles des méthodes éléments finis sont montrés dans le chapitre suivant, particulièrement en utilisant le modèle éléments barres proposé.

Dans le **cinquième chapitre**, les **résultats numériques** sont présentés et discutés. Tout d'abord, les raideurs en flexion identifiées en supposant que les mailles ont une forme de losange sont présentées. L'influence des paramètres sur la raideur en flexion numérique est étudiée : la viscosité du matériau, la force appliquée sur les mailles, l'ouverture des mailles, la taille des échantillons, et les conditions limites. En ce qui concerne les résultats, il a été décidé de modéliser la taille des noeuds en utilisant des mailles hexagonales. Les résultats avec des mailles hexagonales sont présentés et discutés.

Enfin, le manuscrit se termine par une **conclusion** qui vise à présenter une analyse des résultats exposés dans le manuscrit, une discussion à propos de la validité de la méthode proposée et des suggestions pour des travaux futurs.

Une partie de cette thèse a été soumise et acceptée pour publication par le journal "Ocean Engineering" (Morvan et al., 2016).

8.1.4 Contributions principales de cette thèse

- Des essais de tractions uniaxiales, des essais de suspension et des essais de tractions biaxiales ont été réalisés sur un large éventail d'échantillons de filets : deux matériaux (polyéthylène ou polyamide), deux types de côtés de maille (simple ou double fil), trois tailles d'échantillon (3x3, 4x10 and 5x25 mailles).

- Le comportement mécanique des échantillons de filets a été révélé par les résultats expérimentaux et pris en compte pour l'évaluation de la raideur en flexion dans les échantillons de filets.

- Un modèle éléments finis, utilisant des éléments barres et basé sur la théorie des poutres, a été développé. Un outil a été développé pour simuler, en utilisant ce modèle éléments finis, les essais sur les échantillons de filets, et pour identifier, en utilisant l'identification inverse et les résultats expérimentaux, la raideur en flexion dans les échantillons de filets. Le modèle reproduit le champ de déformation hétérogène des échantillons de filets durant les essais de suspension.

- Une méthodologie pour l'évaluation de la résistance à l'ouverture des mailles a été proposée et évaluée. Elle se base sur un modèle éléments finis libre de droits et sur un dispositif expérimental simple et peu coûteux. Des méthodes de mesures ont été proposées pour éviter des incohérences dans les résultats d'identification qui proviendraient des corrélations entre certains paramètres.

8.2 Méthodes existantes pour l'évaluation de la raideur en flexion des fils

Trois modèles de maille de filet sont présentés (partie 2.1) : le modèle de Priour (2013), le modèle analytique d'O'Neill (2002) (avec sa solution asymptotique) et le modèle basée sur les interpolations de De la Prada and Gonzales (2013). Les trois modèles sont simples et offrent des temps de calcul numérique plus courts que dans le cas de modèles éléments finis. Ce sont trois modèles facilement utilisables pour la simulation de filets.

Priour (2013) a proposé une méthode éléments finis, basée sur des éléments triangulaires, pour modéliser le comportement mécanique des filets (partie 2.2). Son outil est capable de modéliser des culs de chalut avec des temps de calcul intéressants. Néanmoins, des travaux sur la modélisation de la raideur en flexion des côtés de maille et sur l'estimation du couple entre deux éléments triangulaires sont nécessaires pour simuler avec précision l'effet de la raideur en flexion.

Quatre méthodes expérimentales existantes pour l'évaluation de la raideur en flexion sont présentées (partie 2.3) : la méthode basée sur le prototype de machine de traction biaxiale ROD-m de Sala et al. (2007), la suspension d'un échantillon en forme de cul de chalut (cylindre) de Balash (2012), la suspension d'un panneau de filet de De la Prada and Gonzales (2014) et l'échantillon en porte-à-faux de Priour and Cognard (2011).

Le modèle analytique présenté par O'Neill (2002) est utilisé dans les méthodes proposées par Sala et al. (2007), Balash (2012) et De la Prada and Gonzales (2014). Néanmoins, O'Neill suppose que les côtés de maille ne sont pas extensibles, et l'approximation qu'il propose n'est valide que dans le cas d'une raideur à la flexion

relativement faible ou d'un chargement élevé.

Les essais de traction biaxiale présentés par Sala et al. (2007) nécessitent un équipement complexe et coûteux (pas encore commercialisable) alors que De la Prada and Gonzales (2014) proposent de suspendre des échantillons de filets. Malgré le coût peu élevé de la méthode proposée par De la Prada, elle suppose que la déformation dans les panneaux de filets suspendus est homogène, ce qui représente une hypothèse forte.

Sala et al. (2007) et De la Prada and Gonzales (2014) considèrent la taille des noeuds dans les filets : la taille est identifiée par identification inverse, la structure des noeuds et la dispersion dans les résultats rendant la mesure expérimentale des dimensions difficile. Cependant, les résultats des identifications ne sont pas toujours cohérents en raison des corrélations fortes entre les paramètres géométriques.

Priour and Cognard (2011) ne prennent pas en compte la taille des noeuds, contrairement à Sala et De la Prada. Il serait nécessaire d'étudier l'effet des dimensions des noeuds sur les résultats d'identification. Notons, de plus, la nécessité d'utiliser des filets à mailles fermées dans la méthode proposée par Priour and Cognard (2011).

La méthode présentée par Balash (2012) est intéressante car elle utilise des essais d'échantillons de filets cylindriques, similaires en forme aux culs de chalut. Néanmoins, en choisissant d'utiliser la solution asymptotique proposée par O'Neill, l'auteur fait des hypothèses fortes : pas d'extension des fils, précision seulement lorsque la flexion est relativement faible ou que le chargement est élevé. La méthode pourrait être étudiée plus en profondeur (plus d'essais expérimentaux, de descriptions des résultats et des identifications).

Les études existantes donnent des informations pour la mise en place d'une méthodologie permettant l'évaluation de la raideur en flexion des côtés de maille. Tout d'abord, l'élongation, la flexion et la torsion des côtés de maille pourraient être modélisés. Ensuite, la méthode expérimentale peu chère proposée par De la Prada and Gonzales (2014) pourrait être utilisée avec un modèle numérique simulant la déformation non uniforme dans les échantillons suspendus. Puis l'effet de la taille des noeuds dans le modèle numérique sur la résistance à l'ouverture des mailles identifiée pourrait être étudiée. Une méthode permettant la mesure expérimentale de la taille des noeuds pourrait être proposée. Enfin, la méthode proposée devrait être validée par des essais sur un large éventail de filets de différents matériaux, de différentes tailles, avec des côtés de maille de différentes longueurs, et à différents niveaux de chargement.

8.3 Méthode expérimentale et échantillons de filets

Dans cette partie, la méthode expérimentale et les échantillons de filets utilisés sont présentés. Une méthode d'évaluation de la raideur axiale d'un fil tressé est présentée.

8.3.1 Expériences

Trois types d'essais ont été effectués pour évaluer la raideur en flexion des côtés de maille : des essais de traction uniaxiale sur machine de traction classique (partie 3.1.1), des essais de suspension (partie 3.1.2) du même type que ceux proposés par De la Prada and Gonzales (2014), et des essais de traction biaxiale (partie 3.1.3) du même type que ceux proposés par Sala et al. (2007).

Dans le cas d'un essai de traction uniaxiale, l'échantillon est monté sur une machine de traction classique, équipée d'un capteur de force. L'essai est contrôlé par déplacement de la traverse de la machine et les étapes de relaxation sont effectuées par blocage du déplacement de la traverse. Un extensomètre laser permet de mesurer la hauteur de la maille au centre de l'échantillon (L_{mesh} sur la figure 8.2).

Dans le cas d'un essai de suspension, l'échantillon rectangulaire est suspendu par une extrémité de telle manière que la direction T du filet est verticale. Le filet est soumis à son poids propre et à des forces par maille Fm_T appliquées dans la direction T sur les noeuds les plus bas de l'échantillon (Figure 8.3). Quand un panneau est suspendu, les positions de tous ses noeuds sont mesurées en utilisant une caméra et un logiciel conçu et développé au laboratoire et permettant l'enregistrement des images à une fréquence choisie.

Dans le cas d'un essai de traction biaxiale, le filet de taille 3x3 mailles est monté sur une machine et soumis à des forces dans les directions T et N simultanément. La machine est symétrique dans les directions T et N. Les conditions limites sont décrites sur la figure 8.4. De la même manière que lors des essais de suspension, les positions de tous les noeuds sont mesurées. Le dispositif expérimental mis en place et utilisé ne permet probablement pas des mesures d'efforts et de déplacements aussi précis qu'avec le protype ROD-m de Sala et al. (2007). Cependant, cette machine coûte, très certainement, moins cher et la dispersion dans les résultats obtenus avec des échantillons et des conditions expérimentales similaires permet de montrer une précision cohérente (chapitre 4).

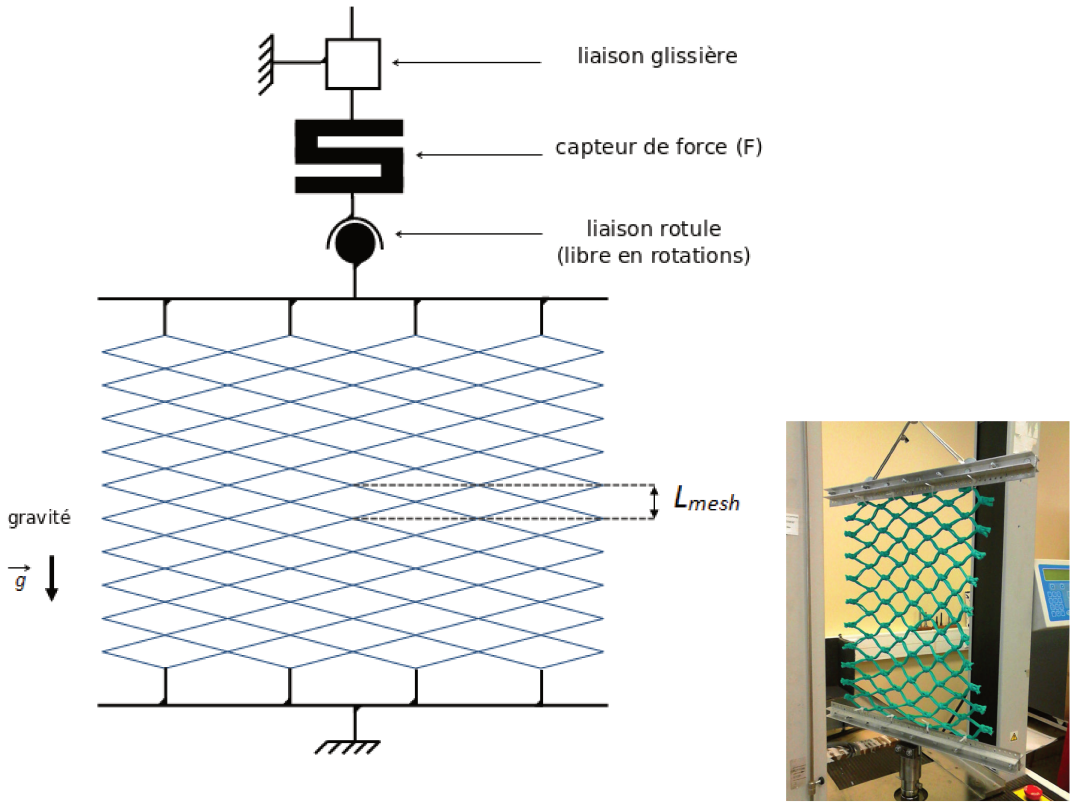

FIGURE 8.2 – Schéma (à gauche) et photographie (à droite) de l'essai de traction uniaxiale. La hauteur L_{mesh} de la maille au milieu de l'échantillon de filet est mesurée.

8.3.2 Échantillons de filet pour les expériences

Un large éventail de filets de pêche communément utilisés dans les culs de chalut ont été testés : quatre matériaux (trois types de polyéthylène, polyamide), côtés de maille simples et doubles, trois tailles d'échantillons (échantillons 3x3 mailles pour les essais de traction biaxiale, 4x10 et 5x25 mailles pour les essais de traction uniaxiale et les essais de suspension), et plusieurs longueurs de côtés de maille (30, 40, 50 et 60 mm).

Huit types d'échantillons ont été utilisés :

- Filets à mailles simples, en PE *vert*, avec une longueur de côté de maille de 40 *mm*, de taille 4x10 mailles (partie 3.2.4)
- Filets à mailles doubles, en PE *vert*, avec une longueur de côté de maille de 49 *mm*, de taille 3x3 mailles (partie 3.2.4)
- Filets à mailles doubles, en PE *vert*, avec une longueur de côté de maille de 49 *mm*, de taille 4x10 mailles (partie 3.2.4)

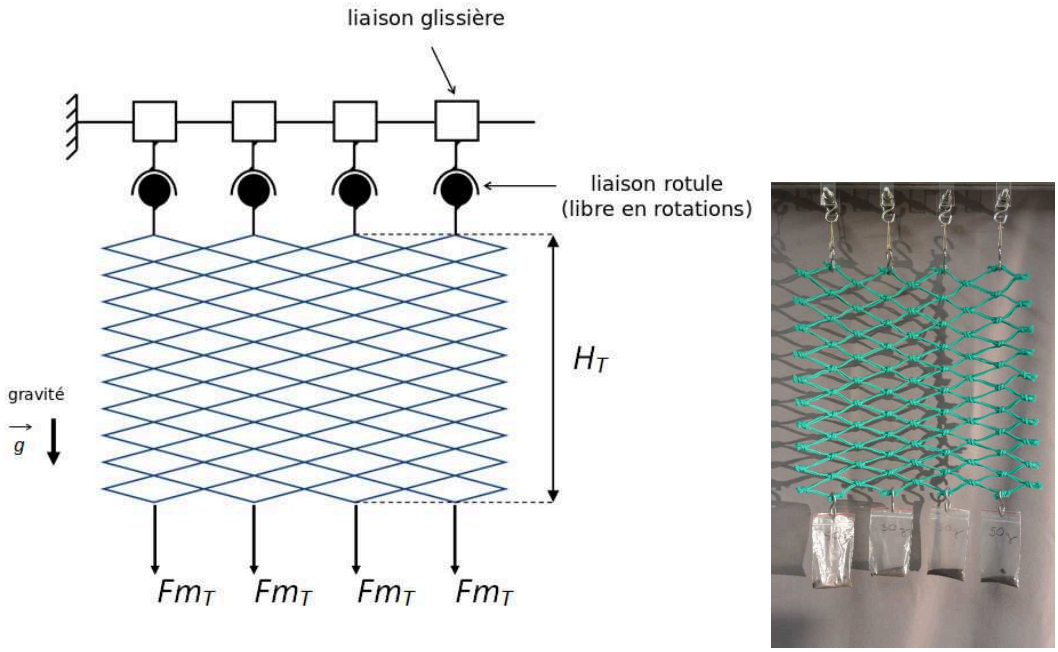

FIGURE 8.3 – Schéma (à gauche) et photographie (à droite) de l'essai de suspension. Le panneau de filet est suspendu par l'une de ses extrémités et soumis à son poids propre et aux forces Fm_T appliquées aux noeuds les plus bas. Fm_T est appelé effort par maille dans la direction T.

- Filets à mailles doubles, en PE *vert*, avec une longueur de côté de maille de 49 mm, de taille 5x25 mailles (partie 3.2.4)
- Filets à mailles doubles, en PE *vert*, avec une longueur de côté de maille de 60 mm, de taille 4x10 mailles (partie 3.2.4)
- Filets à mailles simples, en PE *Breztop*, avec une longueur de côté de maille de 40 mm, de taille 4x10 mailles (partie 3.2.5)
- Filets à mailles simples, en PE *Brezline*, avec une longueur de côté de maille de 60 mm, de taille 4x10 mailles (partie 3.2.6)
- Filets à mailles simples, en PA, avec une longueur de côté de maille de 30 mm, de taille 4x10 mailles (partie 3.2.7)

8.3.3 Évaluation de la raideur axiale d'un fil tréssé

Des essais de traction ont été effectués pour évaluer la raideur en traction des fils constituant les filets étudiés. En raison du comportement mécanique visco-elasto-plastique du polyéthylène, l'évaluation de la raideur axiale n'est pas évidente. L'évaluation de la raideur axiale par mesure des modules de comportement axial à court-

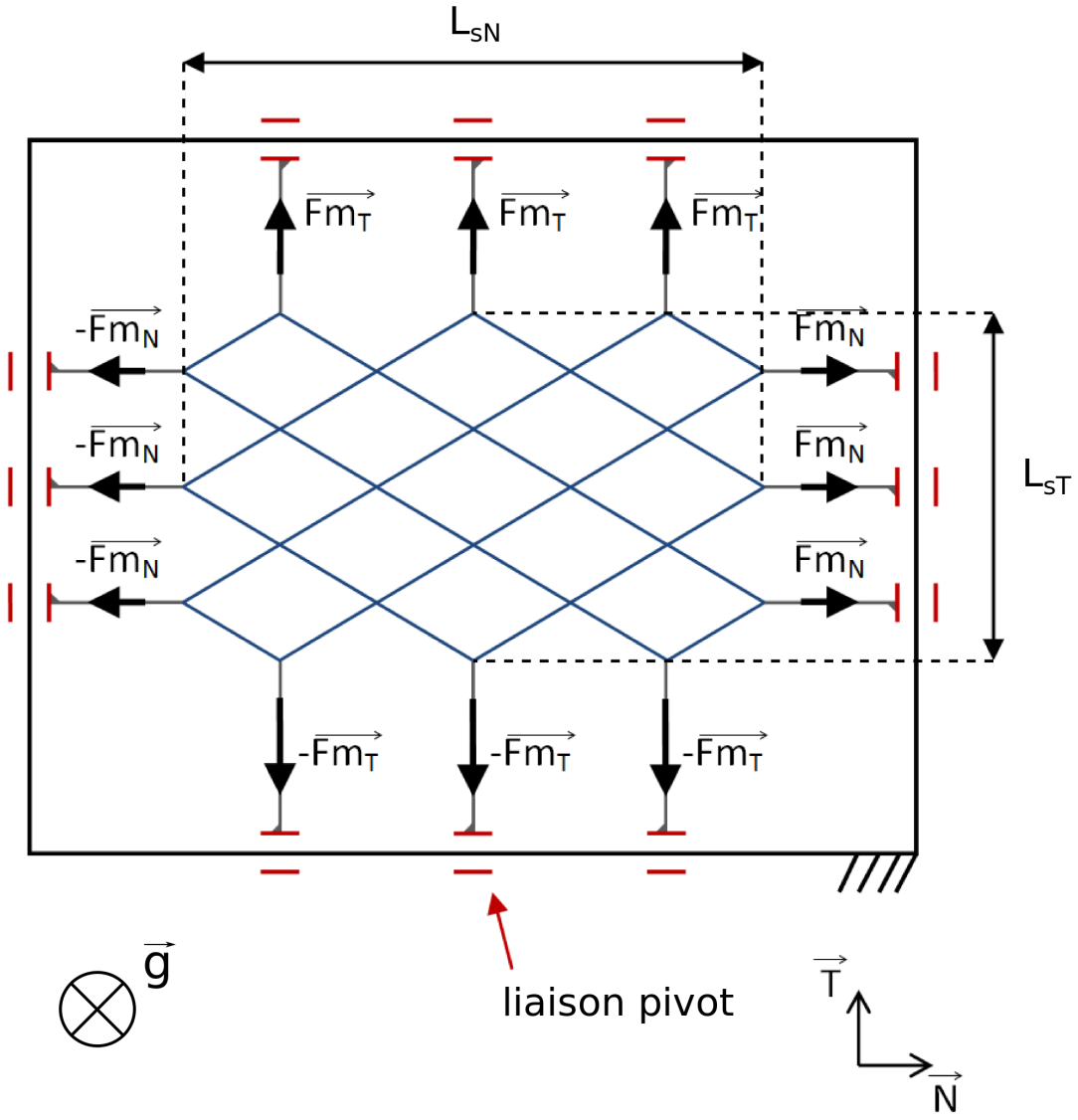

FIGURE 8.4 – Schéma de l'essai de traction biaxiale. L'échantillon de filet de taille 3x3 mailles, monté sur la machine, est soumis à des forces par maille Fm_T et Fm_N dans les directions T et N respectivement. L_{sT} et L_{sN} sont les longueurs de l'échantillon dans les directions T et N respectivement.

terme (Bles et al., 2009) et à long-terme est présentée.

Le module de raideur axial à court-terme augmente lorsque la déformation axiale augmente. On peut supposer que, dans le cas des fils tressés en polyéthylène, pour une déformation logarithmique faible (<0.055), le module de raideur axial à court-terme est inférieur à 14000 N.

Pour évaluer le module de raideur axial à long-terme, nous supposons que l'effet de la viscosité est annulé à la fin des étapes de relaxation. Une raideur axiale de 2444 N est obtenue.

Les résultats obtenus (à long terme) sont utilisés dans les modèles numériques pour évaluer l'effet de la viscosité durant les essais de suspension, de traction uniaxiale ou de traction biaxiale.

8.4 Résultats expérimentaux

Les essais de traction uniaxiale et de suspension fournissent des résultats révélant le comportement visco-elasto-plastique des filets.

La viscosité est révélée par l'évolution des forces durant les étapes de relaxation (Fig. 4.1), la réponse en force durant l'essai de traction cyclique et l'évolution de la hauteur totale de l'échantillon H_T durant les étapes de fluage (Figs. 4.7 à 4.9). L'élasticité non-linéaire est montrée sur les figures 4.2, 4.3 et 4.5.

La figure 4.1 montre que l'ouverture o_T reste élevée à la décharge (avec des étapes de relaxation de 15 minutes). Ainsi, la maille ne revient pas à son état initial. La structure présente une déformation permanente (ou viscosité à long-terme).

Au regard de l'évolution de la hauteur totale H_T des échantillons durant les étapes de fluage (Figs. 4.7 à 4.9), nous pouvons supposer que dans le cas des essais de suspension sur filets en PE *vert*, PE *Breztop* ou PE *Brezline*, la contribution de la composante mécanique visqueuse de la déformation est annulée après 30 minutes de fluage. Dans le cas de filets en PA, l'effet de la viscosité n'est rapidement plus observable.

Les figure 4.7 à 4.15 montrent une faible dispersion dans les résultats fournis par les essais de suspension : les résultats obtenus avec différents échantillons provenant du même type de filet sont très proches. De plus, la déformation dans les filets est clairement non uniforme. Ce point est important : les essais de suspension sont simples à mettre en oeuvre mais la déformation dans un échantillon suspendu n'est pas uniforme.

La figure 4.16 montre que l'étape de prétension dans la direction T cause une déformation permanente dans cette direction. Lorsque les résultats des essais sur des filets avec des côtés de maille de 50 mm et des essais sur des filets avec des côtés de maille de 60 mm, constitués de fils identiques, sont comparés, il apparaît que dans le cas des côtés de maille de 50 mm, la force par maille Fm_T appliquée augmente plus vite lorsque l'ouverture o_T augmente. Donc la résistance à l'ouverture des mailles

dans le cas de côtés de maille de 50 mm est plus grande que dans le cas de côtés de maille de 60 mm. Cette différence peut être expliquée par la différence géométrique de la structure, l'influence des noeuds sur le comportement mécanique des filets, et/ou les intéractions différentes entre les fils constituant le côté de maille. En effet, dans le cas d'un filet à mailles doubles, les intéractions entre les fils peuvent être supposées plus fortes lorsque le côté de maille est plus court.

En modélisant la forme d'un demi-côté de maille par un arc de cercle, une relation polynômiale est révélée entre la courbure $\frac{1}{R}$ et l'ouverture de maille o_T dans la direction T (Fig. 4.19). En modélisant la forme d'un demi-côté de maille par un arc de cercle et en supposant qu'il n'y a pas de déformation axiale des fils, la relation entre les ouvertures calculées o_N et o_T, dans les directions N et T respectivement, est proche de la relation obtenue expérimentalement (Fig. 4.17). La courbure étant directement liée à la raideur en flexion avec l'hypothèse d'un comportement mécanique de poutre, l'étude de paramètres en fonction de l'ouverture o_T (ou o_N) apparaît cohérente.

Les essais de traction biaxiale montrent que plus l'effort Fm_N dans la direction N est grand, moins l'ouverture de maille o_T dans la direction T est grande, comme attendu (Fig. 4.20).

L'utilisation et la cohérence des trois types d'expériences sont validées par la comparaison des résultats (figures 4.21, 4.22, 4.23).

Enfin, le comportement mécanique visco-elasto-plastique observé dans les résultats expérimentaux apporte des informations pour la mise en place d'un protocole expérimental. Les mesures devraient être effectuées après, au moins, 30 minutes de fluage dans le cas d'essais de suspension et 15 minutes de relaxation dans le cas d'essais de traction uniaxiale. Dans le cas d'essais de traction biaxiale, la mesure de l'effet de la viscosité n'est pas possible avec l'équipement utilisé. Ainsi, l'effet de la viscosité est supposé négligeable. Ensuite, le comportement cyclique montre que le chargement doit être croissant, éventuellement interrompu par des étapes de fluage ou de relaxation.

8.5 Méthodes numériques

Pour commencer, un modèle quasi-analytique est présenté. Celui-ci est basé sur la théorie des poutres et autorise de large rotations. Il est proposé pour simuler les essais de traction uniaxiale, en supposant que la maille au centre de l'échantillon est soumise à un effort uniaxial pur dans la direction T.

Ensuite, trois modèles éléments finis sont présentés :

- Le code de calcul Abaqus Standard. Les côtés de maille sont modélisés par des poutres de Timoshenko. Un programme numérique implémenté en langage Python permet de simuler les essais sur filet et d'identifier la raideur à l'ouverture par identification inverse.

- Un modèle éléments finis 2D, basé sur la théorie des poutres, et utilisant une formulation corotationnelle. La formulation corotationnelle, présentée dans Le et al. (2011), permet de traiter le cas des grandes rotations et des petites déformations. Ce modèle est implémenté en langage Python et montre de bonnes performances de calcul et des résultats mécaniques en accord avec le logiciel commercial Abaqus Standard. Il est une première étape vers le développement d'un modèle 3D. De plus, il offre la possibilité de prendre en compte le cisaillement transverse dans les fils et d'utiliser, éventuellement, une loi de comportement non-linéaire.

- Un modèle éléments finis basé sur des éléments barres. C'est un modèle simple implémenté en langage C. Le modèle est présenté dans Morvan et al. (2016). Il permet de modéliser aussi bien des filets à mailles losanges que des filets à mailles hexagonales. Sur un problème mécanique simple de potence, les résultats obtenus avec le modèle éléments barres sont comparés à ceux obtenus avec une solution analytique de mécanique des milieux continus et le code de calcul Abaqus Standard. La comparaison montre que le modèle développé dans cette thèse peut décrire avec précision les déformations des côtés de maille dans un filet. Enfin, la simulation d'une poutre modélisant un côté de maille permet de vérifier que le modèle numérique éléments barres est plus précis que la solution asymptotique proposé par O'Neill.

Quelque soit le modèle utilisé, on connaît les forces dans le filet simulé, et les positions de ses noeuds. Ces positions permettent de calculer une fonction-objectif et d'identifier, en minimisant ou en cherchant le zéro de cette fonction, la valeur de la raideur à la flexion EI.

Dans le cas des essais de traction uniaxiale, la fonction-objectif est la différence entre la hauteur expérimentale et la hauteur numérique de la maille au milieu de l'échantillon testé. Le zéro de la fonction-objectif est recherché en utilisant la méthode de dichotomie.

Dans le cas des essais de suspension, la fonction-objectif est calculée avec deux méthodes : premièrement, la fonction-objectif est la distance entre les coordonnées des noeuds expérimentaux et numériques, et est minimisée en utilisant l'algorithme proposé par Nelder and Mead (1965) ; deuxièmement, la fonction-objectif est la différence entre la hauteur expérimentale et la hauteur numérique de l'échantillon

suspendu, et son zéro est recherché en utilisant la méthode de dichotomie. Après comparaison des deux méthodes, la deuxième méthode est plus simple et suffisamment précise.

Dans le cas des essais de traction biaxiale, la fonction-objectif est la différence entre les résultats de la division L_{sT}/L_{sN} obtenus expérimentalement et numériquement. L_{sT} et L_{sN} sont les longueurs totales de l'échantillon dans les directions T et N respectivement. Le zéro de la fonction-objectif est recherché en utilisant la méthode de dichotomie.

8.6 Résultats numériques

8.6.1 Mailles losanges

Dans cette partie, la raideur à la flexion est identifiée en supposant que les mailles ont une forme losange et en utilisant la méthode d'identification inverse présentée précédemment. Cela signifie que les noeuds sont modélisés par des points.

Les résultats des identifications à partir des essais de traction uniaxiale (partie 6.1.1), de suspension (partie 6.1.2), et de traction biaxiale (partie 6.1.3) sont présentés.

La figure 6.1 montre l'importance de prendre en compte la viscosité du matériau qui influence grandement la raideur à la flexion identifiée. Donc, avec l'hypothèse d'un comportement visco-elasto-plastique, les étapes de relaxation permettent de réduire l'effet de la viscosité et d'améliorer l'évaluation de la raideur à la flexion ; en effet, plus la durée de relaxation est grande, moins le temps a d'effet sur la valeur de EI. La figure 6.3 montre que l'ouverture o_T reste élevée durant la décharge (avec des étapes de relaxation de 15 minutes). Donc la maille ne revient pas à son état initial. La structure présente une déformation permanente ou une viscosité à long-terme.

La figure 6.1 montre que la raideur à la flexion identifiée avec le modèle analytique est inférieure à celle identifiée avec le code de calcul Abaqus Standard. La différence relative entre les deux courbes va de 4.40 % pour une force par maille de 1.59 N à 12.77 % pour une force par maille de 12.38 N. D'après le modèle éléments finis Abaqus Standard de l'essai de traction uniaxiale, la maille au milieu de l'échantillon est soumise à une force de traction dans la direction T et à une force de compression dans la direction N. Cependant, le modèle analytique ne prend en compte que l'effort de traction. Nous pouvons supposer que, pour obtenir la même ouverture de maille dans la direction T sans effort de compression, une raideur en flexion plus faible est nécessaire. Nous pouvons noter que pour un niveau de chargement faible, dans le cas d'un essai de traction uniaxiale, la raideur en flexion identifiée avec le

modèle analytique est proche de celle évaluée avec le modèle éléments poutres.

Les figures 6.2 et 6.3 montrent l'évolution de la raideur en flexion identifiée en fonction de la force Fm_T appliquée sur la maille et en fonction de l'ouverture o_T respectivement. Nous pouvons noter que la variation du paramètre EI durant l'essai est plus petite lorsque EI a été calculé à la fin de chaque étape de relaxation.

Durant l'effort de traction uniaxiale sur filets à mailles simples en PE *vert*, la force par maille au début des étapes de relaxation va de 2.40 N à 12.38 N (Fig. 6.2). Durant les essais de suspension sur le même type de filet, les échantillons sont soumis à des forces par maille appliquées dans le bas des filets allant de 0.3235 N à 2.775 N (Fig. 6.4). La force par maille appliquée sur les mailles les plus en haut va de 0.46 N à 2.91 N à cause du poids du filet. Le chargement appliqué sur les mailles durant les essais de suspension sur filets à mailles simples en PE *vert* représente environ le quart de l'effort appliqué durant l'essai de traction uniaxiale. Il faut noter que la raideur en flexion identifiée pour la valeur la plus petite de force par maille appliquée lors de l'essai de traction uniaxiale est proche des valeurs identifiées pour les essais de suspension.

Lorsque la force Fm_T augmente, et donc lorsque l'ouverture de maille augmente, les efforts de traction dans les côtés de maille augmentent, et nous pouvons nous attendre à une réduction du diamètre des fils. Un plus petit diamètre signifie un plus petit moment d'inertie I. Ainsi, nous pouvons supposer une réduction de EI lorsque l'effort augmente. Néanmoins, les résultats ne montrent aucune décroissance de EI lorsque Fm_T augmente. Dans les cas des filets à mailles simples en PE *vert* (Fig. 6.3), des filets à mailles doubles en PE *vert* (Fig. 6.6), des filets à mailles simples en PE *Breztop* (Fig. 6.8) et des filets à mailles simples en PA (Fig. 6.10), une augmentation de la raideur en flexion identifiée est observée. Cela peut être dû à la complexité de la structure tressée du fil : lorsque le niveau de chargement augmente, l'effort de cisaillement et le moment de flexion dans le fil augmentent, donc la forme de la section du fil peut changer grandement et affecter la raideur en flexion EI.

La comparaison des hauteurs numériques et expérimentales (Figs. 4.10 à 4.15) montre que le modèle éléments barres simule le champ de déformation hétérogène dans les échantillons de filet suspendus.

De plus, la figure 6.11 montre que dans le cas de filets à mailles doubles en PE *vert*, la raideur en flexion EI ne dépend pas du nombre de mailles dans l'échantillon : les raideurs à la flexion EI identifiées sur des filets de tailles 4x10 et 5x25 mailles sont similaires.

Les figures 6.5 à 6.10 montrent que le coefficient de variation de EI est plus grand lorsque la valeur de Fm_T est proche de zéro. Dans le cas de forces plus éle-

vées, le coefficient de variation est inférieur à 10%.

Les essais de traction biaxiale permettent l'étude de l'influence du chargement Fm_N dans la direction N sur la raideur à la flexion EI évaluée. La raideur à la flexion identifiée dans le cas des essais de traction biaxiale est révélée plus grande que dans le cas des essais de suspension pour une même ouverture de maille o_T (figures 6.12 et 6.14).

L'augmentation de la raideur en flexion identifiée lorsque la force par maille Fm_T augmente, et les différences entre les résultats des identifications à partir des essais de traction biaxiale et des essais de suspension pourraient être expliquées par le fait que la taille des noeuds n'est pas prise en compte.

8.6.2 Mailles hexagonales

En utilisant le modèle éléments barres et en prenant en compte la taille des noeuds, la raideur à la flexion des filets à mailles doubles en PE *vert* de tailles 4x10 et 5x25 mailles, avec des côtés de maille de longueurs 50 mm et 60 mm, est identifiée.

Comme attendu, la raideur en flexion identifiée EI est plus faible lorsque nous prenons en compte la longueur des noeuds dans la direction N (figures 6.19, 6.20, 6.23 et 6.24). En effet, plus le noeud est long dans la direction N, plus le côté de maille est court et plus l'angle entre le côté de maille et la direction N est grand.

En modélisant le noeud avec une longueur de 10 mm, nous n'observons pas la même évolution de la raideur en flexion identifiée que dans le cas d'un noeud modélisé par un point (maille losange). Premièrement, la raideur à la flexion n'augmente plus avec la force Fm_T (figures 6.19 et 6.23). De plus, nous pouvons supposer une raideur à la flexion constante en fonction de la force par maille Fm_T. Puis, l'évolution en fonction de l'ouverture o_T est plus cohérente. En effet, la figure 6.20 révèle une continuité entre les évolutions des raideurs à l'ouverture des échantillons de tailles 4x10 et 5x25 mailles, malgré une prétension dans une direction différente et une taille en nombre de mailles différente. Et les identifications à partir des essais de traction biaxiale révèlent une continuité avec les évolutions des raideurs en flexion en fonction de l'ouverture o_T (Fig. 6.24) d'échantillons soumis à 3 types différents de chargement biaxiale. Ainsi, nous pouvons supposer que la raideur en flexion ne dépend pas de la direction de prétension, du nombre de mailles dans les échantillons suspendus ou de l'effort Fm_N appliqué dans la direction N dans le cas d'essais de traction biaxiale, mais la raideur en flexion dépend de l'ouverture dans la direction T.

Alors que nous nous attendions à obtenir une raideur en flexion identique, la figure 6.22 montre une raideur en flexion plus faible avec un côté de maille de longueur 60 mm qu'avec un côté de maille de longueur 50 mm, dans le cas de filets

à mailles doubles en PE *vert*. Cette différence peut s'expliquer par l'effet du noeud sur le comportement mécanique du côté de maille et par les intéractions, entre les deux fils constituant le côté de mailles, qui dépendent en partie de la longueur du côté de maille. De plus, bien que les échantillons de filet aient la même structure et soient constitués des mêmes fils, ils sont soumis à des conditions de fabrication différentes (température, durée, efforts de traction). Des conditions de fabrication différentes peuvent expliquer des comportements mécaniques différents. Nous notons aussi que, malgré le niveau de chargement différent, la forme de l'évolution de la raideur en flexion en fonction de l'ouverture est très similaire dans les deux cas de filets.

Les résultats d'identification à partir des essais de suspension et de traction biaxiale sont proches : les évolutions des raideurs en flexion EI identifiées en fonction de l'ouverture o_T sont quantitativement et qualitativement proches (Fig. 6.26).

La courbure dans les fils est approximée en modélisant un demi-côté de maille par un arc de cercle de rayon R. L'évolution de la raideur à la flexion identifiée en fonction de la courbure κ (Fig. 6.27) est cohérente avec l'évolution de la raideur en flexion EI identifiée en fonction de l'ouverture o_T (Fig. 6.26).

En supposant que la raideur en flexion EI dépende de l'ouverture o_T dans la direction T (liée à l'ouverture o_N de la maille dans la direction N et à la courbure du fil), et non du niveau d'effort appliqué, nous pouvons écrire que les essais avec un chargement plus élevé ne sont pas utiles pour évaluer EI, c'est-à-dire, indirectement, pour évaluer la résistance à l'ouverture d'une maille. De plus, les mesures lors des essais de suspension nous permettent d'évaluer un EI proche de celui identifié à partir d'essais de traction biaxiale, ce qui valide la méthode d'identification utilisant des essais de suspension.

8.7 Conclusions

8.7.1 Implications pour la recherche

La thèse offre une avancée scientifique pour l'évaluation de la résistance à l'ouverture des mailles :

- Malgré la complexité de la structure et du comportement mécanique d'un filet, un simple **modèle élément barre** permettant la simulation d'un filet soumis à de larges déformations est proposé. Contrairement aux modèles existants dans la littérature, le modèle élément barre a reproduit le champ de déformation hétérogène du filet. Un compromis est fait entre la simplicité et la précision.

- La thèse offre **des données expérimentales** provenant d'essais de traction uniaxiale, d'essais de suspension et d'essais de traction biaxiale réalisés sur un large éventail d'échantillons de filets : deux matériaux (polyéthylène ou polyamide), deux types de côtés de maille (simple ou double fil), trois tailles d'échantillon (3x3, 4x10 et 5x25 mailles).
- Le **comportement mécanique visco-elasto-plastique** des échantillons de filet a été révélé par des résultats expérimentaux.
- Le développement d'une **méthode plus précise et plus simple** pour évaluer la résistance à l'ouverture des mailles : la méthode est basée sur des essais expérimentaux de suspension, comme proposé par De la Prada and Gonzales (2013), nécessitant un dispositif expérimental plus simple que la machine de traction biaxiale développée par Sala et al. (2007), et sur un modèle numérique éléments barres permettant la simulation d'une déformation non uniforme dans les panneaux de filet suspendus. Un article décrivant cette méthode a été soumis et accepté pour publication par le journal "Ocean Engineering" (Morvan et al., 2016). De plus, la méthode prend en compte le comportement mécanique visco-elasto-plastique des filets : tout d'abord les mesures étaient effectuées après des étapes de fluage de 30 minutes pour réduire l'effet de la viscosité ; ensuite le chargement appliqué était monotone croissant pour éviter l'effet d'hystérésis d'un chargement cyclique. Les échantillons de filet étaient initiallement soumis à une étape de prétension, introduisant une déformation plastique mais n'influant pas sur la raideur en flexion identifiée, pour éviter tout effet de glissement des noeuds.
- Nous avons montré la relation entre la raideur en flexion identifiée et l'ouverture de maille dans la direction T. De plus, il a été révélé, dans le cas de filet en PE vert à doubles mailles, que la raideur en flexion était **identique** qu'elle soit identifiée à partir des résultats expérimentaux des **essais de suspension** ou des **essais de traction biaxiale**. Ce résultat a validé la méthode pour le cas de filet en PE vert à mailles doubles.
- L'influence de la taille du noeud modélisé numériquement sur l'évolution de la raideur en flexion identifiée en fonction du chargement appliqué ou de l'ouverture de maille dans la direction T a été montrée.

8.7.2 Suggestions pour les travaux futurs

Les travaux possibles sont nombreux :

- L'évolution révélée de la raideur à l'ouverture identifiée en fonction de l'ouverture de maille et l'influence de la longueur des côtés de maille sur la raideur en flexion identifiée ont montré que le modèle numérique pourrait être amélioré en prenant en compte des phénomènes influant sur le comportement mécanique des filets. Le cisaillement et la torsion des fils pourraient être modélisés.

Les intéractions de contact-frottement des fils pourraient aussi être modélisés pour apporter de la précision aux résultats numériques et apporter de nouveaux éléments pour la compréhension du comportement mécanique des filets. Le modèle pourrait être amélioré en se basant sur les données expérimentales fournies par cette thèse.

- Les comparaisons des raideurs à la flexion identifiées à partir des mesures lors des essais de suspension et des essais de traction biaxiale sur d'autres types de filets pourrait apporter une validation solide de la méthodologie pour l'identification de la raideur en flexion utilisant des essais de suspension. Dans le cas de résultats ne validant pas cette hypothèse, et par souci de simplicité, nous recommanderions la définition des raideurs en flexion identifiées par la méthode utilisant les essais de suspension comme référence pour la mise en place d'une réglementation sur la résistance à l'ouverture des mailles dans les engins de pêche.

- L'influence de la longueur des côtés de maille sur les raideurs en la flexion identifiées pourrait être étudiée plus largement en testant des échantillons de filet avec un large évantail de longueurs de côtés de maille différentes. Ces échantillons aux côtés de maille de longueurs différentes devraient être constitués du même fil, et devraient avoir été fabriqués dans les mêmes conditions (température, chargement et durée de l'étirage à chaud).

- Les noeuds pourraient être modélisés avec plus de précision. Le modèle pourrait prendre en compte la taille des noeuds dans les directions T et N, les intéractions entre les fils des côtés de maille et les noeuds, le possible changement de section du fil (en particulier près du noeud), et l'asymétrie dans la forme des noeuds.

- Parce qu'il est nécessaire de réglementer la sélectivité des engins de pêche et d'être capable d'identifier la résistance à l'ouverture des mailles avec une méthode simple et un équipement peu cher, l'outil numérique d'identification développé dans cette thèse et basé sur un modèle éléments barres pourrait être rendu portable. Nous pourrions imaginer, par exemple, un outil numérique gratuit utilisable avec un smartphone. Dans ce cas, nous pourrions nous attendre à une grande utilisation de la méthode présentée dans cette thèse.

- L'influence du vieillissement des filets soumis à un environnement marin sur la résistance à l'ouverture des mailles dans les engins de pêche devrait être étudiée. Nous pourrions imaginer une collaboration avec des pêcheurs professionnels : en testant des filets avant et après plusieurs mois d'utilisation. Un tel travail pourrait permettre la construction d'un modèle pouvant simuler l'évolution de la raideur à l'ouverture des mailles dans les engins de pêche en fonction de leur utilisation.

Appendix

A Numbering of the meshes in a netting sample

The meshes are numbered from the left to the right and from the top to the bottom in a netting sample.

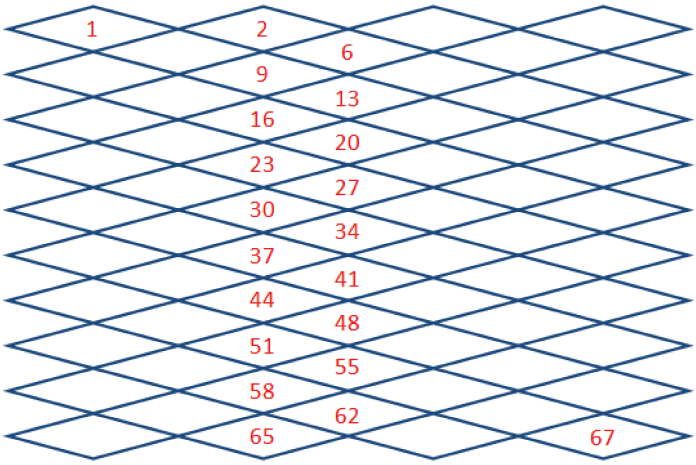

Figure A.1 – Numbering of the meshes in a 4x10-mesh netting sample.

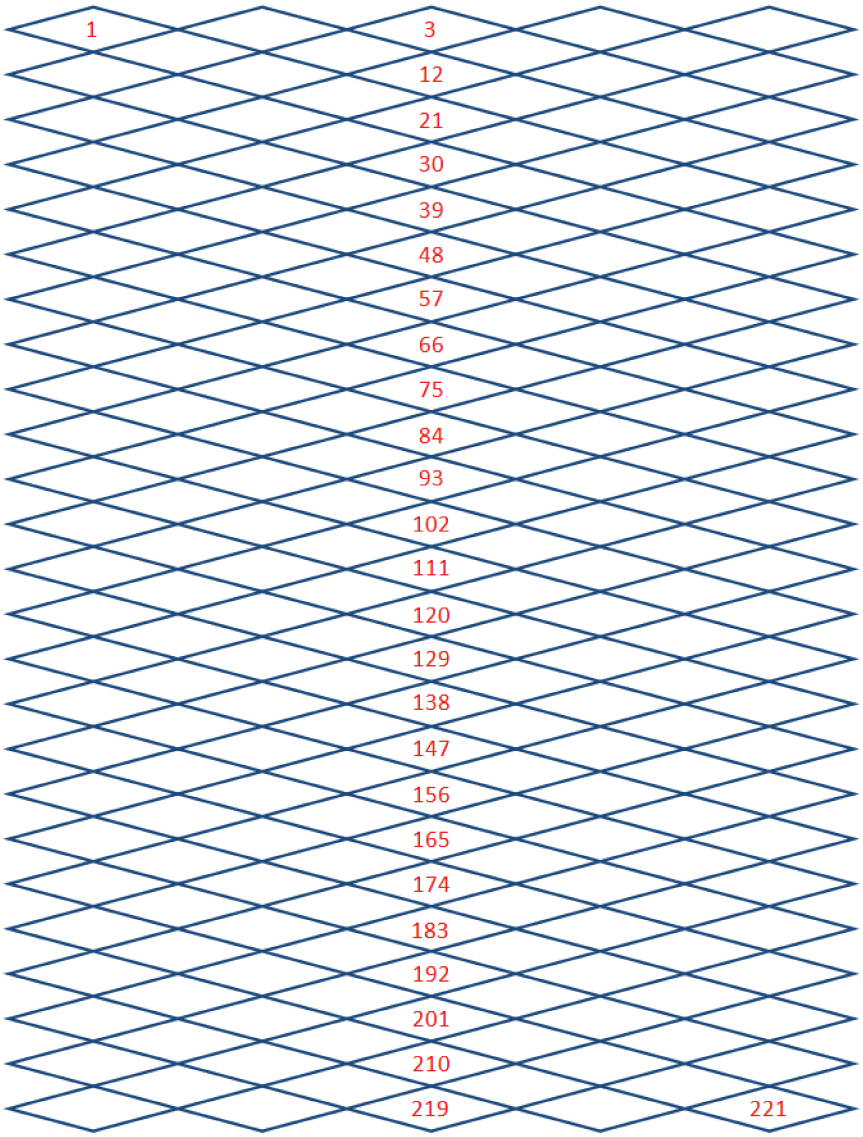

Figure A.2 – Numbering of the meshes in a 5x25-mesh netting sample.

APPENDIX

B The half mesh side shape modelled by a circle arc.

Figure B.1 defines some geometrical parameters in a deformed mesh side O_1O_2: I is the centre of the mesh side, θ_0 is the angle between the N-direction and the mesh side initially, θ_0 is the angle between the N-direction and the deformed mesh side.

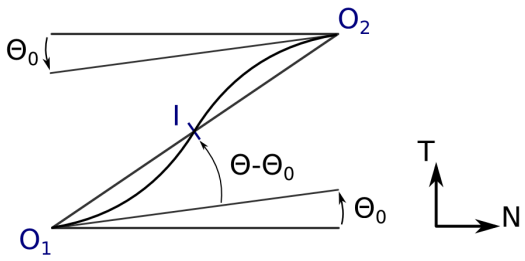

Figure B.1 – Deformed mesh side.

B.1 Expressions of the curvature

The half mesh side is assumed to be a circle arc with a radius R (Fig. B.2). With this assumption, we can write:

$$\sin(\theta - \theta_0) = \frac{O_1 I}{2R} \tag{B.1}$$

Then:

$$R = \frac{O_1 I}{2\sin(\theta - \theta_0)} \tag{B.2}$$

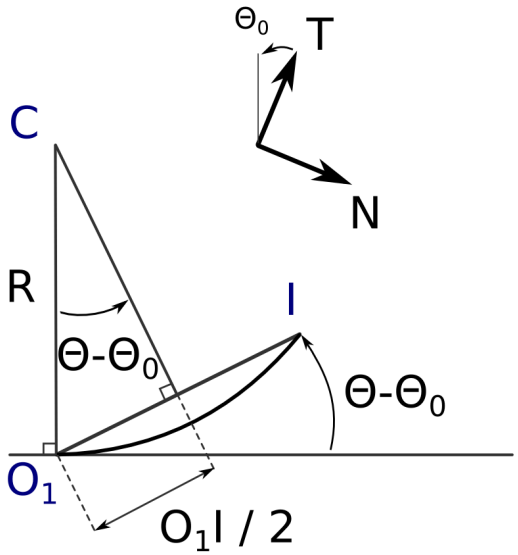

Figure B.2 – The half mesh side is assumed to be a circle arc with a radius R.

Hence:

$$\frac{1}{R} = \frac{2\sin(\theta - \theta_0)}{O_1 I} \tag{B.3}$$

B.2 Expression of $O_1 I$ and θ

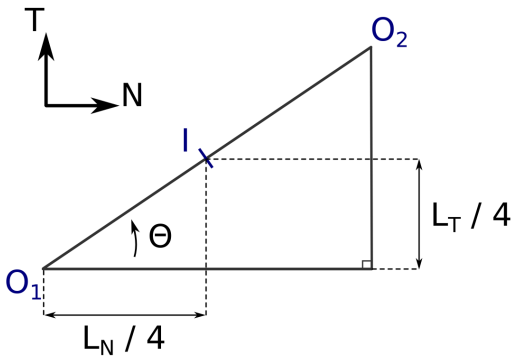

Figure B.3 – Lengths $L_N/4$ and $L_T/4$ of a half mesh side in the N- and T- direction respectively.

First, we calculate the length $O_1 I$ as a function of the openings o_N and o_T in the N- and T- direction respectively.

We have:

$$O_1I = \sqrt{(\frac{L_N}{4})^2 + (\frac{L_T}{4})^2} \tag{B.4}$$

That means:

$$O_1I = \sqrt{(o_N\frac{L_{ms}}{4})^2 + (o_T\frac{L_{ms}}{4})^2} \tag{B.5}$$

Thus:

$$O_1I = \frac{L_{ms}}{4}\sqrt{{o_N}^2 + {o_T}^2} \tag{B.6}$$

Finally, θ is calculated. From Figure B.3, we write:

$$\theta = \arctan\frac{L_T/4}{L_N/4} \tag{B.7}$$

$$\theta = \arctan\frac{L_T}{L_N} \tag{B.8}$$

Thus, with the definition of the openings:

$$\theta = \arctan\frac{o_T}{o_N} \tag{B.9}$$

B.3 Expressions of o_N and o_T

By assuming that there is no stretching in the twine, we write:

$$L_{ms} = 4R(\theta - \theta_0) \tag{B.10}$$

with L_{ms} the length of the mesh side.

Thus, we have:

$$R = \frac{L_{ms}}{4(\theta - \theta_0)} \tag{B.11}$$

Equation B.3 gives:

$$O_1I = 2R\sin(\theta - \theta_0) \tag{B.12}$$

Let r be the distance between the two extremities O_1 and O_2 (Fig. B.1). Using Equation B.12, we have:

$$r = 4R\sin(\theta - \theta_0) \tag{B.13}$$

By replacing R with Equation B.11, we obtain:

$$r = L_{ms}\frac{\sin(\theta - \theta_0)}{\theta - \theta_0} \tag{B.14}$$

And o_N and o_T are expressed:

$$o_N = \frac{2r\cos(\theta)}{L_{ms}} \tag{B.15}$$

$$o_T = \frac{2r\sin(\theta)}{L_{ms}} \tag{B.16}$$

APPENDIX

C Forces in a codend.

A dragged 100x100-mesh codend was simulated with the model proposed by Priour (2013) and presented in Section 2.2. The mesh shape was assumed to be diamond and the speed value was 1 $m.s^{-1}$.

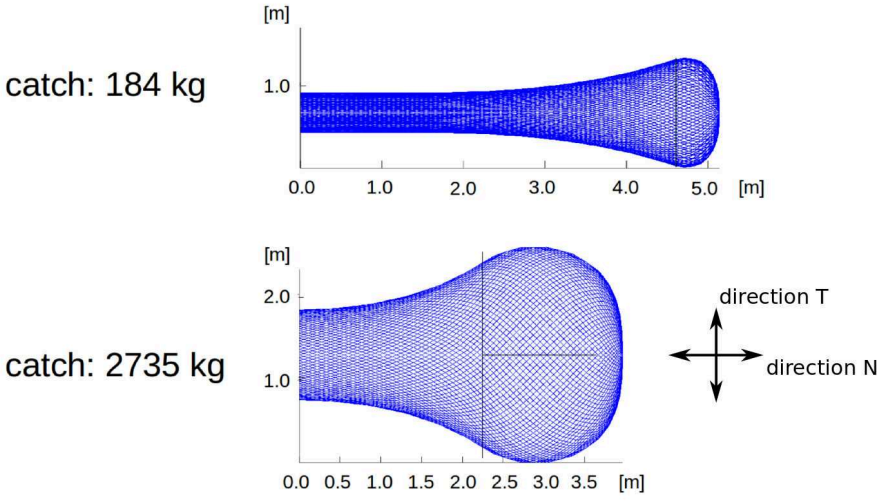

Figure C.1 – Shapes of a 100x100-mesh codend subject to two different catches. The codend was simulated with the model proposed by Priour (2013).

Figure C.1 shows the shape of a codend subject to two different catches. In Figure C.2, the forces by mesh Fm_N and Fm_T in the N- and the T-direction respectively are represented as a function of the catch. The force values were calculated using the tensile forces in the mesh sides of each simulated codend near the limit shaped by the catch, that means where the fishes could escape.

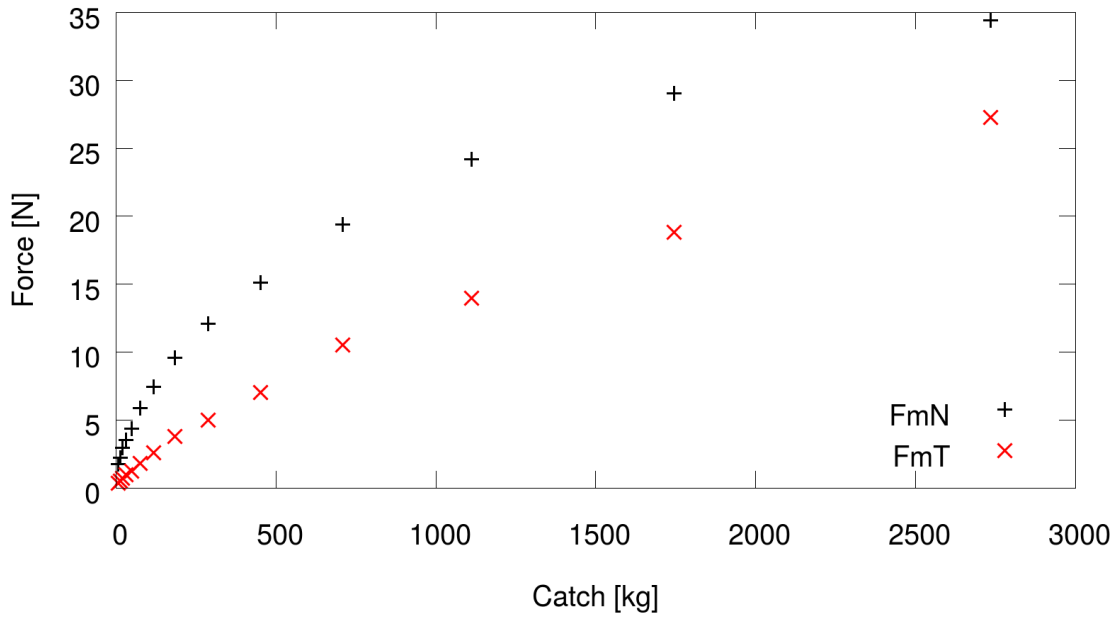

Figure C.2 – Forces by mesh Fm_N and Fm_T in the N- and the T-direction respectively in a dragged 100x100-mesh codend as a function of the catch. The codend was simulated with the model proposed by Priour (2013).

Appendix

D Compression transverse force in a netting sample subject to uniaxial tension.

D.1 4x10-mesh netting sample

Vertical uniaxial tensile tests of a 4x10-mesh netting sample were simulated with the Abaqus Standard tool to study the forces applied on the mesh in the middle of the netting panel, that is to say the studied mesh during experimental uniaxial tensile tests.

Tables D.1 and D.2 show the force by mesh Fm_N in the N-direction in the meshes along the plane of symmetry of the half sample (Fig. D.1) in cases of a force by mesh in the T-direction of 1.0 N and 12.5 N respectively.

Mesh number	Fm_N [N]	Fm_N/Fm_T [-]
6	3.62	3.62
13	2.20	2.20
20	-0.05	-0.05
27	-0.26	-0.26
34	-0.32	-0.32
41	-0.26	-0.26
48	-0.05	-0.05
55	2.20	2.20
62	3.62	3.62

Table D.1 – Simulation of the vertical uniaxial tensile test of a 4x10-mesh netting sample with the Abaqus Standard software tool: force by mesh Fm_N in the N-direction in the meshes along the plane of symmetry of the half sample (Fig. D.1). The netting sample was subjected to a force by mesh of 1.0 N in the T-direction. The strain of the simulated netting was 99 %. The bending stiffness EI of the netting was 4.11 10^{-4} N. The length of the mesh sides was 0.06 m and the mesh angle at rest α_0 was 14 $^\circ$. The mesh numbers are defined in Figure A.1.

Mesh number	Fm_N [N]	Fm_N/Fm_T [-]
6	26.52	2.12
13	14.41	1.15
20	0.62	0.05
27	-0.37	-0.03
34	-0.52	-0.04
41	-0.37	-0.03
48	0.62	0.05
55	14.41	1.15
62	26.52	2.12

Table D.2 – Simulation of the vertical uniaxial tensile test of a 4x10-mesh netting sample with the Abaqus Standard software tool: force by mesh Fm_N in the N-direction in the meshes along the plane of symmetry of the half sample (Fig. D.1). The netting sample was subjected to a force by mesh of 12.5 N in the T-direction. The strain of the simulated netting was 423 %. The bending stiffness EI of the netting was 4.11 10^{-4} N. The length of the mesh sides was 0.06 m and the mesh angle at rest α_0 was 14 $^\circ$. The mesh numbers are defined in Figure A.1.

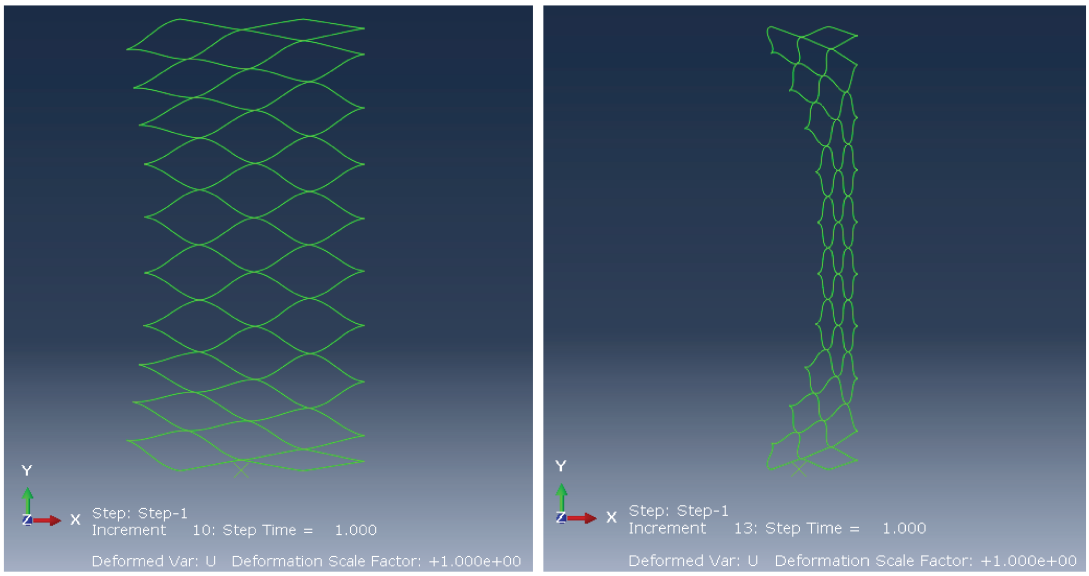

Figure D.1 – Simulated 4x10-mesh netting sample with the Abaqus Standard software tool. The rotations in the netting were assumed to be large. The netting sample was subjected to a force by mesh in the T-direction of 1.0 N (left) and 12.5 N (right). The bending stiffness EI of the netting was 4.11 10^{-4} N. The length of the mesh sides was 0.06 m and the mesh angle at rest α_0 was 14 $^\circ$.

Bibliography

C. Balash. *Prawn Trawl Shape due to Flexural Rigidity and Hydrodynamic Forces.* PhD thesis, University of Tasmania, 2012.

C. Balash, D. Sterling, J. Binns, G. Thomas, and N. Bose. Drag characterisation of prawn-trawl bodies. *Ocean Engineering*, 113:18–23, 2016.

G. Bles, W.K. Nowacki, and A. Tourabi. Experimental study of the cyclic visco-elasto-plastic behaviour of a polyamide fibre strap. *International Journal of Solids and Structures*, 46:2693–2705, 2009.

L. K. Boerema. Some experiments on factors influencing mesh selection in trawls. *ICES Journal of Marine Science*, 21 (2):175–191, 1956.

M. K. Broadhurst, D. J. Sterling, and R. B. Millar. Increasing lateral mesh openings in penaeid trawls to improve selection and reduce drag. *Fisheries Research*, 170: 68–75, 2015.

Amelia De la Prada and Manuel Gonzales. Nonlinear stiffness models of a net twine to describe mesh resistance to opening of flexible net structures. *Journal of engineering for the maritime environment*, 2013.

Amelia De la Prada and Manuel Gonzales. Quantifying mesh resistance to opening of netting panels: experimental method, regression models, and parameter estimation strategies. *Journal of Marine Science*, 2014.

The State of World Fisheries and Aquaculture 2016. Contributiong to food security and nutrition for all. FAO, Rome, 2016.

B. Herrmann, D. Priour, and A. Krag Ludvig. Theoretical study of the effect of round straps on the selectivity in a diamond mesh cod-end. *Fisheries Research*, 80:148–157, 2006.

Bent Herrmann, Harald Wienbeck, Waldemar Moderhak, Daniel Stepputtis, and Ludvig Ahm Krag. The influence of twine thickness, twine number and netting orientation on codend selectivity. *Fisheries research*, 145:22–36, 2013.

ISO. Fishing nets - netting - basic terms and definitions. In *International Standard Organisation 1107*, 2003.

Andrew Johnson and Cheslav Balash. Experimental modelling of transverse oscillations in aquaculture netting parallel to the flow - sounds baffling. *Journal of China Ocean Engineering*, 29(3):391–400, 2015.

G. Klust. *Fibre Ropes for Fishing Gear*. Fishing News Books Ltd., 1983.

Thanh-Nam Le, Jean-Marc Battini, and Mohammed Hjiaj. Efficient formulation for dynamics of corotational 2d beams. *Comput Mech*, 48:153–161, 2011.

Waldemar Moderhak. Influence of twine parameters on the shapes of meshes and t90 codends. In *International Workshop Methods for the Development and Evaluation of Maritime Technologies (DEMaT'07), ROSTOCK, Germany*, 2007.

B. Morvan, D. Priour, Z. Guede, and G. Bles. Finite element model for the assessment of the mesh resistance to opening of fishing nets. *Ocean Engineering*, 123:303 – 313, 2016. ISSN 0029-8018. doi: http://dx.doi.org/10.1016/j.oceaneng.2016.07.026. URL `http://www.sciencedirect.com/science/article/pii/S0029801816302736`.

J.A. Nelder and R. Mead. A simplex method for function minimization. *The Computer Journal*, 7:308–313, 1965.

O'Neill. Bending of twines and fibres under tension. *Journal of the Textile Institute*, 93:1–10, 2002.

FG O'Neill. A theoretical study of the factors which influence the measurement of fishing netting mesh size. *Ocean engineering*, 30(16):2053–2063, 2003.

J. M. Ortega and W. C. Rheinboldt. *Iterative Solution Of Nonlinear Equations in Several Variables*. Society for Industrial and Applied Mathematics, 2000. ISBN 978-0-89871-461-6. doi: 10.1137/1.9780898719468.

E. P. Popov and T. A. Balan. *Engineering Mechanics of Solids*. Pearson, 1998.

D. Priour and J.Y. Cognard. Investigation of methods for the assessment of the flexural stiffness of netting panels. In *10th International Workshop Methods for the Development and Evaluation of Maritime Technologies (DEMaT'11), SPLIT, Croatie 2011.*, 2011.

Daniel Priour. *A Finite Element Method for Netting. Application to Fish Cages and Fishing Gear*. Springer Netherlands, 1st edition, 2013. ISBN ISBN 978-94-007-6844-4.

J.H.B. Robertson and P.A.M. Stewart. A comparison of size selection of haddock and whiting by square and diamond mesh codends. *J. Cons. Int. Explor. Mer*, 44:148–161, 1988.

A. Sala, A. Lucchetti, and G. Buglioni. The change in physical properties of some nylon (pa) netting samples before and after use. *Fisheries Research*, 69(2):181 – 188, 2004.

A. Sala, F.G. O'Neill, G. Buglioni, A. Lucchetti, V. Palumbo, and R.J. Fryer. Experimental method for quantifying resistance to the opening of netting panels. *ICES Journal of Marine. Science*, 64:1573–1578, 2007.

The European Parliament and the European Council. Regulation (eu) no 1380/2013 on the common fisheries policy, 11th December 2013.

Tadeusz Uhl. The inverse identification problem and its technical application. *Archive of Applied Mechanics*, 77(5):325–337, 2007. ISSN 1432-0681. doi: 10.1007/s00419-006-0086-9. URL `http://dx.doi.org/10.1007/s00419-006-0086-9`.

Jean Weissenberger. Fisheries: why technical measures matter. Technical report, European Parliamentary Research Service, 2 June 2014.

Méthodologie pour l'évaluation de la résistance à l'ouverture d'une maille de filet

Résumé : L'évaluation de la résistance à l'ouverture des mailles dans les filets de pêche est un enjeu important pour l'évaluation de la sélectivité des chaluts, et plus largement des engins de pêche. Les objectifs de cette thèse sont de développer et d'évaluer une méthodologie pour l'évaluation de la résistance à l'ouverture des mailles dans les filets. Différentes méthodes existent déjà (Sala et al., 2007; Priour and Cognard, 2011; Balash, 2012; De la Prada and Gonzales, 2014). Notre objectif est de proposer une méthode expérimentale simple et ne nécessitant pas d'équipements coûteux pour pouvoir être déployée facilement dans les laboratoires et dans l'industrie de la pêche, combinée avec un modèle numérique capable de représenter le comportement mécanique non-linéaire d'un filet. Le filet, constitué de fils tressés ou toronnés, en Polyéthylène ou Polyamide, présente une structure complexe. De plus, les filets peuvent être soumis à de grandes déformations. Afin d'étudier la réponse mécanique des filets à différents types de sollicitations et de créer une base de données expérimentale, de nombreux essais ont été effectués sur un large éventail de filets de pêche. Plusieurs méthodes numériques pour l'évaluation de la résistance à l'ouverture des mailles à partir de données expérimentales ont été développées. Ces travaux offrent une avancée scientifique pour l'évaluation de la résistance à l'ouverture des mailles : malgré le comportement mécanique visco-élasto-plastique des échantillons de filet, une méthodologie plus simple et plus précise que celles existantes, basée sur un dispositif expérimental simple et un modèle éléments finis libre de droits, est présentée.

Mots-clés : filet, maille, résistance à l'ouverture, fil tressé, raideur en flexion, expérience, modèle numérique, grande déformation, comportement mécanique, identification inverse, polyéthylène, polyamide.

Methodology for the evaluation of the resistance to opening of a netting mesh

Abstract: The evaluation of the mesh resistance to opening in fishing nets is an important issue to assess the selectivity of trawls, and more broadly of fishing gear. The objectives of this thesis are to develop and to assess a methodology for the evaluation of the mesh resistance to opening in netting structures. Several methods are already proposed (Sala et al., 2007; Priour and Cognard, 2011; Balash, 2012; De la Prada and Gonzales, 2014). This thesis aims at proposing a simple experimental method that does not require expensive devices to be easily spread in laboratories and in the fishing industry, a simple test combined with a numerical model able to represent the non-linear mechanical behaviour of a tested netting panel. The netting structure, constituted of braided or stranded twines, made of Polyethylene or Polyamide, is complex. Moreover, the fishing nets can be subjected to large deformation. In order to study the mechanical response of netting samples to different types of solicitations and to obtain experimental data, numerous experimental tests were performed on a large range of netting samples. Several numerical methods for the evaluation of the mesh resistance to opening using experimental data were developed. This work offers scientific advance for the evaluation of the mesh resistance to opening: despite the visco-elasto-plastic mechanical behaviour of netting samples, one more accurate and simpler methodology than the existing ones, based on a simple experimental set up and on a free of rights finite element model, is presented.

Keywords: netting, mesh, resistance to opening, braided twine, bending stiffness, experiment, numerical model, large deformation, mechanical behaviour, inverse identification, polyethylene, polyamide.